A Novel Technique for Evaluating The Degradation of Engine Components Non-destructively

A thesis submitted for the degree of Doctor of Philosophy

by

Md. Shawkat Ali

Department of Mechanical Engineering
Brunel University

September 2002

Abstract

Impedance spectroscopy (IS) was used to evaluate the microstructural changes of a thermally-grown oxide (TGO) layer on a nickel-based superalloy or bond coat, with or without a thermal barrier coating (TBC) system, at various temperatures. TBC is used for hot section parts of gas turbine engine, such as turbine blades and vanes. However, spallation of TBC can take place due to long-term operation at high temperature. The spallation is mainly caused by both microstructural changes and thermal stresses as a result of oxide layer (mainly alumina) formation and growth at the interface between the TBC and bond coat. The electrical resistance and capacitance of the oxide layer, formed from oxidation of IN738LC superalloy at high temperature, were obtained from fitting the results of the measured impedance diagrams based on an equivalent circuit model. The equivalent circuit model should represent the features of the oxide layer or the TBC system. The electrical resistance of the oxide layer increased with increasing oxidation time for samples exposed to air at 900°C. Similar results were obtained for the NiCrCoAlY bond coat samples and the TBC systems. The capacitance decreased with increasing thickness of the alumina layer.

The activation energy of electrical conduction was used to characterise the alumina layer formed on the bond coat at 900°C, 1000°C and 1100°C. The activation energy values for the alumina layer, formed at various temperatures, decrease with increasing impurity or porosity. Changes in the electrical properties of TGOs are correlated with those in their microstructure and microchemistry. The degradation of a TBC can be identified, when the electrical resistance of the TGO decreases with increasing oxidation time. The fast decrease in resistivity corresponds to the compositional change in the TGO from α-Al_2O_3 to a mixture of α-Cr_2O_3 and (Ni or Co)(Cr or Al)$_2O_4$ spinel. The disappearance of α-Al_2O_3 in the TGO makes the scale non-protective and leads to cracks and spallation of TBCs.

Non-destructive testing of the crack formation in a TBC system is essential for predicting the failure and lifetime of TBCs in service. IS was used to evaluate the crack formation in the TBC system due to thermal cycling. During the thermal

cycling, cracks initiated and propagated along the interface between the TGO and the yttrium stabilised zirconia (YSZ), used as a TBC. This caused the spallation of the TBC eventually. The propagation of cracks at the interface of TGO/YSZ was found to contribute to an increase in the interfacial impedance. The interfacial area determines the interfacial resistance corresponding to the oxygen reaction. Therefore, the crack propagation induced an increase of the interfacial resistance, whereas the interfacial capacitance showed no trend in its alteration with the propagation of the cracks. As a result, the relaxation frequency of the interface moved towards a lower frequency during the propagation of the cracks. Therefore, impedance spectroscopy has been used to examine the crack formation in TBC system non-destructively.

By using scanning electron microscopy and X-ray diffraction techniques, the composition and microstructure of the oxide scales were examined. It was found that their electrical properties were determined, not only by the microstructure of the oxide scales, but also by the composition of the oxide scales. By determining the relationship between the electrical properties, microstructure and composition of the oxide scales, IS could be used as a non-destructive technique for monitoring the oxidation of metallic alloys at high temperature in gas turbine engine components.

Contents

Acknowledgements

I would like to express my deepest gratitude to my supervisor, Dr. Ping Xiao, for his encouragement and guidance throughout my PhD studies. I am grateful to all the technical staff and secretaries in the Department of Materials Engineering and Department of Mechanical Engineering, for their support and help in various ways. Thanks are due to Dr. Sue Woodise for her friendly attitude and professional instruction in setting up the XRD.

I would like to thank my colleagues Junfa Mei, Junqin Li, Shenhua Song, Ammer Jadoon and Xin Wang, for the jokes and friendly arguments.

I want to thank my wife, Bedana Khanom for her patience, support and encouragement throughout all these difficult times. I thank my daughters Anneka Affridha Ali, Nabilah Tasneem Ali, Faizah Tasfia Ali and my son Md Farhan Ali, who were my strength to finish this thesis.

I gratefully acknowledge the assistance of the late Dr Adrian Sanders (Alstom gas turbine Ltd) for supplying samples and would also like to express my gratitude to EPSRC and Alstom gas turbine Ltd for jointly funding the work at Brunel University.

List of Publications

This thesis describes research carried out by the author in the Department of Materials Engineering initially and then the Department of Mechanical Engineering at Brunel University, under the supervision of Dr. Ping Xiao. Publications that have been generated during my PhD studies are listed as follows:

1. Md Shawkat Ali and Ping Xiao, "Characterisation of Oxide Scales Formed on Nickel Superalloy using Impedance Spectroscopy", Materials at High Temperatures, Volume 17, Number 1, 2000, Pages 7-12.
2. Md Shawkat Ali, Shenhua Song and Ping Xiao, "Evaluation of Degradation of Thermal Barrier Coatings using Impedance Spectroscopy", Journal of the European Ceramic Society, Volume 22, Issue 1, January 2002, Pages 101-107.
3. Md Shawkat Ali, Shenhua Song and Ping Xiao, "Degradation of thermal barrier coatings due to thermal cycling up to 1150°C", Journal of Materials Science, Volume 37, Issue 10, May 2002, Pages 2097-2102.
4. Md Shawkat Ali and Ping Xiao, "Non-Destructive Evaluation of Crack Formation in Thermal Barrier Coatings Using Impedance Spectroscopy", submitted to "Surface and Coating Technology".

Some of results presented in this thesis have been published as follows: part of chapter 4 is based on the results published in publication 1; chapter 6 was written with the results published in publication 2; chapter 7 was written with the results presented in publication 4.

Declaration

I declare that, to the best of my knowledge, no portion of the work referred to in this thesis has been submitted in support of an application for another degree or qualification of this or any other university, or other institute of learning.

Md. Shawkat Ali

Dedication

This work is dedicated to my parents,
late Mr Md Abdul Fattah and Mrs Husne-ara Begum
for their endless support and encouragement towards my education.

1. Introduction

1.1. Non-destructive Evaluation of Degradation in Gas Turbine Engine by Impedance Spectroscopy

Applying thermal barrier coatings (TBCs) can reduce the effect of severe temperatures on blades or vanes. These ceramic coatings are good thermal insulators and reduce the heat transfer from the hot gas stream to the blade or vane [Miller, 1995]. A bond coat typically of MCrAlY alloy is applied to metal substrates before application of a TBC. The MCrAlY overlay coatings are complex Ni and/or Co based-alloys in their own right and form a coherent alumina layer on exposure to the atmosphere at high temperature, which provides good protection from oxidation up to an intermediate temperature of 900°C [Seth et al., 1995]. Chromium (15-30%) and Aluminium (6-12%) provide corrosion protection while Yttrium (0.1- 0.5%) improves oxide scale adhesion that is particularly important during thermal cycling of components [Seth et al., 1995]. The primary degradation mechanism is spalling of the TBC resulting from oxidation at the bond coat/TBC interface. Development of a non-destructive method for characterising these systems is important to monitor degradation of TBC systems in engine components while they are still in service without removing them. Currently, there is no suitable non-destructive method that can be used to determine the degradation of engine components with TBCs, because the degradation actually starts under the TBC layer and not in the TBC layer itself. Impedance spectroscopy (IS) is a powerful analytical tool to study coating performance non-destructively and can be used to monitor an oxide layer under a TBC coating to prevent catastrophic engine failure.

Normally impedance is measured directly in the frequency domain by applying an AC voltage to the samples and measuring the resulting current at those frequencies. As such measurements encompass a wide range of AC signal frequencies, various characteristic parameters of the electrochemical cell can be evaluated. In this scenario, the spectra have to be fitted to an equivalent circuit model, which represents the microstructures of the materials being examined. Electrical

parameters for the oxide layer obtained from fitting the results can monitor the degradation of TBC system non-destructively.

1.2. Aims and Objectives of This Thesis

This thesis aims to investigate the usefulness of IS as a non-destructive method to evaluate high temperature degradation of the nickel-based superalloys, with or without TBCs, used in gas turbine engine components. The primary aim of the research is to demonstrate the feasibility of using the impedance technique to characterise oxide scales and the secondary aim is to provide an interpretation of the impedance responses accompanying the damage of TBC systems, which occur in the thermally-grown oxide (TGO) layers formed at high temperature. There are four categories of interpretation which are investigated: (1) the correlation of impedance results to the samples microstructure, (2) the determination of thickness of the TGO, (3) the determination of the accumulated damage in TBCs, and (4) the correlation of the impedance response to the crack initiation and propagation in the TBCs.

To achieve these aims the following objectives have been satisfied:

1. characterisation of oxide layers formed on both nickel-based superalloy and bond coat (chapter 4);
2. characterisation of TGO formed in TBC samples at both low temperature and high temperature (Chapter 5);
3. determination of the degradation of TBCs, leading to fracture (Chapter 6);
4. correlation of the impedance response to the crack initiation and propagation in TBCs (Chapter 7).

2. Literature Review

2.1. Introduction

Thermal barrier coatings (TBCs) have been in use for almost 25 years for the protection of hot-section components in gas turbine engines [Miller, 1997]. A typical TBC system consists of a metallic bond coat sandwiched between a high-temperature superalloy and a thin ceramic, yttria stabilised zirconia (YSZ), top coat [Miller, 1997]. About 300 μm thickness of YSZ reduces the temperature at the bond coat interface by up to 200°C, but premature spallation of the YSZ can result in the exposure of the metal in engine components to dangerously high temperatures. As a result of this high temperature exposure, they suffer from high temperature oxidation/corrosion. So, there is a need for a non-destructive testing technique to monitor the integrity of TBC systems during their service, which would allow one to assess the initial coating quality and remaining service life. Impedance spectroscopy (IS) is such a non-destructive testing method. In this literature review, it is intended to provide a comprehensive discussion on the degradation of TBCs and also a review of the literature on IS applications for characterisation of coatings and oxides.

2.2. Non-destructive Method

Non-destructive testing (NDT) can be defined as a method, where a certain form of energy is applied to test materials and the resultant response from the test materials will indicate the physical state of the test materials without damaging the usefulness of the material. Non-destructive evaluation (NDE) or non-destructive characterisation (NDC) refers to applying a non-destructive method to evaluate or characterise the properties of materials non-destructively. No matter what type of NDT technique it is, a certain form of energy, e.g. ultrasonic waves, optical light or x-radiation, etc. should invariably be utilised and some material properties provide the base for detecting the inhomogeneities. For example, the basic principle utilised in thermography is to apply heat to the test specimen and measure or observe the resulting temperature distribution, by using video-thermographic camera [Curtis et al., 1993]. Flaws alter the temperature distribution on or

in the specimen. Surface-mounted thermal couples can also be used to detect the temperature distribution on the surface of a sample. In the radiography method, x-rays or gamma rays are used, and the thickness and density of and defects in the material determine the resultant radiation intensity from the sample. Therefore, the radiation coming from the sample can generate shadows on photographic films and produce a radiograph to show the physical properties of the material [Nevadunsky and Lucas, 1975]. In the ultrasonic method, ultrasonic impulses generated by a piezoelectric transducer are used, the echo signal resulting from the reflection or the same piezoelectric device or another receiver detects scattering from the object. The phase delay between the reflection from different surfaces is correlated to the material properties [Dunyak et al., 1992].

2.3. Impedance Spectroscopy (IS) as a Non-destructive Method

2.3.1. Introduction

IS is a non-destructive multi-layer technique and is used to determine the electrical properties of ceramic materials [MacDonald, 1987]. Oxide layers formed on metallic materials at high temperature are electrochemical in nature [Wise and Oudar, 1990]. IS can be used to study the electrical properties of these oxide layers [MacDonald, 1987].

The principles [Macdonald and Johnson, 1987] and [Cogger and Evans, 1998], applications [Bard and Faulkner, 1980] and analysis [Mansfeld, 1981] of the impedance method have been discussed in various places. IS can be used to evaluate the electrical behaviour of solid electrolyte materials or semiconductors. These electrical processes include transport of electrons through the electronic conductors and the transfer of electrons at the electrode-electrolyte interfaces, and the flow of charged atoms via defects. The flow rate of charged particles depends on the ohmic resistance of the materials and on the reaction rate at the electrode-electrolyte interfaces. In the IS method, the applied AC voltage is very low. As a result of this low AC voltage, the resulting currents do not destroy samples and the method is non-destructive.

2.3.2. Mathematical Expression of Impedance Signal

The concept of electrical impedance was first introduced by Oliver Heaviside in the 1880s and was soon after developed in terms of vector diagrams and complex representations by A. E. Kennelly and especially C. P. Steinmetz [Macdonald and Johnson, 1987]. Impedance is a more general concept than resistance because it takes phase differences into account.

In order to understand the basis of IS, it is helpful to consider that a monochromatic signal, $\upsilon(t) = V \sin(\omega t)$, is applied to a cell and the resulting steady state current, $i(t) = I \sin(\omega t + \theta)$, is measured. Here θ is the phase difference between the voltage (V) and the current (I), and ω is the angular frequency. θ is zero for purely resistive behaviour [Macdonald and Johnson, 1987]. If we consider first a simple resistor and apply a steady, small sinusoidal potential, $V \sin(\omega t)$, across the resistor, that has a resistance R, then the current through the resistor is determined by:

$$I = \frac{\upsilon(t)}{R} = \frac{V \sin(\omega t)}{R} \qquad (2\text{-}1)$$

When the same signal is applied across a capacitor, that has a capacitance C, then the current through the capacitor is given by:

$$I = \frac{dQ}{dt} = C\frac{d\upsilon(t)}{dt} = C\frac{d(V \sin(\omega t))}{dt} = C\,\omega V \sin(\omega t + \pi/2) \qquad (2\text{-}2)$$

So, the current response from a pure resistor is in the same phase with the applied potential signal, while the current response from the capacitor always leads the potential signal by 90°. It is not difficult to conceive that the current response from any circuit that is composed of both a resistor and a capacitor would have a phase difference with the applied sinusoidal potential signal. The phase difference is in between 0~90° and the impedance, $Z = \frac{V}{I}$, can be expressed in terms of an in-phase component and an out-of-phase component. For this reason, the impedance usually is expressed by a vector quantity, $Z(\omega) = Z' + jZ''$, where Z' is the in-phase component or real part of the complex, Z'' is the out-of-phase component or imaginary part of the complex, and

$j \equiv \sqrt{-1} \equiv \exp(j\pi/2)$. Impedance can be plotted with either rectangular or polar co-ordinates, as shown in figure 2-1 [Macdonald and Johnson, 1987].

Here the two rectangular co-ordinate values are:

Real impedance, $Z' = |Z| \cos\theta$ (2-3)

Imaginary impedance, $Z'' = |Z| \sin\theta$ (2- 4)

Phase angle, $\theta = \tan^{-1} \frac{Z''}{Z'}$ (2- 5)

Impedance modulus, $|Z| = [(Z')^2+(Z'')^2]^{1/2}$ (2- 6)

2.3.3. Impedance Measurement

Impedance measurements are usually made with cells having two identical electrodes applied to the opposite faces of a sample. Normally, impedance is measured directly in the frequency domain by applying a small amplitude of AC voltage (5 to 20 mV) to the sample. So, measuring the phase shift and amplitude, or real or imaginary parts, of the resulting current at that frequency represents the electrical properties of the sample. The small amplitude of AC voltage ensures that there is a linear relationship between the current and potential, and that the response is steady state. Therefore, a measurement result does not change with time and many measurements can be averaged. A wide range of frequencies, usually over several orders of magnitude, is applied so that processes having different time constants can be detected within one experiment [Macdonald and Johnson, 1987]. Commercial instruments are available which measure the impedance as a function of frequency in the frequency range 1mHz to 1MHz and which are easily interfaced with laboratory microcomputers. Real and imaginary components of the electrical response and frequency are obtained from impedance measurements. The results are generally plotted on a complex plot and a Bode plot. The complex plot is a plot of the imaginary part vs. the real part, where the real part is plotted as the ordinate and the imaginary part as the abscissa. One or more semicircles can be resolved in the complex plot depending on the time constant and the frequency range studied. Although a complex impedance plot is frequently called a "Nyquist diagram", it is thought to be a misnomer by J. R. Macdonald [Macdonald and Johnson, 1987] and should be avoided.

A Bode plot shows the dependency of total impedance and phase angle on the frequency. The plots of log $|Z|$ vs. log ω and θ vs. log ω are called Bode plots. Bode plots can give information about two unresolved semicircles in a Niquist plot.

2.3.4. Representation of IS Results

Complex impedance plots and Bode plots are the most commonly used representations of IS results. These representations are straightforward and can be obtained directly by plotting raw experimental data. A semicircular arc in a complex plane plot normally represents a particular physical and chemical process in the bulk or at the electrode/materials interface, while the Bode plot explicitly shows the dependence of the total impedance and phase angle on the frequency. In a complex plane plot, detailed information, such as relaxation frequency, resistance, capacitance and depressed angles etc., can be easily perceived.

There are three other possible complex formalisms which can be derived from the complex impedance, Z*, the electric modulus, M*, the admittance, Y* (or A*), and the prmittivity, ε^*, and these quantities are interrelated [Macdonald and obtained, 1987]:

$$M^* = j\omega C_o Z^* = M' + jM'' \quad (2\text{-}7)$$

$$\varepsilon^* = (M^*)^{-1} \quad (2\text{-}8)$$

$$Y^* = (Z^*)^{-1} \quad (2\text{-}9)$$

$$Y^* = j\omega C_o \varepsilon^* \quad (2\text{-}10)$$

where ω is the angular frequency $2\pi f$, C_o is the vacuum capacitance of the measuring cell and electrodes with an air gap in place of the sample. $C_o = \varepsilon_o/k$, where ε_o is the permittivity of free space (8.854×10^{-14} F/cm), and $k = l/A$, the cell constant where l is the thickness and A is the area [Fletcher et al., 1995].

All these four functions can be plotted in complex planes, and as a result of these, various complex plane diagrams, Z" vs. Z', Y" vs. Y', M" vs. M' and ε" vs. ε' can be obtained. These different diagrams sometimes are called admittance spectra (Y" vs. Y'), modulus spectra (M" vs. M') and dielectric permittivity spectra (ε" vs. ε') etc., but impedance spectroscopy is a general term that is used to include and denote all these spectra

[Macdonald and Johnson, 1987]. If they are plotted as a function of frequency in a way similar to plotting a Bode plot, then so-called 'spectroscopic displays' (Y", Z" and M" etc. vs. $\log_{10}\omega$) are obtained [Hodge et al., 1976]. Figure 2-3 shows various complex plots and figure 2-4 shows various spectroscopic displays for the equivalent circuit in figure 2-2. So, there are many different ways of representing impedance spectra, with each one highlighting different features [Hodge et al., 1976]. Therefore, in order to understand better IS and extract more useful and more precise information from impedance measurement data, proper representations of data are important.

Bauerle [1969] demonstrated the usefulness of the complex admittance approach in solid electrolyte studies, while Armstrong et al. [1974] have favoured the complex impedance formalism for analysing data on β-alumina and $RbAg_4I_5$. Macedo et al. [1972] and Ambrus et al. [1972] were among the first to exploit the modulus approach and used it for analysing conductivity relaxation in glasses and in concentrated aqueous solutions.

Sinclair et al. [2000] showed that combined impedance and modulus spectroscopy can be used to identify the presence of insulating and/or semiconducting regions in different types of electroceramics. They used three La-doped $BaTiO_3$ ceramic samples with different microstructures and plotted combined Z" and M" spectra for these samples. All these three samples were insulators at room temperature and Z" spectra could not distinguish the various electrical microstructure. By contrast, the M" spectra (or M* plot) of these samples were all different. So, M" spectra of these samples showed the difference of the bulk microstructure in the presence of an insulating surface layer or grain boundary regions. Figure 2-6 shows a typical complex impedance, Z*, complex electric modulus, M* and combined imaginary impedance, Z" and imaginary electric modulus, M" spectra for the equivalent circuit in figure 2-5, where $R_1 = 1\ M\Omega$, $C_1 = 100\ pF$, $R_2 = 10\ M\Omega$ and $C_2 = 1\ nF$.

The Debye peak in spectroscopic plots of the imaginary components, Z" and M" versus log ω [Morrison et al., 2001] is described by,

$$Z'' = R\frac{\omega RC}{1+(\omega RC)^2} \tag{2-11}$$

$$M'' = \frac{\varepsilon_o}{C} \times \frac{\omega RC}{1+(\omega RC)^2} \tag{2-12}$$

Where ω is the angular frequency and ε_o is the permittivity of free space.

The magnitudes of the Debye peaks at the peak maxima (ω_{max} RC =1) are given by,

$$Z''_{max} = \frac{R}{2} \tag{2-13}$$

$$M''_{max} = \frac{\varepsilon_o}{2C} \tag{2-14}$$

Hence the magnitude of R and C can be estimated from either Z''_{max} or M''_{max} using Equations 2-13 and 2-14. Figure 2-6c shows that Z" and M" peaks for a particular RC element are coincident on the frequency scale. It also shows that Debye peaks in the Z" spectra are directly proportional to R whereas in M" spectra they are inversely proportional to C. Equations 2-13 and 2-14 indicate that Z" spectra and Z* plot are dominated by the largest R whereas M" spectra and M* plot are dominated by the smallest C.

The frequency at the Debye maxima for each RC element is given by,

$$\omega_{max} = 2\pi f_{max} = \frac{1}{RC} = \frac{1}{\tau} \tag{2-15}$$

where τ is the time constant of the RC element and f_{max} is the relaxation frequency, which are independent of geometry and therefore they are intrinsic properties of the RC element.

2.3.5. General Characterisation Procedure Using IS

A flow diagram of a general characterisation procedure using IS as proposed by Macdonald and Johnson [1987], is given in figure 2-7. It has been realised that the simulation of impedance experiments on its own generally cannot provide a definite analysis of a system, since there are frequently more than one equivalent circuit that fits numerically to a given experimental data set [Macdonald and Johnson, 1987]. Therefore, a set of impedance data could not be properly understood and interpreted before there is a proper physical model for the particular system. An appropriate model is always built based on the adequate knowledge of the particular system, among which the type of charge carriers, the migration path of charge carriers, the charge transfer and mass transfer on the electrode/materials interface etc. are of important concern.

In the characterisation of ionically conducting materials and ceramic semiconductors using IS, it was found that in most cases, the responses from grain, grain boundary and electrode/material interface (electrode effect) are from different frequency regions. Similarly for multilayer coatings (TBCs), the impedance response from different layers such as the YSZ top coat layer and TGO layer resolved in to different frequency regions [Ogawa et al., 1999]. Therefore it is possible to separate the different responses from a single experimental data set by proper representations of IS. But to establish a relationship between degradation in TBCs, due to oxide formation and the subsequent IS response for these TBCs, it is important to understand high temperature degradation mechanisms on TBC samples.

2.4. Thermal Barrier Coating (TBC) System

2.4.1. Introduction

The world's first commercial industrial gas turbine was developed by Brown Boveri and was sold from 1939 onwards [Miller, 1995]. Since those early days the development of industrial gas turbines have been motivated by the need to increase fuel efficiency by raising temperature and by improving individual component efficiencies. Components used in high temperature applications are made with superalloys. Nickel-based superalloys have been used extensively for blades and vanes. Many of these alloys develop a coherent alumina film, which provides good protection from oxidation up to intermediate temperatures of 900°C. Cobalt-based superalloys can only be used for stationary vanes because of their limited high temperature strength compared to nickel-based superalloys, which can be used close to their incipient melting temperature [Seth et al., 1996].

One of the most effective methods to develop oxidation resistance in alloys and coatings at high temperature is to form continuous scales of α-Al_2O_3 via selective oxidation [Birks et al., 1994]. Application of coatings slows the high temperature oxidation in gas turbines. Metallic coatings were developed based on aluminium diffused into the surface of the blade to form a protective oxide layer [Miller, 1995]. But this oxide layer spalled after reaching a certain thickness. Later platinum was added which acted by delaying diffusion of aluminium during service [Miller, 1995]. But, this was not adequate for the most aggressive environments and MCrAlY was developed, where M is Ni or Co [Miller, 1995]. The MCrAlY overlay coating is a complex nickel and/or cobalt-based alloy containing Al and Cr. Chromium (15-30%) and aluminium (6-12%) provide corrosion protection while yttrium (0.1- 0.5%) improves oxide-scale adhesion, which is particularly important during the thermal cycling of components [Seth et al., 1995]. Improvements in corrosion-resistant coatings are now permitting the use of lower chromium content, higher strength aeroalloys (CMSX-4) in land-based gas turbines. This coating is applied either by vacuum plasma spraying or by physical vapour

deposition; while the former process is cheaper and can coat difficult positions on a component more easily.

The effect of temperature on blade or vanes can be reduced by applying thermal barrier coatings (TBCs) [Miller, 1995]. Yttrium stabilised zirconia (YSZ) (6-8% Y_2O_3, balance% ZrO_2) are normally used as a thermal insulator in gas turbine engines and are referred to as thermal barrier coating (TBC). YSZ is applied on to the bond coat. The bond coat is normally used on the substrate to form a more protective oxide layer of α-Al_2O_3 beneath the YSZ layer [Birks et al., 1994]. The use of TBCs, along with internal cooling of the underlying superalloy component, provides major reductions in the surface temperature of the superalloy [Seth et al., 1995]. This has enabled modern gas turbine engines to operate at temperatures well above the melting temperature of superalloys (~1300°C), thereby increasing engine efficiency and performance [Seth et al., 1995]. Alternatively, at somewhat lower operating temperatures, TBCs reduce the metal temperature, making engine components more durable. However, when a TBC system is exposed to high temperature in air, a thin oxide layer grows at the YSZ/bond coat interface. The structure of the TBC system or thermal barrier coated component consists of four layers, with each layer having different physical, thermal and mechanical properties, making it a complex structure. These four layers are substrate, bond coat, thermally grown oxide (TGO) and yttrium stabilised zirconia (YSZ), as in figure 2-8.

2.4.2. High Temperature Oxidation of Alloys

The oxide layer, formed in the TBC system at high temperature, is responsible for the degradation of thermal barrier coatings (TBCs) [Miller, 1995]. So, it is important to understand high temperature oxidation phenomena of alloys to improve TBC durability. High temperature oxidation of alloys is a very complex phenomenon. Current understanding in this field is not very clear. High temperature oxidation of steel, nickel or cobalt-based superalloys and bond coats are electrochemical in nature because the metal transforms into ions by giving up electrons which facilitates oxide film growth on the metal substrate or overlay coating. These oxide layers are semiconductors or lossy dielectric in nature and show electrical resistance or capacitance. Some metals and alloys

form a protective oxide layer and the growth of the oxide layer as a function of time is parabolic in nature [Wise and Oudar, 1990]. If the oxide layer is not protective in nature, then further growth of the oxide layer is linear, because in this situation breakaway oxidation happens from time to time, which prevents formation of the protective oxide layer [Belousov and Bokshtein, 1998]. The growth of the protective oxide layer can be explained more clearly by Wagner's model.

2.4.3. Wagner's Model

Wagner's model provides the theoretical basis for the interpretation of the parabolic rate law, according to which the growth rate of the oxide film is inversely proportional to its thickness [Wise and Oudar, 1990].

$$\frac{dx}{dt} = \frac{k}{x} \qquad \text{or} \qquad x = (2kt)^{1/2} \qquad (2\text{-}16)$$

where, x = oxide layer thickness, t = oxidation time and k = parabolic rate constant.

Wagner's model considers an electrochemical mechanism for metal oxidation.

Assumptions of Wagner's model

- Metal oxidation is first controlled by an interfacial reaction.
- Oxide growth is controlled by diffusion.
- Reaction rate is first linear and than parabolic.
- Cation diffusion grows the oxide layer at the external interface (MO/O_2).
- Anion diffusion grows the oxide layer at the internal interface (M/MO).
- Oxide layer thickness changes according to oxidation time.
- Oxidation rate can be measured as a function of time from the changes of oxide layer thickness.
- In the alloys, the chemical composition of the oxide film and substrate changes with time and so does the oxidation kinetics.
- The metal ions or electronegative species that diffuses through the layer is controlled by the nature of defects predominating in the metal oxide, such as metal ion vacancies, oxygen ion vacancies or metal ion interstitial.

2.4.4. Reactive Elements Effect

Small additions of reactive elements in chromia forming and alumina forming alloys improve high temperature oxidation resistance [Cho et al., 1998] and [Pint and Alexander, 1998]. These reactive elements segregate to the grain boundaries of the oxide layer as ions. The driving force behind this segregation during oxidation is not clear. However, it was observed that rare earth (RE) ions segregation at the metal/scale interface increased adhesion by suppressing interfacial segregation of S, while segregation at scale grain boundaries inhibited outward cation diffusion and grain growth [Cho et al., 1998].

Pint and Alexander [1998] studied 30 different reactive elements (dopants). From their study, it was observed that Y, Nd, Gd, Ti, Nb, Ta and Ca segregate to grain boundary but Mn and V did not. A combination of dopant ion size and oxygen affinity influenced segregation to grain boundaries in thermally-grown alumina scales. Some of these RE ions (Y, Nd, and Gd) produced a fine gain size and reduced grain growth. Fine grain production is not the only criteria to reduce grain growth and improve scale adhesion, because La improved oxidation performance without developing a fine grain structure.

A critical amount of dopant was needed to improve the oxidation performance; too low or too high concentrations are both destructive. A fine structure of grains was lost for low dopant ions and oxidation resistance was reduced. For high dopant ions, the oxide layer adhesion improved further, but faster oxide layer growth caused a shorter time for breakaway oxidation [Pint and Alexander, 1998]. This happened because the dopant has a high affinity for oxygen. A fine grain structure was not the result of nucleation effect but arose because of the reduction of cation diffusion [Pint and Alexander, 1998]. From this study it was observed that a correlation existed between grain boundary segregation of RE ions and microstructural changes (except La). This study also showed that Y doping decreased oxygen diffusivity at grain boundaries [Pint and Alexander, 1998]. So from these studies it was revealed that, RE addition in alloys reduced cation and anion diffusion and increased oxide layer adhesion and oxidation performances.

2.4.5. Degradation of TBCs

Bose and DeMasi-Marcin [1997] discussed the failure of different types of thermal barrier coatings at Pratt & Whitney, USA. During engine operation, several time, temperature and thermal cycle-dependant phenomena take place within the TBC system that ultimately result in the TBC failure by spallation of the top coat. Pratt & Whitney has accumulated more than three decades of experience with TBCs. These coatings were originally developed to reduce surface temperatures of combustors in gas turbine engines. They used three types of TBC system. These were Generation I, Generation II, and Generation III. The generation I TBC system consisted of 7-wt. % YSZ deposited by air plasma spray (APS) on an APS NiCoCrAlY bond coat. The generation II TBC system consisted of 7-wt. % YSZ deposited by air plasma spray (APS) on an LPPS (low-pressure chamber plasma-sprayed) NiCoCrAlY bond coat. This modification improved TBC durability by a factor of 2.5. In the generation III TBC system, further improvements were accomplished by instituting a more strain-tolerant ceramic top layer with electron beam/physical vapour deposition (EB-PVD) of 7 wt. % YSZ on an LPPS (low-pressure chamber plasma-sprayed) NiCoCrAlY bond coat. Different TBC systems are used, each one intended for a particular component and engine. For example, power generation engines operate for long periods of time with only a few shut down cycles. By contrast, aircraft engines operate at full capacity during takeoff and landing for several minutes, resulting in shorter but more numerous thermal cycles. So the conditions for TBC failure are not the same in these two system. Because of differing manufacturing approaches and operating scenarios, several specific mechanisms are involved. Despite these complexities, understanding TBC failure mechanisms is beginning to emerge. The durability of thermal barrier coatings (TBCs) is governed by a sequence of crack nucleation, propagation and coalescence events that accumulate prior to final failure by large scale buckling and spalling [Evans and Mumm et al., 2001]. TGO growth stress and thermal mismatch stress is responsible for TBC degradation.

2.4.5.1. TGO Growth Stress

Evans and Mumm et al. [2001] suggested the TGO growth is essentially parabolic until spalling occurs in a TBC system:

$$h^2 = 2k_p t \quad (2\text{-}17)$$

where h is the thickness, t is the time and k_p is the parabolic rate constant. This equation is similar to equation 2-16, predicted by Wagner [Wise and Oudar, 1990]. Accordingly, growth is diffusion controlled. The alumina grows predominantly by inward diffusion of anions along the TGO grain boundaries but there is a contribution to k_p by outward diffusion of cations. This outward growth appears to be sensitive to cations dissolved in the alumina [Evans and Mumm et al., 2001]. In some cases, the TGO formed on NiCoCrAlY bond coats entrains yttria. The yttria in the TGO is related to the distribution of the Y in the bond coat. When yttria domains of sufficient size are incorporated into the TGO, it thickens more rapidly in these regions and produces thickness imperfections. Simultaneously, the yttria reacts with the surrounding alumina to form YAG (yttrium aluminium garnet). Before activity of Al in the bond coat decreases to a level that would cause a spinel to form, the oxygen flux in the bond coat may exceed the Al flux toward the TGO, whereupon Al_2O_3 precipitates form beneath the TGO in the bond coat [Evans and Mumm et al., 2001]. In some circumstances, as activity of oxygen at the interface increases, the solubilities of Ni and Cr (as well as Fe when present) in the Al_2O_3 also increase [Evans and Mumm et al., 2001]. This condition can result in outward diffusion of cations, through the TGO. Upon encountering higher oxygen activities, these cations can form new oxide phases. For example, in regions between the TGO and TBC, conditions are such that spinel formation is allowed.

The growth of TGO during engine operation is the most important phenomenon responsible for the spallation of TBCs. TGO growth results in a constrained volume expansion that leads to a compressive growth stress in the TBC system [Evans and Mumm et al., 2001]. Tawancy et al. [1998] and Bartlett and Maschio [1995] also showed that growth of oxide layer generated stress in the oxide layer and contributed towards TBCs failure. For anion-control, oxide growth is governed by inward diffusion of oxygen and the new oxide forms at the bond coat/TGO interface [Evans, He and

Hutchinson, 2001]. For cation-control, new oxide is formed at the TGO/YSZ interface, through the outward diffusion of cations (Al as well as Ni, Cr etc.) [Evans, He and Hutchinson, 2001]. During the cation-control oxide growth, inward diffusion of oxygen is still possible and bond coat consumption occurs at the bond coat/TGO interface. Anion-control oxide growth is considered most relevant to alumina formation. The stresses due to growth of TGO is different for the two growth process [Evans, He and Hutchinson, 2001]. The stress is at the bond coat/TGO interface for an anion control process and the stress is at TGO/YSZ interface for a cation control process. Interfacial cracking in TBC samples observed during isothermal heating confirmed that the presence of oxide growth generated stress in TBC system [Chaudhury et al., 1998].

2.4.5.2. Thermal Mismatch Stresses

A critical oxide thickness for spalling does not exist but spalling is dependant on other parameters, such as thermal mismatch stresses [Haynes et al., 1996]. Upon cooling, the thermal expansion mismatch between the bond coat and TGO leads to very high thermal compressive residual stresses in the TGO that reach a maximum at ambient temperature. So, increasing the minimum cycle temperature reduced the thermal mismatch strain on the substrate and its oxide layer and increased the thermal life cycle for an EB-PVD (electron beam - physical vapour deposited) coated heat treated sample [Wright, 1998]. During thermal cycling, progressive roughening of the bond coat/TGO/top coat interfaces occurs due to cyclic creep of the bond coat [Evans and Mumm et al., 2001]. Such roughening, termed ratcheting, requires thermal cycling and does not occur during isothermal exposure. Ratcheting also requires an initial surface geometry imperfection of some minimum dimension and progressive lengthening of the TGO either due to TGO cracking or due to in-plane growth during oxidation [Evans, He and Hutchinson, 2001]. With extensive thermal cycling (EB-PVD TBC system), initial undulations in the TGO increase their amplitude upon thermal cycling [He et al., 2000]. This occurs by "ratcheting" of the TGO into the bond coat. Air plasma sprayed coatings are sprayed on to rough bond coats to facilitate a good mechanical locking of the coating to the bond coat. Surface roughness of the bond coat or alloys can also generate stresses [Freborg et al., 1998]. He et al. [2000] suggested that failure was associated with imperfections

(thick area of TGO layer) located at (or near) the TGO layer, especially those that induce tensile stresses normal to the TBC surface, in the vicinity of the TGO. Diaz et al. [1996] showed that APS TBC with a non-uniform or discontinuous nickel-based bond coat on a steel substrate failed during thermal treatment under an argon atmosphere, whereas a uniform bond coat did not fail under similar thermal conditions. This suggests that the increased residual stress caused by the thermal mismatch develop around imperfections in the metal/ceramic interface.

2.4.6. Failure Mechanism of TBC Systems

Failure of TBC systems occur as a result of the spallation of the TBC top coat [Chaudhury et al., 1997]. As discussed above, degradation of a TBC system is due to oxide growth stresses and thermal mismatch stresses. These stresses are responsible for the TBC spallation, and they are common in both APS TBC and EB-PVD TBC systems. Bose and DeMasi-Marcin [1997] suggested that in almost all TBC systems, including plasma sprayed Generation I and Generation II, and EB-PVD based Generation III, failure occurs due to in-plane compressive residual stresses. A significant portion of the in-plane compressive residual stress develops due to the constrained oxide growth on the bond coat at the ceramic/bond coat interface. These stresses generated by combined thermal expansion mismatch and oxide growth contributed to an overall delamination and spallation of the TBC [Chaudhury et al., 1997]. Buckling-induced delamination might be a possible mechanism for spallation because interfacial separation is greater in the mid section than the edges of the specimen. The combined action of creep, oxidation and thermal cycling were responsible for the progression of cracking [Zhu and Miller, 1998] and [Freborg et al., 1998].

Detailed failure mechanisms in the APS TBC system and the EB-PVD TBC system are different. Trying to understand failure mechanisms of TBCs one has to distinguish between the two most often used TBC coatings: the EB-PVD coating and the APS coating. Two major differences exist between these two systems which are believed to have significant influence on the failure mechanisms [Miller, 1997]. The EB-PVD coating is deposited on a rather smooth bond coat and has a columnar structure, which

leads to a certain degree of strain tolerance for this type of coating. On the other hand, the plasma sprayed coating is sprayed on a rough bond coat to facilitate a good mechanical locking of the coating to the bond coat. Depending on the kinetics of the oxide growth in the presence of the ceramic top layer, the compressive residual stresses increase with time [Bose and DeMasi-Marcin, 1997]. Superimposed on this increasing compressive stress are the cyclic stresses generated by the thermal expansion mismatch between the ceramic and the underlying layer. Failure occurs when the cumulative compressive stress exceeds the compressive strength of the elements at the failure sites [Bose and DeMasi-Marcin, 1997]. Although the failure locations are coating specific, the failure sites are the weak links in the TBC structure. In the APS TBC with APS bond coat, failure occurs in the thermally-grown NiO [Bose and DeMasi-Marcin, 1997]. In the APS TBC with LPPS bond coat, a thin and strong alumina layer forms. The strengthening of the bond layer, therefore, moves the weak link from the TGO to the ceramic, initiating failures within the ceramic coating. In the EB-PVD TBC, strengthening of the ceramic is achieved by using the strain-tolerant structure of the EB-PVD ceramic. Due to the strengthening of the ceramic, the weak link has now shifted to within the TGO or at the TGO/bond coat interface [Bose and DeMasi-Marcin, 1997]. From the above discussion, it was clear that not only the thickness of the oxide layer was responsible for failure but also surface roughness, imperfections and thermal cycling influenced it.

2.5. Non-destructive Testing of TBC System

Several NDT techniques have been used for the inspection of TBCs. Acoustic emission has been used for examination of cracking in TBCs [Ma et al., 2001], where acoustic emissions are pulses of elastic strain energy released spontaneously during deformation. Infrared thermography has been used [Ferber et al., 2000], [Harada et al., 1995], and [Saitoh et al., 1995] for evaluating the delamination of TBCs. In infrared thermography, a pulse of heat is applied to one side of a specimen and the spatial distribution of the heat flux on the opposite surface depends on the homogeneity of the specimen. Peng and Clarke [2000] have developed non-destructive piezospectroscopy to examine the stress level and failure in a TBC systems using the analysis of the shape of the luminescence

spectra. These non-destructive techniques can characterise defects in TBCs only when the defects are formed. These techniques can not be used to determine the extent of degradation and predict the failure in a TBC system. From a review of the literature, it is well known that the growth of the thermally grown oxide (TGO) is a critical factor in controlling the degradation of TBCs [Haynes et al., 1996] and [He et al., 1998], but none of the above techniques can be used to monitor the changes in composition and the growth of TGO.

2.6. Fundamentals of TBC System Characterisation Using IS Method

In IS, the energy applied is the electric field with varying frequency, and the electrical response during measurement is determined by the electrical properties of the materials under investigation. The impedance response for YSZ appeared at higher frequency than that of the TGO and the change in the TGO microstructure and inhomogeneities leads to the change of electrical properties of materials and thereby may cause the change of the impedance spectrum [Ogawa et al., 1999]. The electrical response from different phases, such as, grain and grain boundary, and different physical processes, for example, the electrode/materials interfacial reaction, are normally reflected in different frequency domains. In TBCs, YSZ (yttria stabilised zirconia) as an ionic conductor, the relaxation frequency for the grain interior is always in the high frequency range, and the electrode effect is in the low frequency range, with the grain boundary phase being in the intermediate frequency range [Bonanos et al., 1987]. Therefore, the electrical response from different phases in TBC system (figure 2-8) can be separated in the impedance spectra and the microstructure and properties of oxides can be correlated to the IS parameters. This constitutes the fundamental of using IS for characterising TBC systems.

2.7. Interpretation of Results in IS

The interpretation of data from electrochemical impedance experiments is based on the principle of equivalent circuits, which states that the process that occurs in an electrochemical cell can be modelled using a combination of resistors, capacitors and other elements that give the same response as the electrochemical system. It is assumed

that the electrical behaviour of an equivalent circuit is similar to that of the electrochemical cell. Curves generated from an equivalent circuit model are fitted to experimental curves, while the RC components of an equivalent circuit model represent the characteristics of a real system. In the equivalent circuit model, there can be more than one RC component to represent a sample or specimen [Macdonald and Johnson, 1987].

2.8. Physical and Electrochemical Models

2.8.1. Layer Models [Bonanos et al., 1987]

This model is suitable for representing multilayer materials and materials with well-aligned columnar grains. In the layer models, continuous layers of different electrical properties are placed one after another. Two types of the layer model can be used to analyse impedance data to represent a sample. Typical cases are the series layer model, in which layers are parallel to the electrode, and the parallel layer model, where the layers are aligned perpendicular to the electrode (figure 2-9: a-d). There are two semicircles for the series layer model, in contrast to the parallel layer model, where there are no separate semicircles for the different phases due to the parallel connection.

Nitrogen-stabilised zirconia has a microstructure consisting of well-aligned columnar grains, for which the grain boundary and grain bulk have been successfully characterised using a multi-layer model by taking impedance measurements along and perpendicular to the length direction of columnar grains [Lee et al, 2000].

2.8.2. Brick Layer Model [Bonanos et al., 1987]

The brick layer model was first used by Bauerle [1969] for characterising the grain and grain boundary effects in stabilised zirconia. In the brick layer model, as shown in figure 2-10a, the ceramic is assumed to consist of identical cubic grains separated by a continuous grain boundary phase [Waser and Hagenbeck, 2000]. Since then it has been used frequently in the study of solid electrolytes and electroceramic materials. However

the basic assumptions in the brick layer model, such as homogeneous grain boundaries, cubic grains, identical grain boundary properties etc. are usually violated in real ceramics. It was found that the brick layer is a reasonable model as long as the sample has a spatially-homogeneous distribution of grain sizes, isotropic distribution of grain orientations, isotropic conductivity, a relatively narrow grain size distribution and uniform grain boundary properties. The brick layer model fails when there are imperfect contacts (lateral inhomogeneities) between grains or the grain boundary properties demonstrate a very broad or bimodal distributions [Fleig, 2000] and [Fleig and Maier, 1999].

Grain boundaries often act as barriers to the cross transport of charge carriers in a broad range of electroceramic materials, which show ionic conduction, mixed ionic-electronic conduction or pure electronic conduction [Waser and Hagenbeck, 2000]. Therefore, resistive layers at the grain boundary interfaces are formed. For example, at 500°C the conductivity of grain boundaries in CaO-stabilised zirconia is at least two orders of magnitude lower than that of the grains [Aoki and Chiang, 1996]. In such cases, the electrical conduction along the grain boundary channels perpendicular to the electrode is very small (figure 2-10b) and assumed to be negligible, therefore the equivalent circuit for the brick layer model can be simplified as shown in figure (figure 2-10c).

2.8.3. Constriction Model

The brick layer model assumed a continuous uniform grain boundary region separating the individual grains. However, in many materials, grain boundaries are not uniform or homogeneous. In some regions of materials, the grain boundaries are so thin that the individual grains come in to contact [Bonanos et al. 1987]. Bauerle [1969] suggested that in many instances there were regions of grain boundaries, where good inter-granular contact were established; these were called easy paths ("Path a" as shown in figure 2-11a) [Bonanos et al, 1987]. Later, Bruce and West [1983] proposed a constriction model, when they studied the conductivity of polycrystalline LISICON. This model assumes the charge carrier transport takes place through a constriction mechanism as some sections of

the diffusion paths are blocked by the poorly-conducting phases, such as a glass phase, voids, and any other second-insulating phases.

This model is different from the brick layer model. Here, a medium frequency semicircle emerges in the complex impedance plane plot only because of the reduced grain-to-grain contact area, rather than due to the presence of a continuous grain boundary phase, as is the case in the brick layer model. As shown in figure 2-11b, in such cases, the equivalent circuit for grain boundaries actually consists of two conduction paths, one crossing the insulating phase, another through the direct contact of two grains. The equivalent circuit can be simplified as in figure 2-11c, if the conduction path crossing the insulating phases is neglected.

2.8.4. Continuous Conductive Path Model

All the above mentioned models are based on the assumption that the grain boundary is a poorly conducting phase and there is no continuous conductive paths present in the microstructure. In the real world, however, there are many materials in which continuous conductive paths may exist. One of the well-studied cases is cementitious materials, in which there are basically three kinds of conduction paths and which can be simplified as shown in figure 2-12 [Song, 2000].

A typical feature of the continuous path model is that normally there is only one semicircle corresponding to the bulk effect, because under most cases the continuous conductive paths will dominate the electrical conduction and thus shield the effects from other elements in the circuit. Electrical responses from grain and grain boundary are not resolved and a response from one of them may not show at all in the impedance spectra of cementitious materials. For this reason, it is very difficult to discriminate between grain and grain boundary responses in interpreting IS result of cementitious materials.

The continuous conductive paths can be modelled by a parallel 'RQ' circuit [Christensen et al., 1994]. Here, Q stands for a "constant phase element", with both a capacitance component and an arc depression factor. More reliable values for electrical parameters

are obtained by equivalent circuit modelling of the entire spectrum [Christensen et al., 1994]. The equivalent circuit of the entire spectrum is R_o $(R_2Q_2)(R_eQ_e)$, where the 'RQ' elements in parentheses are themselves in parallel, but the overall network is a series arrangement. In cements there is an "apparent offset resistance" 'R_o' in series with a bulk 'R_2Q_2' network and it is connected to the outside world through an electrode 'R_eQ_e' network [Christensen et al., 1994].

2.9. Electrical Conduction in Oxides

2.9.1. Introduction

Ceramic materials have a wide range of electrical conduction mechanisms. The electrical conductivity is determined mainly by the nature of the atomic bonding or crystal structure. Richerson [1992] discussed electrical behaviour of ceramics in his book. The electrical conductivity associated with ceramics is, in most cases, semi-conductive or ionic. It is important to understand clearly the electrical conductance mechanism for setting up an appropriate physical model and an equivalent circuit, and thereby interpreting the IS result properly.

2.9.2. Metal Oxides as Electronic Conductor

Metals are not the only materials that exhibit electronic conductivity. Some transition metal oxides such as Fe_2O_3, Cr_2O_3, NiO, CoO, V_2O_3, ReO_3, CrO_2, ReO_2, and TiO have high levels of electronic conductivity [Richerson, 1992]. This results from overlap of electron orbitals forming wide, unfilled 'd' or 'f' electron bands energy (in contrast to the 's' electron bands formed in metals). The atomic bonding in insulators and semiconductors results in energy bands that are either completely full or completely empty. There is an energy gap between the outermost filled band (valance band) and adjacent empty band (conduction band) of insulators and semiconductors. This band gap prevents flow of electrons in these materials between the valence and conduction bands and no electron conduction occurs. Electrical conduction in semiconductors is electronic. By definition, semiconductors are materials that have electrical resistivity between that of conductors and insulators. Semiconductors have an energy gap between the filled and

empty electron bands, such that conduction will occur only when sufficient external energy is supplied to overcome the energy gap [Richerson, 1992]. Whereas the band gap is large for insulator and difficult to overcome, it is small enough for semiconductors that a sufficient increase in temperature or in electric field will allow electrons to bridge the gap. So, by applying external energy to a semiconductor, electrons from the filled valance band can move to the conduction band.

Electronic conductivity in semiconductors is due to the presence of donor or acceptor type point defects, which at room temperature are fully ionised, giving rise to delocalised electrons in the conduction band (n-type) and holes in the valence band (p-type) respectively. The conductivity of a semiconductor increases exponentially with temperature [Jiles, 1994]:

$$\sigma_i \propto \exp(-\frac{E_g}{kT}) \qquad (2\text{-}18)$$

where E_g is the band gap and k is the Boltzman constant.

For oxides, such as alumina, having a low electrical conductivity, even minor variations in composition, impurity content, heat treatment, stoichiometry and other variables can have a significant effect on the measured results. Impurity atoms introduce new localised energy levels for electrons at the intermediate positions between the valence band and the conduction band. If the new energy levels are unoccupied and lie close to the energy of the top of the valence band, it is easy to excite electrons out of the filled band into these new acceptor levels [Kingery et al., 1976].

2.9.3. YSZ as Ionic Conductor

For materials having ionic conductivity, the carrier of electrical charge is an ion, and the most prominent materials that exhibit this behaviour are ionically-bonded ceramics [Recherson, 1992]. Electrons are relatively free to move in a metallic conductor under the influence of an electric field, but ions are restricted by their position in a crystal structure. Energy must be added before an ion can move from its position, because the opposite charge of the nearest neighbour ions tries to hold the ions in the equilibrium

position and provides the energy barrier. The energy barrier for most ionic ceramics is high at room temperature. However, as the temperature is increased, thermal vibrations move ions further and further away from their equilibrium positions and boost the ions closer to the top of the energy barrier. When the thermal energy is high enough in a specific material for ions to move over the energy barrier under the influence of an electric field, the materials becomes ionically conductive. The degree of ionic conductivity then increases as the temperature further increases.

One kind of charge carriers that is always present and can contribute to electrical conductivity is the ions present in crystalline materials. Electrical conductivity resulting from ion migration is important in many ceramic materials especially at high temperature [Kingery et al., 1976]. Among the oxide ionic conductors, the most well studied and useful materials to date are those with a fluorite-related structure, especially ones based on ZrO_2, ThO_2, CeO_2 and Bi_2O_3 [Steele, 1989]. For an ion to move through the lattice under the driving force of an electric field, it must have sufficient thermal energy to pass over an energy barrier that corresponds to the intermediate position between lattice sites. Therefore, similar to the case of semiconductors, the ionic conduction as function of temperature can be expressed as [Kingery et al., 1976]:

$$\sigma_i \propto \exp(-\frac{\Delta G}{kT}) \qquad (2\text{-}19)$$

where ΔG is the potential barrier.

However, it is important to note that some materials may exhibit mixed ionic-electronic conductivity.

So, whatever the conduction mechanism, electronic or ionic or mixed conduction, the electrical conductivity of ceramic materials (σ) is thermally activated and can be expressed by an Arrheinius law:

$$\sigma = \sigma_o \exp(-\frac{E_a}{RT}) \qquad (2\text{-}20)$$

Thus the activation energy for conduction (E_a) can be calculated from the slope of the straight line given by $\log\sigma$ vs. $1/T$.

2.10. Electrode/Material Interfaces

2.10.1. Introduction

In a typical complex impedance plot from a ceramic material, we often see either a semicircle or a spike (tail) in the low frequency region which is due to the electrode/material interface; which is also called the electrode effect. The electrode effect is dependent not only on the properties of bulk materials, but also on what type of electrode is used. The response from the electrode/material interface often provides extra information about the electrical properties of the bulk material and even gives implications on the surface state of the bulk material. In terms of different conducting charge carriers in bulk materials, two type of interface can be present in samples. One is an electrode/semiconductor (electronic conductor, e.g. TGO) interface and the other one is an electrode/solid electrolyte (ionic conductor, e.g. YSZ) interface. Electrodes are normally metallic materials.

2.10.2. Electrode/Semiconductor Interfaces

The electrode/semiconductor interfaces can give either ohmic or non-ohmic contact. In the case of an ohmic contact, the electrode effect is hardly identifiable in the impedance spectra, while a semicircle at low frequency can be seen for the non-ohmic contact. There is always a Schottky barrier present at the electrode/semiconductor interface, even an ohmic contact involves a thin depletion layer. The capacitance of a Schottky barrier in some respects resembles a parallel-plate capacitor with a separation between the plates, and the capacitive effect of an ohmic contact does not emerge in an impedance spectrum because the depletion layer is so thin that the carriers can readily tunnel through it [Rhoderick, 1978]. Consequently, electrode/semiconductor interfaces are comprised of both capacitive and resistive elements [Maiti and Basu, 1986] and can be analysed using a circuit of RC in parallel, with the ohmic contact being a special case with an extremely low resistance of the barrier.

It is important to note that an ohmic contact is a distinctively unique characteristic of an electrode/electronic conductor interface. The absence of a semicircular arc in the impedance spectra due to the electrode-sample interface indicates that the conduction process in the sample is electronic [Chiang, Lavik and Blom, 1997], whereas an ionically-conducting sample could not have an ohmic contact with a metal electrode.

2.10.3. Electrode/Solid Electrolyte Interfaces

The electrode/solid electrolyte interface can be either a blocking or a non-blocking one. From an electrochemical point-of-view, an interface is blocking when the charge carrying species cannot cross the interface or exchange charge with the electrode and there is no immediate equilibration of charged species. The interface across which charged species tend to equilibrate once contact has been made is called a non-blocking interface [Armstrong and Todd, 1995]. A non-blocking interface often behaves like a resistance and a capacitance in parallel, which leads to a semicircle in the impedance plane. This is quite like the case of non-ohmic electrode/semiconductor contact. However, an idealised blocking interface should behave like a parallel plate capacitor, which should lead to a straight line perpendicular to real axis in the complex plane.

A non-blocking electrode can behave like a blocking interface if an exchange current at the interface is very low and a blocking electrode can have charge transfer across the interface if an extremely high potential is applied [Armstrong and Todd, 1995]. However, in a small signal impedance measurement the latter case rarely occurs.

An important fact is that almost all the electrode/solid electrolyte non-blocking interfaces show a depressed semicircle in their impedance spectra. It is believed that even an ideally polarisable electrode could exhibit a depressed semicircle, because in the double-layer region energy can be dissipated in various ways other than by charge transfer [Lang and Heusler, 1998]. Due to the distributed nature of the response, a non-blocking interface, which shows a depressed semicircle in the impedance spectra can be simulated by a constant phase element (CPE) in parallel with a resistance. A blocking interface appears

to be a straight line inclined to the real axis at an angle smaller than 90°, which can often be simulated by a single CPE.

2.11. Non-Ideality of Realistic Materials

In practice, experimental data are rarely found to yield a full semicircle with its centre on the real axis of the complex plane. There are three common perturbations, which may still lead to at least part of a semicircular arc in the complex plane [Macdonald and Johnson, 1987]:

1. the arc does not pass through the origin, because there are other arcs appearing at higher frequencies;
2. the centre of an experimental arc is frequently displaced below the real axis because of the presence of distributed elements in the material-electrode system. The relaxation time is not then single-valued but is distributed continuously or discretely around a mean. The angle by which such a semicircular arc is depressed below the real axis is related to the width of the relaxation time distribution and such is an important parameter;
3. arcs can be substantially distorted by other relaxation. Overlapping arcs can appear as a single distorted semicircle.

Normally, IS data plotted in the impedance plane show typical depressed circular arc behaviour [Macdonald and Johnson, 1987]. Simply employing the ideal RC circuit as has been mentioned above usually cannot fit the impedance spectra of realistic materials. For a wide range of materials, the complex plot of impedance (Z^*), electric modulus (M^*) and complex dielectric constant (ε^*) for the bulk effect normally does not show a perfect semicircle as predicted by an ideal 'RC' element circuit. Instead of this, it shows an inclined semicircular arc depressed below the real axis by an angle $\alpha\pi/2$ [Cole and Cole, 1941], and [Jonscher, 1978], as shown in figure 2-13.

The non-ideal response i.e. the dispersion of the relaxation frequency with a small frequency range from the relaxation frequency of real material, has not been fully understood, but many studies point to the chemical and physical, and even geometrical

inhomogeneities in material properties. Jonscher and Reau [1978] proposed that the non-Debye nature of the bulk suggests that the conducting species moving by discontinuous jumps interact with one another in a manner demanded by "screened hopping". Hodge et al. [1976] mentioned that the random orientation of anisotropically conducting crystals and the presence of phases of more than one composition or structure may contribute to the broadening of the Debye peak. Macdonald and Franceschetti [1987] proposed that the non-ideal, distributed response can be described in terms of a distribution of relaxation times which might be associated with a distribution of hopping-barrier-height activation energies because of inhomogeneous material properties. Such a distribution of relaxation times will lead to frequency-dependent effects. A depressed semicircle in the impedance spectrum often is fitted by using a constant phase element (CPE) connected in parallel with a resistor or a capacitor, or a CPE connected in series with a resistor [Raistrick, 1987].

The impedance of the CPE is given by:

$$Z_{CPE} = Y^{-1}{}_{CPE} \tag{2-21}$$

$$Y_{CPE} = A(j\omega)^n = A\omega^n[\cos(\frac{n\pi}{2}) + j\sin(\frac{n\pi}{2})] \tag{2-22}$$

where A and n are frequency-independent parameters which usually depend on temperature, and $0 \le n \le 1$, ω is angular frequency. This admittance has been designated the constant phase element (CPE) admittance. When n=1, the CPE describes an ideal capacitor; when n=0, the CPE acts as a pure resistor [Macdonald and Franceschetti, 1987]. Thus a CPE can represent a wide variety of non-ideal elements.

For a CPE connected in parallel with a resistance R, the total impedance can be expressed by the Debye equation:

$$Z = \frac{R}{1 + (j\omega\tau)^n} \tag{2-23}$$

By combining equation 2-22 and equation 2-23 , we can obtain an equation:

$$(Z' - \frac{R}{2})^2 + [Z'' + \frac{R}{2}\tan(\alpha)]^2 = \frac{R^2}{4}[1 + \tan^2(\alpha)] \tag{2-24}$$

which depicts a full circle which is displaced from the real axis as shown in Fig.2-13 (in

the dotted line), with a diameter of $R\sqrt{1+\tan^2\alpha}$ and the centre at $\left(\frac{R}{2},-\frac{R}{2}\sqrt{(1+\tan^2\alpha)}\right)$, and the depressed angle in the figure 2-13 is related to the exponent n by:

$$\alpha=\frac{(1-n)\pi}{2} \qquad (2-25)$$

When n = 1, α is 0 and the semicircle is an ideal semicircle without any effect of depression. Therefore both exponent, n, in the Debye equation and the depressed angle, α, of the semicircle in the complex impedance plot describes the extent of the departure of real materials from ideal Debye behaviour.

2.12. Effect of Interface Roughness on IS Results

Roughness effect can be better understood according to a theory of lateral charge spreading in the diffusion double layer [Scheider, 1975]. A schematic of a rough surface is shown in Fig. 2-14 (after Scheider), here an ideally polarised electrode is assumed.

At the very first moment when an electrical field is applied, there are no concentration gradients present, and ionic flow follows the lines of electric force (figure 2-14a) to the peak of the mound. As charge accumulates in the double layer at the peak, the folding down of the equipotential lines combines with lateral concentration gradients to cause tangential spreading of ions to the remote portions of the surface (figure 2-14b). As more surface becomes accessible to charge with the elapse of time, the effective capacitance increases [Scheider, 1975]. This qualitatively explains why the capacitive effect of a rough interface increases with decreasing frequency.

Equivalent circuits comprised of various RC networks can model a rough electrode. As the frequency decreases, the more signal travels through the resistive part of the network before being shunted across the interfacial capacitance [Liu, 1985]. This qualitatively explains why the resistive effect of a rough interface also increases with decreasing frequency.

2.13. Application of IS

2.13.1. Introduction

From the above discussion, it is clear that IS can be used successfully as a non-destructive method for the characterisation of a range of materials both in aqueous systems and in solid state systems. IS was used to characterised defects in organic coatings, defects in inorganic coatings (such as protective oxide and TBCs), defects in structural ceramic materials (such as TBCs), oxide electrolytes and electrodes in solid oxide fuel cells (SOFC). In polycrystalline solids, transport properties are strongly affected by the microstructure, and impedance spectra usually contain features that can be related to the microstructure. The combined use of IS and electron microscopy is a powerful means of characterising materials. Some successful applications of IS to characterise a range of materials are discussed below. The purpose of this discussion is to show the wide scope of IS and its ability to characterise TBC systems.

2.13.2. Characterisation of Defects for Organic Coatings in Aqueous Systems

IS was used to study physical and chemical properties of the organic coating, which helped to understand the corrosion process in aggressive aqueous environments. Aqueous corrosion is electrochemical in nature like high temperature oxidation. The IS method was successfully used in the laboratory to predict the protectiveness of organic coatings [Deflorian et al., 1998], [Grandle and Taylor, 1997], [Miszczyk et al., 1997] and [Thompson and Campbell, 1994]. As in an aqueous system, only ions were mobile charge carriers. Aggressive aqueous environment increased the porosity in the coating, which might help mobile charge carriers to defuse through the coating more easily. The aqueous electrolyte moved more easily through the coating, as the coating degraded further [Deflorian et al., 1998], [Grandle and Taylor, 1997]. The higher the ionic resistance of the organic coating, the higher the corrosion resistance [Miszczyk et al., 1997]. All these studies showed that decreasing the electrical resistance of the protective coating increased the degradation of these coating. Based on this phenomena, IS can compare "protectiveness" of different coatings, simply by measuring their impedance.

Further analysis of measured IS data can give electrical parameters of these coatings, which can be used to evaluate coating performance. Deflorian et al. [1998] studied coating degradation and also electric and dielectric behaviour exclusively for paint. They concluded that ionic resistance was the most effective mechanism in the corrosion protection of barrier paints. The electrical resistance and time constant (RC) for organic coatings were normally lower than that of the corrosion product. The time constant dictates the relaxation frequency and if the time constant is lower then the relaxation frequency will be higher. The time constant for organic coatings was in the higher frequency region and the relaxation frequency of corrosion product was in the lower frequency region [Deflorian et al., 1998]. Thus monitoring this low frequency region would help to monitor the corrosion product and predict the remaining life of the coating. Grandle and Taylor [1997] studied the statistical aspects of organic coatings using coated aluminium beverage containers and found that the IS method was statistically valid for the study of organic coating failure in aggressive environments. This study also revealed that the information on coating degradation obtained from IS data after one month was confirmed by visual examination of coating degradation after 8 months . So the IS result can be an indicator for the long-term performance of coatings.

2.13.3. Application of IS for the Evaluation of Oxides

IS was also used to study inorganic coatings in aggressive aqueous environments. Some preliminary work was carried out by IS on the aqueous system using three electrodes to study high temperature oxide layers formed on steel [Pan et al., 1998] and iron-based superalloys [Escudero et al., 1995]. Oxide scales protect substrate alloys in the same way that organic coatings protect metal substrates by reducing the ion movement through the coatings [Pan et al., 1998]. Sometimes, high temperature oxidation can be referred to as high temperature corrosion, as the formation of oxides lead to the degradation of metal components in engines. Monitoring the changes of this corrosion product can give an early warning of the degradation of engine components. Metals are highly conductive, so if there are no other semiconductor or ionic conductor present then only the corrosion product, oxide scale, dictates the electrical characteristics of the interface. A complex impedance plot for oxidised metal showed that high temperature corrosion formed oxide

scale [Pan et al., 1998]. Changes of this oxide scale changed the complex plot accordingly. Pan et al. [1998] suggested that the oxide film consists of a compact inner layer (b) and a porous outer layer (p). Impedance measurements were carried out in an aqueous system. They proposed an electrical circuit for this oxide film based on a series-layer physical model. From the impedance analysis, the resistance values obtained for the compact inner layer (b) and a porous outer layer (p) were R_b and R_p respectively. The value of R_b or R_p was a function of the diffusion of ions through any kind of defects in the coating. So, as the ion diffusion was increased, the electrical resistance decreased and at the same time the protectiveness of the coatings was reduced. Thus the higher the electrical resistance, the higher the corrosion protection [Thompson and Campbell, 1994].

Barberis and Frichet [1999] studied oxide scale formed on Zircaloy-4 type alloys with different tin contents. The oxide scale was divided in to two layer, an inner compact layer and an outer porous layer. In this study, Bode diagrams represented the impedance measurements. It was observed that the phase angle was low at high and low frequencies, but in between, the phase angle evolved between 60° and 85°; indicating that the oxide scale is mainly capacitive. This was confirmed by the impedance spectra, where the impedance increased with decreasing frequency [Barberis and Frichet, 1999].

In solid state electrochemistry, IS has been used extensively to study oxide materials. Zhu and Ding [2000] investigated the microstructure and chemical state of a TiO_2 coating using the IS method. IS results showed overlapping semicircles for the grain boundaries and grain body. The high frequency semicircle corresponds to the response of the grain body and low frequency semicircle corresponds to the response of the grain boundaries. Zhu and Ding [2000] showed that the high frequency semicircle in the complex impedance spectra for the porous coating was depressed because of non-uniformity. However, the high frequency semicircle in complex impedance spectra for the dense coating was almost not depressed. Zhu and Ding [2000] also showed that the electrical parameters, such as resistance and capacitance, were closely associated with the microstructure of coating. In the TiO_2 coating, a dense compact structure results in the reduction of grain boundary electrical thickness and an increased capacitance. For the high temperature measurements, the composition of some oxides may change by thermal

dissociation. So it is necessary to take precautions to maintain a constant oxide composition during the temperature-dependent conductance measurement. In this case, Teske et al. [2000] studied an oxide with mixed ionic/electronic conduction and showed that an activation energy can be obtained from the temperature dependence of the conductivity at a constant oxygen to metal stoichiometry of the oxide. This activation energy is fixed for a specific oxide, so the measurement of the activation energy by IS can give valuable information about the oxide itself.

Morrison et al. [2001] used IS for the characterisation of lanthanum-doped barium titanate ceramics. The IS result demonstrates the usefulness of combined Z", M" spectroscopic plots to probe the electrical microstructure of lanthanum-doped barium titanate heated under a variety of oxygen partial pressures. The Z", M" spectra from samples heated in oxygen and in argon at 1350°C represent two extreme types of behaviour, in which samples are either insulating (heated in air) or semiconducting (heated in argon) at room temperature. In all cases both bulk and grain-boundary response were detected, where Z" plot highlights phenomena with the largest resistance whereas M" picks out those with smallest capacitance [Morrison et al., 2001].

Gillies et al. [2000] used IS for the electrical characterisation of thin alumina layers. In this study, they used parallel 'RC' elements to represent a single oxide layer. They showed that for oxide scale, the electrical resistance increased and capacitance decreased with increasing oxidation time. Gillies et al. [2000] suggested that there are several reasons why the resistance of a barrier could increase as a function of oxidation time. The most obvious reason was that the physical thickness of the oxide increased. If electron transport occurs via tunnelling, then the resistance increases exponentially with the thickness. Alternatively, the thickness of the oxide could remain constant, but the stoichiometry of either the whole barrier or a fraction of it could change due to over oxidation. This in turn might alter the barrier height. It is also possible that the resistance simply increased because the non-tunnelling leak current was reduced by the oxidation of metallic 'Al', which previously formed electrical paths through the oxide layer. The importance of impedance measurements is that they provide a fingerprint of the oxide and help to characterise it.

Vermoyal et al. [1999] carried out an impedance study on corrosion films formed on zirconium-based alloys and showed that a good correlation existed between oxide thickness calculated from IS measurements and weight gain measurements with those estimated by metallographic examinations. The study also showed that the capacitance of the oxide layer was dependant on the frequency as observed with other oxides formed at high temperature, in agreement with Jonscher's law of dielectric relaxation [Jonscher, 1978]. Vermoyal et al. [1999] showed Bode diagrams, Nyquist diagrams, Cole-Cole diagrams, and Arrhenius diagrams of the conductance, activation energy and Arrhenius diagrams of the dispersion factor. Plots could be separated into two linear sections in both Arrhenius diagrams of the conductance and Arrhenius diagrams of the dispersion factor. This could indicate that the oxide scale is divided into two layers, which are a porous layer and a condensed layer. Vermoyal et al. [1999] showed that modulation of the amplitude of the excitation voltage between 10 and 500 mV did not induce any variation of either the impedance diagram shape or impedance modulus. So the low frequency resistance in this study was attributed to the total oxide resistance rather than a charge transfer resistance.

2.13.4. Application of IS for the Study of YSZ

YSZ is the most widely used solid electrolyte material. Chun and Mizutani [2001] studied YSZ thin films of polycrystalline ceramic and single crystal thin film deposited by a CVD process. Grain and grain boundary response were observed for polycrystalline YSZ. However, single crystals free of grain boundaries gave only one semicircle, and the overlapping of semicircles corresponding to grain and grain boundaries was observed for thin films deposited by the CVD process. The overlapping of semicircles corresponding to grain boundary and electrode can be resolved by varying the oxygen partial pressure [Chun and Mizutani, 2001]. By changing the oxygen partial pressure, the electrode semicircle will vary while the grain boundary semicircle is independent of this parameter. Chun and Mizutani [2001] used two parallel 'RC' elements in series in an equivalent circuit model, as widely used to represent oxide scale, to represent grain and grain boundary responses. The activation energy calculated from the impedance analysis was used to compare different YSZ thin films. No film thickness-dependence on the

activation energy of film appeared for films thicker than 1μm because of no changes in the grain size [Chun and Mizutani, 2001]. So activation energy can be used to study oxide microstructure, because changes in activation energy will represent microstructural changes.

Curtis et al. [1994] studied YSZ using IS. Two semicircles were observed in their Nyquist plot. The semicircle at high frequency on the left relates to the grain interior and the semicircle at low frequency on the right relates to the grain boundaries. This study showed that conductivity of the grain interior did not change very much with change in the YSZ particle size, but the conductivity of grain boundaries decreased with increasing particle size. Increasing the pore density with increased YSZ particle size in the grain-boundary region presented a major obstacle for oxygen ion movement through the YSZ [Curtis et al., 1994]. This was considered to be the source of the increase in the grain-boundary impedance.

Ji et al. [1999] studied alumina-doped YSZ electrolyte and showed that the 4% alumina content in YSZ electrolyte reduced the grain boundary impedance. No changes were observed in the high frequency semicircle related to the grain interior. This study indicated that impurities in the YSZ layer can be monitored by the IS method. Feighery and Irvine [1999] made a similar study and demonstrated that small additions of alumina decreased the grain boundary impedance, but more than a 10% alumina addition reduced the ionic conductivity. Decreasing conductivity and increasing capacitance was observed due to increased cracking and porosity in YSZ [Ji et al., 1999]. So IS can be used to monitor deterioration of YSZ at high temperature.

Garcia et al. [1998] showed the usefulness of IS in characterising YSZ in a multilayer system. The high frequency part of the complex impedance represented the YSZ layer and its extrapolation on the real axis allowed one to determine the resistance value for the YSZ layer. Garcia et al. [1998] deduced conductivity values which were used to calculate the activation energy. The activation energy values were used to compare YSZ thin films with a YSZ single crystal, which suggested that YSZ thin films behave as

single crystal. This means the resistance observed for YSZ thin films is from the grains rather than the grain boundaries [Garcia et al., 1998].

Zirconia and functionally-graded zirconia, which is a TBC material were studied using the IS method. Steil et al. [1997] studied densification of YSZ. In this study, silver was used as an electrode material. It gives electrode semicircles that relax at lower frequencies than platinum, thus enabling an easier and more accurate separation of the bulk responses from the overall impedance diagram. Some problems could be raised with silver painting on porous YSZ samples, because a painted silver coating, cured at 600°C for 2 hours, could diffuse deeply into the pores. Steil et al. [1997] cured silver below 500°C and did all their measurements at constant temperatures of 350°C and 400°C, where both the bulk and microstructural defect responses could be observed over a broad frequency range. In this experiment, all measurements were carried out with dry gases. They mentioned that this point was important for measurements performed below 140°C, otherwise humidity would induce a significant conductivity in the porous samples. They used platinum electrodes for high temperature measurements (above 700°C).

Dessemond et al. [1993] studied the electrical conduction-blocking effects of voids and second phases in stabilised zirconia and showed that a fraction of the mobile oxide ions were blocked at the surfaces of voids (cracks, pores etc.). The surfaces of voids generated the same blocking effects as the precipitated second phases. Dessemond et al. [1993] used a blocking factor α_R (the fraction of the electrical carriers blocked at the impermeable internal surfaces, under the measuring conditions, with respect to the total number of electrical carriers in the sample) to explain the effect of blockers in YSZ and YSZ-Al_2O_3 composites. They observed that increasing the measuring temperature reduced the blocking effect of impermeable internal surfaces which ultimately disappeared at very high temperature. They showed that the variation of α_R with temperature is approximately linear between T_i (a temperature where α_R start to decrease) and T_d (a temperature where the blocking effect practically disappears). According to

work of Barnerd (cited in the work of Desmond et al., 1993), the transition temperature for α_R would be higher for the higher blocking factor [Dessemond et. al., 1993].

Steil et al. [1997] studied the use of platinum and silver electrodes to evaluate the sintering effect on YSZ and showed that silver as an electrode is more useful for this work. They showed that the platinum electrode semicircle was much bigger than the silver electrode semicircle and also the platinum electrode semicircle overlapped with the grain boundary semicircle. Sintering normally changes the pore size in YSZ material and these pores are located in the grain boundary regions. Any sintering effect will be in the grain boundary region and the platinum electrode would not be suitable for this type of work. The silver electrode semicircle was at a much lower frequency than the grain boundary semicircle, so this could be used as a suitable electrode material for the monitoring of the sintering effect on YSZ material. Increasing the sintering temperature reduced the grain boundary semicircle. This was because YSZ is an ionic conductor and increasing the sintering temperature reduced the pore size, which reduced the ion blocking effect by pores in the grain boundary regions [Steil et al., 1997]. They also compared variations of the blocking factor with the volume concentration of pores and alumina inclusions. This comparison showed that similar concentrations of pores and alumina grains of fairly similar diameters resulted in very similar blocking factors. This demonstrated that only the geometry of the blockers determines the blocking process in ionic conductors like YSZ [Steil et al., 1997].

Kleitz et al. [1995] studied ion blocking in YSZ material. They compared impedance diagrams of a single crystal and a sintered pellet of the same shape and size and of the same material. With respect to the single crystal, the sintered material diagram exhibited an additional feature and was identified as a grain boundary response. Grain boundary blocking was effectively only below a certain frequency threshold. Above this frequency threshold, the electrical behaviours of both materials were identical. Kleitz et al. [1995] observed that increasing the measurement temperature reduced the blocked volume. So, increasing the temperature increases the matrix conductivity and blocking vanishes.

Muccilo and Kleitz [1996] studied MgO-partially stabilised zirconia and their impedance diagrams showed the characteristic grain and grain boundary semicircles, as well as an extra arc at intermediate frequencies. This extra arc was identified as a characteristic of partial blocking of electrolyte conduction by the monoclinic grains. The activation energy of this blocking process was slightly higher than the bulk activation energy. So, Muccilo and Kleitz [1996] confirmed that decomposition of cubic zirconia to monoclinic zirconia could be detected and characterised by IS.

Santos et al. [1998] compared impedance diagrams from polycrystalline yttria-stabilised tetragonal zirconia (Y-TZP) with different grain sizes to those of cubic yttria-stabilised zirconia (YSZ) samples with a similar grain size. The blocking effects in Y-TZP and YSZ appeared surprisingly similar. Reducing the grain size reduced grain boundary semicircles. This was because reducing the grain size reduced the pore size in the grain boundary region. This indicated that IS can be used to monitor the microstructure in ceramics, but a model is necessary to find the electrical parameters that are represented in test ceramics. Microstructural changes in low conducting ceramics during heat treatment were analysed using a brick layer model [Fleig and Maier, 1998]. The corresponding brick layer model was assembled in the following way: the grains of realistic ceramic were counted and the average grain size was calculated by the ratio of the sample area to the number of grains. Squares of this average grain size constitute the brick layer model. For most of the microstructures considered in this paper, the IS spectrum differed only slightly from the spectrum expected for the corresponding brick layer geometry with an identical number of grains per unit area.

2.13.5. Application of IS for the Evaluation of a Gas Sensor Material

Varghese and Malhotra [2000] studied the electrical behaviour of nanocrystalline SnO_2 thin films using IS. In this study, they showed that humidity, temperature and the reducing gas environment could influence the electrical properties of SnO_2 thin films. Since the interaction of the material with the gaseous medium depends on the microstructure as well as the surface states, IS is very useful in gathering details of the gas-solid interaction. Varghese and Malhotra [2000] demonstrated that SnO_2 was highly

sensitive to ethanol and proposed an equivalent circuit model based on two parallel RC elements connected in series. To explain the deviation from ideal semicircular behaviour, they adopted the approach of the universal dielectric behaviour introduced by Jonscher [1978].

2.14. Summary

From the above literature review, it is clear that IS is a powerful non-destructive technique for solid state research. The most important advantage of this method is the ability to determine all of the time constants in the frequency range for a particular sample in a single experiment. It can be used to study a TBC system.

TBC is used for the protection of hot-section components in gas turbine engines by reducing the temperature on the alloy. A TBC system consists of a metallic bond coat sandwiched between a high-temperature superalloy and a YSZ, top coat. As a result of high temperature exposure, premature spallation of the YSZ can result in the high temperature oxidation, corrosion and failure of engine components. Oxide layer formation at high temperature in a TBC system is responsible for TBC failure. Oxide layers formed on metallic materials at high temperature are electrochemical in nature. IS can be used to study the electrical properties of these oxide layers. It is a cheap, quick and convenient method. It can be used to monitor the integrity of TBC systems during their service, which allows one to assess the initial coating quality and remaining service life.

Interpretation of IS spectra needs a sound understanding of electrical conduction mechanisms of a TBC system and establishment of a proper equivalent circuit model. The model must represent the physical system and the electrical parameters determined from the fit result must be physically reasonable. Otherwise, the model may have to be modified to relate microstructural features and the entire analysis process repeated. A similar analysis process is required for all materials, whether they are oxide, ceramic or organic coatings. Thus the method is very straightforward.

YSZ is an ionic conductor, an oxide layer is an electronic conductor and an electrode is also electronic conductor. There are three kinds of interface in a TBC system: electrode/YSZ interface, YSZ/oxide interface and oxide/electrode interface. The oxide is a semiconductor material. The heterogeneity at the interface such as the presence of cracks can be related to IS parameters. The electrode effect can reflect the properties of bulk materials that may be used for non-destructive testing of that material.

There are many ways of representing IS spectra. Impedance spectra emphasise the electrical resistance of different phases, while modulus spectra demonstrate the electrical capacitance of these phases. According to this literature review, it is clear that impedance spectra are more suitable for studying TBC systems. Constant phase elements (CPE) are used in the equivalent circuit model to fit IS spectra because both YSZ and oxide layer show non-ideal behaviour. The depression angle of a semicircle in a complex impedance plot can show the extent of the relaxation frequency dispersion of a material.

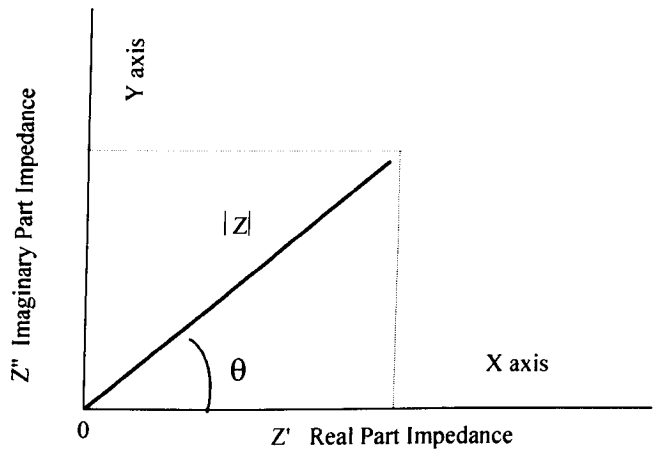

Figure 2-1: The impedance Z plotted as a planar vector using rectangular and polar co-ordinates.

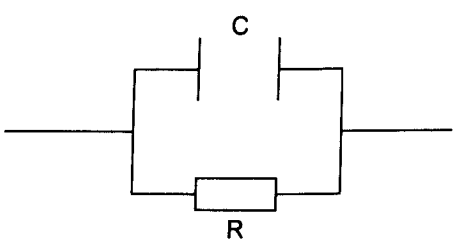

Figure 2-2: A typical equivalent circuit consisting of a parallel RC element.

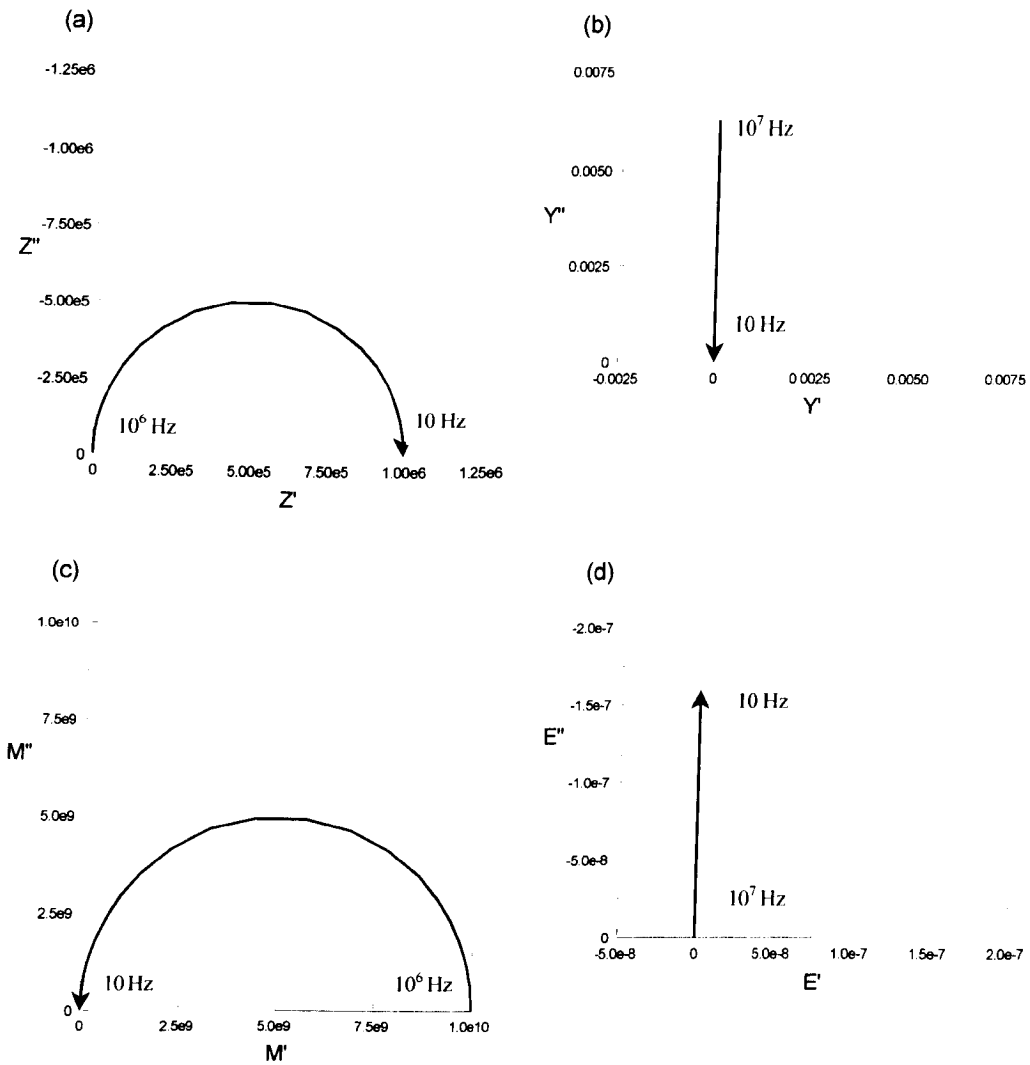

Figure 2-3: Complex formalism (a) impedance, Z*, (b) admittance, Y*, (c) electric modulus, M* and (d) prmittivity, E* or ε*, for the equivalent circuit in figure 2-2 where R = 1 MΩ and C = 100 pF . Arrows indicate the direction of decreasing frequency. Impedance measurements start at high frequency and finish at low frequency.

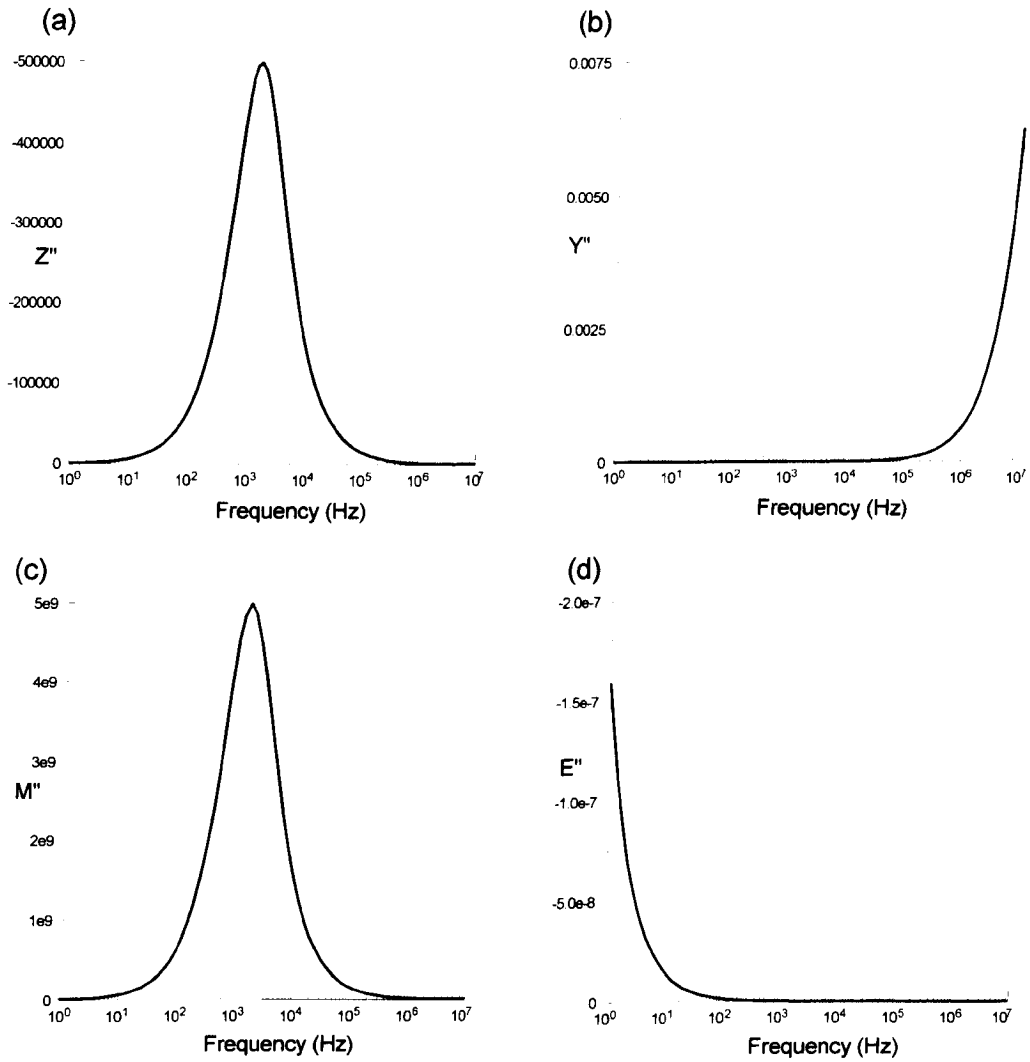

Figure 2-4: Spectroscopic plots for imaginary component as a function of log (frequency, f) (a) Z" vs. $\log_{10}f$, (b) Y" vs. $\log_{10}f$, (c) M" vs. $\log_{10}f$ and (d) E" or ε" vs. $\log_{10}f$ for the equivalent circuit in figure 2-2, where R = 1 MΩ and C = 100 pF .

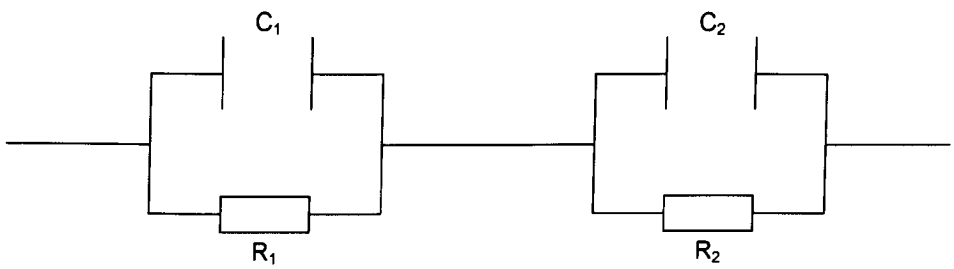

Figure 2-5: A typical equivalent circuit consisting of two parallel RC elements connected in series.

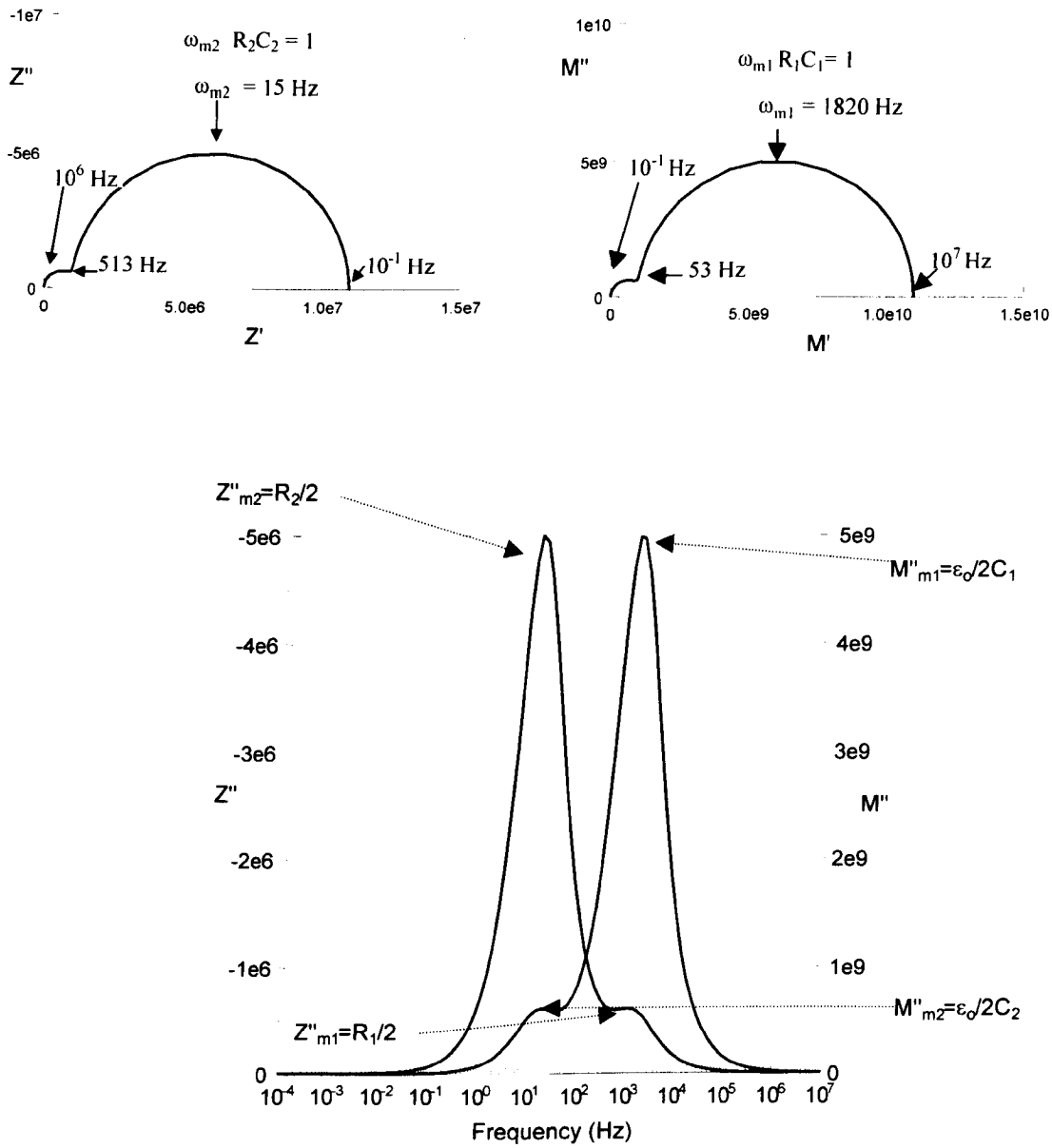

Figure 2-6: (a) Complex impedance, Z*, (b) complex electric modulus, M* and (c) combined imaginary impedance, Z'' and imaginary electric modulus, M'' spectra for the equivalent circuit in figure 2-5, where R_1 = 1 MW , C_1 = 100 pF , R_2 = 10 MW and C_2 = 1 nF .

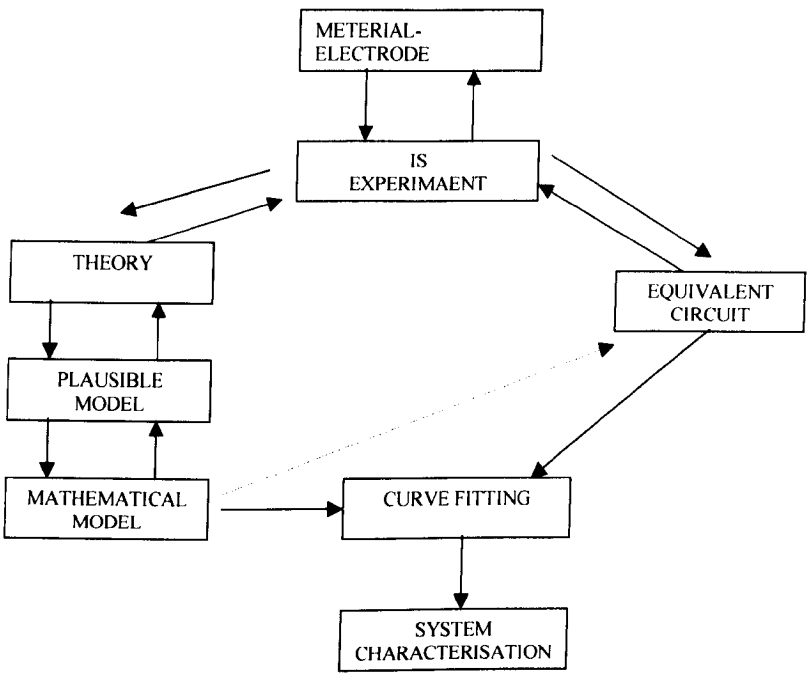

Figure 2-7: Flow diagram for the measurement and characterisation of a material-electrode system.

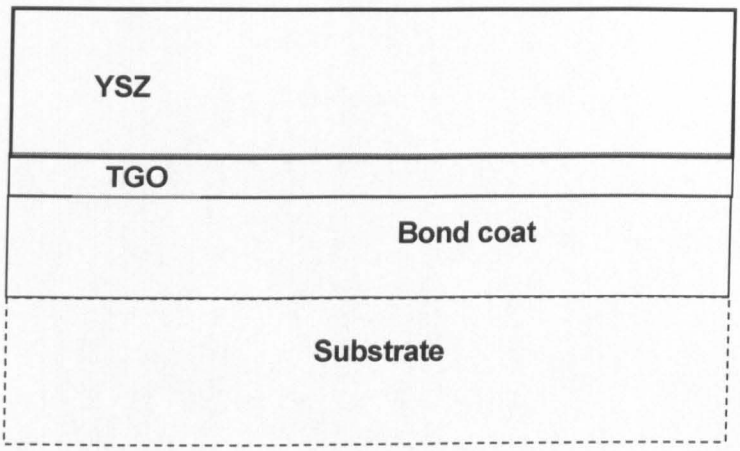

Figure 2-8: Typical thermal barrier coating system.

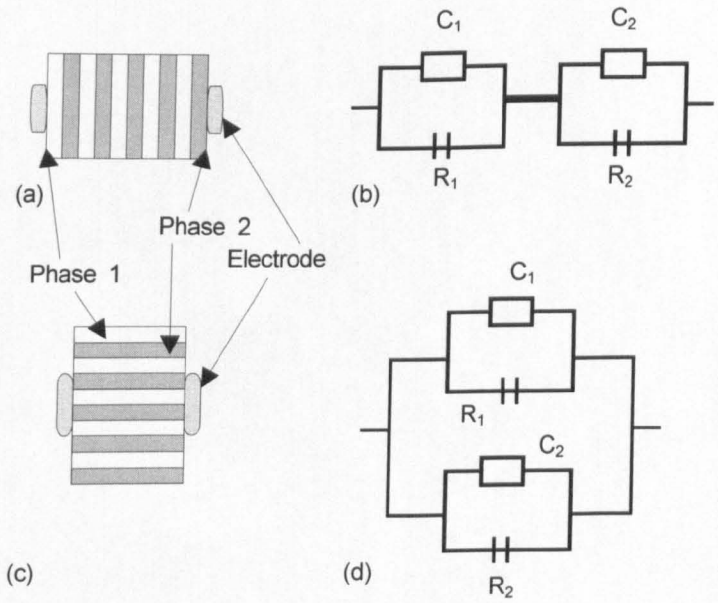

Figure 2-9: (a) Series layer model. (b) Equivalent circuit of series layer model. (c) Parallel layer model. (d) Equivalent circuit of parallel layer model. (Note: the electrode effect is not included in this diagram.)

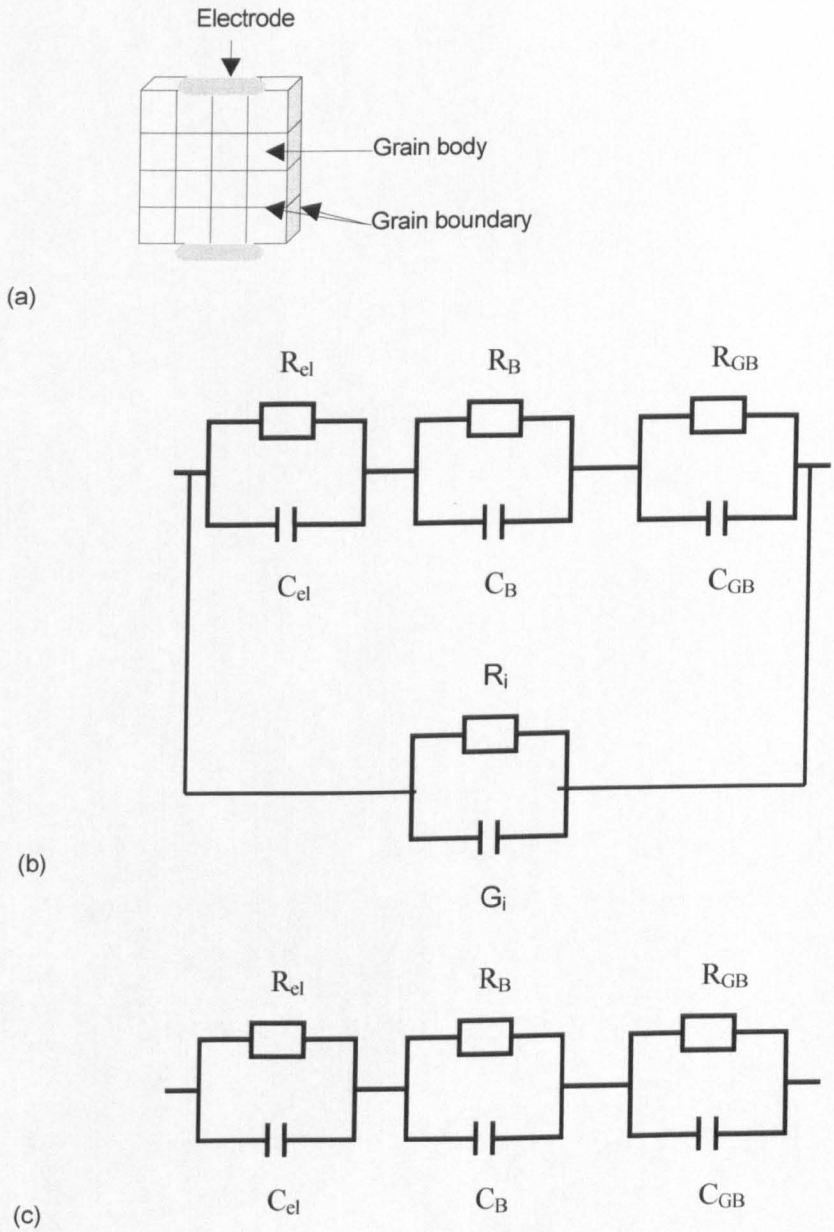

Figure 2-10: (a) Schematic of the real ceramic microstructure. (b) Bricklayer model and equivalent electrical network consisting of different RC element. (c) Simplified bricklayer model and equivalent electrical network consisting of different RC elements. Indices: el = electrode/ceramic interface, B = bulk, G_i = grain boundary channels perpendicular to the electrode interface, GB = grain boundary channels parallel to the electrode interface [Waser and Hagenbeck, 2000]. (Note: the electrode effect is not included in this diagram.)

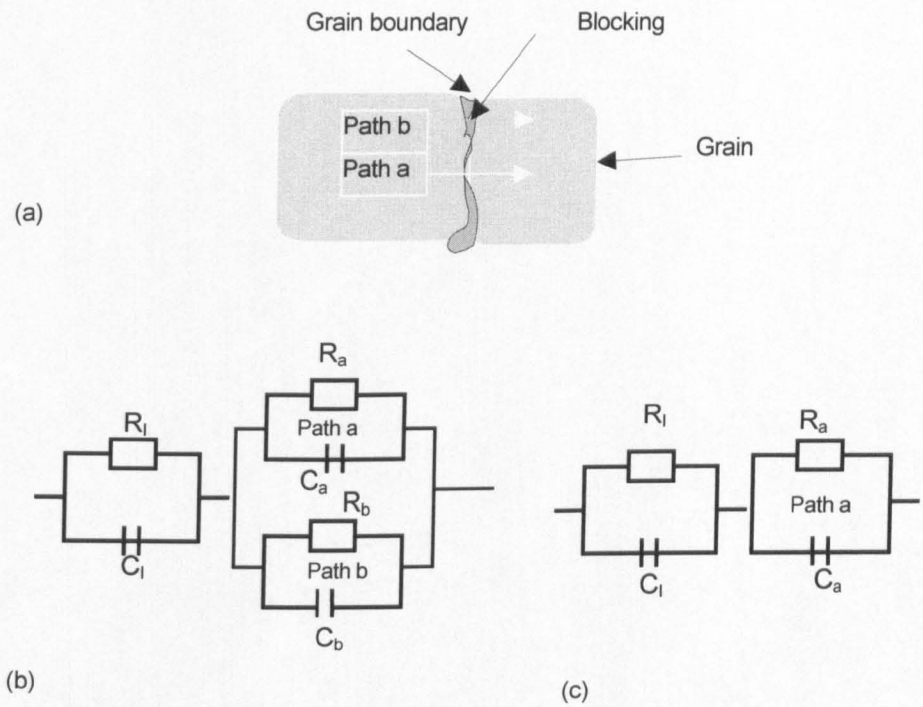

Figure 2-11: (a) Schematic of the constriction model, with the dark areas representing insulating phase. (b) Equivalent circuit of the constriction model. (c) Simplified equivalent circuit of the constriction model. (Note: the electrode effect is not included in this diagram)

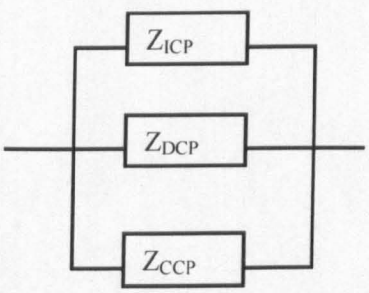

Z_{ICP}: impedance of the 'insulator' conductive paths
Z_{DCP}: impedance of the discontinuous conductive paths
Z_{CCP}: impedance of the continuous conductive paths

Figure 2-12: Extracted electric conduction model for concrete.

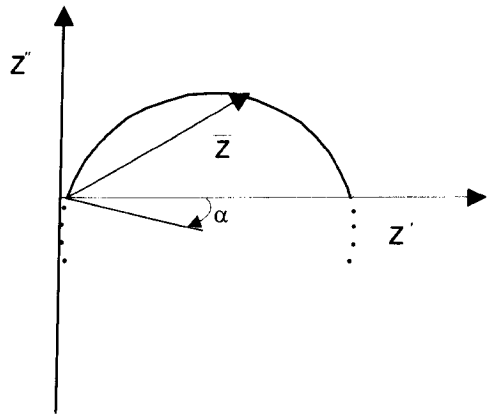

Figure 2-13: The depressed semicircle in complex plane impedance plot.

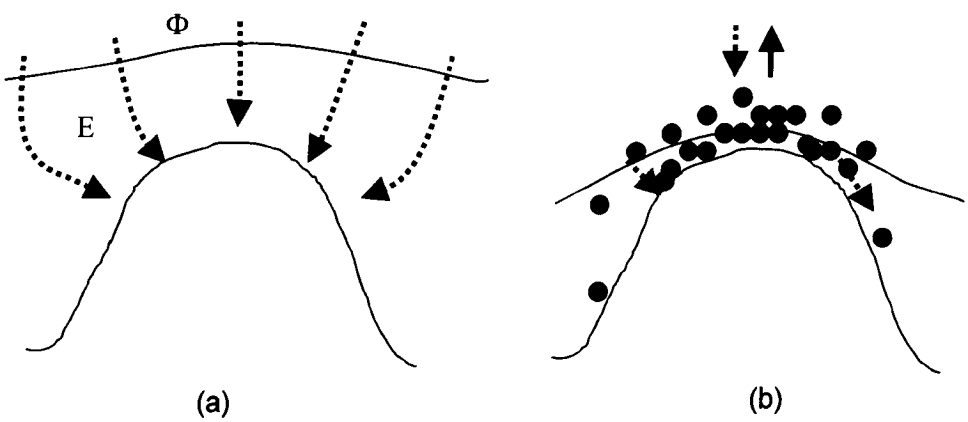

Figure 2-14: A schematic of a "mound" type of surface irregularity [Scheider, 1975].

3. Experimental Procedure

3.1 Introduction

In order to asses the viability of impedance measurements for non-destructive testing or evaluation of samples, it is important to conduct destructive methods to establish the relationship between impedance response and the physical characteristics of the sample that are responsible for this impedance response. Destructive methods which can be conducted on samples are scanning electron microscopy (SEM) for metallagraphic examination, energy dispersive X-ray analysis (EDX) for composition analysis and X-ray diffraction (XRD) for crystallographic analysis. Samples were prepared for impedance analysis, metallographic examination, energy dispersive X-ray analysis and X-ray diffraction analysis.

3.2. Materials

Sermatech Ltd., Lincoln, UK supplied all the materials used in these experiments. These materials were nickel-based IN738LC superalloy (for composition see table 3.1), metallic NiCrCoAlY bond coat (for composition see table 3.2) applied on nickel-based Haynes-230 superalloy (for composition see table 3.3), a thermal barrier coating (TBC) system and yttrium stabilised zirconia (YSZ) coated on metallic aluminium. The YSZ contains 8 wt.% Y_2O_3 and 92 wt.% ZrO_2. These materials were used in this study because they are used in the components of gas turbine engines for electricity generation. The IN738LC superalloy was used because it is an alumina-forming alloy like the NiCrCoAlY bond coat. The TBC systems consisted of three layers, the first layer was Haynes-230 nickel-based superalloy substrate, the second layer was vacuum plasma-sprayed NiCrCoAlY bond coat, and the third layer was air plasma-sprayed YSZ (Metco 204 NS TBC top coat). The thickness of the bond coat was ~80 to 100 μm and the thickness of YSZ applied on bond coat was ~250 to 300 μm. Haynes-230 is a chromia-forming alloy. The YSZ plate (~2 mm thick) was obtained by dissolving away the metallic aluminium substrate in concentrated NaOH solution.

Table 3.1: The Composition of IN738LC superalloy (wt%).

Ni	Cr	Al	Co	Ti	Mo	W	Nb	C	B	Zr
63.12*	16	3.5	8.5	3.5	1.75	2.6	0.85	0.11	0.009	0.06

* as balance

Table 3.2: The composition of NiCrCoAlY bond coat (wt%).

Ni	Cr	Co	Al	Y
32	21	38.5	8	0.5

Table 3.3: The composition of Haynes-230 superalloy (wt%).

Ni	Cr	W	Mo	Fe	Co	Mn	Si	Al	C	La	B
57*	22	14	2	3	5	0.5	0.4	0.3	0.10	0.02	0.015

* as balance

3.3. Sample Preparation

TBC samples and bond coat samples were supplied as plates of 20mm × 60mm × 2 mm in size. Nickel-based superalloy samples were supplied as a 15mm diameter and 200mm long rod. Samples were cut to size using a Discotom-2 cutter before the ageing process. Bond coat and IN738LC samples were ground using SiC paper (No.1200) and cleaned using acetone before oxidation. TBC samples 20mm × 20mm × 2mm or 10mm × 10mm × 2mm in size, bond coat samples 10mm × 10mm × 2mm in size, YSZ samples 20mm × 20mm × 2mm in size and nickel-based superalloy samples of 15mm diameter and 2mm thickness, were thermally aged. A Chamber furnace was used for the thermal ageing process. Samples were kept at specific temperatures in air for a specific duration, depending on the experimental requirements. The heating and cooling rates were 10K.minute^{-1}. Five samples for each oxidation time were prepared. Three samples were chosen randomly from the five samples for impedance measurements.

3.4. Electrode Preparation for Impedance Measurements

Impedance measurements can be made on solid samples by pressing a metal foil directly to the surface. The surface of solid materials, such as YSZ or oxide is not flat, which makes it difficult to establish a good contact between the electrode and sample. As a result of this poor contact, the contact area between these two is very low compare to the overall surface area directly under the electrode. To ensure a good contact, painted electrodes were normally used for all experiments.

After thermal cycling, one side of the metal substrate without the TBC was polished using silicon carbide paper to remove the oxide layer. Then samples were cleaned in an ultrasonic bath with water and washed with acetone. The other side with the TBC was painted with a silver conductive ink (E800, Johnson Matthew Electronics, UK) or platinum conductive ink (Engelhar Clal U.K. Ltd, Cinderford, Gloucester, U.K.). The silver paint was fired at 450°C in air for 30 minutes. The platinum paint was first cured at 120°C in air for 30 minutes and then fired at 1200°C in air for 10 minutes to promote the adhesion to the TBC. The heating and cooling rates were 10K.minute^{-1} during electrode processing. Since preliminary experimental results showed that the electrode area had no effect on the impedance measurements, the conductive ink was painted on the TBC samples with an area of either 5mm × 5mm or 10mm × 10mm. For bond coat alloys, the oxide formed on one side of the substrate was polished away using silicon carbide paper. Then the bond coat samples were cleaned in an ultrasonic bath with water and washed with acetone. The other side with oxide formed on the bond coat was painted with silver conductive ink and fired at the required temperature. The painted area for this oxide was 5mm × 5mm and the paint acted as one electrode while the metal substrate acted as the other electrode. For the IN738LC superalloys, the oxide formed on one side of the substrate was polished away using silicon carbide paper and cleaned in an ultrasonic bath with acetone. The other side with oxide was painted with silver conductive ink and fired at the required temperature. The paint area was 5mm × 5mm, which acted as one electrode with the substrate as the other electrode. For the YSZ layer after removing aluminium substrates, both sides were painted with

silver paint and fired at required temperatures. In this case, the painted area was 10mm × 10mm. Two platinum wires were used as leads for connection via platinum foil to both sides of the sample or measurement cell to the impedance spectroscopy (IS).

3.5. Sample Holder for Impedance Measurements

A typical sample holder as shown in figure 3-1 was used for all impedance measurements. Nuts and bolds were used to ensure an intimate contact between the conductive ink and platinum foil. The platinum foil was connected to the platinum wire and the platinum wire was covered with thin alumina insulator tubes. For high temperature measurements, the sample holder containing the sample connected to the measurement wire, was inserted in to the electromagnetic shield (figure 3-2). Then, this electromagnetic shield was safely placed in a tube furnace for high temperature impedance measurements and measurement wires were connected to the IS.

3.6. Impedance Measurements

Impedance measurements were conducted using a Solarton SI 1255 HF Frequency Response Analyser (FRA) coupled with a Solarton 1296 Dielectric Interface, which was computer-controlled. Using Zview impedance analysis software (Scribner Associates Inc, Southern Pines, NC), spectral analysis was performed to extract the electrical and dielectric properties of samples. In these measurement, an AC (alternating current) amplitude of 10 mV or 100 mV was employed and the AC frequency was in the range of 1×10^{-4} Hz to 1×10^{7} Hz with 6 readings per decade. The measurements were performed at different temperatures in air. The heating and cooling rates were $10K.minute^{-1}$. To ensure the steady state of the sample, impedance measurements were made after the samples had been placed in a measurement condition for 30 minutes. Metal and ceramic shielding as shown in figure 3-2 was used as an electromagnetic shield around the sample holder to reduce interference from the furnace and the metal was earthed. The measurement

temperature and applied voltage were 400°C and 10mV respectively for TBC samples which was used to show the impedance responses for different electrodes. The painted area for these samples were 5mm x 5mm. The measurement temperature and applied voltage were 400°C and 10-500mV respectively for TBC samples, thermally cycled up to 1200°C for 400 hours, to study the effect of the applied AC voltage on the impedance results.

3.7. Metallographic Examination

After impedance measurements, cross-sections of the samples were prepared. A J840 Scanning Electron Microscopy (SEM) equipped with an Energy Dispersive X-ray (EDX) Microanalyzer (AN10000, Oxford Instruments) was employed to evaluate the thermally-grown oxides (TGOs) in these samples. Samples were mounted in phenolic resin and then cross-sections were cut using a low speed diamond saw to reduce damage in the samples. The surface of each cross-section was manually ground using 180, 400, 800, 1200 and 2500 grit SiC papers. After grinding, the surface was polished using both 6μm and 1μm diamond paste. The samples were ultrasonically cleaned in water, rinsed in ethanol and coated with gold or carbon. SEM was used to study the microstructure of the cross section of samples. It identified cracks and spallation in the samples. EDX analysis together with electron microscopy enables the quantification of elements within samples and was used extensively for analysis of TGO regions. The Standards used for ZAF correction were pure metals.

3.8. Crystallography

Crystal structures of oxide scales were determined by X-ray Diffraction (XRD). X-ray diffraction measurements were performed using a Philips diffractometer (PW1050), with a Ni-filtered CuKα radiation. The step size was 0.01° and angular scan speed was 1°minute^{-1}. The angular scan range was 10° to 90°.

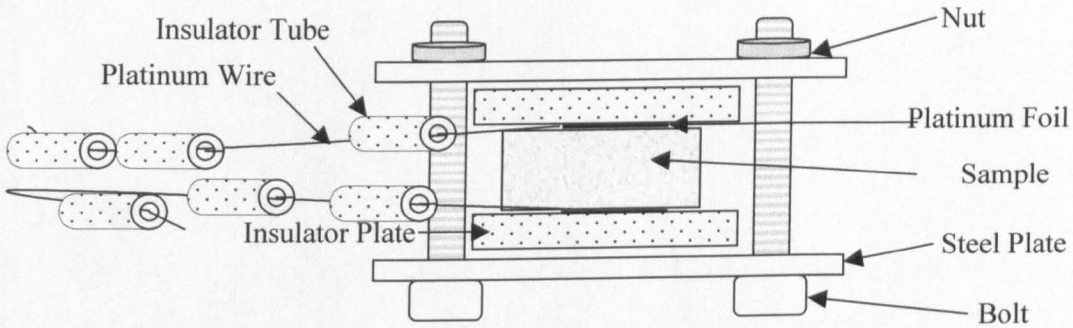

Figure 3-1: A typical sample holder for impedance measurements.

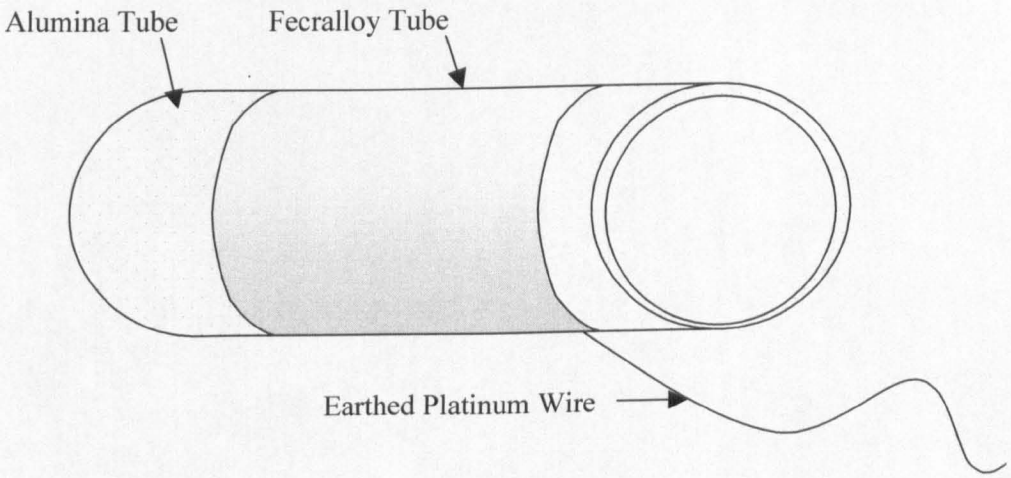

Figure 3-2: Electromagnetic shield connected to ground.

4. Microstructure Evaluation of the Oxide Scales by IS

4.1. Introduction

High temperature oxidation resistance is a primary requirement for application of a metallic material at high temperature. This may be achieved by forming a protective oxide scale on its surface [Birks et al., 1994]. The protective ability of an oxide scale is dependent on its ability to reduce the rate of the oxidation reaction by acting as a diffusion barrier between the metallic material and the oxidising environment. Most of the oxide scales formed on metals and alloys are semiconductors. Electrical properties of oxide scales may be related to their microstructures.

In this chapter, impedance spectroscopy (IS) has been used to characterise oxide scales formed on IN738LC superalloy and NiCrAlCoY bond coat at high temperatures in air. The aim of this chapter is to develop IS for non-destructive evaluation of oxide scales. Electrical resistance and capacitance of the oxide scales can be obtained from the simulation of the measured impedance diagrams based on the equivalent circuit model, which represents the features of the oxide scales.

4.2. Experimental Procedure

4.2.1. Oxidation Treatment

The samples were oxidised in air for the range of temperatures and times as indicated in table 4-1. Five samples were oxidised at each condition (i.e. 1100°C for 100 hours etc.).

Table 4-1: Oxidation treatment of the samples.

Materials	Exposure temperatures (°C)	Oxidation time (Hour)	Holding periods at the exposure temperatures in the different thermal cycles (Hour)		
			Thermal cycle 1	Thermal cycle 2	Thermal cycle 3
Nickel-based alloy IN738LC	900	18	18		
		110	110		
		157	157		
		175	175		
		267	267		
	1200	4	4		
		5	5		
		8	8		
		10	10		
Bond coat NiCoCrAlY	900	500	500		
		1000	1000		
		1500	1500		
		2000	2000		
		2500	2500		
	1000	10	10		
		50	50		
		100	100		
		170	170		
		180	180		
		190	190		
	1100	100	100		
		200	100	100	
		300	100	100	100

4.2.2. Impedance Measurements

Three samples were chosen randomly from the five samples for impedance measurements. The silver conductive ink was used for both IN738LC and bond coat samples. The paint area was 5mm × 5mm, which acted as one electrode with the substrate as another electrode. For IN738LC samples, impedance measurements were made at room temperature in air. For bond coat samples, impedance measurements were made at room temperature, 200°C, 300°C and 400°C in air. In the measurement, an AC (alternating current) amplitude of 10 mV was employed. The AC frequency was in the range of 1Hz to 1×10^6 Hz for IN738LC samples and 1Hz to 1×10^7 Hz for bond coat samples.

4.3. Results

4.3.1. IN738LC Superalloy

Figure 4-1a & 4-1b show both Bode plots and a complex plot from impedance measurements at room temperature for the oxide scales, formed on a nickel-based superalloy, IN738LC, after oxidation at 900°C for 267 hours in air. Bode plots show the relationships of impedance or phase angle with frequency, where there are two peaks in the phase angle vs. frequency plot. This indicates that the oxide scales show two relaxation frequencies under an AC electric field. The complex plot, which is known as a Nyquist plot, shows the relationship between the real and imaginary parts of impedance. The lines with dots are experimental results whereas the plain lines are the best simulation results by assuming the oxide scales acted as a series connection of two RC circuits (figure 4-1c).

Clearly the fitting of both Bode plots and the Nyquist plot are not satisfactory. This suggests that the equivalent circuit of figure 4-1c does not represent the features of the oxide layers. The oxide scale is not a simple duplex layer of oxides.

Figure 4-2a and 4-2b show the microstructure of the cross section of the oxide layers formed from oxidation of IN738LC at 900°C in air for 110 and 267 hours respectively. Apparently there was some internal oxidation which leads to the formation of oxide inside the alloy but close to the metal/oxide interface. Both the metal/oxide interface and the surface of the oxide are rough. The microanalysis of the oxide layer indicates the complex composition of the oxide scales (figure 4-2c). Pure metals were used as standards in ZAF correction.

So, capacitors of the equivalent circuit (figure 4-1c) should be replaced by constant phase elements (CPE) due to heterogeneity of the oxide scale. As a result of this modification, equivalent circuit of the oxide layers became a series connection of two R-CPE circuits (figure 4-3c). The CPE represents impedance that is dependent on frequency. As the oxide scale consists of a few oxides, which have different relaxation frequencies, the CPE should be a better representation of the oxide scale than a single capacitor. Series connection of two R-CPE circuits (figure 4-3c) gave a much better fitting of both the Bode plots and the complex plot (figure 4-3a and 4-3b). Resistance of both oxide layers was obtained from the fitting result based on the equivalent circuit in figure 4-3c.

Figure 4-4 shows the relation between the thickness of oxide scales and oxidation duration. The parabolic nature of oxide growth indicates that the initial formation of the oxide scale reduced further oxide formation. So oxides formed on IN738LC superalloy is a protective oxide and reduces further degradation of this alloy.

Figure 4-5 shows the relationship between resistance vs. thickness. There is a general trend of increasing resistance with increasing thickness of the oxide scale with the exception that there is a sudden drop of electrical resistance when the oxide scale grows to a thickness of 5μm. This indicates that there might be cracks in the oxide scale at this point. Silver paint could be penetrate deeper in to the scale. The formation of cracks lead to the penetration of the silver paint from the electrode, which would reduce the resistance significantly by decreasing the effective thickness of oxide scale.

From SEM observation and microanalysis of the oxide scales formed at 900°C, it could be deduced that the thickness of the nickel rich layer that contains aluminium increased with increasing oxidation time (figure 4-6). The thickness of the chromium rich layer first increased and then decreased with increasing oxidation time (figure 4-7). This is because after oxidation for a certain period more aluminium and nickel was oxidised and the inner oxide layer grew at the expense of the outer oxide layer, which is a chromium rich layer.

Further study needs to be carried out to explain this phenomena. The oxide scale formed from oxidation at 1200°C up to 104 hours showed a very low electrical resistance and did not show any semicircle in the complex plot. This suggests that there is no continuous oxide layer formed on metal substrates under these conditions.

4.3.2. NiCoCrAlY Bond Coat

Figures 4-8 and 4-9 show examples of impedance spectra measured at 400°C for the oxide scales, formed on a bond coat alloy (NiCrCoAlY) after oxidation at 900°C for 500 hours, 1500 hours and 2000 hours in air. The spectra are presented in the form of Bode diagrams (figure 4-8) and a complex diagram (figure 4-9). These data show that only one time constant charge process is occurring in the scales. Figure 4-10 shows the spectroscopic display of Z" vs. frequency (f) for the above oxide scales measured at 400°C, where the relaxation frequency for this single time constant charge process is between 10^3Hz-10^4Hz. The complex plot shows a depressed semicircle, where the size of the semicircle increased with increasing oxidation time. Thus, the experimental results are interpreted by means of an equivalent circuit model as shown in figure 4-13a, where only one parallel R-CPE circuit can represent the oxide scale formed on the bond coat.

Figures 4-11a and 4-11b show SEM images of oxide scales formed at 900°C for 1500 hours and at 1100°C for 300 hours respectively. These images show only one dark oxide layer with a discontinuous grey layer or spots.

Figures 4-11c and 4-11d show backscattered images for the above oxide scales which indicate that these scales have a single-layer structure. EDX analysis confirmed that the dark layers were mainly alumina layers with about 87%wt. Al in their elemental composition. Further elemental analysis confirm that the grey areas in the oxide scale were oxides of Cr, Ni, Co and Al with no fixed composition.

Figure 4-12a shows the XRD pattern for bond coat alloy, which is used as a reference for the XRD pattern for oxide scales. Figures 4-12b and 4-12c show the XRD patterns for oxide scales formed on the bond coat from oxidation at 900°C for 1500 hours and at 1100°C for 300 hours respectively. These show that oxides of Ni, Cr and Co are present as spinels. Therefore, the oxide scale formed on the bond coat at 900°C for 1500 hours shows one layer structure of mainly an α-Al_2O_3 layer with impurities of other oxides, such as $NiAl_2O_4$ (NiO and Al_2O_3), $NiCr_2O_4$ (NiO and Cr_2O_3) and $CoAl_2O_4$ (CoO and Al_2O_3) etc. XRD analysis identified α-Al_2O_3 and normal Al_2O_3 in oxide scales. However, oxide scale formed on the bond coat at 1100°C for 300 hours shows a two layer-structure of mainly α-Al_2O_3 layer and a discontinuous layer of other oxides, such as $NiAl_2O_4$ (NiO and Al_2O_3), $NiCr_2O_4$ (NiO and Cr_2O_3) and $CoAl_2O_4$ (CoO and Al_2O_3) etc. This explains why the impedance diagrams (figures 4-8, 4-9 and 4-10) show only one time constant.

Figure 4-13a shows the equivalent circuit for a single-layer structured oxide scale formed on the bond coat alloy. A CPE was used instead of C, because the oxide composition was not uniform in all areas and also grey spots were identified in the dark oxide (figure 4-11). This non-uniformity in the oxide scale can contribute to a spreading of relaxation frequency as predicted by Macdonald in his work [Macdonald and Franceschetti, 1987]. Figures 4-13b and 4-13c show changes of the electrical resistance and electrical capacitance with ageing at 900°C in air, where the resistance increased and capacitance decreased with increased ageing time. This may be due to a thickness change of the oxide scales with oxidation.

4.4. Discussion

4.4.1. IN738LC Superalloy

A two-layer structure appeared in the oxide scale formed on the IN738LC superalloy with an outer layer rich in chromium and an inner layer rich in aluminium and nickel. Both layers should show two semicircles in the IS spectrum with different relaxation frequencies. The relaxation frequency is a characteristic of a material and can be calculated as:

$$f_{max} = \frac{\sigma}{2\pi\varepsilon\varepsilon_0} \qquad (4\text{-}1)$$

where f_{max} is the relaxation frequency, σ is the conductivity, ε is the dielectric constant, ε_0=8.854x10^{-12} F m^{-1} is the permitivity of empty space.

Table 4-2: Electrical properties of oxides at room temperature.

Oxides	TiO_2	Cr_2O_3	α-Al_2O_3	NiO
σ ($\Omega^{-1}m^{-1}$)	$\approx 1.1x10^{-3}$ [Lide, 1998]	$\approx 1.7x10^{-5}$ [Lide, 1998]	$\approx 10^{-12}$ [Lide, 1998]	$\approx 10^{-11}$ [Birks et al., 1994], [Moses, 1978] and [Richerson, 1992]
ε	$\approx$114 [Lide, 1998]	$\approx$ 12 [Lide, 1998]	$\approx$10 [Lide, 1998]	$\approx$11.9 [Lide, 1998]
f_{max} (Hz)	$\approx 10^5$	$\approx 10^4$	$\approx 10^{-3}$	$\approx 1.5x10^{-2}$

Table 4-2 shows the electrical properties of α-Al_2O_3, Cr_2O_3, NiO and TiO_2. According to equation 4-1, the theoretical relaxation frequencies for TiO_2, Cr_2O_3, α-Al_2O_3 and NiO are ~10^5 , ~10^4, ~10^{-3} and ~10^{-2}Hz, respectively. The relaxation frequencies for the first semicircle and the second semicircle for the oxide scale formed on IN738LC superalloy aged at 900°C for 267 hours are about ~10^3 Hz and 17 Hz, respectively (figure 4-14). It is reasonable to assume that the first semicircle

related to the measurement of chromium-rich layer and the second semicircle related to the measurement of nickel-rich layer.

Here IS measurements indicate that there are different composition zones across the oxide scales. There was no clear boundary between the two layers across the oxide scales (figures 4-2a & 4-2b). XRD analysis (figure 4-2d) shows that α-Al_2O_3, Cr_2O_3, NiO and $NiCr_2O_4$ are present in the oxide scales. Therefore, the oxide layers do not consist of single phases. This is in agreement with the measured impedance diagrams where the simulation of simple RC circuits could not give good fitting of the experimental results (figure 4-1). Moreover the depressed semi-circle in the complex plot also suggests the presence of mixed phases together with rough surfaces of the oxide scales and rough oxide/ substrate interfaces.

The oxide scale formed by oxidation at 900°C in air for 18 hours showed one semicircle in the complex plot with a relaxation frequency 3585Hz (figure 4-14), which is close to that of chromia. EDX analysis of this oxide scale gives the composition (wt.%) as 41%Cr, 21%Ti, 19%Al and 13%Ni, which confirms the high concentration of chromia and titania and low concentration of nickel oxide. The high concentration of chromia and titania leads to a high relaxation frequency of this oxide scale.

4.4.2. NiCoCrAlY Bond Coat

4.4.2.1. Relaxation Frequency

The relaxation frequency of pure alumina was obtained using equation 4-1.

Table 4-3: f_{max} pure alumina.

Oxides	Temperature (°C)	ε [Lide, 1998]	σ [Wirth, 1991] ($\Omega^{-1}m^{-1}$)	f_{max} (Hz)
99.6% Al_2O_3	25	≈10	$\approx 10^{-12}$	$\approx 1.8*10^{-3}$
	300	≈10	$\approx 10^{-10}$	$\approx 1.8*10^{-1}$
	500	≈10	$\approx 10^{-8}$	$\approx 1.8*10^{+1}$

The relaxation frequency can be calculated as:

$$f_{max} = \frac{1}{2\pi RC} \qquad (4\text{-}2)$$

where R is the electrical resistance (ohms) and C is the capacitance (farads). A single relaxation frequency is observed for aged bond coat samples, since it shows only one semicircle in its complex plot.

Table 4-4: f_{max} of oxide scale formed on the bond coat aged at 900°C for 2000 hours.

Oxide scales	Temperature (°C)	C (Farads)	R (Ω)	f_{max} (Hz)
≈87 % Al_2O_3	25	$7*10^{-10}$	$4.5*10^{7}$	5.06
	200	$1.33*10^{-9}$	$6*10^{6}$	$2*10^{2}$
	300	$4.28*10^{-9}$	$8*10^{4}$	$4.65*10^{2}$
	400	$4.13*10^{-9}$	$2.8*10^{4}$	$1.37*10^{3}$

Table 4-5: f_{max} of oxide scale formed on the bond coat aged at 900°C for 2500 hours.

Oxide scales	Temperature (°C)	C (Farads)	R (Ω)	f_{max} (Hz)
≈87 % Al_2O_3	25	$1*10^{-9}$	$2.37*10^{8}$	$6.72*10^{-1}$
	200	$1.7*10^{-9}$	$2.90*10^{6}$	$3.23*10^{1}$
	300	$1.9*10^{-9}$	$3*10^{5}$	$2.79*10^{2}$
	400	$2.5*10^{-9}$	$4.2*10^{4}$	$1.53*10^{3}$

The theoretical relaxation frequencies at room temperature for Cr_2O_3 and α-Al_2O_3 are $\sim10^{4}$ and $\sim10^{-3}$, respectively (table 4-2). For the oxide scale, $f_{max} \approx 5$ Hz ~ 0.7 Hz at 25°C (table 4-4 and 4-5). If it is pure α-Al_2O_3, then the relaxation frequency should be $\sim10^{-3}$.

Therefore, it is reasonable to assume that Cr_2O_3 impurities in α-Al_2O_3 scales increased the relaxation frequencies of the oxide scales formed on the bond coat. Again similar relaxation frequencies observed for samples aged for 2000 hours and 2500 hours indicate that the oxide scales are similar. EDX analysis show that both oxide scales are similar and the Al content (wt.%) in the oxide scales is ~87%.

4.4.2.2. Conductivity Mechanism

The electrical resistances of the oxide scale formed at different temperatures, were converted to the conductivity σ using the equation:

$$\sigma = \frac{l}{R*A} \qquad (4\text{-}3)$$

where 'σ' is the conductivity, 'R' is the electrical resistance, 'l' is the scale thickness and 'A' is the effective area.

Experimental conductivity data was plotted to fit the Arrhenius equation:

$$\ln \sigma = \ln \sigma^{\circ} - \frac{E_a}{kT} \qquad (4\text{-}4)$$

where 'σ' is the conductivity, 'σ°' is the constant, 'E_a' is the activation energy, 'k' is the Boltzmann's constant and 'T' is the temperature in Kelvin.

Figures 4-15, 4-16 and 4-17 show ln σ vs. T plots for oxide scales formed at 900°C, 1000°C and 1100°C, respectively. The plots are not linear which suggests there are more than one conduction process.

Figure 4-18 shows Arrhenious plot of ln σ vs. T (temperature in Kelvin) for pure α-Al_2O_3 using data from Wirth [1991]. The ln σ vs. T plot was divided into two regions, which indicates that the electrical conduction process for the α-Al_2O_3 thin film is not the same at all temperatures. The temperature dependence of the electrical conductivity changes at around 200°C for pure α-Al_2O_3. A similar result has been observed previously, which shows that the temperature dependence of electrical conductivity for α-Al_2O_3 is not linear and the transition point for conductivity mechanism changes is around 200°C [Richerson, 1992]. This may be because the conductivity at low temperatures is dominated by the grains and at high temperatures it is dominated by the grain boundaries. This may be the reason for non-linear plot of ln σ vs. T for oxide scales formed on the bond coat as shown in figures 4-15, 4-16 and 4-17.

4.4.2.3. Activation Energy

Conductivity plots (figures 4-15, 4-16 and 4-17) were used to deduce activation energies. The activation energy can be used to characterise the oxides formed on bond coats at various temperatures. A similar activation energy value indicates that the oxides formed at different temperature were the same types of oxides, which was confirmed by using SEM, EDX and XRD analysis.

Conductivity plot of figures 4-18 was used to deduce activation energy for pure alumina. The activation energy for the formation of pure alumina is about 1.12 eV (Table 4-6). In this study, the activation energy was observed to be between 0.44 eV

and 80 eV (Tables 4-7, 4-8 and 4-9). Liu et al. [1999] found activation energies between 0.5-0.6 eV for thermally-grown pure NiO. EDX analysis suggests that the alumina scale formed on the bond coat is not pure alumina. It contained some NiO and Cr_2O_3. So increasing the impurities in the alumina scale reduced the activation energy for forming the coating.

Table 4-6: Activation energy of pure alumina.

Thin film of pure alumina (99.5% Al_2O_3) [Wirth, 1991]	
E_a (eV) (300°C-700°C)	1.12

Table 4-7: Activation energy (E_a) of the bond coat aged at 900°C in air.

Oxidation time	500 hours	1000 hours	1500 hours
E_a (eV) (20°C-200°C)	0.24 ± 0.01	0.37 ± 0.09	0.13 ± 0.08
E_a (eV) (200°C-400°C)	0.48 ± 0.07	0.50 ± 0.08	0.18 ± 0.15

Table 4-8: Activation energy (E_a) of the bond coat aged at 1000°C in air.

Oxidation time	10 hours	170 hours	180 hours
E_a (eV) (200°C-400°C)	0.56 ± 0.03	0.44 ± 0.11	0.80 ± 0.14

Table 4-9: Activation energy (E_a) of the bond coat aged at 1100°C in air.

Oxidation time	100 hours	200 hours	300 hours
E_a (eV) (20°C-300°C)	0.31 ± 0.01	0.30 ± 0.2	0.37 ± 0.03
E_a (eV) (300°C-400°C)	2.21 ± 1.21	0.53 ± 0.02	0.48 ± 0.02

4.5. Summary

Solid state impedance spectroscopy is an effective and reliable method to investigate the electrical conductivity and defect structure in oxide scales formed at high temperatures. The electrical resistance of oxide scales increased with increasing ageing time as seen for the IN738LC superalloy samples and also in the bond coat samples exposed to air at 900°C. However, for the IN738LC superalloy samples, aged at 1200°C, the oxide scales showed a very low electrical resistance. Normally, resistance was found to increase with the increase of oxide layer thickness, but a sudden drop of resistance happens only if cracks are initiated or spallation occurs. With the high temperature process, cracking and spallation in the oxide scales occurred continuously and this can be established by IS. Again, the capacitance decreased with increasing oxidation as well as with the thickness of the oxide scale, as observed in the bond coat samples aged at 900°C.

Oxide scales formed on bond coat alloys at all temperature were α-Al_2O_3 with impurities of other oxides (oxides of Cr, Ni and Co etc.). The relaxation frequency can be used to study α-Al_2O_3 scales formed on the bond coat. A higher relaxation frequency value was observed for oxide scales formed on the bond coat compared to that of pure α-Al_2O_3, which indicated impurities in the oxide scales. An Arrhenious conductivity plot shows that the oxide scales formed on bond coat alloys follow the same pattern as that of pure α-Al_2O_3 thin films. The activation energy is the other electrical parameter, which shows that oxide scales formed on bond coats are not pure alumina and that impurities of NiO influenced it. This impurity reduced the activation energy of formation of α-Al_2O_3 scales. The activation energy can also indicate the "protectiveness" of these oxide scale. The activation energy for pure α-Al_2O_3 is higher than the alumina formed on the bond coat. So a higher activation energy value indicates a higher oxidation protectiveness of these oxide scales.

By using scanning electron microscopy and X-ray diffraction techniques, the composition and microstructure of the oxide scales were examined. It was found

that the electrical properties were determined, not only by the microstructure of the oxide scales, but also by the composition of the oxide scales. Relaxation frequency and activation energy can be used to characterise the microstructure of the oxide scales. Relaxation frequency and activation energy also change with changing composition of the oxide layer.

It is shown that IS is a powerful tool to examine oxidation phenomena in high temperature alloys. By determining the relationship between electrical properties, microstructure and composition of oxide scales, IS may be used as a non-destructive technique for monitoring the oxidation of metallic alloys at high temperature.

(a) Bode plots:

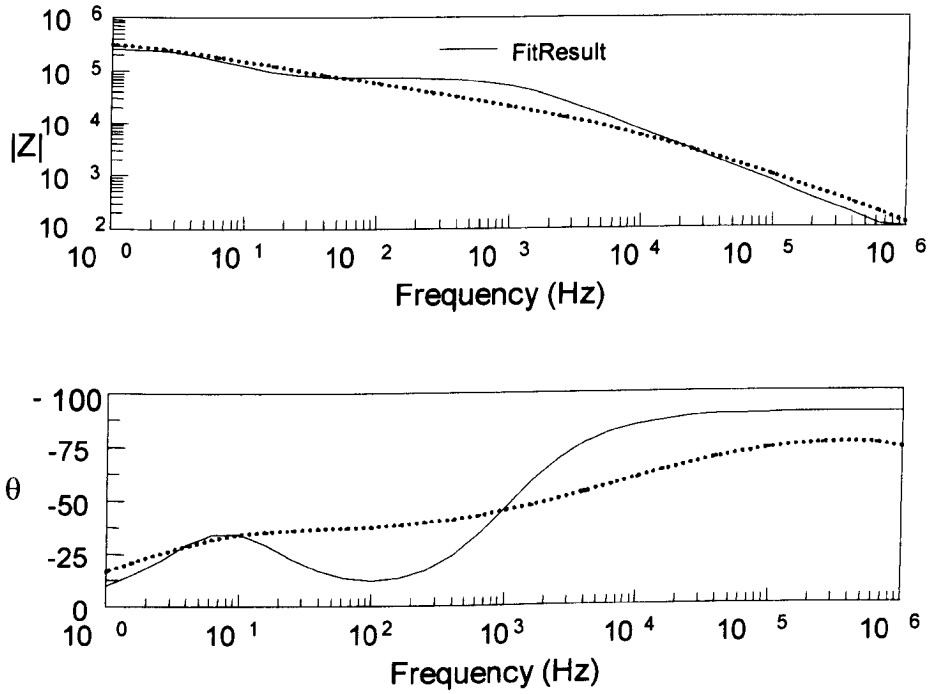

(b) Complex plot:

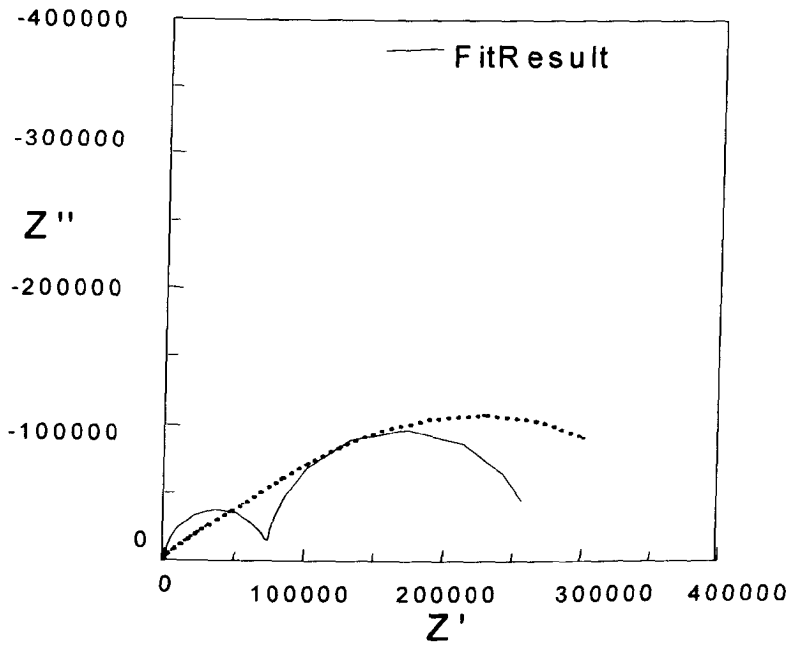

(c) Equivalent circuit A:

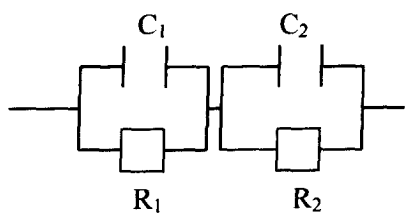

Figure 4-1: Impedance results for the oxide scale of IN738LC superalloy aged at 900°C for 267 hours in air, where experimental results are shown using the dotted line and simulation results based on equivalent circuit 'A' are shown using a plain line (room temperature measurements); (a) Bode plots, (b) Complex plot and (c) Equivalent circuit A.

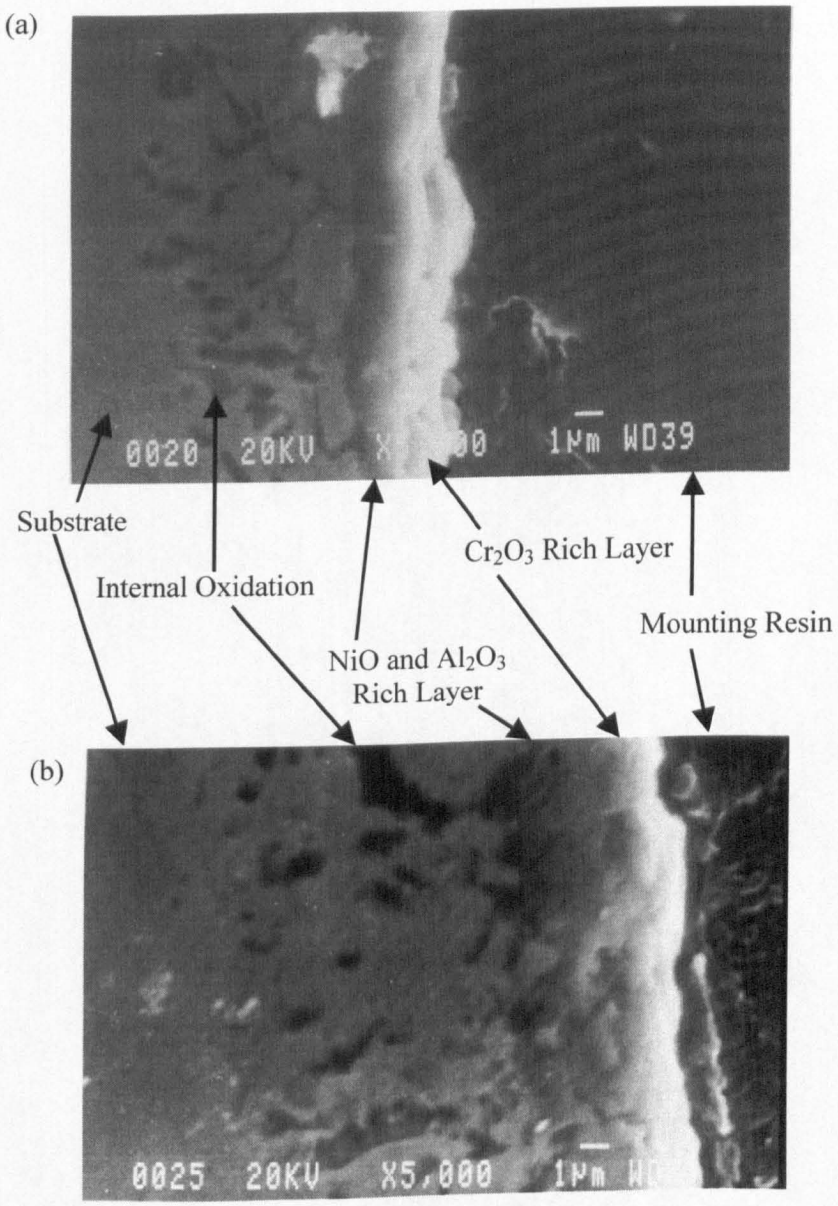
(a)
0020 20KV X 00 1μm WD39
Substrate
Internal Oxidation
NiO and Al_2O_3 Rich Layer
Cr_2O_3 Rich Layer
Mounting Resin
(b)
0025 20KV X5,000 1μm

(c)

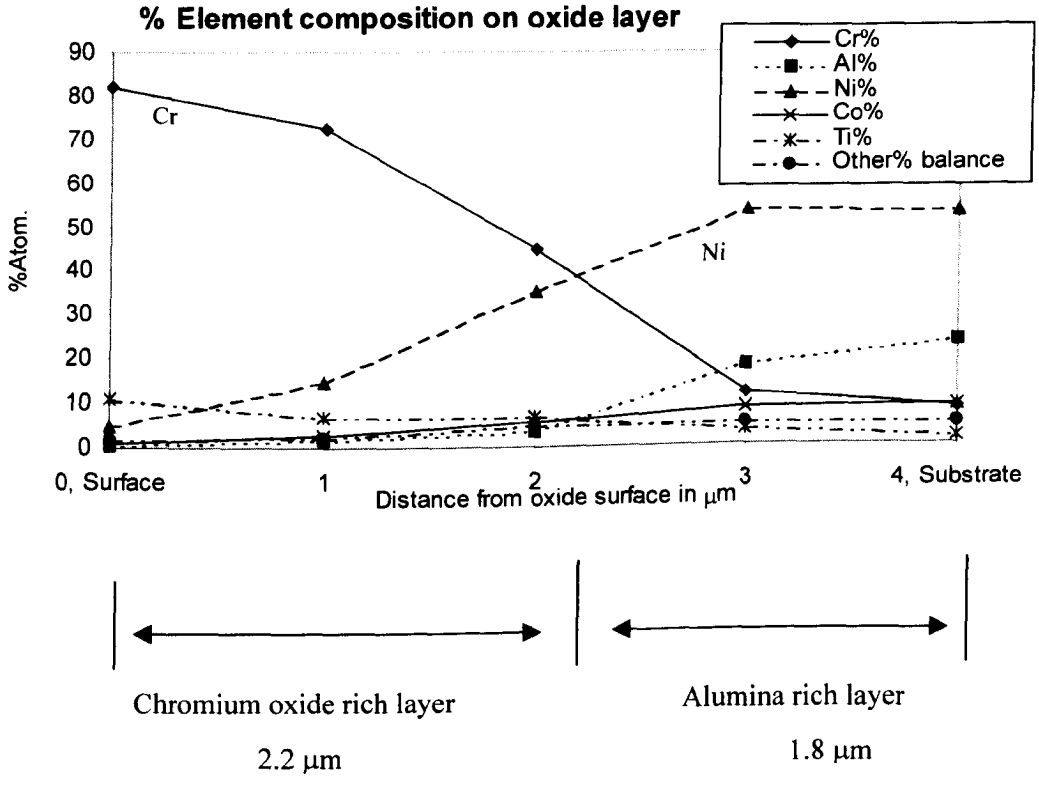
% Element composition on oxide layer
Cr%
Al%
Ni%
Co%
Ti%
Other% balance
%Atom.
90
80
70
60
50
40
30
20
10
0
Cr
Ni
0, Surface
1
2
3
4, Substrate
Distance from oxide surface in μm
Chromium oxide rich layer
2.2 μm
Alumina rich layer
1.8 μm

(d)

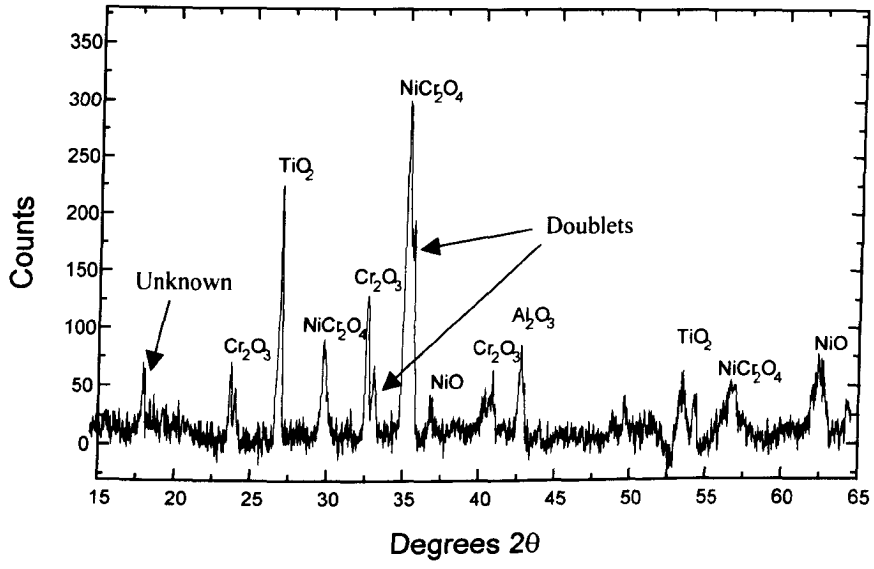

Figure 4-2: (a) SEM micrograph of IN738LC superalloy, oxidised at 900°C for 110 hours in air; (b) SEM micrograph of IN738LC superalloy, oxidised at 900°C for 267 hours in air; (c) EDX analysis of IN738LC superalloy, oxidised at 900°C for 110 hours in air: (d) XRD pattern for surface of oxide formed on IN738LC superalloy at 1200°C for 4 hours in air.

(a) Bode plots:

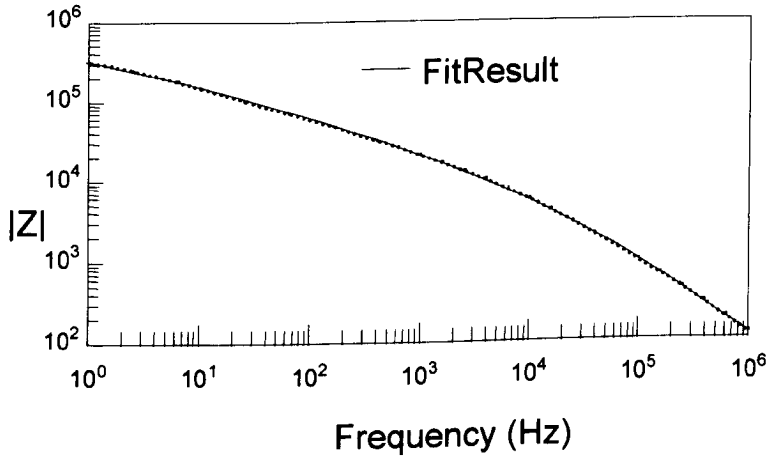

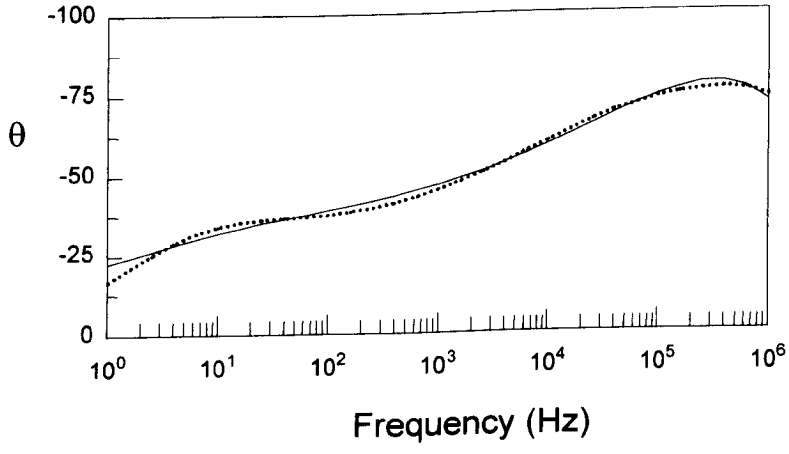

(b) Complex plot:

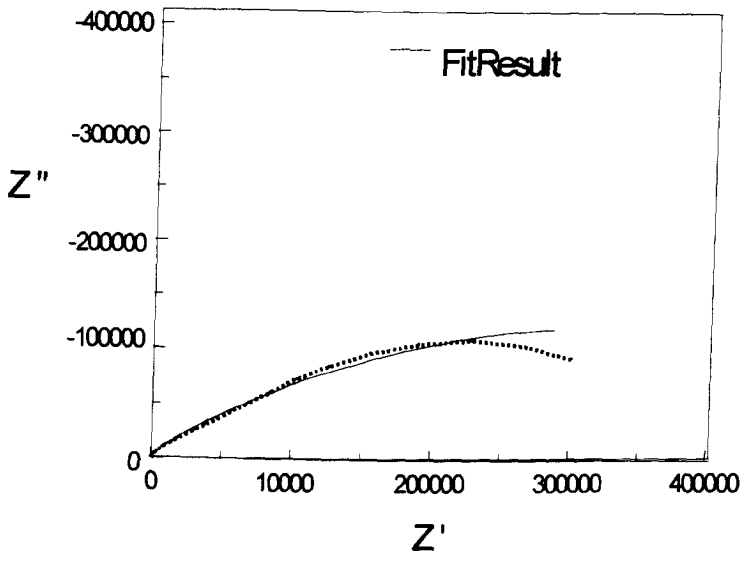

(c) Equivalent circuit B:

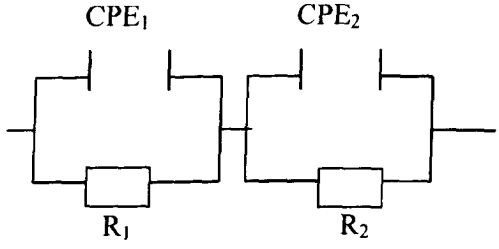

Figure 4-3: Impedance results for the oxide scale of IN738LC superalloy, oxidised at 900°C for 267 hours in air, where experimental results are shown using the dotted line and simulation results based on equivalent circuit 'B' are shown using a plain line (room temperature measurements); (a) Bode plots, (b) Complex plot and (c) Equivalent circuit B.

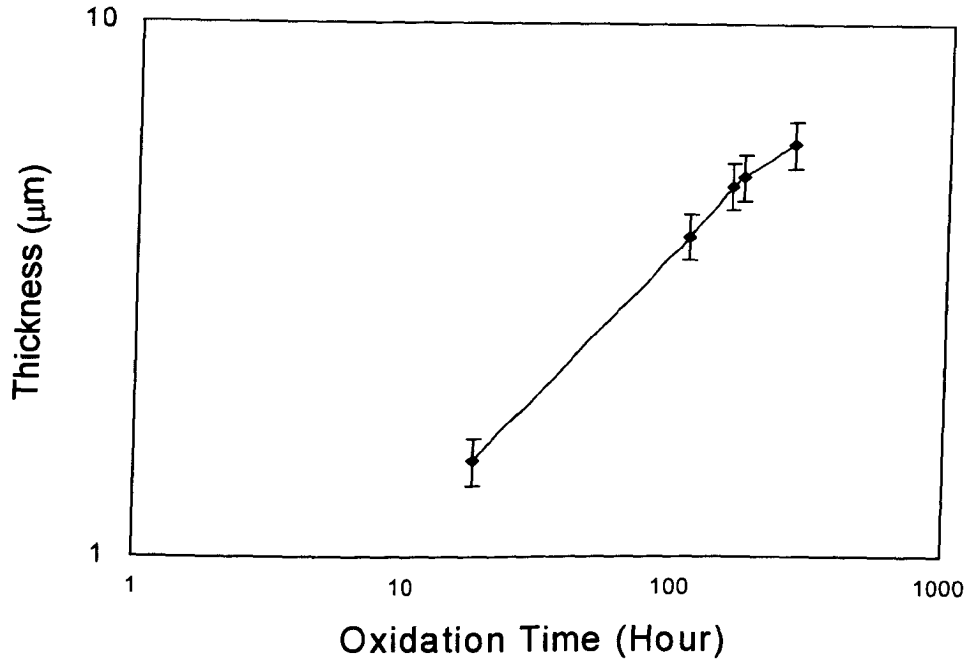

Figure 4-4: Variation of the oxide scale thickness with oxidation time for the IN738LC samples oxidised at 900°C in air for 18 to 267 hours.

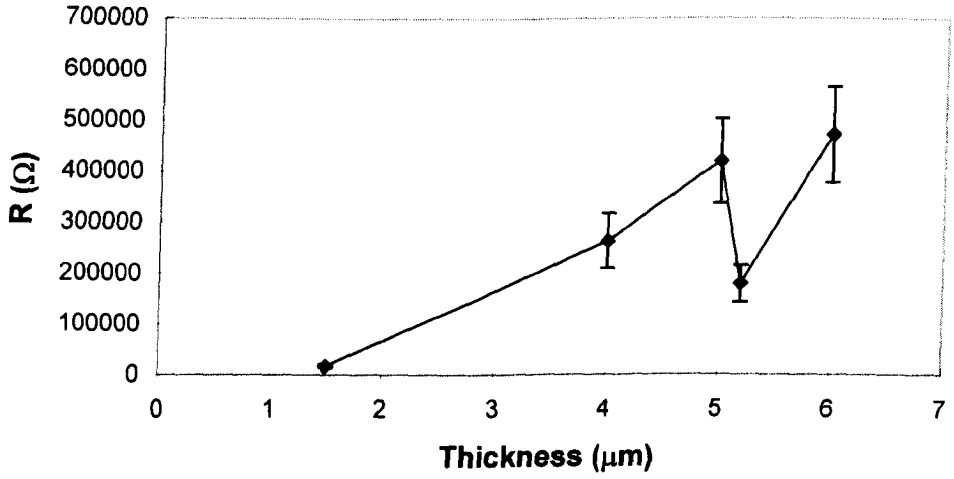

Figure 4-5: Thickness vs. electrical resistance of the oxide scales formed on IN738LC from oxidation at 900°C for 18-267 hours in air.

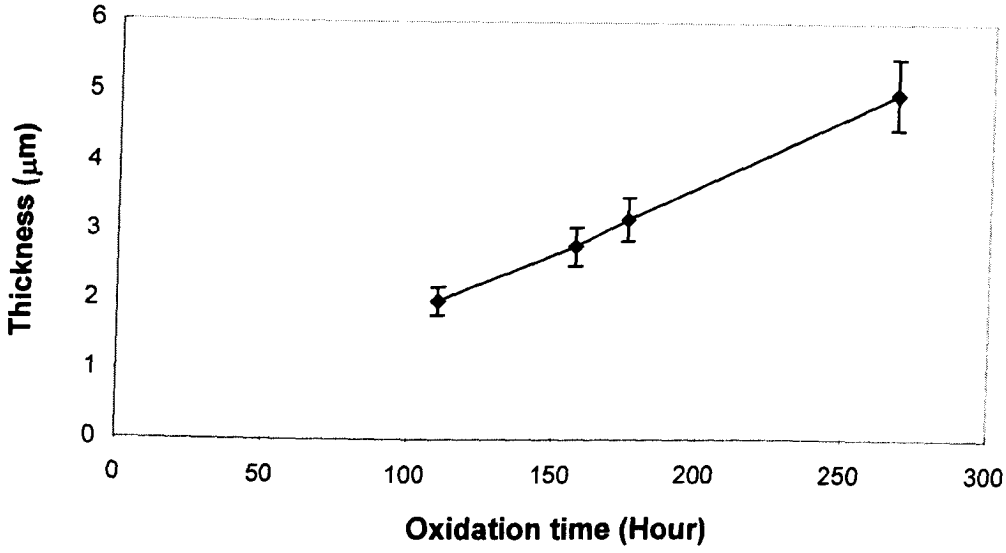

Figure 4-6: Oxidation time vs. thickness of Al_2O_3 rich NiO layer formed on IN738LC from oxidation at 900°C for 18-267 hours in air.

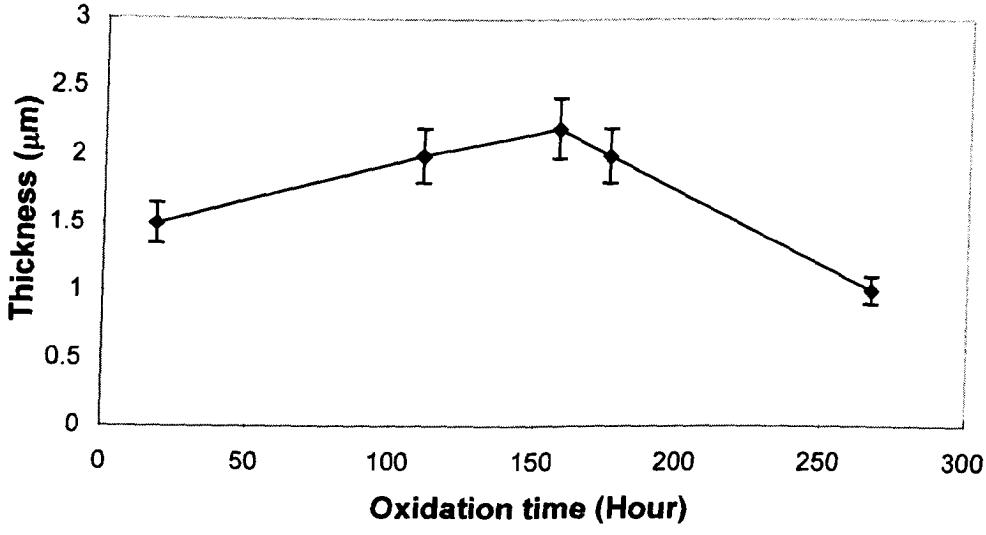

Figure 4-7: Oxidation time vs. thickness of chromia rich layer formed on IN738LC from oxidation at 900°C for 18-267 hours in air.

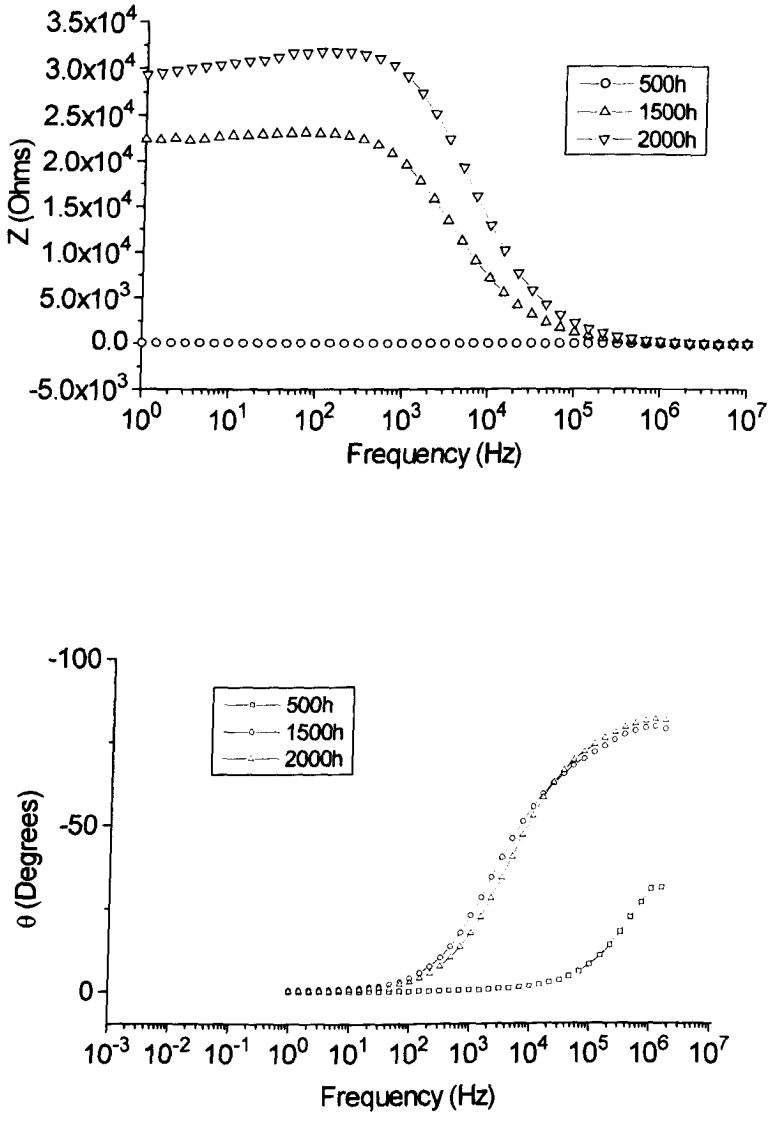

Figure 4-8: Bode plots of oxide scales formed on the bond coat oxidised at 900°C in air for 500 hours, 1500 hours and 2000 hours (400°C measurement temperature).

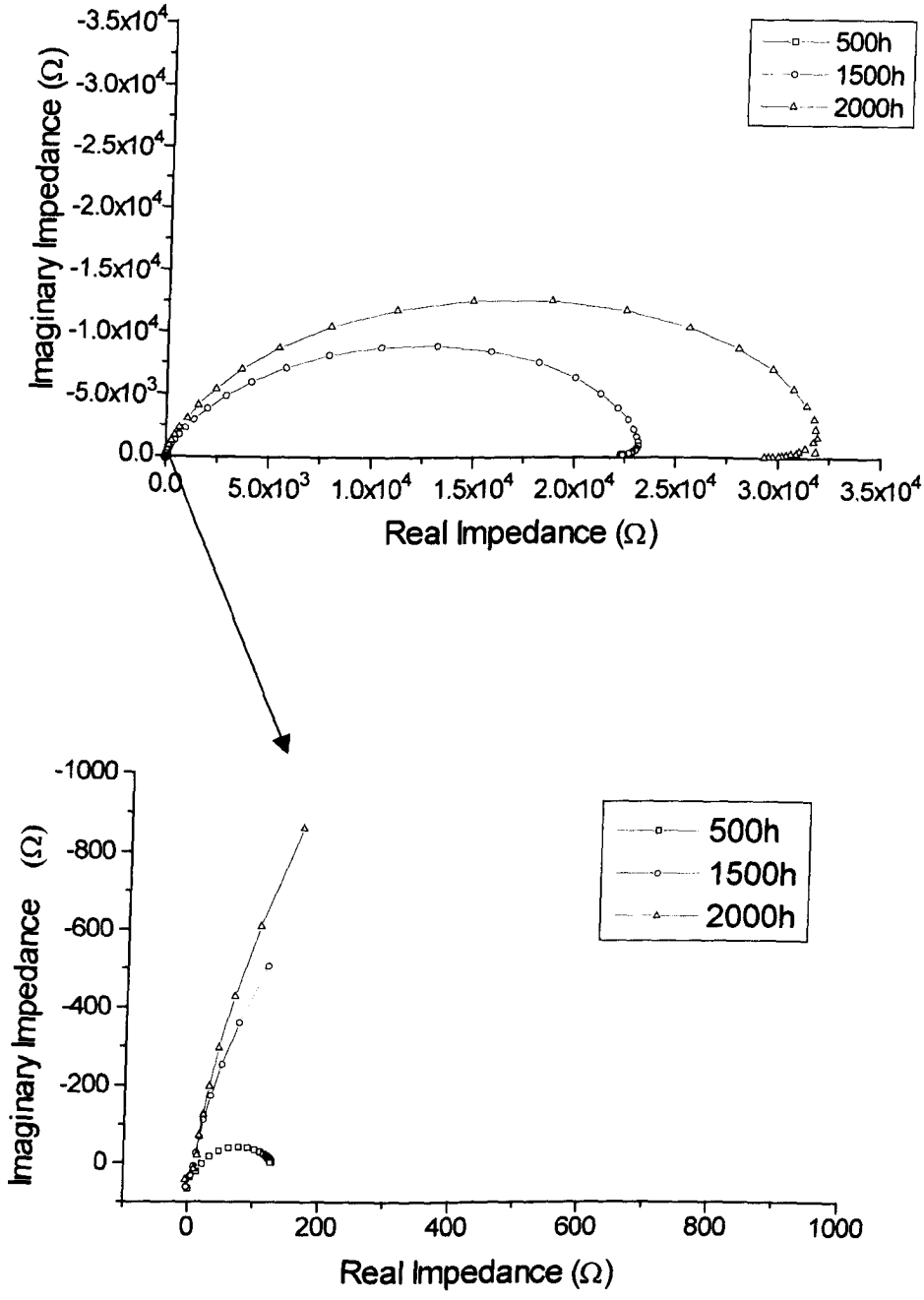

Figure 4-9: Complex plots of oxide scales formed on the bond coat oxidised at 900°C in air for 500 hours, 1500 hours and 2000 hours (400°C measurement temperature).

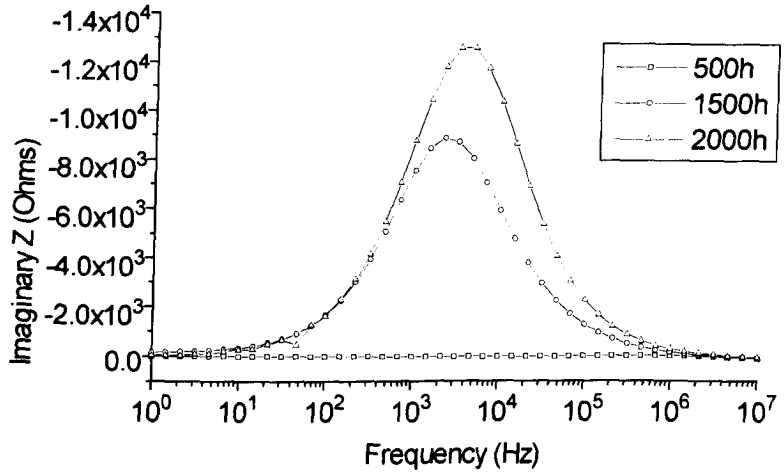

Figure 4-10: Imaginary impedance vs. log frequency of oxide scales formed on the bond coat oxidised at 900°C in air for 500 hours, 1500 hours and 2000 hours (400°C measurement temperature).

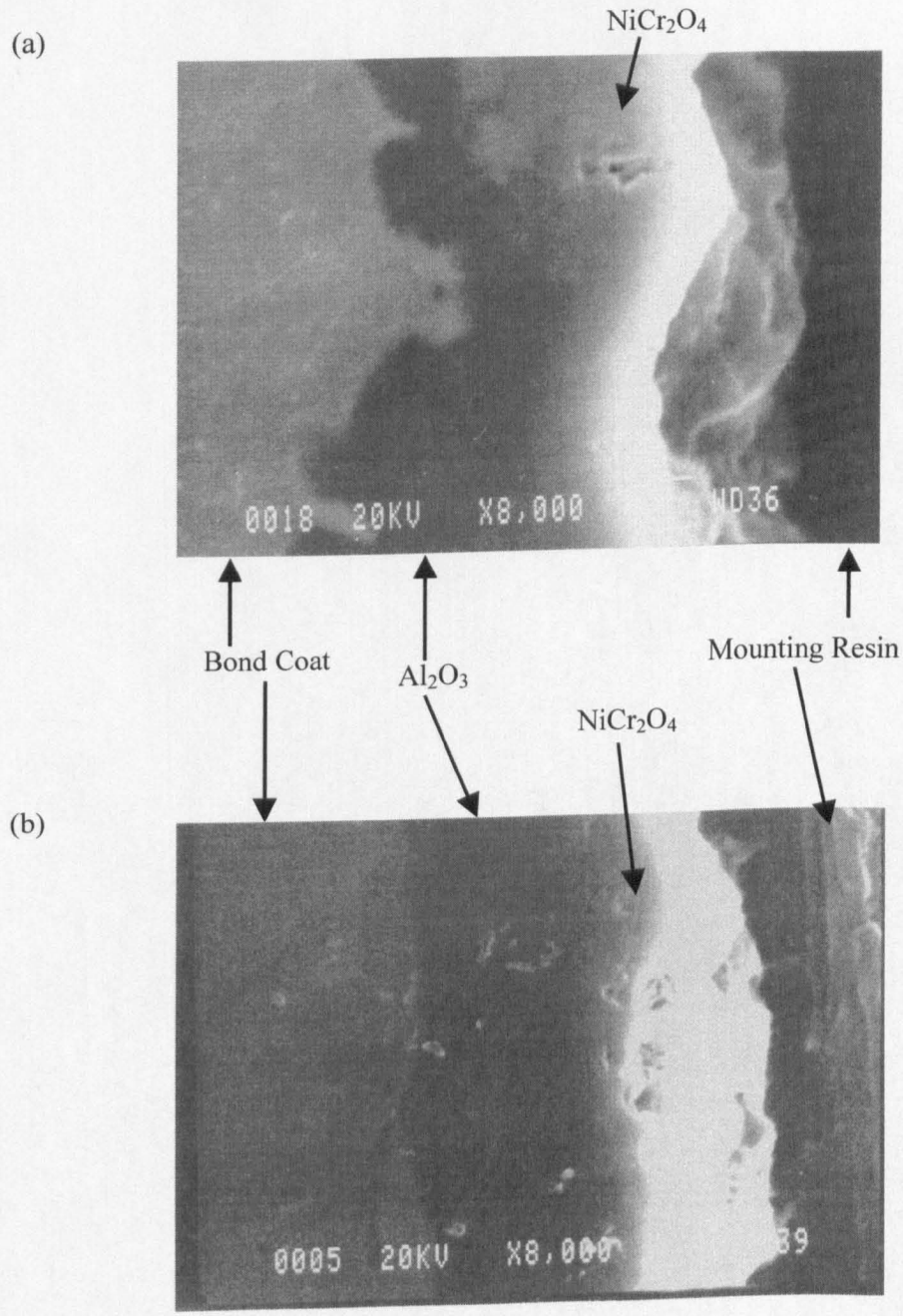
(a)
$NiCr_2O_4$
0018 20KV X8,000 WD36
Bond Coat
Al_2O_3
$NiCr_2O_4$
Mounting Resin
(b)
0005 20KV X8,000

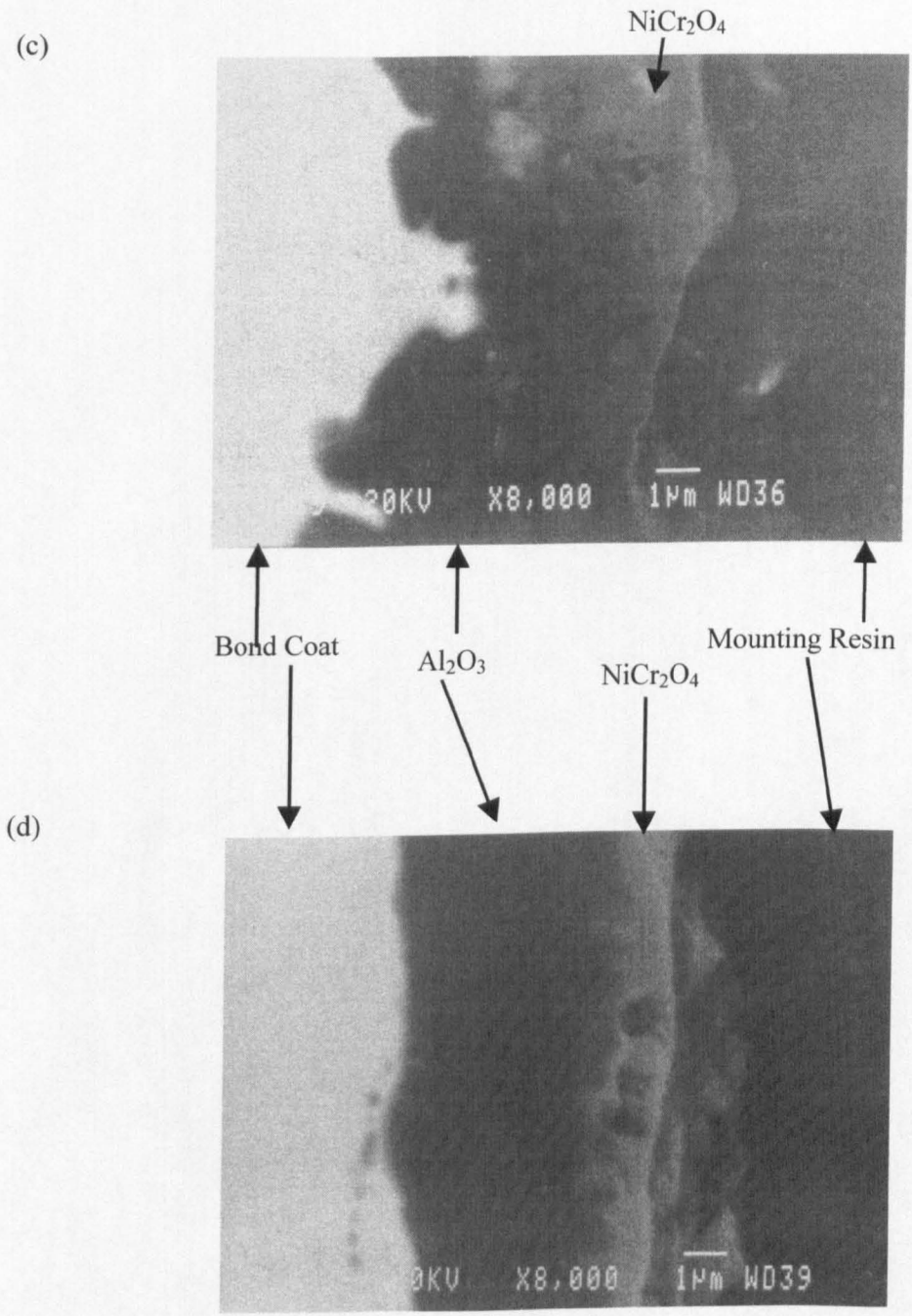

Figure 4-11: (a) SEM image of the bond coat oxidised at 900°C for 1500 hours in air; (b) SEM image of the bond coat oxidised at 1100°C for 300 hours in air; (c) Backscattered image of the bond coat oxidised at 900°C for 1500 hours in air; (d) Backscattered image of the bond coat oxidised at 1100°C for 300 hours in air.

(a)

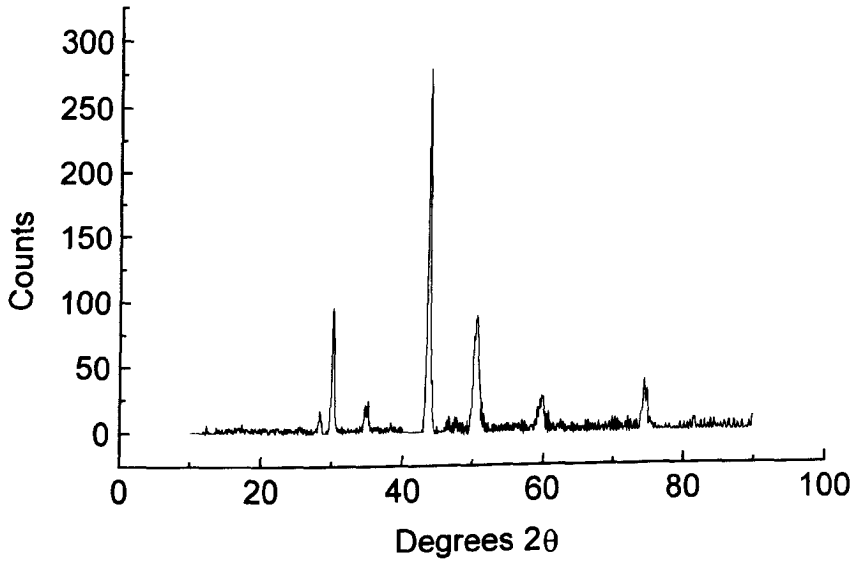
300
250
200
150
100
50
0
Counts
0
20
40
60
80
100
Degrees 2θ

(b)

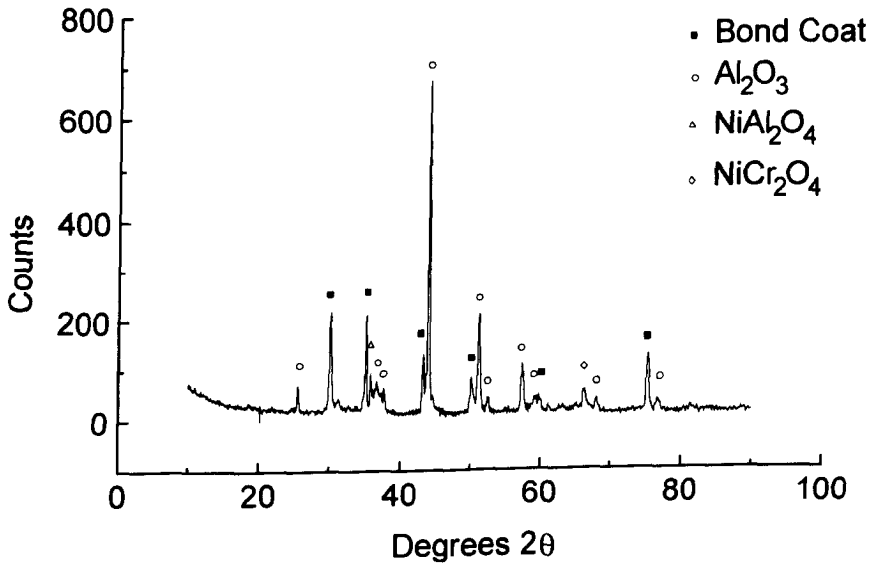
800
600
400
200
0
Counts
0
20
40
60
80
100
Degrees 2θ
Bond Coat
Al_2O_3
$NiAl_2O_4$
$NiCr_2O_4$

(c)

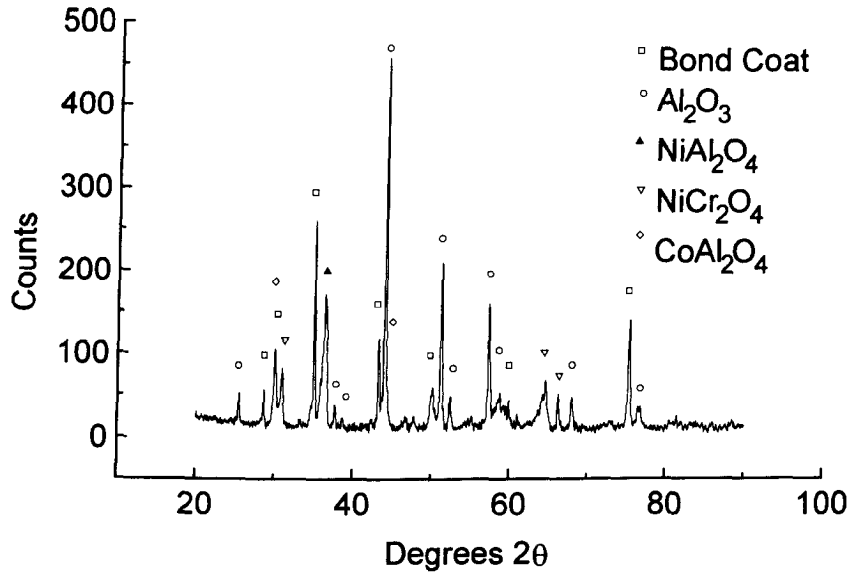

Figure 4-12: (a) XRD pattern for the bond coat alloy; (b) XRD pattern for the oxide scale formed on the bond coat oxidised at 900°C for 1500 hours; (c) XRD pattern for the oxide scale formed on the bond coat oxidised at 1100°C for 300 hours.

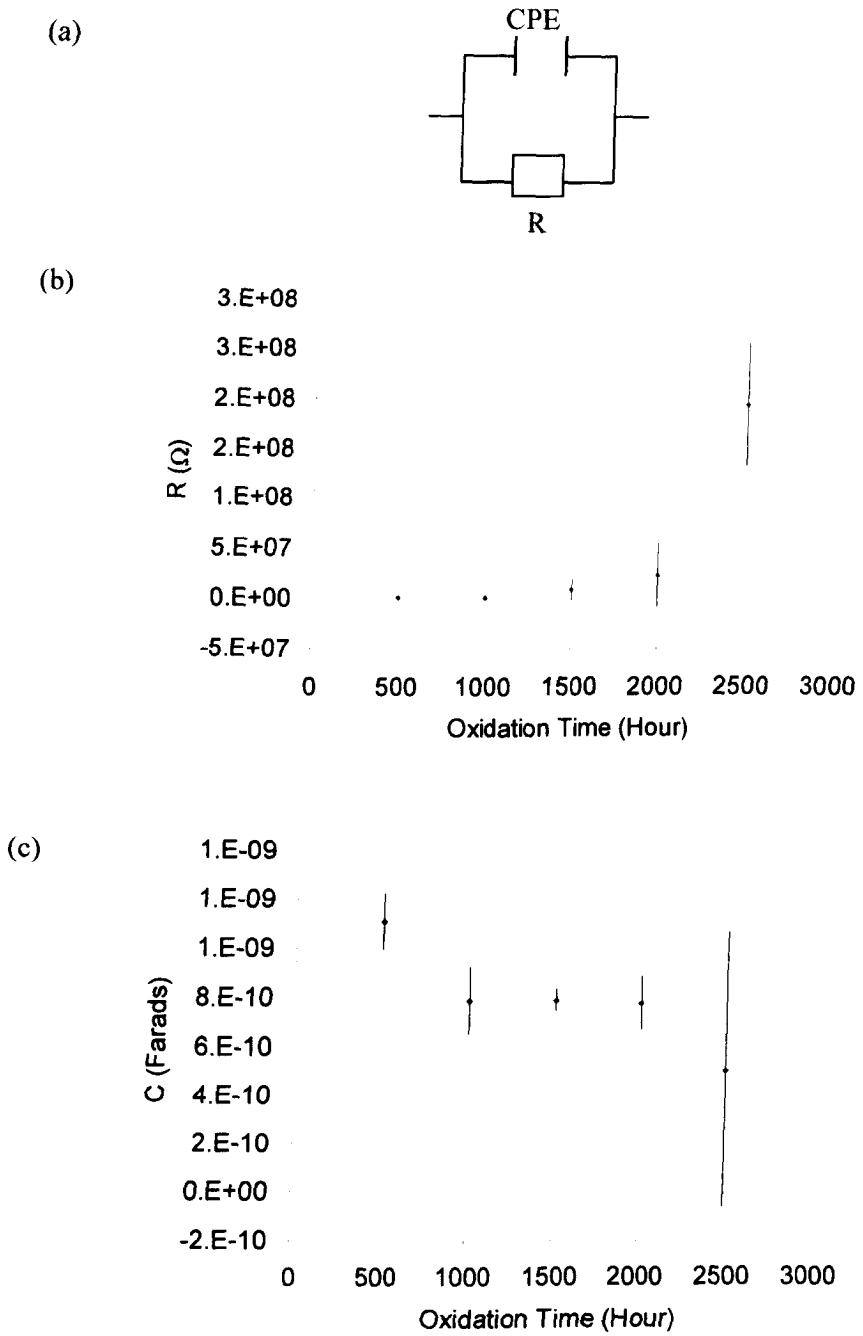

Figure 4-13: (a) Equivalent circuit for the oxide scale formed on the bond coat; (b) Resistance vs. oxidation time for oxide scales formed on the bond coat at 900°C in air; (c) Capacitance vs. oxidation time for oxide scales formed on the bond coat at 900°C in air. (400°C measurement temperature).

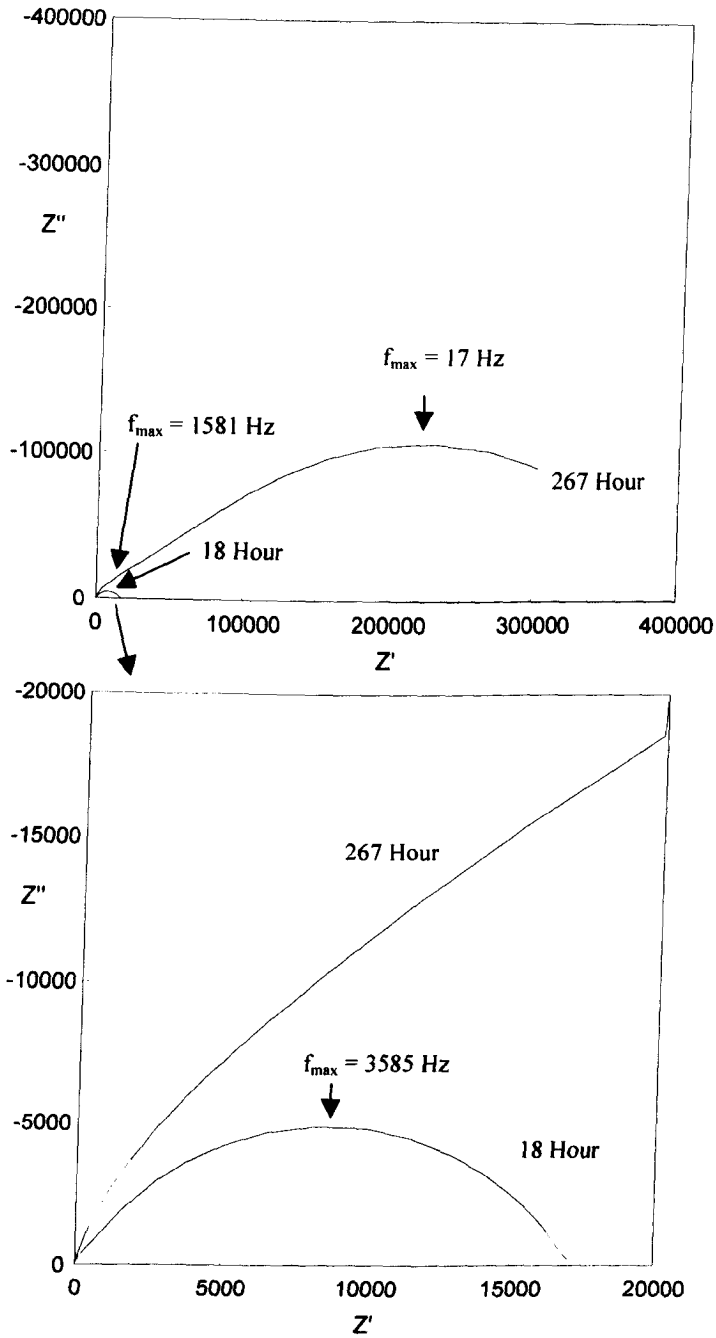

Figure 4-14: Complex impedance plots of IN738LC superalloy oxidised at 900°C for 18 hours and 267 hours in air (400°C measurement temperature).

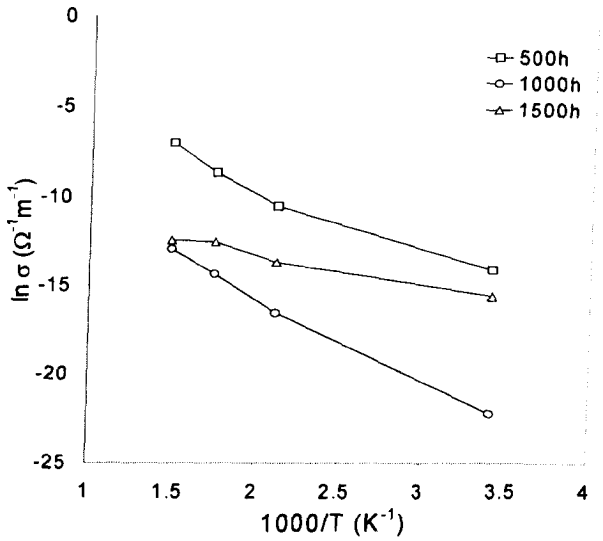

Figure 4-15: Temperature dependence of the electrical conductivity for the thermally grown oxide (TGO) layer formed on bond coat samples oxidised at 900°C in air for 500, 1000 and 1500 hours.

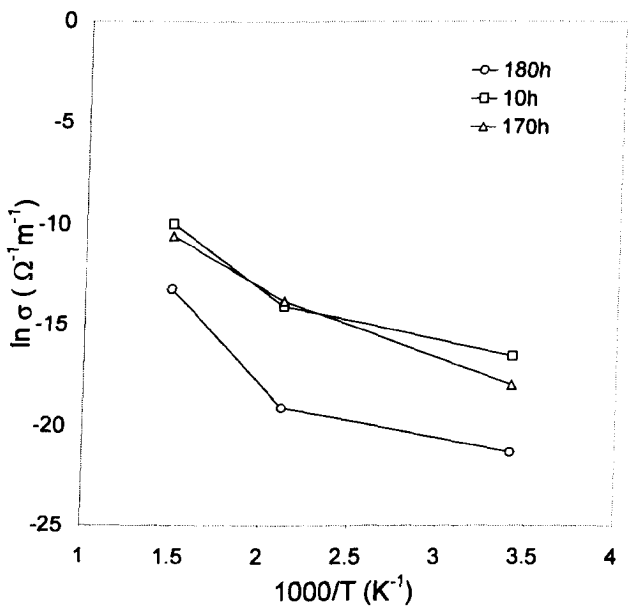

Figure 4-16: Temperature dependence of the electrical conductivity for the TGO layer formed on the bond coat samples oxidised at 1000°C in air for 10, 170, 180 hours.

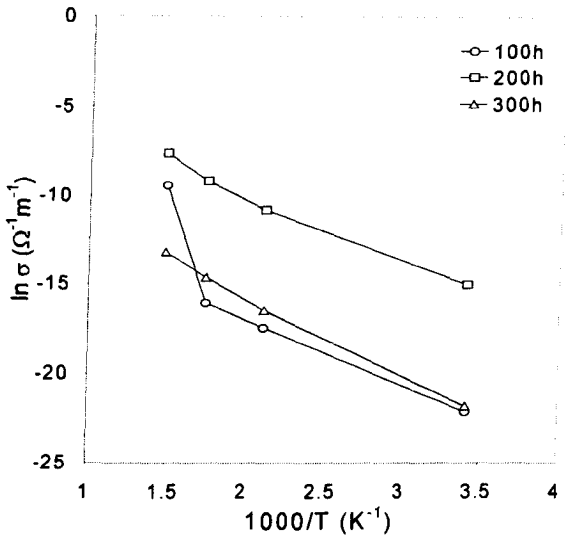

Figure 4-17: Temperature dependence of the electrical conductivity for the TGO layer formed on the bond coat samples oxidised at 1100°C in air for 100, 200, 300 hours.

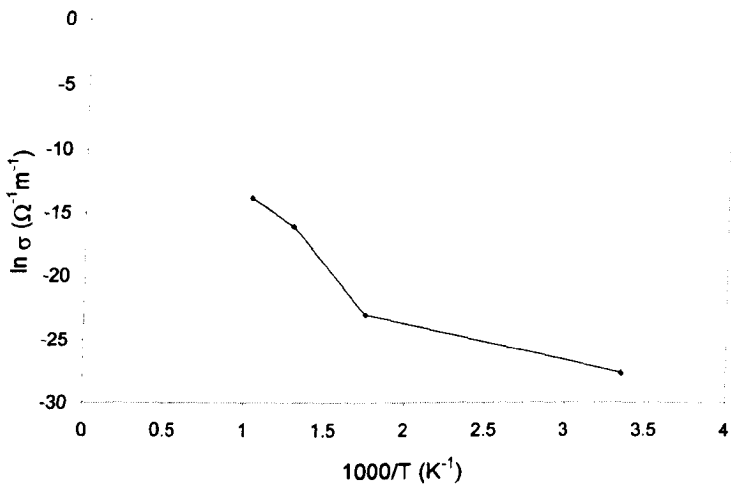

Figure 4-18: Temperature dependence of the theoretical electrical conductivity for pure alumina.

5. IS Study of TGO Layer in a TBC System

5.1. Introduction

Yttria-stabilised zirconia (YSZ) has been used as a thermal insulator in gas turbine engines, because of its low thermal conductivity and comparatively high thermal expansion coefficient, as well as a good chemical and thermal stability [Haynes et al., 1996], [Miller, 1997], [Bose and DeMasi-Marcin, 1997] and [Sergo and Clarke, 1998]. It is sprayed on a bond coat using an air plasma spray (APS) technique to increase turbine engine operation temperature and is known as a thermal barrier coating (TBC). The bond coat is MCrAlY (M = Ni and/or Co) alloy produced by a vacuum plasma spray (VPS) technique.

At high temperature in air, the bond coat is oxidised and forms thermally-grown oxide (TGO). The growth of TGO, between the heat-insulating YSZ top coat and the oxidation-resistant bond coat, are responsible for the spallation of the YSZ top coat [Haynes et al., 1996]. Non-destructive monitoring of the microstructure of the TGO layer can give early warning about the possible failure of engine components. In service conditions, the oxidation temperature is relatively low in the land-based turbines for electricity generation and it will take several years to degrade a sample at this temperature. Therefore, it is not practical to do an oxidation study at the actual engine operating temperature. Thus if the TGO formed at high temperature is similar to the TGO formed at low temperature, then the oxidation study, performed at high temperature in the laboratory environment, can represent the oxidation-degradation phenomena in the engine-service condition.

Impedance spectroscopy (IS) can be used to measure TBCs with multi-layer structures. It can be used to extract the electrical parameters of TGO layers formed at 1030°C and 1200°C. TGOs formed in TBC samples at these two temperatures are compared in this chapter. The microstructure of TBC samples may change with increasing oxidation time. Electrical parameters are related to the microstructure of TBC samples. The electrical parameters, such as impedance, resistance, capacitance,

relaxation frequency and activation energy can be used to monitor the characteristics of oxide scales.

5.2. Experimental Procedure

5.2.1. Thermal Ageing

The TBC samples were subjected to thermal exposures in air for the range of temperatures and times indicated in table 5-1. Five samples for each oxidation time were prepared. A bond coat sample (20mm × 20mm × 2mm) was oxidised at 1030°C in air for 50 hours for XRD analysis.

Table 5-1: Thermal ageing of the TBC samples

Exposure temperatures (°C)	Oxidation time (Hour)	Holding periods at exposure temperatures in the different thermal cycles (Hour)						
		Thermal cycle 1	Thermal cycle 2	Thermal cycle 3	Thermal cycle 4	Thermal cycle 5	Thermal cycle 6	Thermal cycle 7
1030	10	10						
	50	10	40					
	200	10	40	150				
	500	10	40	150	300			
	1000	10	40	150	300	500		
1200	1	1						
	5	5						
	10	5	5					
	50	5	5	40				
	100	5	5	40	50			
	200	5	5	40	50	100		
	400	5	5	40	50	100	117	83

5.2.2. Impedance Measurements

Silver electrodes (10mm × 10mm) were used for impedance measurements. IS measurements were performed at 400°C on three samples for each ageing condition. These samples were chosen randomly. The average values of the electrical properties obtained from the measurements were taken as the experimental results. For the activation energy calculations, the sample that showed the highest measured impedance value between the three aged samples was selected. IS measurements were performed on these samples from 200°C to 400°C for each ageing condition.

5.3. Results

5.3.1. Microstructure of TBC Systems

The microstructure of the TBC systems was characterised using SEM, EDX and XRD in order to establish a relationship between the TBC microstructure and impedance measurement results. Figure 5-1 shows the SEM image of the cross section of the as-received TBC system containing three layers in its microstructure. The top coat is the porous YSZ layer. Under the top coat, a metallic bond coat layer on top of superalloy substrate was observed. As expected, a TGO layer was not present in the as-received TBC sample.

Figure 5-2a shows SEM images taken from different regions of the cross section of the TBC sample, aged at 1030°C in air for 10 hours, and it clearly indicates that the thickness of the TGO layer is not uniform. This TGO layer is the dark oxide layer. Figure 5-2b shows SEM images taken from different regions of the cross section of a TBC sample, aged at 1030°C in air for 50 hours. In this figure, the TGO layer is still dark and not uniform, like the 10 hour sample, but its thickness has increased and islands of grey oxide are observed in some areas . Figure 5-2c shows SEM images taken from different regions of the cross section of a TBC sample, aged at 1030°C in air for 200 hours. Here islands of grey oxide are observed on top of the continuous dark oxide layer. Figure 5-2d shows SEM images taken from different regions of

the cross section of a TBC sample, aged at 1030°C in air for 500 hours. These SEM images show a discontinuous grey oxide layer formed on top of the dark oxide layer and that it has become thicker. Figure 5-2e shows SEM images taken from different regions of the cross section of a TBC sample, aged at 1030°C in air for 1000 hours. In this figure, grey oxide layer has become continuous.

The above observations confirm that the grey oxide layer formed after the formation of dark oxide layer. Initially it formed as islands of grey oxide on top of the dark oxide layer. Later, with increasing thermal ageing, it became thicker and formed a continuous grey oxide layer.

Figure 5-3a shows an SEM image of a cross section of a TBC sample, aged at 1200°C in air for 1 hour, where the TGO is a dark oxide layer. This dark oxide layer is similar to the previously-observed dark oxides in TBC samples aged at 1030°C. Figure 5-3b shows an SEM image of a cross section of a TBC sample, aged at 1200°C in air for 10 hours. Here a discontinuous grey oxide layer has formed on top of the continuous dark oxide layer. Figure 5-3c shows an SEM image of a cross section of a TBC sample aged at 1200°C in air for 50 hours, but again in this sample the grey oxide layer is not continuous and there is primarily a dark oxide layer. Figure 5-3d shows an SEM image of a cross section of a TBC sample aged at 1200°C in air for 100 hours, where a continuous grey oxide layer is formed on top of continuous dark oxide layer.

Therefore, after careful observation and detailed analysis of all SEM images, it is concluded that TGO formation follows the same pattern at both oxidation temperatures. First a non-uniform and continuous dark oxide layer was formed and then a grey oxide layer started to form as islands on top of that. With increasing thermal ageing, islands of grey oxide joined together and became a continuous layer. From the SEM images, the thickness of the overall TGO layer is not uniform.

Microanalysis was carried out using EDX on the dark oxide layer and grey oxide layer of TBC samples, thermally aged at 1030°C for 50 hours, 500 hours and 1000 hours (figure 5-4a and 5-4c). Standards used in ZAF correction were pure metals. The dark oxide layer mainly contained an oxide of Al with impurities of the oxides of Ni, Cr and Co (figure 5-4a). It was not possible to do EDX analysis on the TGO layer of TBC samples aged at 1030°C for 10 hours, because the oxide layer was too thin. However, the colour of this oxide is dark, which indicates that this is an alumina layer. The thickness of the dark oxide layers in the TGO formed at 1030°C were 4 μm, 5 μm and 7 μm for 50 hours, 500 hours and 1000 hours, respectively. This shows that the thickness of the dark oxide layers was sufficient for EDX analysis, which uses a circular area of ~1 μm diameter of a sample. So, other layers such as the bond coat or grey oxide layer did not interfere with the EDX analysis of dark oxide layer. The elemental composition of the dark oxide layer is up to 93±1% Al with the balance Ni, Cr and Co for the 50 hours aged sample. The elemental composition of Al in the dark oxide layer decreased with increased thermal ageing and at the same time the elemental composition of other elements increased with increasing thermal ageing.

Figure 5-4c shows EDX analyses of the grey oxide layer of TBC samples aged at 1030°C for 500 hours and 1000 hours, which indicate that the grey oxide layer mainly contained oxides of Al, Ni, Cr and Co and is referred to as a mixed oxide layer. The oxides of Cr and Ni increased in the mixed oxide layer with increased thermal ageing time. Figure 5-5 shows EDX analysis in the middle of bond coat, aged at 1030°C for various periods, which indicates that the Cr and Ni content increased in the bond coat with increased ageing time, but the Al and Co content decreased. In the middle of the bond coat of the 0 hour sample (as-received sample) to 50 hour sample aged at 1030°C, a sudden increase of Cr and Ni and sudden decrease of Al indicated that Al could move very rapidly to the bond coat surface. At the same time, there was a sudden reduction of the Co content, which helped to increase Ni and Cr contents in the middle of the bond coat. Al formed a protective oxide layer at the bond coat/YSZ interface and reduced further oxide formation of Al

and other elements. For samples aged for more than 50 hours, the composition of elements in the middle of the bond coat did not change very rapidly. This indicated that although Al moved very rapidly to the surface of the bond coat from inside the bond coat, it remained as metal in there for a long time. So a saturation of Al in the bond coat surface reduced Al movement from inside the bond coat.

EDX and XRD analyses confirmed that Co formed a spinel oxide on top of the alumina layer (figure 5-4a and 5-6). EDX analysis was also performed on the cross section of TBC samples aged at 1200°C and the dark oxide layer mainly contained alumina with small amounts of oxides of Ni, Cr and Co (figure 5-4b). The Al content in the dark oxide layer was 84±1% for TBC samples, aged at 1200°C for 10 hours. The Al content increased with ageing and reached 95±1% for the 400 hour-aged samples (figure 5-4b). This suggests that Al moves very rapidly at 1200°C to the surface of the bond coat to compensate for the reduction of Al in the bond coat surface during ageing.

Figure 5-6 shows the XRD pattern from the oxide scale formed on the NiCrCoAlY bond coat aged at 1050°C for 50 hours in air. This XRD pattern shows the presence of $(Ni,Co)(Cr,Al)_2O_4$ spinel and α-Al_2O_3, but it did not show the presence of Cr_2O_3, NiO and CoO. This confirms that the dark oxide is alumina and the grey oxide is $(Ni,Co)(Cr,Al)_2O_4$.

Figure 5-7 shows the oxidation kinetics of bond coats of TBC samples, thermally aged at 1030°C and 1200°C. During the initial stage of oxidation, while alumina was formed, the oxidation kinetics followed a parabolic law for TBC samples at all thermal ageing conditions. Figure 5-7 shows that the slope of the straight line is higher for the higher temperature, which indicates that the TGO formation rate is higher at higher temperature. However, the TGO layer is still protective because it follows a parabolic growth law. Therefore, the TGO is normally a protective alumina layer in the early stages of thermal ageing. When the sample was aged for a longer periods, the Al content in the bond coat became low. Further ageing of samples lead to the formation of $(Ni,Co)(Cr,Al)_2O_4$ mixed oxide. The mixed oxide formed at

the YSZ/alumina interface. The oxide layer thickness for samples, aged at 1030°C for 1000 hours and 1200°C for 100 hours, are above the straight lines obtained from fitting to a parabolic relation of the earlier data (figure 5-7). This indicates that the oxidation kinetics changed with the formation of the mixed oxide layer and increased. This also suggests that the formation of mixed oxides reduced the oxidation protection of the TBC system. Again, a decreasing alumina content in the dark oxide layer or mixed oxide formation on top of the dark oxide layer suggests that cations diffused through the dark alumina layer. Internal oxidation in the bond coat suggests that oxygen ions diffused through the alumina layer and formed alumina on the bond coat surface or sub-surface.

5.3.2. Impedance Results

Figure 5-8 shows Bode plots at 400°C for TBC samples aged at 1030°C in air for 0 hour to 1000 hours. In the Bode impedance plots, the impedance of the TBC samples increased in the frequency range 1Hz to 10^5Hz with increasing thermal ageing time. In the Bode phase angle plots, changes were observed in the phase angle at frequencies between 1Hz to 10^5Hz with increasing thermal ageing time. The changes in the impedance magnitude and phase angle in figure 5-8 are suspected to be related to some or all of the microstructural changes that the samples may have undergone during long term exposure at 1030°C. These microstructural changes for long times at 1030°C could include:

(1) formation of oxide layer;
(2) growth of oxide layer thickness;
(3) oxide layer composition change;
(4) crack formation in the oxide layer or oxide/YSZ interface;
(5) nucleation and growth of new oxide, such as mixed oxide.

Figure 5-9 shows the complex plots at 400°C for TBC samples, aged at 1030°C in air for 0 hour to 1000 hours, where the high frequency arc is very small. The low frequency semicircle increased in size with increasing exposure time. This also

suggests that microstructural changes occurred during exposure at 1030°C with increasing ageing time.

For TBC samples aged at 1030°C, the phase angle plot is divided into three frequency ranges; namely a high frequency range (10^5Hz to 10^7Hz), an intermediate frequency range (10^3Hz to 10^5Hz) and a low frequency range (1Hz to 10^3Hz) (figure 5-8b). Changes were observed in the phase angle plot with increased ageing of samples in two of the frequency ranges, namely intermediate and low frequency ranges. Figure 5-9b shows the complex plots at 400°C for TBC samples, aged at 1030°C in air for 0 and 10 hours. The as-received TBC sample did not have any TGO layer. So, the semicircle observed for this sample in the frequency range 10^3Hz to 10^5Hz was caused by YSZ grain boundaries. A similar result has been given in the literature, where the impedance response of YSZ grain boundaries appeared at a lower frequency than that of the bulk [Bonanos et al., 1987]. So for impedance analysis, changes observed in the frequency range from 1Hz to 10^3Hz should be the impedance response for the TGO layer and this is free from any effect of YSZ grain boundaries. A magnification of the high frequency region reveals that low frequency semicircles are much bigger than the high frequency semicircles (figure 5-9b). They are also much bigger than the response from YSZ grain boundaries. The changes that are observed in the intermediate frequencies (10^3Hz to 10^5Hz) in the phase angle plot did not produce any semicircle in the complex plot (figure 5-9a). The depressed semicircle that appeared in the low frequency region (frequency range 1Hz to 10^5Hz) in the complex plot may also contain an impedance response for the intermediate frequency region as observed in the phase angle plot for these samples. However, its effect on the low frequency semicircle would be very small.

Impedance results for TBC samples exposed at 1200°C were slightly different from the impedance results of TBC samples exposed at 1030°C. There was no intermediate frequency response for these TBC samples as shown in figure 5-10 and the low frequency end of phase angle plot was at a slightly higher frequency. Figure 5-10 shows Bode plots at 400°C for TBC samples aged at 1200°C. A variation in

the impedance response was observed in the frequency range from 10Hz to 10^5Hz. The low frequency end moved from 1Hz for TBC samples aged at 1030°C to 10 Hz for TBC samples aged at 1200°C. This suggests that the TGO formed at 1200°C might be slightly different from the TGO formed at 1030°C. Even though the composition of the dark oxide was similar at both ageing temperatures, porosity might be the reason for this, as increasing porosity will increase the relaxation frequency of an electronic conductor like NiO [Song and Xiao, 2001]. Figure 5-11 shows the complex plots of TBC samples aged at 1200°C, where the diameter of the low frequency semicircle increased with increasing ageing.

5.4. Discussion

5.4.1 Feasibility of IS Analysis of Aged TBC Systems

Upon analysing all the data, it appears that electrical measurements are able to detect changes in TBC samples that were previously undetected by other non-destructive testing methods, such as acoustic emission [Ma et al., 2001] or infrared (IR) imaging [Ferber et al., 2000], which only detect cracks in a TBC system. The trend detected in impedance results may be the result of changes that the TBC samples have undergone as a result of thermal exposure.

Three peaks in the phase angle plots (figure 5-8) suggest that three semicircles may be present in the complex plots. However, only two arcs are clearly observed in the complex plots (figure 5-9), which indicates that the resolution between arcs is not good. The third semicircle in the intermediate frequency range, second from the left, must have overlapped with a large low frequency semicircle. Identification of these semicircles is important to give a meaningful relationship between semicircles and microstructures of TBC samples. It is possible to extract the electrical parameters of this third semicircle using an equivalent circuit model, which will be discussed later.

5.4.2. Identification of Semicircles

From the SEM and EDX analyses, it is confirmed that aged TBC systems consist of a YSZ layer, a TGO layer and a metallic bond coat with a superalloy substrate. The silver electrode impedance at 400°C will be at a lower frequency than 1Hz [Steil et al., 1997]. The frequency range for these experiments was 1Hz to 10^7Hz, so the electrode impedance did not appear in the IS spectrum.

The relaxation frequency, the frequency (f_{max}) at the apex of a semicircle, is an important parameter in impedance diagrams. The relaxation frequency is a characteristic of materials and can be used for identification.

The f_{max} can be determined using the equation [MacDonald and Johnson, 1987],

$$f_{max} = \frac{\sigma}{2\pi\varepsilon\varepsilon_0} \qquad (5\text{-}1)$$

where σ is the conductivity, π is 3.14, ε is the dielectric constant and ε_0 is the vacuum permitivity, that is 8.85×10^{-12} F/m.

This parameter can be used as a 'fingerprint' of the relaxing species. An attempt is made based on the relaxation frequency to confirm that the low frequency semicircle is from alumina and the high frequency semicircle is from YSZ. For a pure α-Al_2O_3 layer at 200°C, σ is $< 10^{-11}$ $\Omega^{-1}m^{-1}$ [Richerson, 1992] and ε is 9.5 [Wirth, 1991]. Therefore, the theoretical f_{max} for an α-Al_2O_3 layer at 200°C is $\approx$ 0.2 Hz. Similarly, σ is $< 10^{-6}$ $\Omega^{-1}m^{-1}$ and ε is 35 for YSZ at 197°C [Ogawa et al., 1999]. So, the theoretical f_{max} for YSZ at 197°C is 514 Hz . Therefore it is confirmed by relaxation frequency analysis that the high frequency semicircle is for the YSZ layer and the low frequency semicircle is for the TGO layer, which is predominantly α-Al_2O_3.

5.4.3. Analysis of IS Spectra

Steil et al. (1997) observed that the impedance response for grain boundaries appeared at a lower frequency than the impedance response for YSZ grains. Thus, the second semicircle (second from left in figure 5-9b) for the 0 hour sample (as-received sample) should be the response for YSZ grain boundaries. Pan et al. (1998) observed that the impedance response for a porous oxide appeared at a higher frequency than that of a thick oxide. As observed in the phase angle plots (figure 5-8), changes were observed in two peaks between 1Hz to 10^5Hz (intermediate frequency and low frequency region). Thermal ageing grew the oxide in TBC samples and at the same time the porosity of the YSZ layer did not change as seen in SEM images (figure 5-2). So the variation observed in these two peaks should be the result of oxide growth. The impedance response for the TGO appeared in the frequency region from 1Hz to 10^5Hz, whereas the impedance response for YSZ grains appeared in the frequency range from 10^5Hz to 10^7Hz.

Changes that occurred in the impedance measurements in the frequency range between 1Hz to 10^5Hz, confirm changes in the microstructure of the TGO. Figure 5-12 show impedances for the TGO layer and the YSZ layer of samples aged at 1030°C in air for 10 hours to 1000 hours, which shows that the magnitude of the impedance for the YSZ layer did not change with ageing, but the magnitude of the impedance for the TGO layer increased with thermal ageing. This may be because the thickness of the TGO layer increased. The magnitude of the impedance for the TGO layer may have increased for some other reason, such as an increasing density in the oxide layer. There is possibly an additional reason. A two-layer structure is common in oxide scales, one dense inner layer and another porous outer layer on top of the dense inner layer [Pan et al., 1998]. Here, the thickness of the dense layer and the magnitude of its impedance may increase without an increase in the actual TGO layer thickness with increased ageing.

The impedance response observed in the intermediate frequency region could be from the grain boundaries, porous oxide or mixed oxide. In this study, it was

observed that the alumina layer contained small amounts of other oxides and it might have been a porous layer at higher temperature or in the early stages of oxidation. It was also observed that the TGO had a duplex structure consisting of a mixed oxide layer and an alumina layer. Therefore, the low frequency semicircle was used for the characterisation of the TBC system because the changes observed in this semicircle with thermal ageing are noticeable. This semicircle was also free from the impedance response from YSZ grain boundaries.

The low frequency semicircle (frequency range 1Hz to 10^3Hz) is much bigger than the high frequency semicircle (frequency range 10^5Hz to 10^7Hz). Again the diameter of the low frequency semicircle increased with thermal ageing of samples. The frequency at the end of the low frequency semicircle changed from 50 Hz for TBC samples aged for 10 hours to 1 Hz for TBC samples aged for 50 hours (figure 5-9). This suggests that the relaxation frequency decreased with increasing ageing and thus there must be some changes in the oxide layer with thermal ageing. The thickness of the oxide layer grew with ageing, but this should not change the relaxation frequency. Only changes in the oxide composition or porosity should change the relaxation frequency. From the SEM images it is clear that the oxide layer formed in the TBC systems at 1030°C for 10 hours and 50 hours are both dark oxides, which were identified as alumina (figure 5-2). Only porosity in the oxide could have changed during the thermal ageing here. Song and Xiao [2001] presented an IS study of pure NiO, where they showed that increasing porosity increased the relaxation frequency of an electronic conductor like NiO. So, in this case, the impedance response observed for the TGO could suggest a two-layer structure, an outer porous layer and an inner thicker layer [Pan et al., 1998]. The inner thicker layer could start to form at the interface of the metal alloy/porous oxide interface after formation of the porous oxide. In this duplex structure, the thickness of the dense alumina layer would increase and the thickness of the porous alumina layer would decrease because the YSZ top coat would suppress volume expansion due to TGO growth. An increasing density of the alumina layer could increase the electrical resistance of this layer and the relaxation frequency is inversely proportional to it, so the low frequency semicircle would move towards a lower

frequency. Thus any changes in the low frequency semicircle in the complex plots, in this experiment between 10^1Hz to 10^5Hz at 400°C (because the intermediate frequency semicircle was consumed by low frequency semicircle), were due to TGO growth.

Figure 5-13 shows the relaxation frequencies of the alumina layer, formed at 1030°C in air for 10 hours to 1000 hours. The relaxation frequency changed between 10 hours to 50 hours, but it did not change between 50 hours to 1000 hours. This indicates that the electrical properties of the alumina layer did not change much during 50 hours to 1000 hours ageing time. The above discussion suggests that a relationship exists between the TGO growth in the TBC system and the impedance response. Therefore, impedance can be used to characterise the thermal ageing of the TBC system.

Further impedance analysis was carried out assuming that the high frequency semicircle is from the YSZ, the intermediate semicircle is from the mixed oxide and the low frequency semicircle is from the alumina. An equivalent circuit model can be used to separate the electrical parameters for all these three layer. Electrical parameters such as resistance and capacitance can be used for evolution of other parameters such as electrical conductivity, dielectric constant and relaxation frequency.

5.4.4. Equivalent Circuit Model

Figure 5-14 is the proposed equivalent circuit model based on the microstructure of the aged TBC system. The model represent three electrically-distinct regions, each modelled on a single parallel R-C element. These are the YSZ layer (grain body) (R_1-CPE_1), YSZ grain boundary/porous or mixed oxide (R_2-CPE_2) and alumina layer (R_3-CPE_3). Constant phase elements (CPE) were used instead of capacitance (C). The oxide layer is not ideal capacitor [MacDonald and Franceschetti, 1987]. This deviation may be modelled by the use of a constant phase element.

The impedance of a CPE is given by

$$Z_{CPE}(j\omega) = A^{-1}(j\omega)^{-n} \quad (5\text{-}2)$$

where A is a constant that is independent of frequency, ω is angular frequency and $j = (-1)^{1/2}$ and n is an exponential index which represents a dispersion of relaxation frequency [Amaral and Muller, 1999].

When n=1, the CPE represent an ideal capacitor with A equal to the capacitance C. In reality, n is less than 1. When n=0, the CPE acts as a pure resistor. Therefore R, C and n represent methods by which results may be fitted. In general, the CPE behaviour may originate from some feature of an oxide film such as surface roughness or inhomogenety, which may cause a frequency dispersion. For this reason, a CPE was also used for YSZ layer. The effect of inhomogeneous materials on capacitance has been discussed in the literature [Delouis et al., 1993] and [Rammelt and Reinhard, 1995].

5.4.5. Characterisation of Aged TBC Samples

The resistance and capacitance values were obtained from equivalent circuit model analyses using simulation software. Figure 5-15 shows that the resistance value obtained for the intermediate frequency range semicircle slightly increased with ageing. Again figure 5-16 shows that the capacitance value of the intermediate frequency semicircle slightly decreased with increased ageing. However, these slight variations in resistance and capacitance values for mixed oxides are not suitable for the non-destructive characterisation of TGO growth. So only the changes observed in the frequency range 1Hz to 10^3Hz were considered for TGO growth and this TGO is alumina.

As long as the alumina layer is a continuous layer, the resistance and capacitance value for the alumina layer obtained from the fitting of results in the low frequency semicircle were plotted against ageing time (figure 5-17 and 5-18) and the thickness of alumina (figure 5-19 and 5-20). Increasing electrical resistance and decreasing capacitance with increasing ageing time indicated that the thickness of the alumina

layer increased with increasing ageing time (figure 5-17 and 5-18). Increasing TGO thickness with thermal ageing for these TBC samples is shown in figure 5-7a. The resistance of the dark alumina layer increased and the capacitance of the dark alumina layer decreased with increasing thickness. Therefore, the thickness of TGO can be obtained from electrical parameters such as resistance or capacitance using IS.

5.4.6. Activation Energy

Similar to the relaxation frequency, the geometry of samples or their origin does not effect the activation energy (E_a). The activation energy is a characteristic of a material and so it can be used to compare the alumina layer formed at different temperatures or formed at the same temperature in TBC samples of different origin.

The conductivity of the TGO layer was calculated from the resistance value for each sample. Experimental conductivity data were plotted to fit the Arrhenius equation:

$$\ln \sigma = \ln \sigma^{o} - \frac{E_a}{kT} \qquad (5\text{-}3)$$

where σ is the conductivity of the TGO, σ^{o} is the pre-exponential constant, E_a is the activation energy, k is the Boltzmann's constant and T is the absolute temperature. Clearly, $\ln(\sigma)$ has a linear relationship with the reciprocal of temperature. Figure 5-21 shows the temperature dependence of electrical conductivity for alumina of TBC samples, thermally aged at 1030°C for various times, which is a straight line and follows the Arrhenius equation over the temperature range from 200°C to 400°C. Figure 5-22 shows the temperature dependence of the electrical conductivity for alumina of TBC samples, thermally aged at 1200°C for various times, which is a straight line and follows the Arrhenius equation over the temperature range from 200°C to 400°C. From the slope of these straight lines, activation energies were calculated. The activation energy is a characteristic of that particular alumina layer and any changes in the activation energy indicate changes in the alumina layer.

Activation energy values (E_a) are summarised in Table 5-2 and 5-3 . The activation energy decreases with thermal ageing of TBC samples.

Table 5-2: Activation energy (E_a) of alumina for TBC samples, aged at 1030°C in air for 10 hours to 1000 hours, for the temperature range from 200°C to 400°C.

Thermal ageing time of samples (Hours)	10	50	200	500	1000
E_a (eV)	0.96	0.88	0.80	0.81	0.77

Table 5-3: Activation energy (E_a) of alumina for TBC samples, aged at 1200°C in air for 10 hours to 400 hours, for the temperature range from 200°C to 400°C.

Thermal ageing time of samples (Hours)	10	100	400
E_a (eV)	0.96	0.82	0.83

Two ageing conditions were chosen in order to compare the TBC samples in terms of their activation energy. From the SEM images, it was observed that TBC samples aged at 1030°C for 10 hours and 1200°C for 10 hours consists only of a continuous alumina layer in their TGO microstructures (figure 5-2a and 5-3b). The activation energy for these samples are 0.96 eV for the sample aged at 1030°C for 10 hours and 0.96 eV for the sample aged at 1200°C for 10 hours. In the above samples, the dark layer is mainly alumina with traces of other oxides (oxides of Ni, Cr and Co). This shows that, although the ageing temperatures were different for the TBC samples, the composition and properties of the protective oxide layers (alumina) are similar. Again, it was observed that the activation energy for the TBC samples aged at 1030°C decreased with ageing time indicating a decrease in the protectiveness of the TGO. For the 1030°C aged samples, the activation energies for 50 hours, 200 hours, 500 hours and 1000 hours aged samples were 0.88 eV, 0.83 eV, 0.80 eV and 0.77 eV respectively. The alumina content for 50 hours, 200 hours, 500 hours and 1000 hours samples were 93%, 88%, 82% and 46% respectively. A similar variation in activation energy results were observed for the TBC samples, aged at 1200°C, with increasing ageing time, but in these samples the alumina content increased with ageing time in the dark oxide layer. This may be because the

diffusion of Al from the bond coat is faster at the higher temperature and it supplied enough Al to keep the alumina scale intact. If the composition of the alumina did not change the activation energy in these samples, then what did cause this change? Porosity can develop at high temperature in the TGO layer as observed by Song and Xiao [2001]. The changes of activation energy for this series of samples may be because of the formation of porosity, due to the higher rate of diffusion of Al and other metal ions through the grain boundary regions.

SEM images show that mixed oxide scale is formed between the almina and the YSZ layer. The ions of Ni, Cr, Co and Al migrate through the grain boundary region of the alumina scales alongside the oxygen diffusion through it to the bond coat. This internal diffusion of oxygen causes internal oxidation of the bond coat. Thus the oxides of these ions will be present in the grain boundary regions of the alumina layer. The electrical resistivity of alumina will be highest when it is pure that is greater than 10^{14} ohms-cm, but it will decrease with increasing impurity in it [Wirth, 1991]. From the SEM images, it was observed that the mixed oxide was present for all samples that gave lower activation energies. The activation energy for the alumina layer, consisting only of the alumina layer in the TGO microstructure, is between 0.88 eV to 0.96 eV and the activation energy for the alumina layer, consisting of both alumina and mixed oxides layers in the TGO microstructure, is between 0.77 eV to 0.83 eV.

The theoretical activation energy for 99.5% Al_2O_3 is calculated using a graphical method from the data in table 5-4 for a thin film. It is 1.12 eV in the temperature range from 25°C to 700°C. This value is higher, as expected, than the experimental results but should be near to them. Thin-film alumina is fabricated from alumina raw materials, which are in the micrometre size range and the raw materials are of very high purity. In the present study, the alumina scale was not pure. EDX analysis shows that alumina scales contained traces of the oxide of Ni, Cr, Co and Cr (figure 5-4a). The activation energy of pure NiO formed at 800°C in air is 0.5~0.6 eV in the temperature range from 25°C to 700°C [Liu et al., 1999]. EDX analysis also shows that the content of Al_2O_3 decreased and NiO increased in the dark oxide

scale (figure 5-4a). Hence the activation energy value ~0.96 eV obtained from the experimental results for the protective alumina scale is reasonable for these samples. A further decrease of the activation energy means an increasing impurity or porosity content in this scale and these will degrade the thermal protectiveness of the TGO layer still further. Thus monitoring the activation energy can give a prior indication of the degradation of TBC samples and the values of activation energies can also be used to compare TGOs formed under different oxidation conditions.

Table 5-4: Electrical resistivity of thin film 99.5% Al_2O_3 [Wirth, 1991].

Samples	Temperature (°C)	Resistivity (Ω-cm)	Activation Energy E_a (eV) (300°C-700°C)
Alumina Thin film	25°C	$>10^{14}$	1.12
	300°C	$>10^{12}$	
	500°C	$>10^{9}$	
	700°C	$>10^{8}$	

5.5. Summary

Impedance spectroscopy has been used successfully to evaluate the microstructure of TGOs formed at 1030°C and 1200°C in air. SEM images and microanalyses in conjunction with XRD analyses confirm that the dark layer mainly contains α-Al_2O_3 with traces of other oxides. The grey oxide layer in the TGOs mainly contains the oxides of Al, Cr, Ni and Co. The composition and microstructural changes in the TGO are caused by the depletion of Al in the bond coat, due to its consumption from the formation and growth of Al_2O_3 at the bond coat/YSZ interface. The less active elements, Cr, Ni and Co formed $(Ni,Co)(Cr,Al)_2O_4$ spinel at the alumina scale/YSZ interface. It appears that the Cr, Ni, and Co diffused through the Al_2O_3 scale to form the $(Ni,Co)(Cr,Al)_2O_4$ spinel. Oxygen also penetrated through the Al_2O_3 layer to reach the bond coat and produced oxides inside the bond coat.

The electrical parameters, such as impedance, resistance, capacitance, relaxation frequency and activation energy were used to study oxide scales. The sample geometry or origin can affect the impedance, resistance and capacitance values, but the relaxation frequency and activation energy are the characteristics of materials and will not be affected by these factors. Again the activation energy is a more effective measure of the protectiveness of the oxide. Hence the activation energy was used to compare TGOs formed at various temperature in TBC samples. It was observed that changes of activation energy are related to the changes happening in the microstructure of TBC samples. The activation energy for the dark alumina oxide layer decreased with the formation of the grey mixed oxide in the TGO. For the TGO formed at 1030°C, the activation energy decreased with decreasing alumina content in the dark oxide scale. For the TGO formed at 1200°C, the activation energy for the dark oxide scale decreased with the formation of the mixed oxide, but without any changes of alumina content in the dark oxide layer. This decrease of activation energy for the TGO formed at high temperature may be because of the porosity in the dark oxide. The microstructural and composition changes in the TGO at the metal/YSZ interface induced the degradation of TBC samples. The TGO changes gradually from Al_2O_3 to a two-phase structure of Al_2O_3 and $(Ni,Co)(Cr,Al)_2O_4$ spinel, which correspond to the changes in their electrical properties. Similar activation energies for the TGO were observed for samples aged at 1200°C. This confirms that the TGO formed at high temperature could have the same oxidation protectiveness as the TGO formed at the lower temperature. The value of the activation energy can be used to monitor protectiveness of TGO non-destructively and help to monitor TBC degradation.

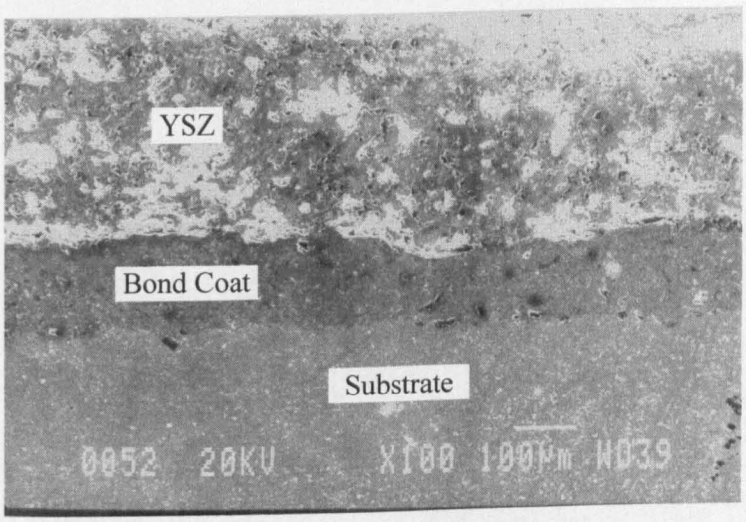

Figure 5-1: SEM image shows the cross section of TBC sample as received (not thermally aged).

(a)

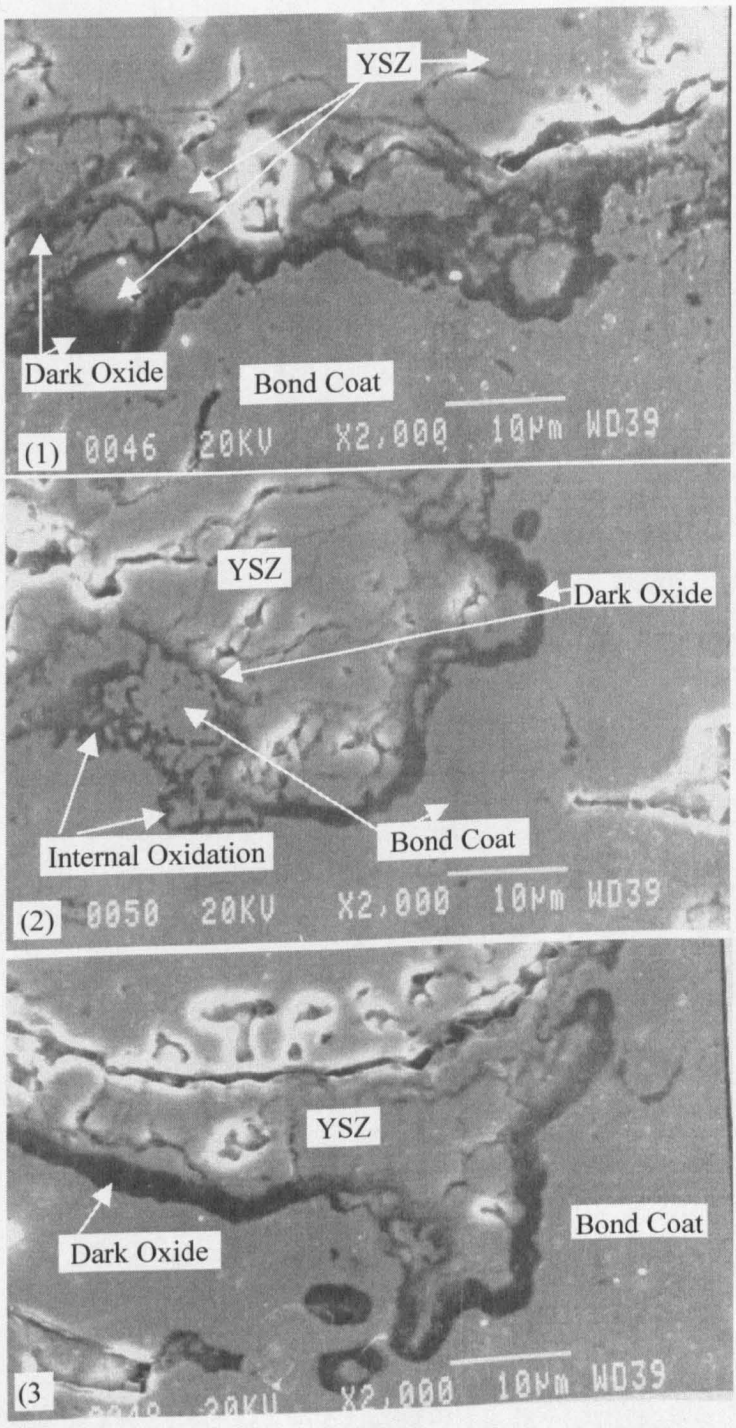
YSZ
Dark Oxide
Bond Coat
(1) 0046 20KV X2,000 10μm WD39
YSZ
Dark Oxide
Internal Oxidation
Bond Coat
(2) 0050 20KV X2,000 10μm WD39
YSZ
Dark Oxide
Bond Coat
(3 20KV X2,000 10μm WD39

(b)

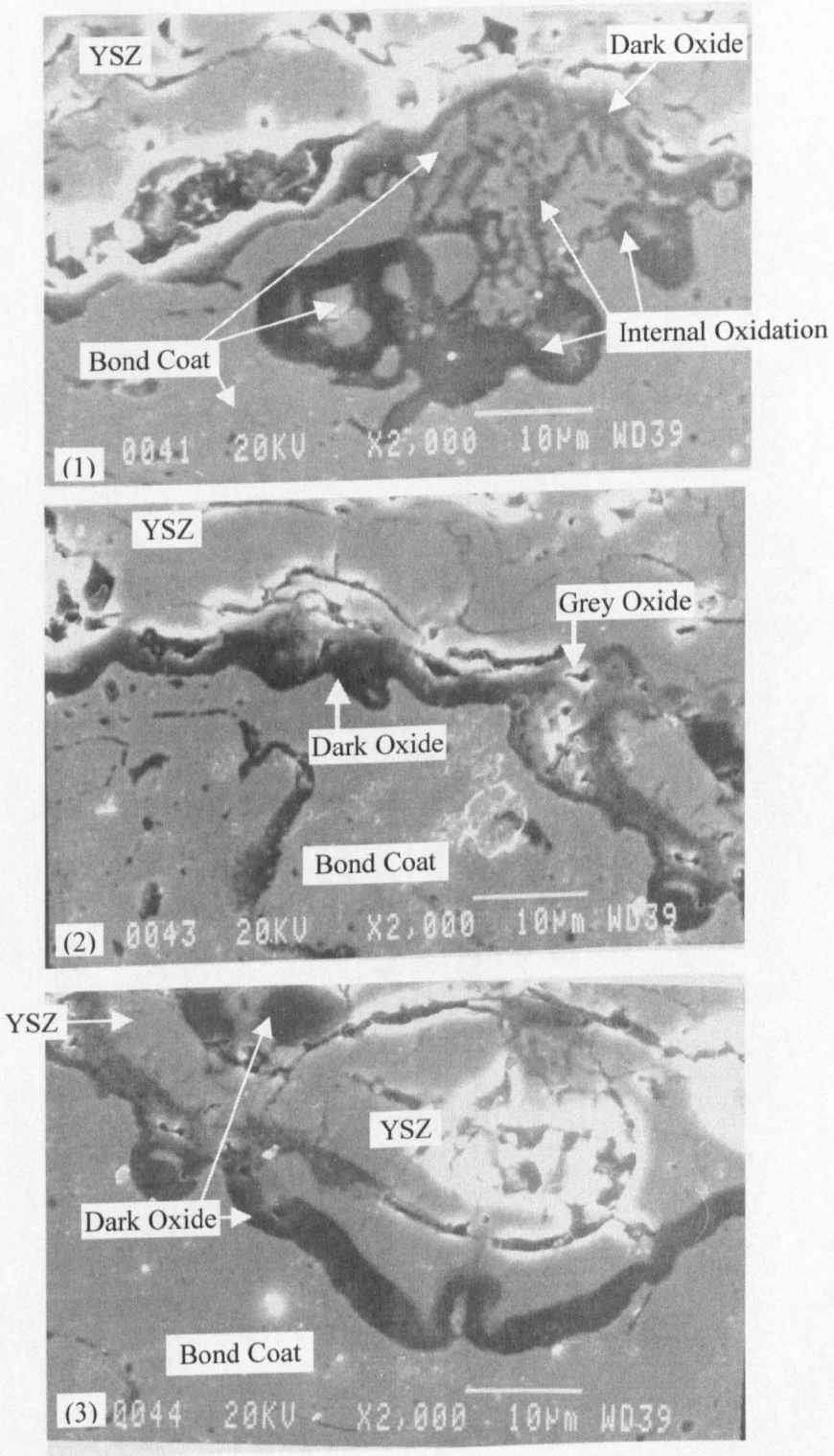
YSZ
Dark Oxide
Internal Oxidation
Bond Coat
(1) 0041 20KV X2,000 10μm WD39
YSZ
Grey Oxide
Dark Oxide
Bond Coat
(2) 0043 20KV X2,000 10μm WD39
YSZ
YSZ
Dark Oxide
Bond Coat
(3) 0044 20KV X2,000 10μm WD39

(c)

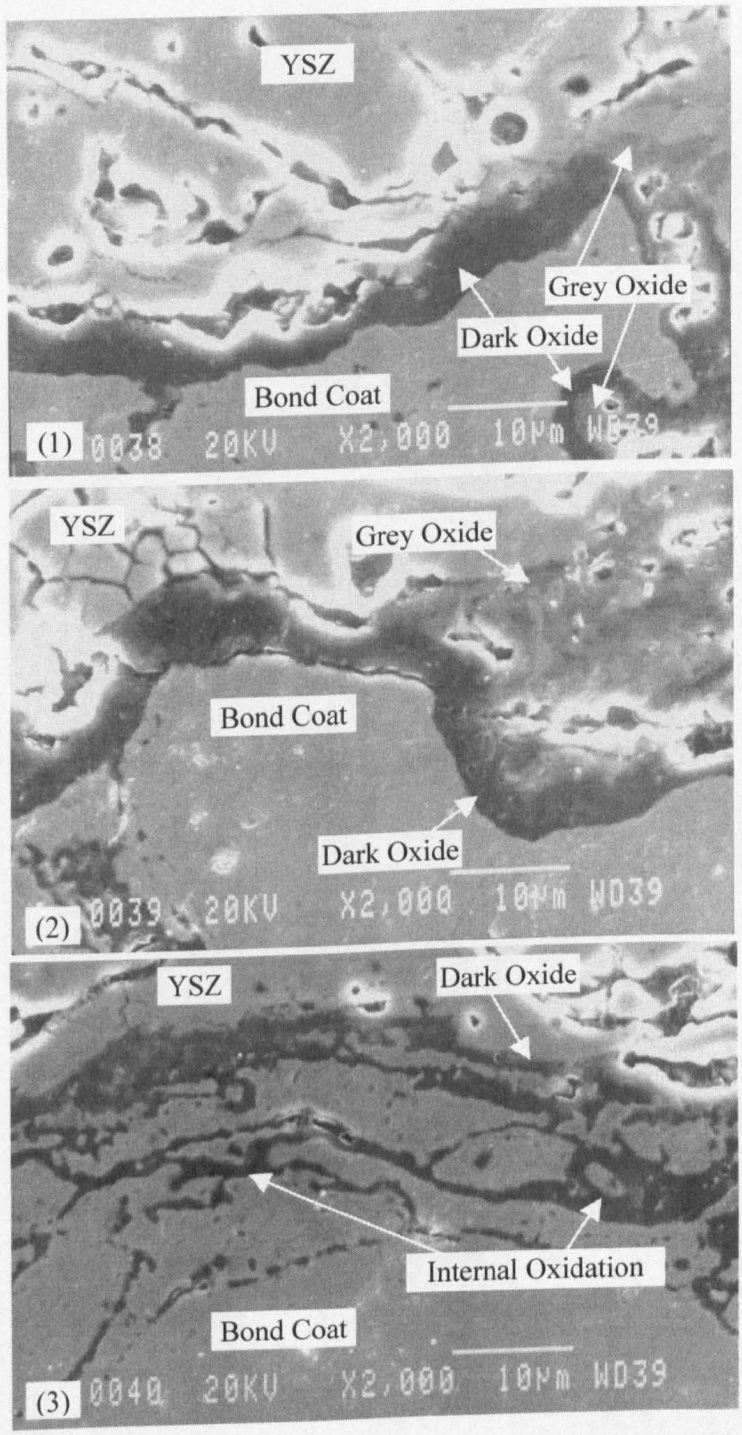
YSZ
Grey Oxide
Dark Oxide
Bond Coat
(1) 0038 20KV X2,000 10μm WD39
YSZ
Grey Oxide
Bond Coat
Dark Oxide
(2) 0039 20KV X2,000 10μm WD39
YSZ
Dark Oxide
Internal Oxidation
Bond Coat
(3) 0040 20KV X2,000 10μm WD39

(d)

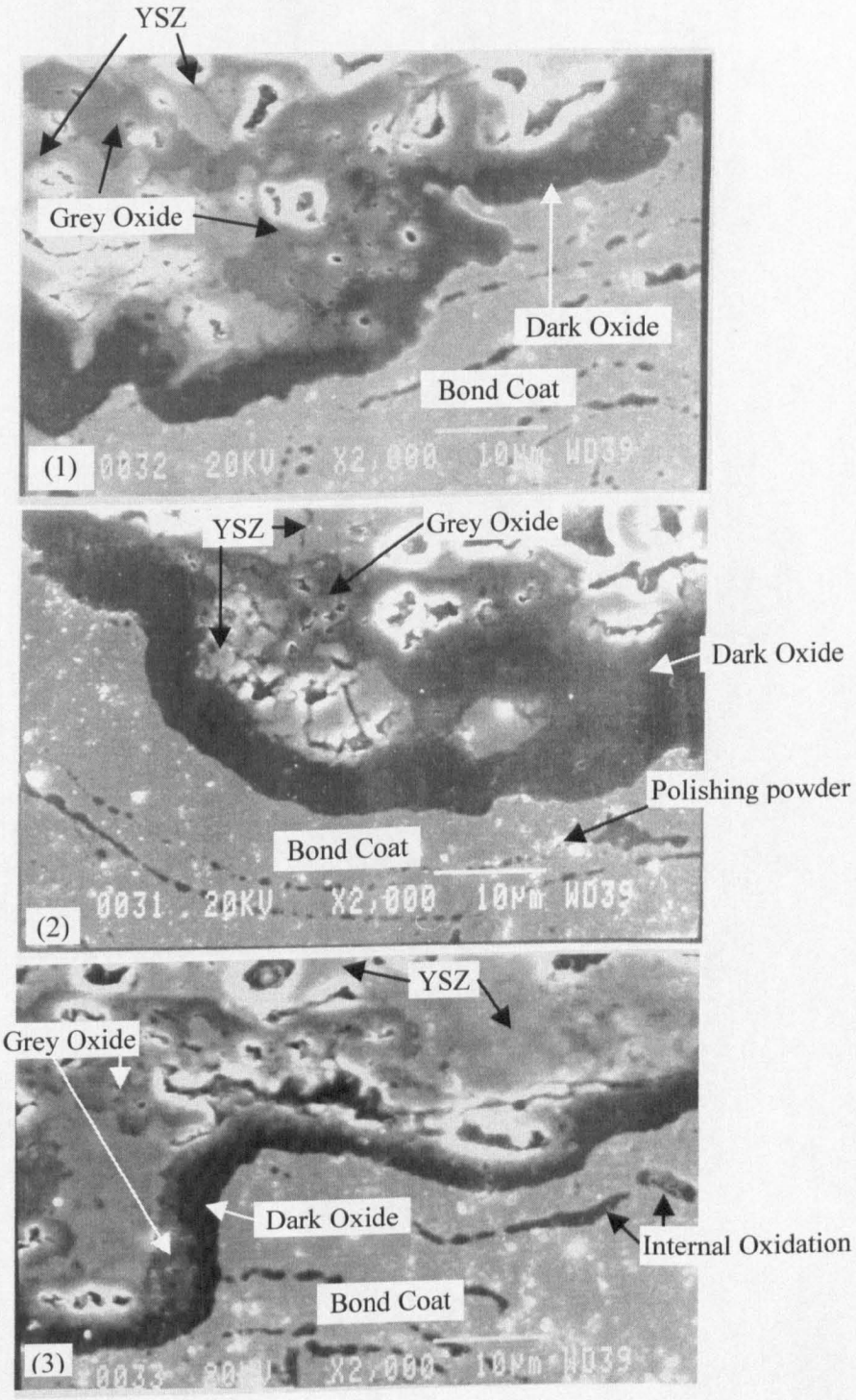
YSZ
Grey Oxide
Dark Oxide
Bond Coat
(1)
YSZ
Grey Oxide
Dark Oxide
Polishing powder
Bond Coat
(2)
YSZ
Grey Oxide
Dark Oxide
Internal Oxidation
Bond Coat
(3)

(e)

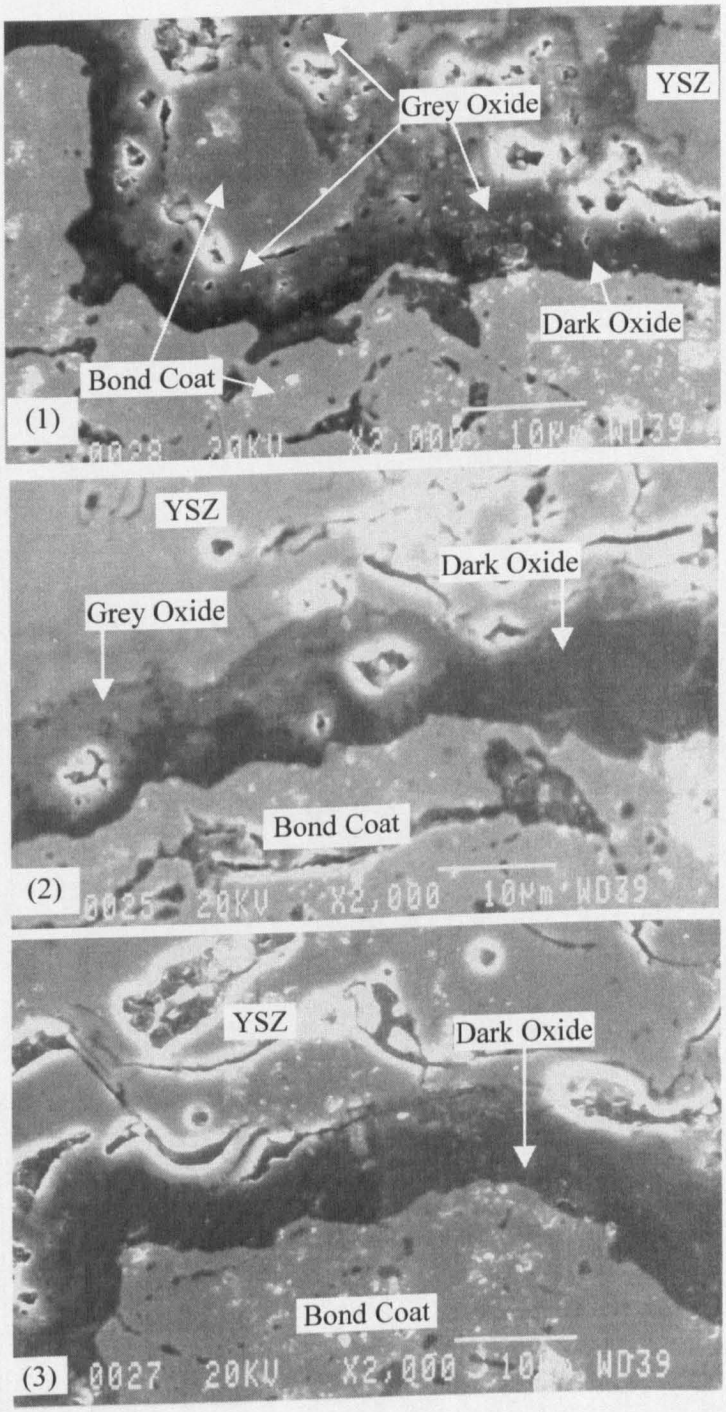

Figure 5-2: SEM images show different regions from the cross sections of TBC samples thermally aged at 1030°C in air for (a) 10 hours, (b) 50 hours, (c) 200 hours, (d) 500 hours and (e) 1000 hours.

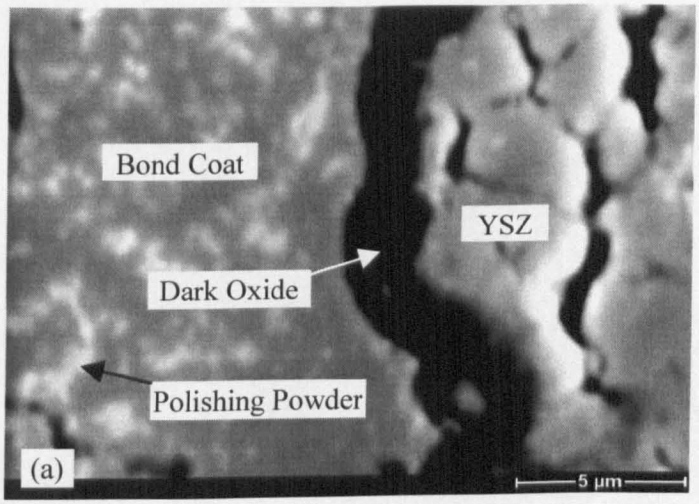
Bond Coat
YSZ
Dark Oxide
Polishing Powder
(a)
5 μm

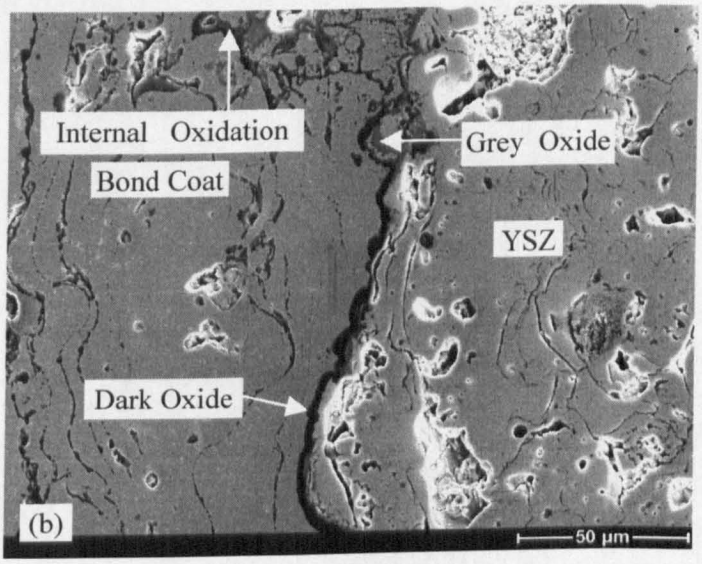
Internal Oxidation
Grey Oxide
Bond Coat
YSZ
Dark Oxide
(b)
50 μm

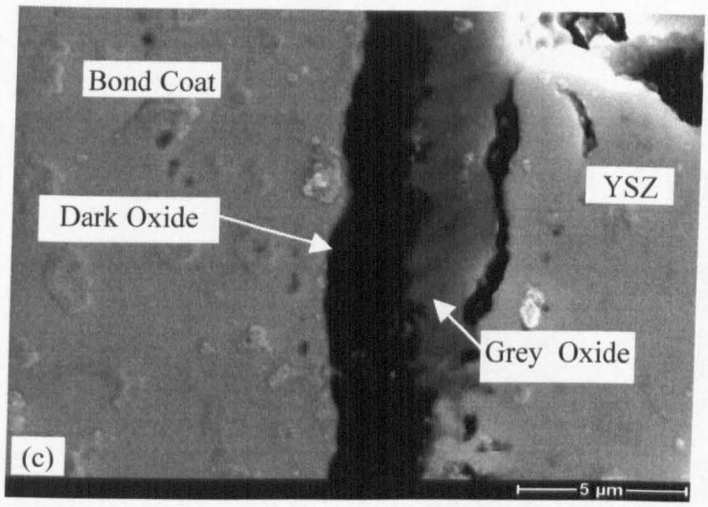

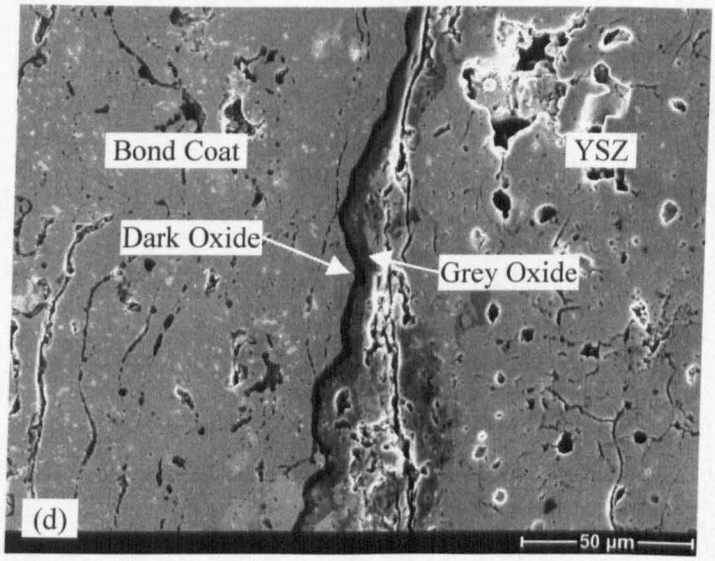

Figure 5-3: SEM images show the cross section of TBC samples thermally aged at 1200°C in air for (a) 1 hour, (b) 10 hours, (c) 50 hours and (d) 100 hours.

(a)

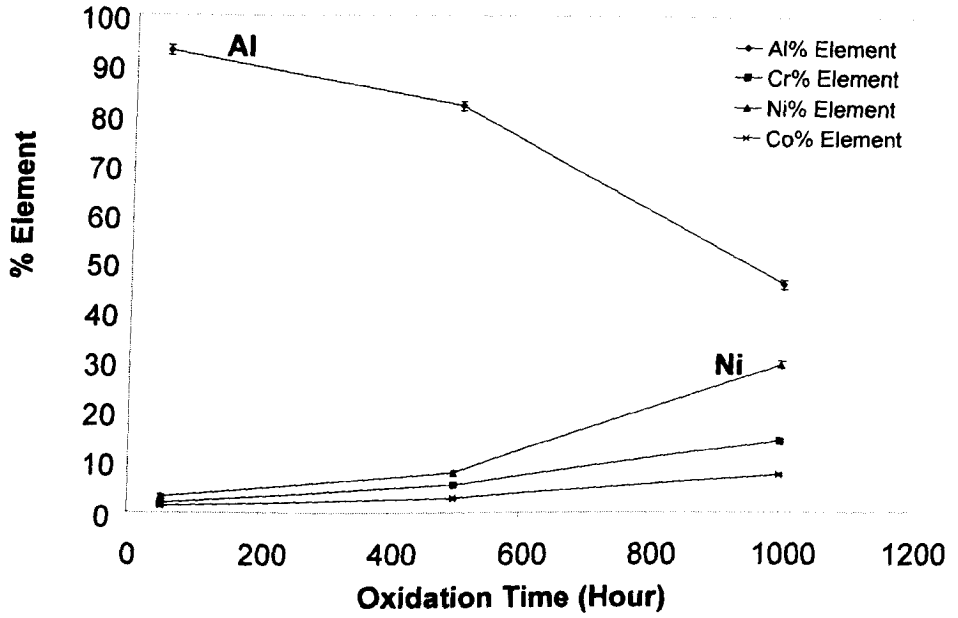
Al
Ni
Al% Element
Cr% Element
Ni% Element
Co% Element
% Element
Oxidation Time (Hour)
0
10
20
30
40
50
60
70
80
90
100
0
200
400
600
800
1000
1200

(b)

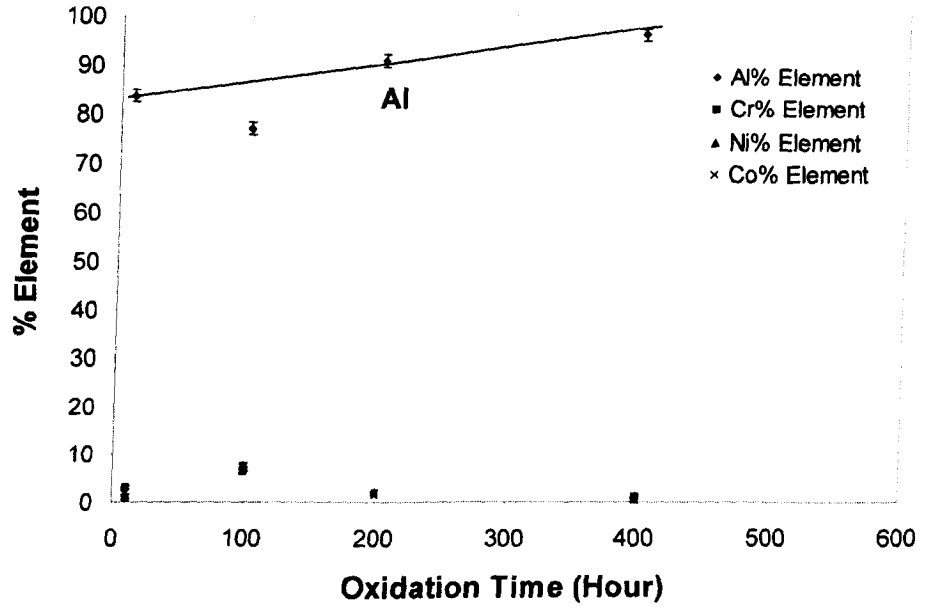
Al
Al% Element
Cr% Element
Ni% Element
Co% Element
% Element
Oxidation Time (Hour)
0
10
20
30
40
50
60
70
80
90
100
0
100
200
300
400
500
600

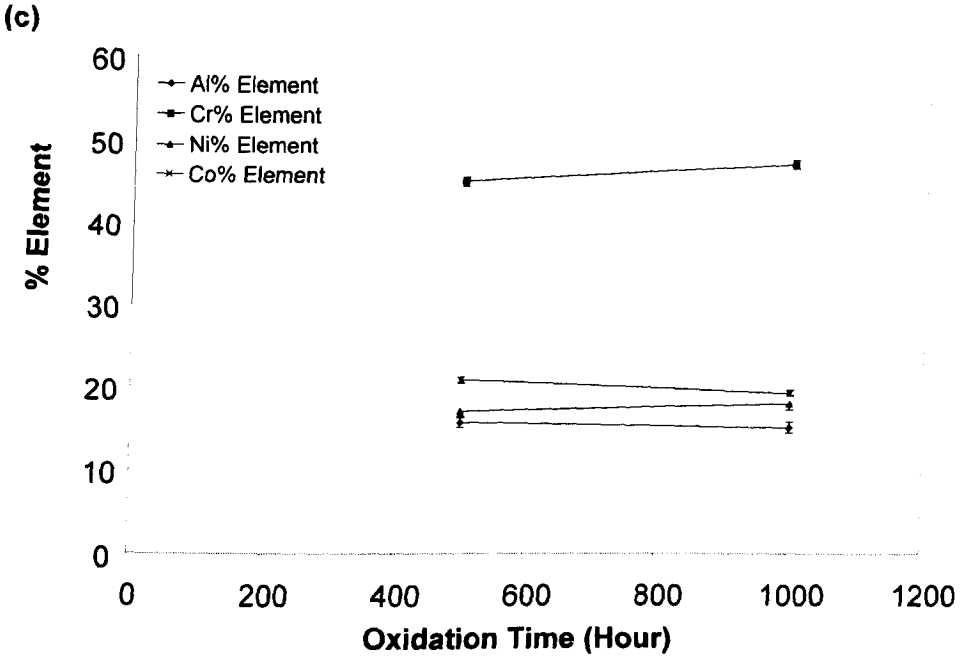

Figure 5-4: (a) Variation of elemental composition with oxidation time in the dark oxide layer of TBC samples aged at 1030°C in air. (b) Variation of elemental composition with oxidation time in the dark oxide layer of TBC samples aged at 1200°C in air. (c) Variation of elemental composition with oxidation time in the grey oxide layer of TBC samples aged at 1030°C in air.

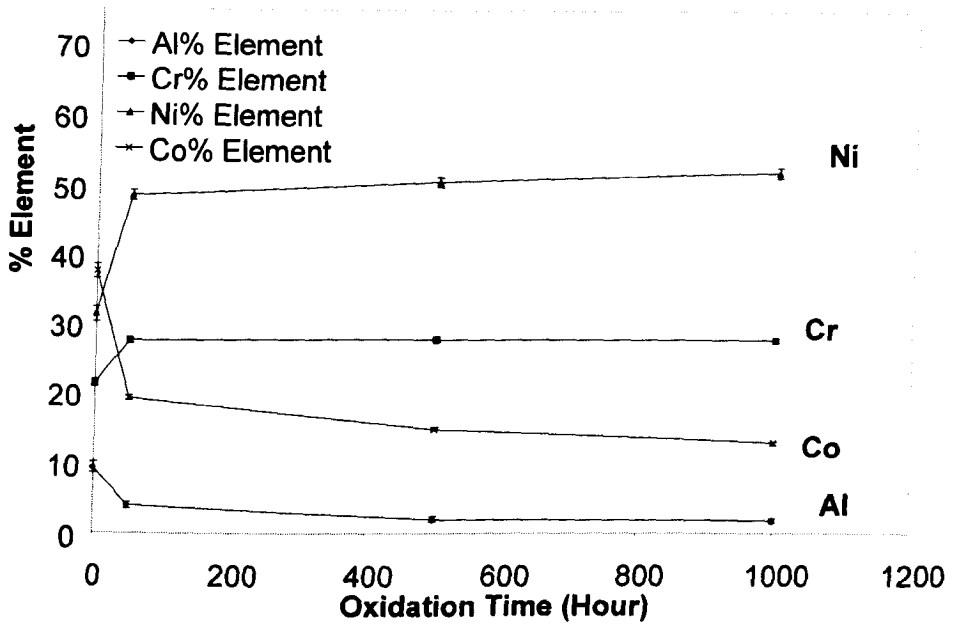

Figure 5-5: Variation of elemental composition with oxidation time in the middle of the bond coat of TBC samples aged at 1030°C in air.

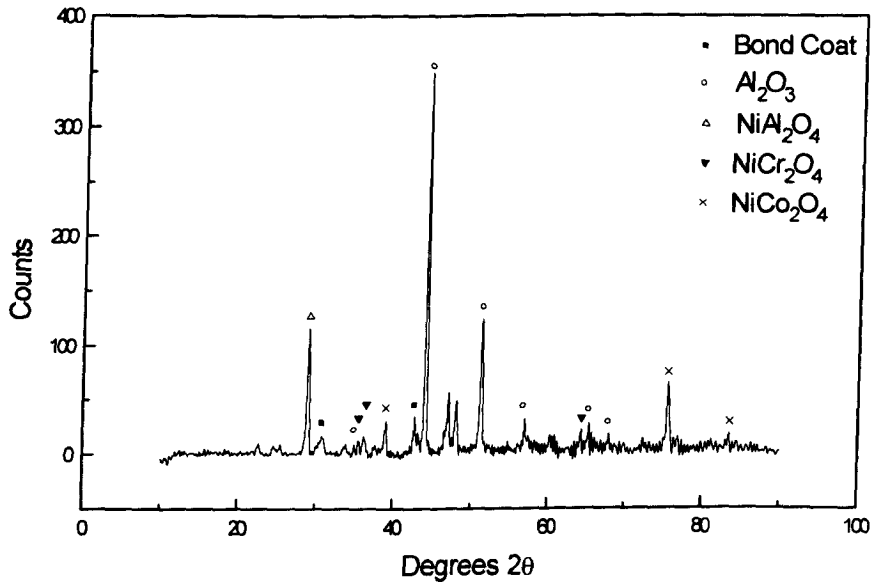

Figure 5-6: XRD pattern of oxide scale formed on NiCrCoAlY bond coat oxidised at 1030°C for 50 hours in air.

(a)

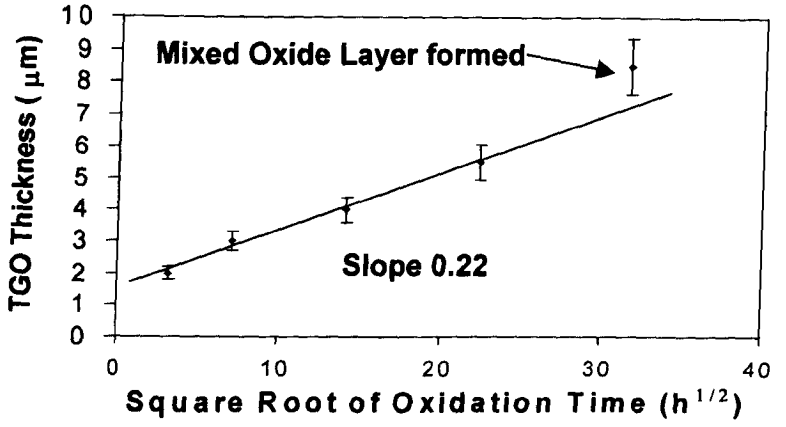

(b)

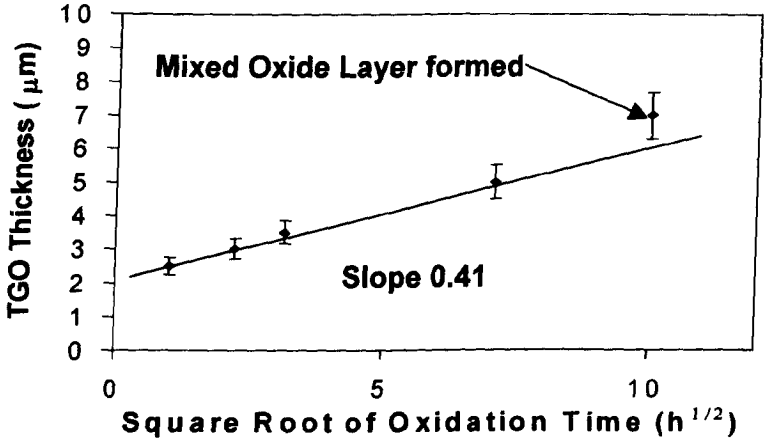

Figure 5-7: (a) Variation of the TGO layer thickness with oxidation time for TBC samples aged at 1030°C in air. (b) Variation of the TGO layer thickness with oxidation time for TBC samples aged at 1200°C in air.

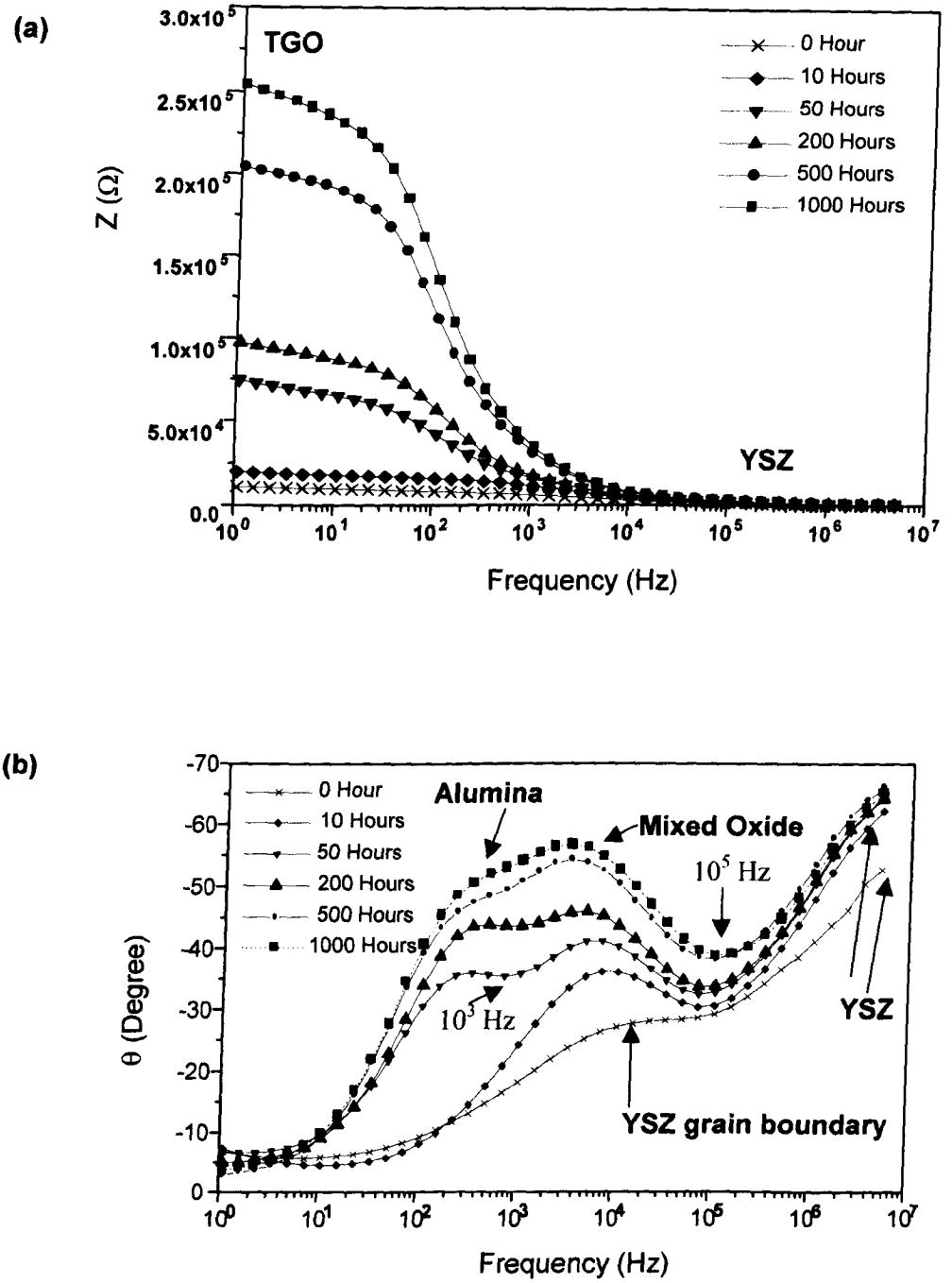

Figure 5-8: Bode plots for TBC samples aged at 1030°C in air for 0 hour to 1000 hours, (a) Impedance vs. frequency plot; (b) Phase angle vs. frequency plot.

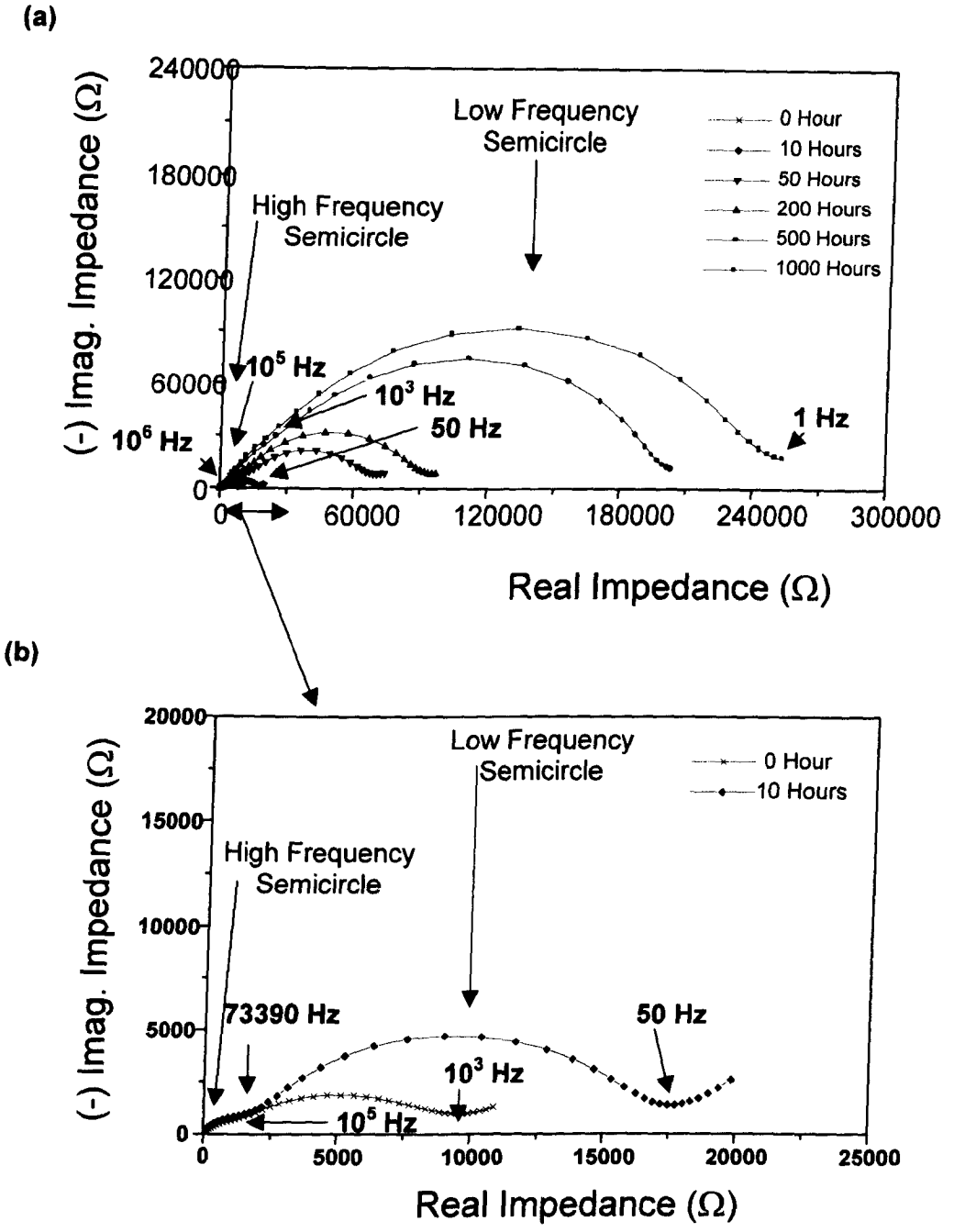

Figure 5-9: (a) Complex plots for TBC samples aged at 1030°C in air for 0 hour to 1000 hours; (b) Complex plots for TBC samples aged at 1030°C in air for 0 hour and 10 hours.

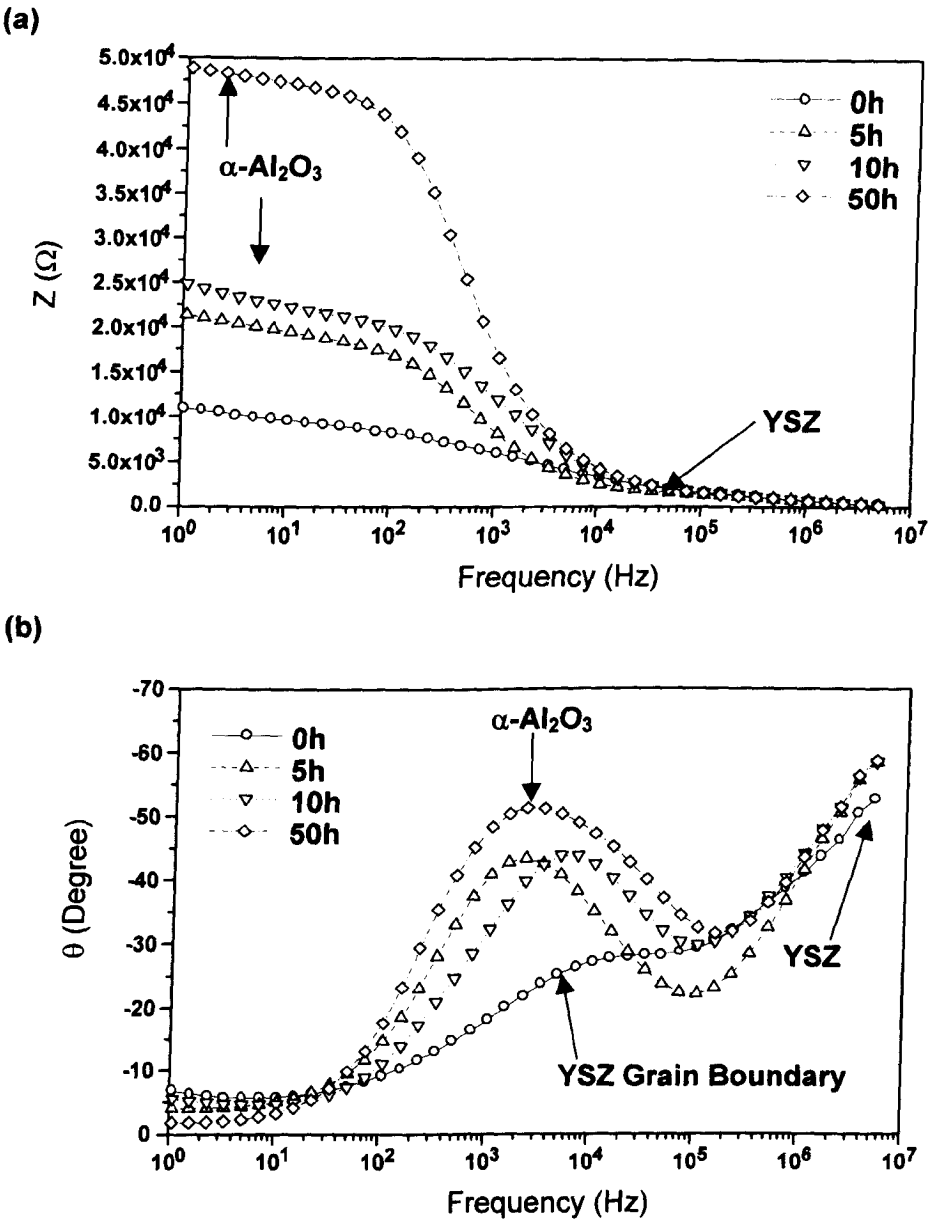

Figure 5-10: Bode plots for TBC samples aged at 1200°C in air for 0 hour to 50 hours, (a) impedance vs. frequency; (b) phase angle vs. frequency.

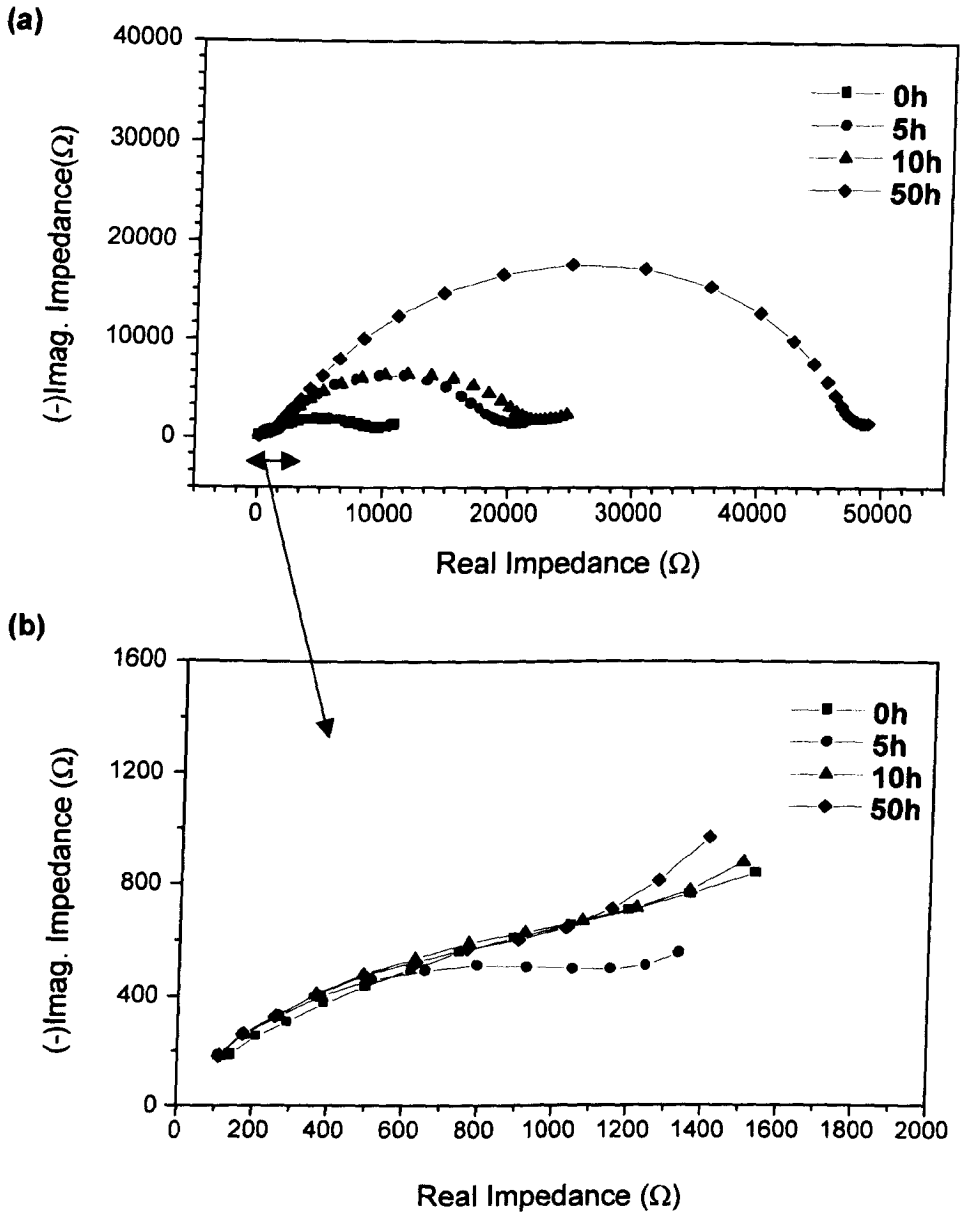

Figure 5-11: Complex plots for TBC samples aged at 1200°C in air for 0 hour to 50 hours.

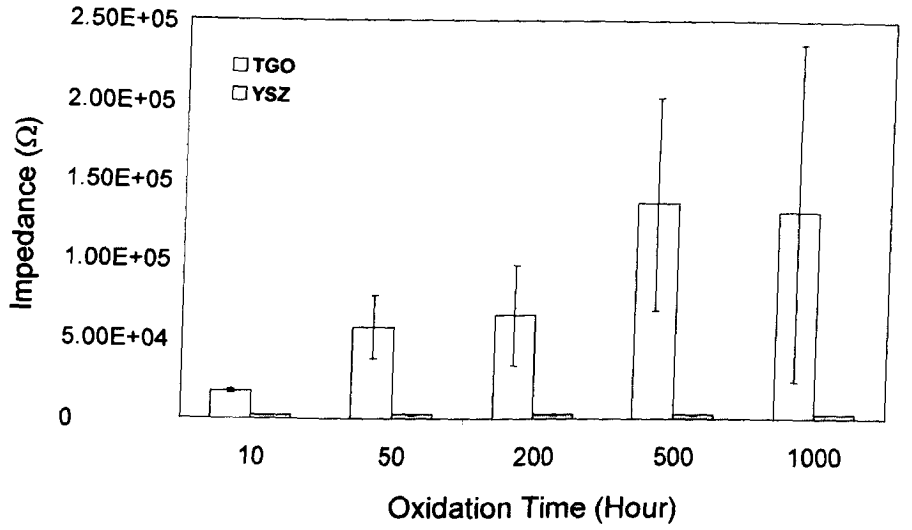

Figure 5-12: Impedance vs. oxidation time for the TGO layer and the YSZ layer of TBC samples thermally aged at 1030°C in air for 10 hour to 1000 hours.

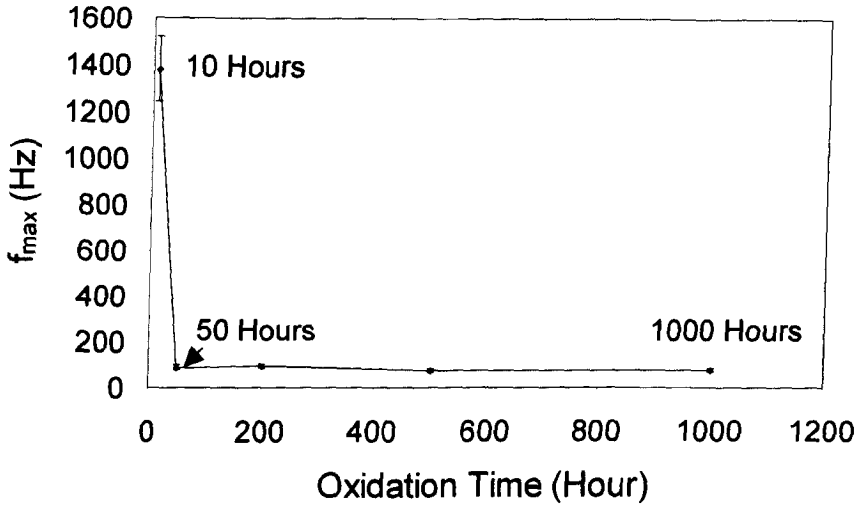

Figure 5-13: The variation of the relaxation frequency of TGO layers with oxidation time at 400°C for TBC samples, thermally aged at 1030°C in air.

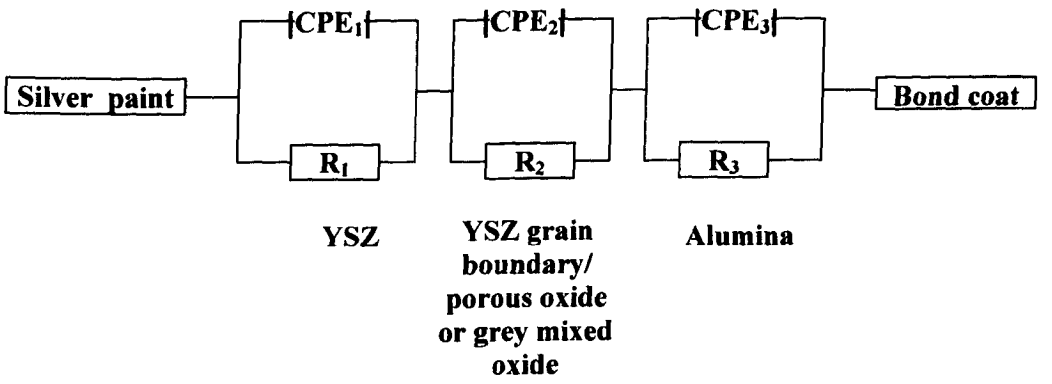

Figure 5-14: Equivalent circuit model for thermally aged TBC sample.

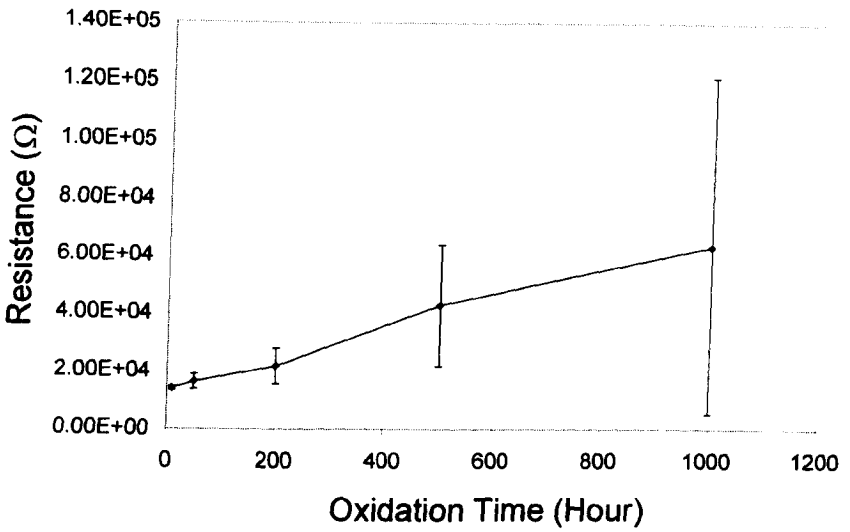

Figure 5-15: Variation of electrical resistance with oxidation time at 400°C for the intermediate frequency semicircle, second from left, (IS response for the mixed oxide layer or the YSZ grain boundaries) of TBC samples thermally aged at 1030°C in air for 10 hour to 1000 hours.

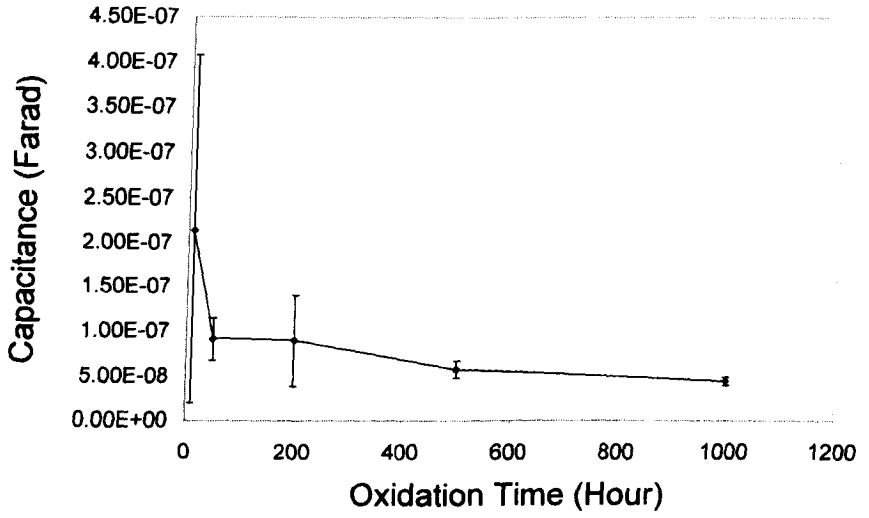

Figure 5-16: Variation of capacitance with oxidation time at 400°C for the intermediate frequency semicircle, second from left, (IS response for the mixed oxide layer or the YSZ grain boundaries) of TBC samples thermally aged at 1030°C in air for 10 hour to 1000 hours.

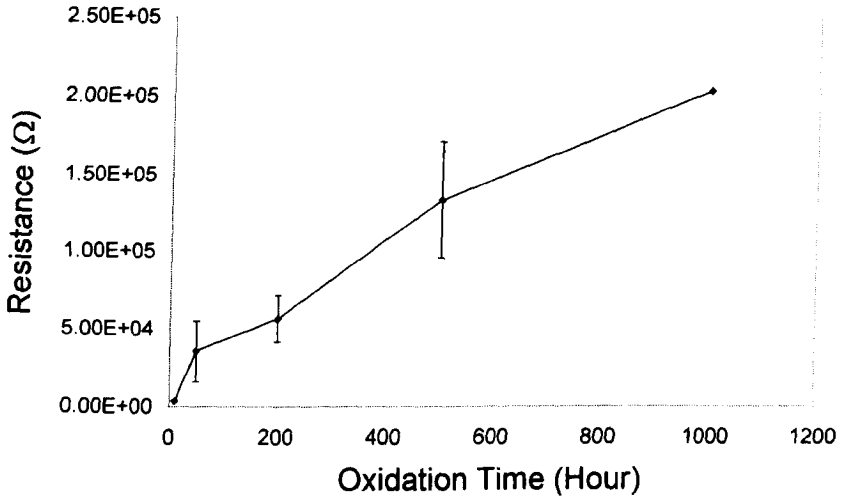

Figure 5-17: The variation of the electrical resistance of alumina layers with time for TBC samples, thermally aged at 1030°C in air.

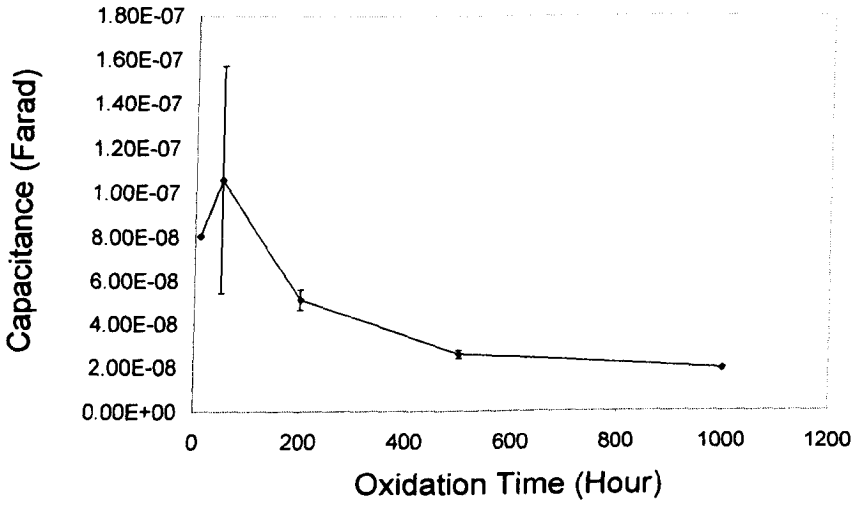

Figure 5-18: The variation of the capacitance of alumina layers with time for TBC samples, thermally aged at 1030°C in air.

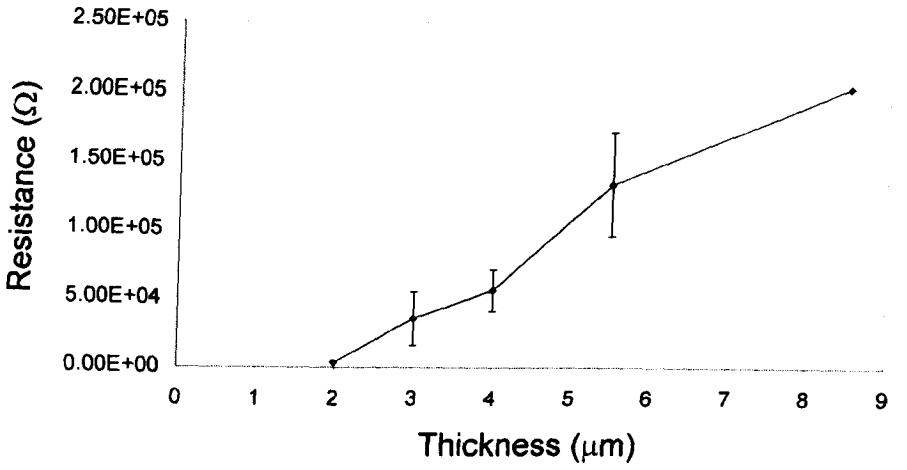

Figure 5-19: The variation of the electrical resistance of alumina layers with thickness for TBC samples thermally aged at 1030°C in air for 10 hour to 1000 hours.

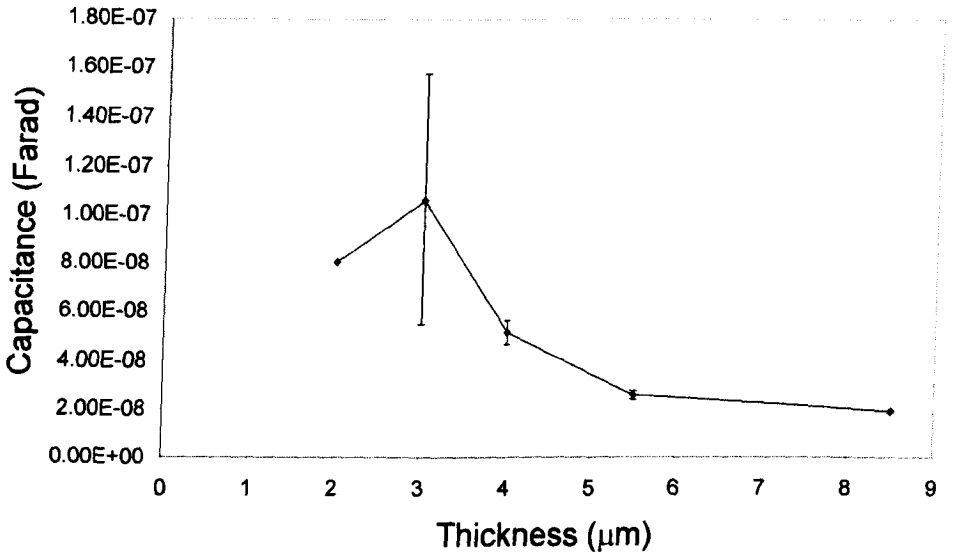

Figure 5-20: The variation of the capacitance of alumina layers with thickness for TBC samples thermally aged at 1030°C in air for 10 hour to 1000 hours.

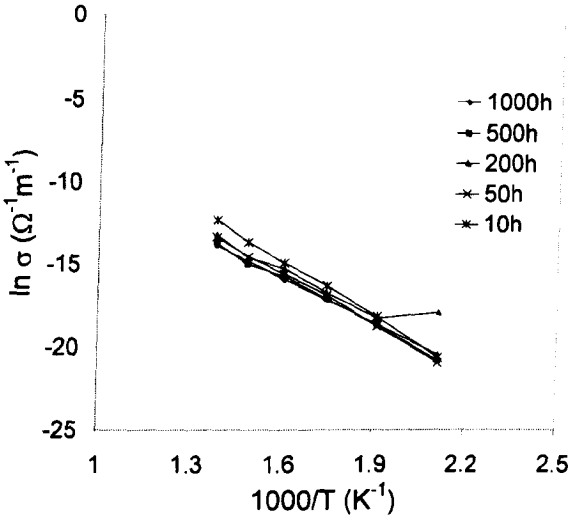

Figure 5-21: Temperature dependence of the electrical conductivity for alumina layers formed in TBC samples at 1030°C in air for 10 hours to 1000 hours.

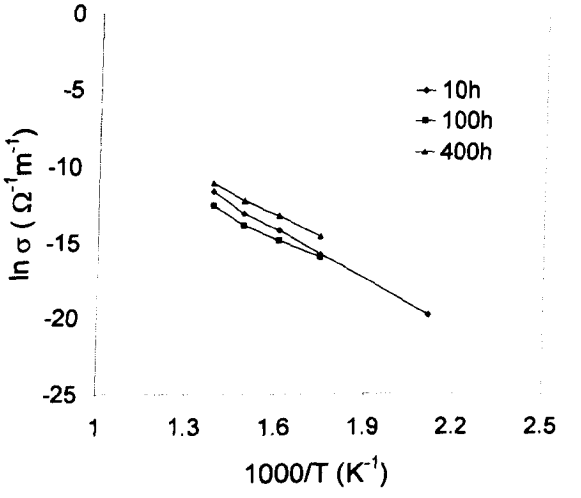

Figure 5-22: Temperature dependence of the electrical conductivity for alumina layers formed in TBC samples at 1200°C in air for 10 hours to 400 hours.

6. Non-destructive Evaluation of Degradation in TBCs by IS

6.1. Introduction

Impedance spectroscopy (IS) is used to evaluate the degradation of thermal barrier coatings (TBCs) on a superalloy at 1150°C. The use of zirconia-based thermal barrier coatings (TBCs) on turbine blades is being considered for increasing gas operating temperatures [Haynes et al., 1996], [Miller, 1997], [Bose and DeMasi-Marcin, 1997] and [Sergo and Clarke, 1998]. A typical TBC system is composed of an oxidation-resistant metallic bond coat on the superalloy substrate and a heat-insulating ceramic top coat attached to the bond coat. The bond coat provides a rough surface for bonding the YSZ and protects the substrate from oxidation by forming a continuous protective oxide scale (usually α-Al_2O_3) between the bond coat and top coat. Microstructural evolution of thermally-grown oxides (TGOs) at the metal/YSZ interface is responsible for the spallation of TBCs. In this chapter, impedance results and microstructural observations are described and discussed. A comparison of electrical properties and microstrucural features of TGOs are made to derive their relationship, which may be used to evaluate the degradation process of TBCs in engineering practice. Moreover, the implication of this study is addressed.

6.2. Experimental Procedure

6.2.1. Thermal Ageing

The TBC samples were aged in air at 1150°C for the range of times indicated in table 6-1. Five samples for each oxidation time were prepared.

Table 6-1: Thermal ageing of the TBC samples

Exposure temperature (°C)	Oxidation time (Hour)	Holding periods at exposure temperature in the different thermal cycles (Hour)					
		Thermal cycle 1	Thermal cycle 2	Thermal cycle 3	Thermal cycle 4	Thermal cycle 5	Thermal cycle 6
1150	10	10					
	100	100					
	200	100	100				
	1000	100	100	300	500		
	1500	100	100	300	500	500	
	2000	100	100	300	500	500	500

6.2.2. Impedance Measurements

Three samples were chosen randomly from the five samples for impedance measurements. In the measurements, an AC (alternating current) amplitude of 10 mV was employed and the AC frequency was in the range of 1 Hz to 1×10^7 Hz. The electrode area (painted area) was 5mm × 5mm square. The measurements were performed at 400°C.

6.3. Results

6.3.1. Impedance Results

Typical complex plots for the samples aged for different times are presented in figure 6-1. Obviously, there are two semicircles on each complex plot, corresponding to two layers in the TBC sample. One of the two layers is the YSZ top coat and the other is the TGO layer. It has been confirmed that the high-frequency semicircle (on the left hand side) corresponds to the YSZ top coat and the low-frequency semicircle (on the right hand side) corresponds to the TGO layer [Wang et al., 2001].

To obtain the electrical properties of the TGO layer, it is necessary to establish an equivalent circuit to fit the measured spectra. The two semicircles may be modelled by two R-C components with a series connection (figure 6-2). In the model, a CPE is the constant phase element which is more suitable to describe the behaviour of a non-ideal capacitor which depends on frequency [MacDonald and Franceschetti, 1987]. This is because solid electrode surfaces generally are inhomogeneous due to geometric factors (*e.g.* surface roughness), which may cause a frequency dispersion as a result of heterogeneous current density distribution, *i.e.*, C is not an ideal capacitor. These effects may be described empirically by the concept of the CPE [Rammelt and Reinhard, 1995]. As this study is just concerned with the electrical properties rather than the dielectric properties, the details on the CPE will not be given here, which can be found in the reference [Rammelt and Reinhard, 1995].

The typical fitted results for a measured spectrum are shown in figure 6-3. Clearly, the fitted results are in good agreement with those measured. The resistance used in the fitting will be therefore taken as the measured result. The thickness of the TGO was determined by SEM and this was used to calculate the resistivity of the TGO. The resistance and resistivity values of the TGO scale are represented in figure 6-4 as a function of scale thickness. In addition, the oxidation time is also given for each data point. Clearly, the resistance increased with increased scale growth from 1

hours to 10 hours, then decreased from 10 hours to 1000 hours and finally remained unchanged up to 2000 hours. The resistivity did not change between 1 and 10 hours, indicating that the microstructure and microchemistry of the scale did not vary apparently during oxidation. After then the resistivity decreased with increasing oxidation time in the whole time range, whilst the decreasing rate was much higher between 10 and 1000 hours than between 1000 and 2000 hours. This implies that the TGO degraded very quickly from a protective scale to a non-protective scale in the range from 10 hours to 1000 hours because the resistivity shifts very fast in the low value direction.

6.3.2. Oxidation Kinetics and Microscopy

The oxidation kinetics of the bond coat are represented in figure 6-5. Clearly, the oxidation follows a parabolic law up to 1000 hours. In this stage, the oxide scale is protective because its growth rate is quite low. Further oxidation leads the scale growth rate to increase substantially. As a result, catastrophic oxidation appears with a dramatic increase in scale thickness.

Cross sections of TBC samples are presented in scanning electron micrographs (figure 6-6). Obviously, the oxide scale evolves during high temperature exposure. In general, for the 1 and 10 hour-aged samples, there is mainly a dense dark-coloured oxide scale present with a very small amount of grey-coloured oxide attached on the YSZ side for the 10 hour-aged sample (figure 6-6b). For the 100 hour-aged sample, the dark-coloured scale is still very dense with an apparent layer of porous grey-coloured oxide attached on the YSZ side (figure 6-6c). For the 100 hour-aged sample, the dark scale is less dense than that for the 10 hour-aged sample. Beyond 1000 hours ageing, the dark scale almost disappears and the less-protective grey scale is dominant (figures 6-6d and 6-6e). This could be the reason why the growth rate of the scale increases considerably after 1000 hours ageing. In addition, some dark oxides are formed inside the bond coat by internal reactions.

XRD was conducted on the thermally grown oxide surface by the complete spallation of YSZ. An XRD pattern is represented in figure 6-7, indicating that there exists a $(Ni,Co)(Cr,Al)_2O_4$ spinel, α-Al_2O_3, α-Cr_2O_3, and YSZ. The elemental information for different oxide layers was determined by EDX microanalysis (figure 6-8). Pure metals were used as standards in the ZAF corrections. The microanalysis in conjunction with the XRD results demonstrates that the dark oxide is predominantly comprised of α-Al_2O_3 for the samples aged for less than 1000 hours whilst α-Al_2O_3 and α-Cr_2O_3 are the major components of the dark oxide for the samples aged for more than 1000 hours. In addition, the amount of α-Cr_2O_3 increases with increasing oxidation time. The grey oxide scale mainly contains Al, Cr, Ni and Co. For ageing times shorter than 1000 hours, the levels of Al, Cr, and Ni do not change apparently, but they change sharply when the oxidation time is longer than 1000 hours with the Cr and Ni level increasing and the Al level decreasing (figure 6-8). It may be concluded in terms of both EDX and XRD results that the grey oxide scales are mainly composed of a $(Ni,Co)(Cr,Al)_2O_4$ spinel and α-Al_2O_3 when the oxidation time is shorter than 1000 hours. But, the grey oxide scales are composed of a $(Ni,Co)(Cr,Al)_2O_4$ spinel, α-Al_2O_3 and α-Cr_2O_3, when the oxidation time is longer than 1000 hours. The YSZ detected by XRD could be that which is retained on the oxide scale after its spallation. These phenomena have also been confirmed by Shillington and Clarke [1999].

6.4. Discussion

6.4.1. Degradation of TBC Systems

As shown above, the α-alumina-dominant dark oxide scale degrades in the ageing process. This manifests itself by a decrease in the amount of α-Al_2O_3 and an increase in the amount of α-Cr_2O_3 with increasing oxidation time, leading to an increase in porosity (figures 6-6) until the mixed grey oxides dominate in the scales. The degradation of α-Al_2O_3 may be caused by Al depletion in the bond coat because of its consumption in the formation and growth of the TGOs at the metal/YSZ interface, leading to an insufficient quantity of Al available for the further formation and growth of degradation of α-Al_2O_3. In this scenario, the less active elements, Cr, Ni and Co, can form α-Cr_2O_3 and a (Ni,Co)(Cr,Al)$_2O_4$ spinel. Formation of α-Cr_2O_3 and the spinel could be responsible for the microcracking of the TGOs. During cooling and heating in the thermal cycling treatment, microcracks may be formed because of internal stresses created by the thermal expansion mismatch between different materials. The α-Al_2O_3 film can be continuously formed if the Al content in the bond coat is still sufficient to fill up the spaces created by the microcracks. However, if Al is depleted in the bond coat to a certain extent, the continuous formation of α-Al_2O_3 will terminate. In such an instance, Cr, Ni, and Co may easily diffuse to the α-Al_2O_3 scale surface by fast surface diffusion to form α-Cr_2O_3 and the (Ni,Co)(Cr,Al)$_2O_4$ spinel. Of course, oxygen may also penetrate into the scale or to the bond coat/scale interface. It appears that α-Al_2O_3 may dissolve in the mixed oxide at high temperatures, because after 1000 hours ageing the dark oxide scale nearly vanishes.

As indicated in figure 6-6, cracks are initiated and propagated in the mixed grey oxides adjacent to the YSZ parallel to the bond coat surface. The internal stresses created by the oxide formation and growth as well as the thermal expansion mismatch between different materials are likely to be the main reason for this phenomenon [Schutze, 1997]. For longer aged samples, more severe porosity

appears in the grey mixed oxide layer (figure 6-6), leading cracks to be formed more easily. This porosity could be developed by transformation of solid Cr_2O_3 into gaseous CrO_3 at the oxidation temperature (1150°C) [Kubaschewski and Hopkins, 1967].

6.4.2. Relation of Electrical Properties to Microstructural Features

The oxidation kinetics indicate that the scale thickness increases slowly between 10 and 1000 hours and rapidly between 1000 and 2000 hours (figure 6-5). Microstructural observations demonstrate that a reaction layer is formed between the bond coat and the YSZ top coat. In the reaction layer, there are two oxide layers. One is a somewhat pure alumina layer and the other is a mixed oxide layer consisting mainly of α-Cr_2O_3 and the $(Ni,Co)(Cr,Al)_2O_4$ spinel. The α-alumina layer gradually dies away prior to the complete spallation of the YSZ. In addition, the amount of chromium oxide in the mixed oxide layer increases with increasing oxidation time. For longer aged samples, more severe porosity appears in the grey oxides, leading to cracking (figure 6-6). In theory, two semicircles in the complex plot should be obtained for the TGOs before the dark oxide layer vanishes. One of the two semicircles is for the dark oxide layer and the other for the grey oxide layer. However, only one semicircle is actually obtained for the TGOs (figure 6-1) in the impedance spectra. This may be because the dark oxide is not an absolutely continuous α-Al_2O_3 layer but is partially mixed with α-Cr_2O_3. As a consequence, the TGOs are overall characterised by one semicircle in the impedance spectra.

It should be noted that the changes with ageing time in the resistivity of the oxide scale (figure 6-4) are different from those in its growth rate (figure 6-5). To understand this, it is necessary to know whether the electronic conductivity is dominant in the electrical conduction of both α-Al_2O_3 and the mixed oxides. This is because the parabolic growth rate constant, k_r, is proportional to $\sigma_e\sigma_i/(\sigma_e+\sigma_i)$, where σ_e and σ_i are the electronic conductivity and ionic conductivity, respectively [Birks and Meier, 1983]. If the electronic conductivity is dominant, k_r will mainly depend on σ_i, *i.e.* the diffusion of reactive elements. The growth rate of the oxide scale has

no relevance to its conductivity. It has been universally acknowledged [Kubaschewski and Hopkins, 1967] and [Chiang, Birnie and Kingery, 1997] that α-Cr_2O_3 and the $(Ni,Co)(Cr,Al)_2O_4$ spinel are both electronic semiconductors and that their electronic conductivity is very dominant in their electrical conduction. α-Al_2O_3 is normally regarded as an insulator and it is unclear whether its electronic conductivity is dominant and thus, its ionic conductivity is evaluated theoretically.

The ionic conductivity, σ_i, can be evaluated by [Chiang, Birnie and Kingery, 1997]:

$$\sigma_i = \frac{C_i Z_i^2 e^2 D_i}{kT} \tag{6-1}$$

where C_i is the vacancy concentration (the number of vacancies per unit volume). Z_i is the valance number (3 for Al and 2 for O), e is the charge (1.60×10^{-19} C), D_i is the diffusion coefficient for ions, k is the Boltzmann constant, and T is the absolute temperature. The atomic fraction of vacancies, n_i, is approximately given by [Chiang, Birnie and Kingery, 1997]:

$$n_i = \exp(\frac{-E_v}{2kT}) \tag{6-2}$$

where E_v is the vacancy formation energy. The formation energies for Al and O ions in α-Al_2O_3 are 6.2 eV and 6.1 eV, respectively [Chiang, Birnie and Kingery, 1997]. The atomic fractions of vacancies for Al and O ions are obtained as 1.3×10^{-11} and 2.0×10^{-11} respectively at 1150°C and 1.0×11^{-23} and 3.6×10^{-25}, respectively at 400°C. After conversion, the vacancy concentrations for Al and O ions are 6.2×10^{17} and 1.4×10^{18} m^{-3} respectively at 1150°C and 4.7×10^{5} and 2.5×10^{4} m^{-3} respectively at 400°C. The diffusion coefficients for Al and O ions are 2.2×10^{-18} and 5.0×10^{-26} m^2s^{-1} respectively at 1150°C and 1.0×10^{-25} and 5.6×10^{-33} m^2s^{-1} respectively at 400°C [Chiang, Birnie and Kingery, 1997]. With the above data, the ionic conductivity for Al and O are 1.6×10^{-17} and 9.1×10^{-21} $\Omega^{-1}m^{-1}$ respectively at 1150°C and 1.2×10^{-34} and 1.7×10^{-44} $\Omega^{-1}m^{-1}$ respectively at 400°C. The overall conductivity (combined electronic and ionic conductivity) of α-Al_2O_3 is about 10^{-5} $\Omega^{-1}m^{-1}$ at 1150°C and 10^{-10} $\Omega^{-1}m^{-1}$ at 400°C [Samsonov, 1973]. Clearly, the electronic conductivity is very

dominant in the electrical conduction of α-Al_2O_3 and therefore its growth rate is controlled by the diffusion of reactive elements.

In the light of all the preceding information, it may be said that the scale growth is controlled by diffusion of reactive elements (Al, Cr, Ni and Co) in the α-Al_2O_3 layer during oxidation from 1 hours to 1000 hours and in the mixed oxide layer after 1000 hours. This is because the dark alumina layer almost disappears after 1000 hours ageing and the diffusion rates of Al, Cr, Ni and Co in α-Al_2O_3 are usually much lower than those in α-Cr_2O_3 [Chiang, Birnie and Kingery, 1997].

Song and Xiao [2001] demonstrated that the resistivity for electronic semiconductors like NiO decrease with increasing porosity because the hole/electron concentration increases. As a consequence, the fast decrease in resistivity during ageing from 10 hours to 1000 hours could correspond to the degradation process of α-Al_2O_3 to a mixture of α-Cr_2O_3 and the $(Ni,Co)(Cr,Al)_2O_4$ spinel. The slow decrease in resistivity after 1000 hours ageing could correspond to the degradation process of the mixed oxides. This may be because the resistivity is more sensitive to the porosity in the α-Al_2O_3 than in the α-Cr_2O_3/ $(Ni,Co)(Cr,Al)_2O_4$ spinel mixed oxides. The degradation of α-Al_2O_3 is more important because it leads to the scale becoming non-protective although the process is slow.

6.4.3. Implications

Although the Al depletion-based spallation was found to take place after a relatively short time oxidation, it should be noted that the oxidation temperature adopted in this work (1150°C) is much higher than the actual bond coat operating temperature (900 – 1000°C). Nevertheless, this does indicate the need for a sufficient Al content in the bond coat and the underlying alloy to compensate for Al consumption during oxidation. This is especially important for MCrAlY bond coats since there are sufficient quantities of Cr, Ni and Co in these coats to change the composition of the

thermally-grown oxide from α-Al_2O_3 to one of the other oxides after long-term service.

6.5. Summary

Impedance spectroscopy (IS) has been used to evaluate the degradation of thermal barrier coatings (TBCs) on a superalloy at 1150°C. The degradation of the thermally grown oxides (TGOs) at the metal/YSZ interface is responsible for the spallation of TBCs. Changes in the electrical properties of TGOs are related to those in their microstructure and microchemistry. The resistivity decreases with increasing oxidation time over the whole time range and the decreasing rate is much higher between 10 and 1000 hours than between 1000 and 2000 hours. This causes when the oxidation time is between 10 and 1000 hours, the resistance of TGOs to decrease with increasing oxidation time and then remain unchanged until 2000 hours although the scale thickness increases. During thermal cycling at 1150°C, the bond coat in the TBC system was oxidised to form an alumina layer and a mixed oxide layer between the top coat of the yittria stabilised zirconia (YSZ) and the bond coat of the MCrAlY alloy. The mixed oxide layer mainly consists of α-Cr_2O_3 and a $(Ni,Co)(Cr,Al)_2O_4$ spinel phase, which are formed above the α-alumina layer. The alumina layer gradually disappeared during the oxidation while the content of chromium in the mixed oxide increased with increasing oxidation time. Changes in the electrical properties of TGOs have been correlated with those in their microstructure and microchemistry. The degradation of TGOs from α-Al_2O_3 to a mixture of α-Cr_2O_3 and the $(Ni,Co)(Cr,Al)_2O_4$ spinel, and their microstructural and microchemical evolution are responsible for the changes in the electrical properties.

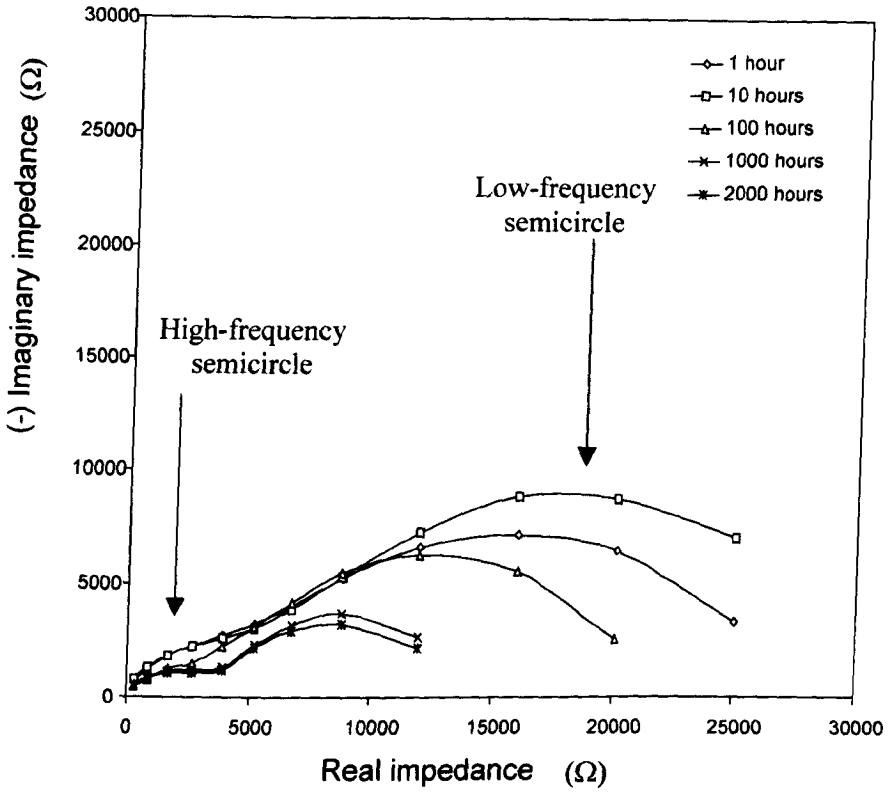

Figure 6-1: Typical Complex plots for the samples aged in air at 1150°C for different periods.

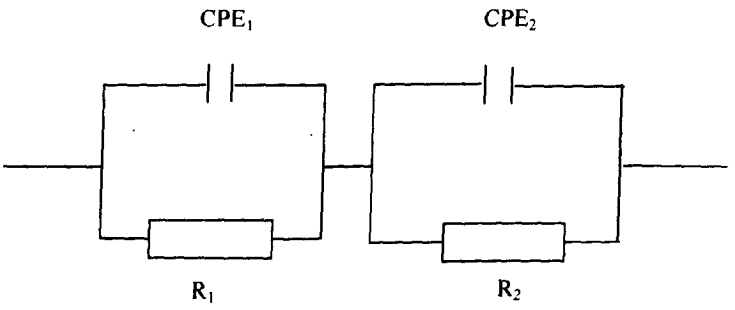

Figure 6-2: Equivalent circuit model for a TBC system.

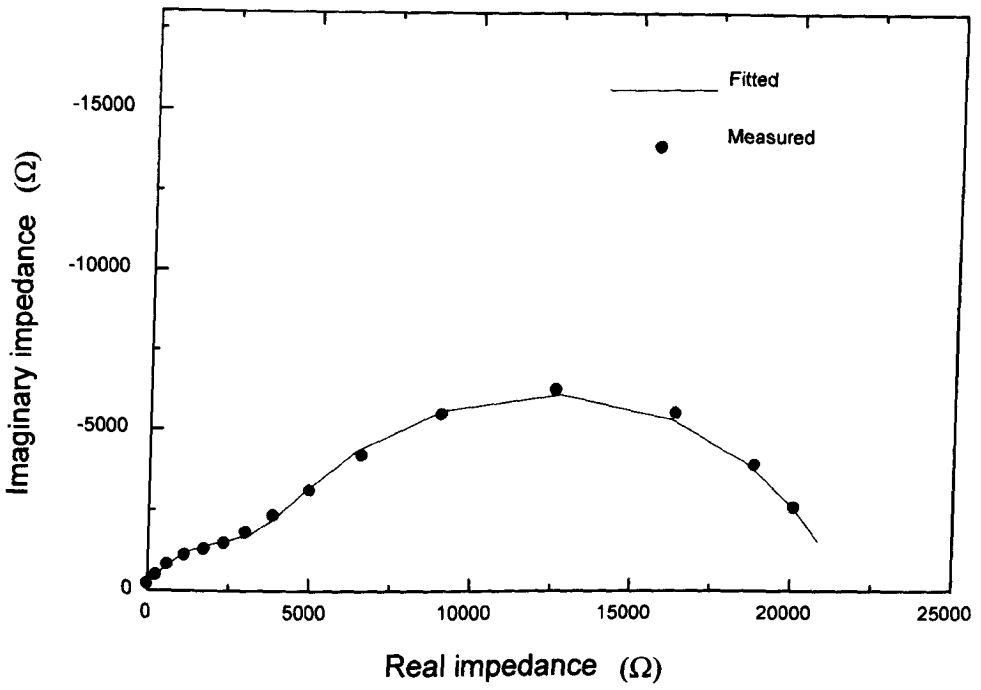

Figure 6-3: Fitted spectra based on the equivalent circuit model together with the measured results for sample aged in air at 1150°C for 100 hours.

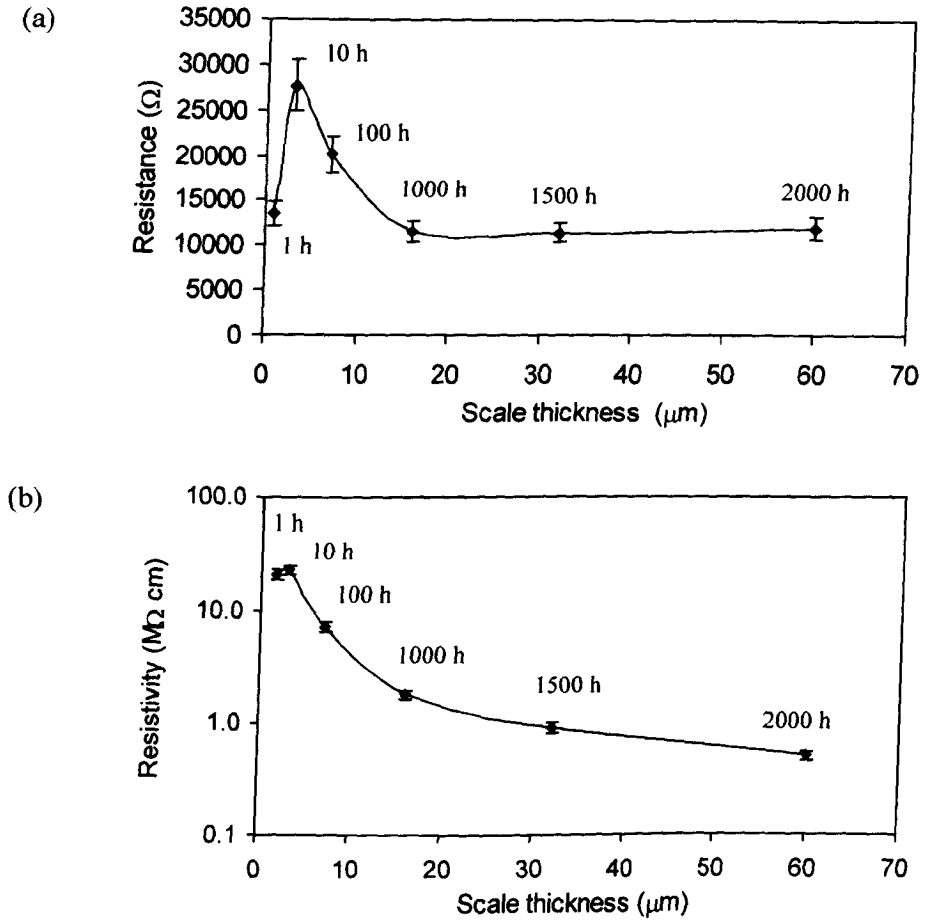

Figure 6-4. (a) Resistance vs. scale thickness and (b) resistivity vs. scale thickness for the TGO layer with the oxidation periods marked on each data point.

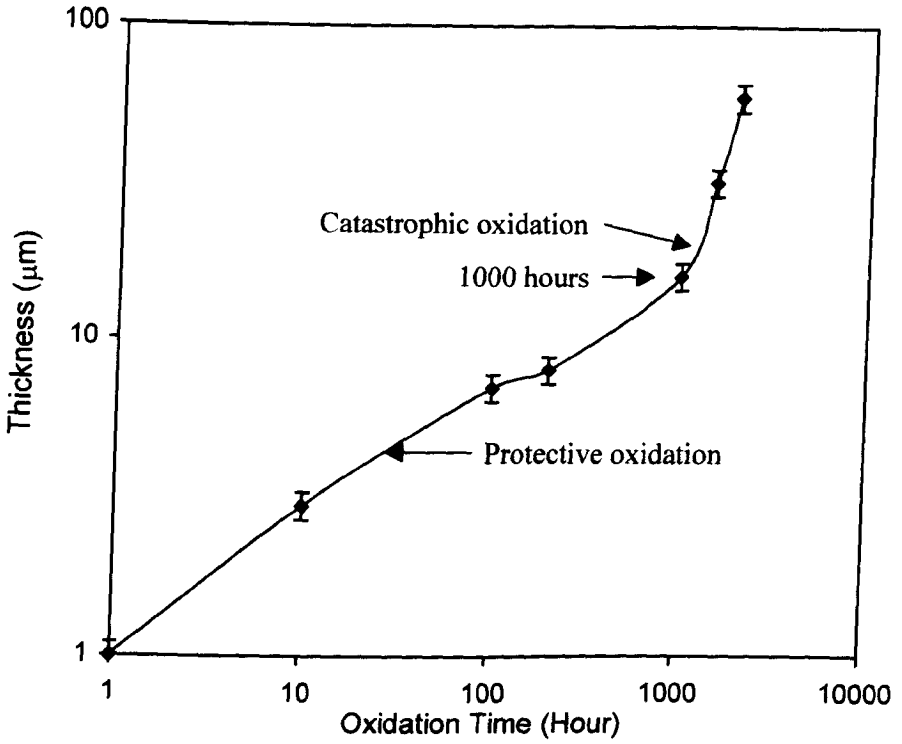

Figure 6-5. Variation of the oxide scale thickness with oxidation time for the TBC coated samples aged in air at 1150°C.

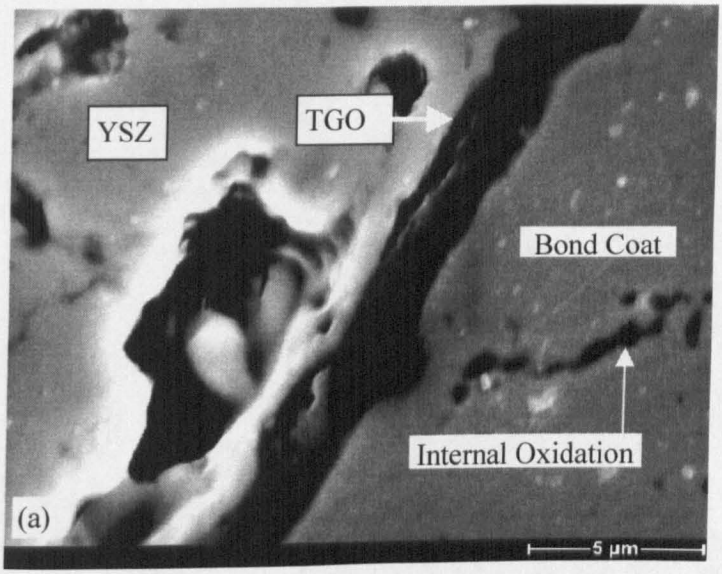
YSZ
TGO
Bond Coat
Internal Oxidation
(a)
5 µm

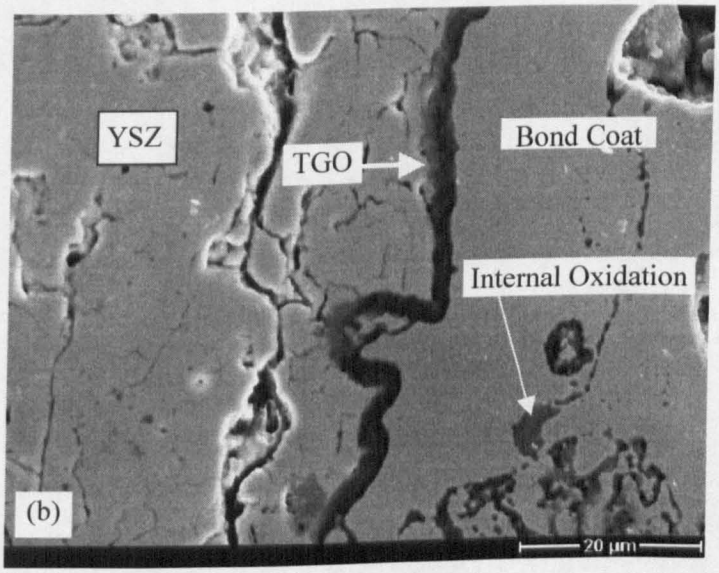
YSZ
TGO
Bond Coat
Internal Oxidation
(b)
20 µm

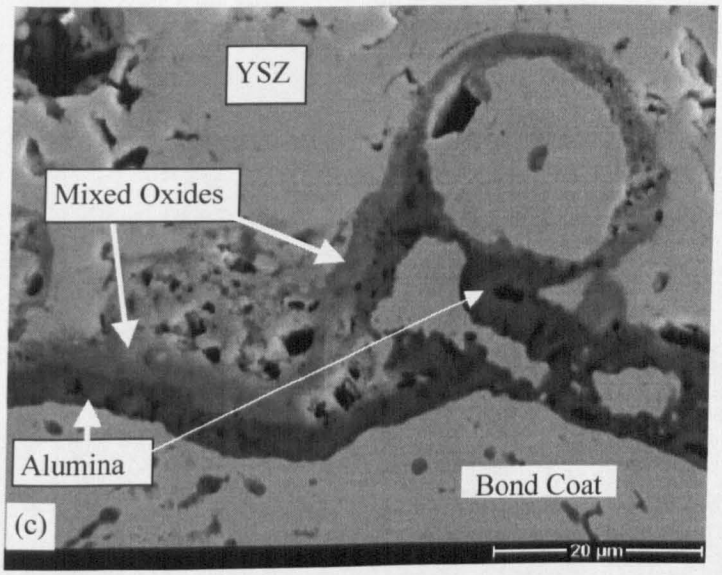
YSZ
Mixed Oxides
Alumina
Bond Coat
(c)
20 µm

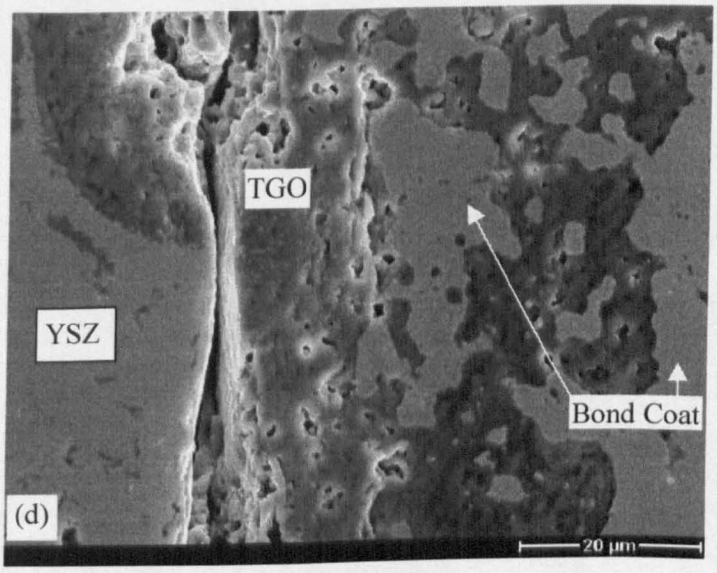
TGO
YSZ
Bond Coat
(d)
20 µm

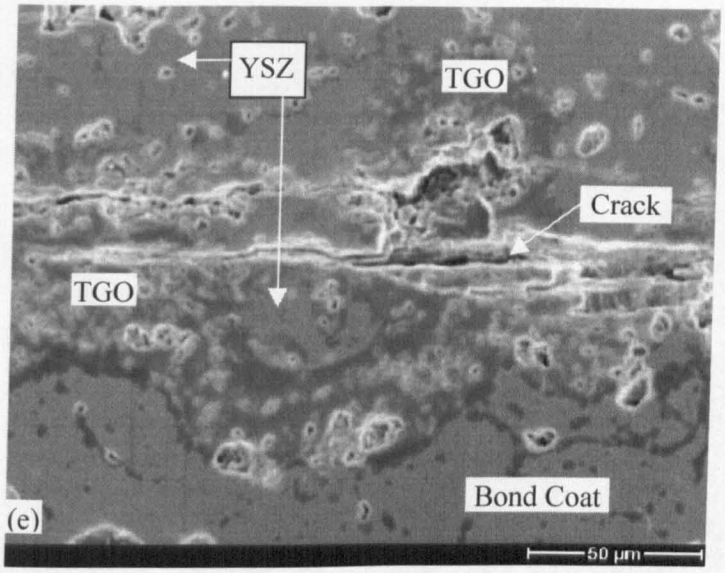

Figure 6-6. Scanning electron micrographs showing the cross sections of the samples aged in air at 1150°C for (a) 1 hour, (b) 10 hours, (c) 100 hours, (d) 1000 hours and (e) 2000 hours.

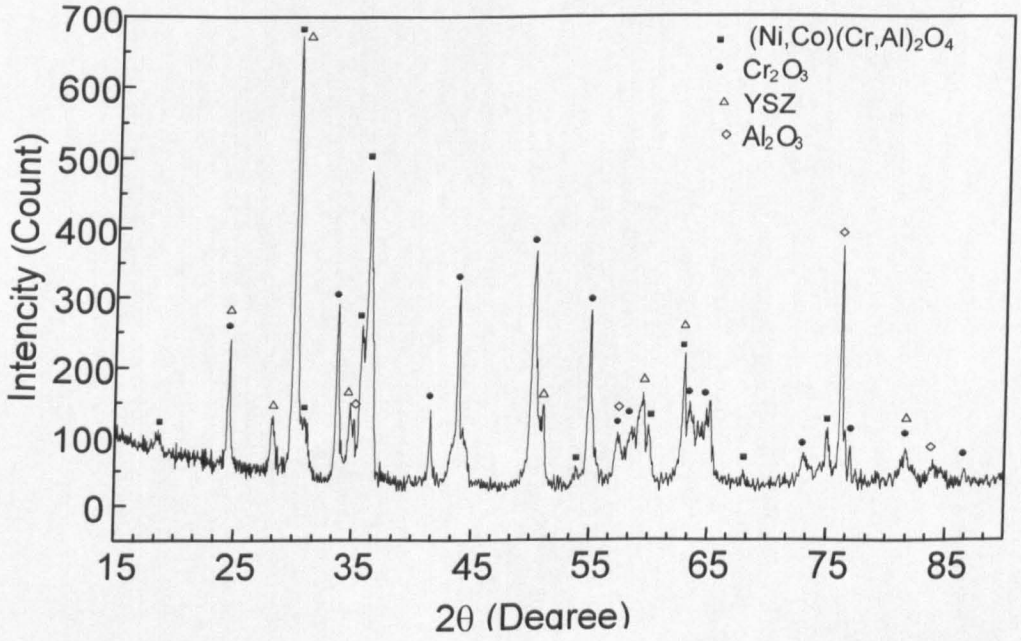

Figure 6-7. X-ray diffraction pattern for the exposed oxide scales attached to the bond coat for the samples aged in air at 1150°C for 2000 hours.

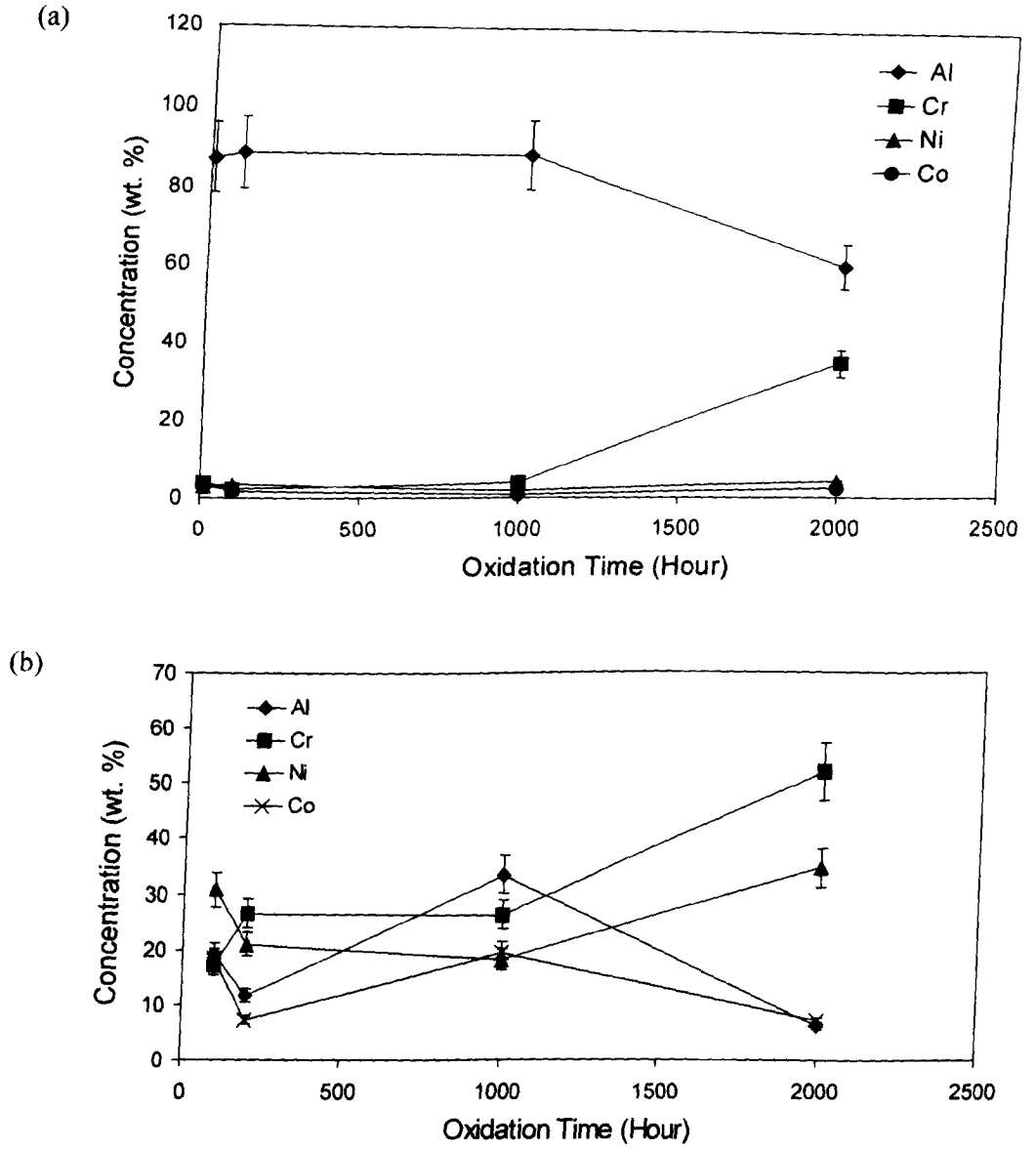

Figure 6-8. EDX microanalysis for (a) the dark oxide layer and (b) the grey oxide layer in the samples aged in air at 1150°C for different periods.

7. Non-Destructive Evaluation of Crack Formation in TBCs Using IS

7.1. Introduction

Non-destructive testing of the crack formation in a thermal barrier coating (TBC) system is essential for predicting the failure and lifetime of TBCs in service. Yttrium stabilised zirconia (YSZ) (6-8% Y_2O_3, balance ZrO_2) is normally used as a thermal insulator on gas turbine engine components and referred to as a thermal barrier coating (TBC). One of the most effective methods to develop oxidation resistance in alloys or coatings at high temperature is to form continuous scales of α-Al_2O_3 and Cr_2O_3 via selective oxidation [Birks et al., 1994], [Quadakkers and Bennett, 1994 and [Haynes et al., 1996]. However, the growth of these oxide scales build up stresses at the scale/metal interface due to volume changes during oxidation and the mismatch of the coefficients of thermal expansion (CTE) between the TBC, TGO and the substrate/bond coat during thermal cycling [He et al., 1998]. As the stresses increase, cracks initiate and propagate in the TGO/TBC interface, which leads to spallation of the TBC.

There are some non-destructive methods that can be used to study the crack formation. For example, the basic principle utilised in thermography is to apply heat to the test specimen and measure or observe the resulting temperature distribution, by using a video-thermographic camera [Curtis et al., 1993]. Flaws alter the temperature distribution on or in the samples. Surface-mounted thermal couples can also be used to detect the temperature distribution on the surface of a sample. In the radiography method, x-rays or gamma rays are used, and the thickness, density of and defects in the material determines the resultant radiation intensity from the sample. The radiation coming from the sample can generate shadows on photographic films and produce a radiograph to show the physical structure of the material [Nevadunsky and Lucas, 1975]. In the ultrasonic method, ultrasonic impulses generated by a piezoelectric transducer are used, the echo signal resulting from the reflection to the same piezoelectric device or another receiver detects

scattering from the object. The phase delay between the reflection from different surfaces is correlated to the material properties [Dunyak et al., 1992].

However, none of these are multilayer techniques and defects in the top coat may influence the results. Impedance spectroscopy (IS) is a multi-layer electrical technique, which gives information about the different layers in a single experiment. The propagation of cracks along the TGO/YSZ interface reduces the interfacial area, where the oxidation occurred. Changes in the TGO/YSZ interface may effect the electrical resistance of the interface. IS can be used to extract electrical parameters such as the electrical resistance of TBC/TGO interface. This chapter discusses the use of IS as a non-destructive tool for monitoring cracks in TBC systems.

7.2. Experimental Procedure

7.2.1. Thermal Ageing

The samples were subjected to thermal exposures in air for the range of temperatures and times indicated in table 7-1. Five samples for each oxidation time were prepared. It should be noted that the aim of the thermal cycling was to generate cracks in the TBCs, while the details of the thermal cycles are unimportant.

Table 7-1: Thermal ageing of the samples.

Materials	Exposure temperatures (°C)	Oxidation time (Hour)	Holding periods at exposure temperatures in the different thermal cycles (Hour)						
			Thermal cycle 1	Thermal cycle 2	Thermal cycle 3	Thermal cycle 4	Thermal cycle 5	Thermal cycle 6	Thermal cycle 7
TBC System	1150	10	10						
		100	100						
		200	100	100					
		1000	100	100	300	500			
		1500	100	100	300	500	500		
		2000	100	100	300	500	500	500	
	1200	5	5						
		10	5	5					
		50	5	5	40				
		100	5	5	40	50			
		200	5	5	40	50	100		
		317	5	5	40	50	100	117	83
		400	5	5	40	50	100	117	83
YSZ	1200	5	5						
		100	5	5	90				
		200	5	5	90	100			
Bond coat	1030	100	10	40	50				

7.2.2. Impedance Measurements

Three samples were chosen randomly from the five samples for impedance measurements. Since the experimental results showed that the electrode area has no effect on the impedance measurements, the silver or platinum conductive ink was painted on the TBC with an area of either 5mm × 5mm or 10mm × 10mm. A silver conductive ink was painted on the oxide formed on bond coat with an area of 5mm × 5mm. The paint acted as one electrode while the metal substrate acted as another electrode. For the YSZ layer without a metallic substrate, both sides were painted with silver paint. In this case the painted area was 10 mm × 10 mm.

Impedance measurements were carried out at 400°C with applied voltages of 10 mV and 100mv. The frequency range for impedance measurements was $5x10^{6}$ to 10^{-4} Hz. The applied voltage was 10mV for the TBC samples, thermally cycled up to 1150°C. The painted area for these samples were 5mm × 5mm. The applied voltage was 100mV for the TBC samples, thermally cycled up to 1200°C. The painted area for these samples were 10mm × 10mm. The applied voltage was 100mV for the YSZ samples and the applied voltage was 10mV for the bond coat samples.

7.3. Results

7.3.1. TBC Samples After Thermal Cycling

TBC samples after thermal cycling consist of the bond coat, a thermally grown oxide (TGO), some cracks and the top coat (YSZ) as shown in figure 7-1. Figure 7-2 shows SEM images of samples aged at 1150°C and figure 7-3 shows SEM images of samples aged at 1200°C. A two-layer structure in the oxide scales is clearly observed at both ageing temperatures. EDX analysis was carried out on the oxide scales to show the elemental compositions. Pure metals were used as standards in the ZAF corrections. In the dark oxide layer, the elemental composition is 85-95%wt. Al balanced with Cr, Co and Ni. In the dark layer, the Al content is ≈ 95%wt. near the bond coat and ≈ 85%wt. near the grey oxide. In the grey oxide layer, the elemental composition is 15-35%wt. Al balanced with Cr, Co and Ni. The Al content reduced in the grey oxide layer as the sample was aged for longer durations. The major element in the grey oxide region is Cr, which is between 30-60%wt. Cr balanced with Ni, Co and Al. As the EDX analysis uses a circular area of ~1 μm diameter of a sample, so the EDX analyses were performed in areas of the dark oxide where impurities from other layers would not interfere. These areas were a minimum of 1 μm away from the bond coat or grey oxide. Therefore, SEM and EDX analysis showed that the TGO contained two oxide layers. The first continuous layer (dark layer) alongside the bond coat is predominately alumina. The second grey layer on top of the dark layer is a mixed oxide layer. Both EDX and XRD analyses confirmed the presence of Al_2O_3, Cr_2O_3 and the mixed oxide containing Al, Co, Cr and Ni in the oxide scale (figure 7-4). Small islands of YSZ were observed inside the mixed oxides.

7.3.2. Impedance Results

Figure 7-5 shows the equivalent circuit model of the TBC after thermal cycling. Here the resistance of the metallic substrate and circuit wire were negligible in comparison with that of the TGO, TGO/YSZ interface, YSZ layer and YSZ/Ag or Pt

electrode interface. Figure 7-6 shows the impedance spectrum of the oxide layer formed after the oxidation of bond coat at 1030°C for 100 hours. One depressed semicircle was observed in the frequency range of 10^5-10^3 Hz while no semicircle was observed at lower frequencies down to 10^{-4}Hz where the electrode effect normally appeared [Steil et al., 1997]. It has been universally acknowledged that α-Cr_2O_3 and the $(Ni,Co)(Cr,Al)_2O_4$ spinel are both electronic semiconductors and their electronic conductivity is dominant in their electrical conduction [Kubaschewski and Hopkins, 1967] and [Chiang, Birnie and Kingery, 1997]. α-Al_2O_3 is normally regarded as an insulator, but it is also an electronic conductor at the impedance measurement temperature of this study [Ali et al., 2002]. Thus the silver electrode and the oxide are both electronic conductors and no electrical barrier appeared at the silver/oxide interface.

Figure 7-7 shows the impedance diagram (phase angle vs. frequency) of TBC samples, after they were thermally cycled up to 1150°C in air for 200 hours, using various electrode materials. The electrode materials used in this experiment were silver paste, platinum paste and platinum wire. The different electrode systems gave two peaks in the phase angle plots which appeared at frequencies higher than 10^3 Hz for each electrode material are very similar. This indicates that the peak angles at frequencies of 10^3-10^4 Hz and around 10^6 Hz correspond to the TGO and top coat YSZ, respectively, which is in agreement with previous studies [Ogawa et al., 1999] and [Wang et al., 2001]. However, with the use of different electrode systems for the same sample, a third phase angle in a range of 10^2Hz-10^{-4}Hz appeared at different frequencies. Therefore, these peak phase angles can be identified as the electrode response. Similar phenomena were found in a previous study [Steil et al., 1997]. The electrode response here should include the electrode effect at the Ag/YSZ interface and the interface impedance at the TGO/YSZ interface. The electrode effect and the interface impedance were further examined by using different applied voltages in the impedance measurements of TBCs.

Figure 7-8 shows complex plots of TBC samples with applied voltages from 10 mV to 500 mV. The first two semicircles from the left correspond to YSZ and TGO and

are very similar with different applied voltages. However, the third semicircle from the left which corresponds to the electrode effect and interface impedance shows a considerable change in spectrum, where an almost linear plot at a low applied voltage gradually changed into another semicircle with increasing applied voltage. This indicates that both the Ag/YSZ and/or TGO/YSZ interface behaved as a blocking interface at a lower applied voltage, whereas the interfaces acted as a non-blocking interface at a higher applied voltage. The blocking interfaces behaved like double layer capacitors whereas the non-blocking interface behaved like a double layer capacitor in parallel with a charge transfer resistor.

Figure 7-9 shows the capacitance at the electrode/YSZ and TGO/YSZ interfaces as a function of the thermal cycling time. Apart from the initial change of the capacitance at the beginning of thermal cycling, the capacitance showed little change during thermal cycling. Figure 7-10 shows the impedance spectra of TBC samples measured at 400°C after thermal cycling at 1150°C. The low frequency semicircle increased with increased ageing time. Figure 7-11 shows the impedance spectra of TBC samples measured at 400°C after thermal cycling at 1200°C, where the low frequency semicircle (third from left) increased with increased ageing time. Similar phenomena in the low frequency semicircle were found in both figure 7-10 and figure 7-11. Again, the semicircle corresponding to the TGO (second from left) increased with the increase of the thermal cycling time (figure 7-11). This suggests that the TGO grew during the thermal cycling, leading to an increase in the resistance of the TGO [Ogawa et al., 1999]. Growth of a TGO can cause stress in the TGO layer, which will increase with thermal cycling due to a difference in the coefficients of thermal expansion (CTE) between the YSZ and TGO and the substrate/bond coat. As these stresses increase, cracks initiate and propagate at the TGO/TBC interface [He et al., 1998]. These cracks might be the reason for the increased size of the low frequency semicircle with increased duration of the thermal cycles.

Figure 7-12 shows the impedance spectra of the YSZ after thermal cycling at 1200°C for 5 hours, 100 hours and 200 hours. This figure shows only a slight change in the

impedance spectra from the YSZ due to ageing. The silver painted area for each sample is not exactly the same for each sample, there could have been 5-10% variation in electrode area, and so, this slight change in impedance spectra from the YSZ samples could be a result of variations in sample preparation.

Figure 7-13 shows the impedance spectra of both the TBC and YSZ before thermal cycling. The difference between these two spectra indicates that the bond coat/YSZ interface impedance in the TBC is much higher than that at the Ag/YSZ interface, which appeared in the impedance measurements of both TBC and YSZ. There is no significant change in the electrode effect at the Ag/YSZ interface at lower frequencies than 10^{-2} Hz after thermal cycling of the YSZ (figure 7-12). Figure 7-14 shows the impedance spectra of both TBC and YSZ samples after thermal cycling at 1200°C for 317 hrs. The impedance of the YSZ sample is much smaller than that of the TBC sample, showing two semicircles corresponding to the TGO and the electrode/interface. As the YSZ/Ag interface induced much smaller impedance in the measurements of the spalled YSZ top coat, the large semicircle in the impedance spectra of the TBC should mainly correspond to the TGO/YSZ interface. The possible change of the Ag/YSZ interface due to thermal cycling was very limited compared to the change in the TGO/YSZ interface impedance due to the TGO growth. Thus changes in the semicircle responsible for the TGO/YSZ interface with thermal ageing can be used to monitor the interfacial degradation. Figure 7-15 shows that the interfacial resistance increased with an increase in the thermal cycling time. The relaxation frequency for the TGO/YSZ interface shows a gradual decrease as the thermal cycling time increased (figure 7-16). Figure 7-17 shows the microstructures of the TBC samples (sample 1 and sample 3), which were exposed to the same thermal cycling condition.

7.4. Discussion

There were three interfaces between the layers, substrate/bond coat interface, bond coat/TGO interface and TGO/YSZ interface. YSZ is an ionic conductor whilst Ag, Pt and the TGO are electronic conductors [Ali et al., 2002], [Kubaschewski and Hopkins, 1967], [Chiang, Birnie and Kingery, 1997], [Lide, 1998] and [Schutze, 1997]. The electrochemical cells of the TBCs can be described as:

Pt or Ag, O_2 | YSZ | TGO, O_2

where both metals and TGO acted as electrodes while YSZ acted as electrolyte. The electrode reaction at both electrodes is:

$$O_{2(g)} + 4e^- = 2O^{2-} \text{ (YSZ)} \qquad (7\text{-}1)$$

The impedance corresponding to the reaction at the metal/YSZ interface is called the electrode effect. Here, we define the impedance corresponding to the reaction at the TGO/YSZ interface as the interface impedance.

7.4.1 Electrode and TGO/YSZ Interface Impedance

Figure 7-9 shows that apart from the initial changes of the capacitance (capacitance at the electrode/YSZ and TGO/YSZ interfaces) at the beginning of thermal cycling, there are little changes during further thermal cycling. This indicates that the microstructural and compositional change in the TGO during thermal cycling did not have a significant effect on the double layer capacitance. On the other hand, the double layer capacitance is much larger (~mF) than that of the TGO (~μF) and the YSZ (~nF). The double layer capacitance can be calculated according to:

$$C_{dl} = \frac{\varepsilon_0 \varepsilon A}{d} \qquad (7\text{-}2)$$

where d is the thickness of the double layer, A is the interface area and $\varepsilon_0 = 8.85 \times 10^{-12}$ Fm^{-1}. As $A = 10^{-4}$ m^2, $C_{dl} = 0.002$ F and it is assumed that $\varepsilon = 2$. Then according to equation 7-2, 'd' is calculated as 2×10^{-11} m, which is close to the diameter of ions. This calculation further confirms that the third semicircle corresponds to the electrode and interface effect, which is in agreement with previous studies [Brant and Dessemond, 2000] and [Bieberle and Gauckler, 2000].

7.4.2. Relationship Between Interface Impedance and Horizontal Cracks

Figure 7-10 shows that the semicircles corresponding to the YSZ and TGO are too small to be shown clearly since the semicircle corresponding to the electrode/interface effect is much larger than that of the YSZ and TGO. It should be noted that it is impossible to distinguish the effect of the electrode and that of the TGO/YSZ interface using the Ag electrode. However, it is clearly seen that the electrical behaviour of the electrode/interface changed from a nearly non-blocking interface to a blocking interface as the thermal cycling time increased. In another words, the electrical resistance of the interfaces increased as thermal cycling was carried out.

Thermal cycling of TBCs at 1150°C and 1200°C induced the growth of the TGO and therefore, led to the formation of cracks. The cracks propagated along the direction of the TGO/YSZ interface at positions close to the interface (figures 7-2 and 7-3). In the TBC after thermal cycling at 1150°C, no crack was found in the sample after 10 hours thermal cycling. Cracks initiated in the 200 hours thermally cycled sample while large cracks appeared in the 1000 hours thermally cycled sample (figure 7-2). The impedance of the interface increased with an increase in the thermal cycling time (figure 7-10). A similar behaviour was found in the impedance measurements of TBC samples after thermal cycling at 1200°C (figure 7-11), where the interfacial resistance increased with an increase in the thermal cycling time (figure 7-15). It is clearly seen that crack propagation led to an increase in the interfacial resistance where the crack propagation along the TGO/YSZ interface reduced the area of the interface and increased the blocking factor for the interfacial reaction.

The measurements of relaxation frequency for the TGO/YSZ interface shows a gradual decrease as the thermal cycling time increased (figure 7-16). The relaxation frequency can be related to resistance according to the following equation:

$$f_{max} = \frac{1}{2\pi RC} \qquad (7\text{-}3)$$

where f_{max} is relaxation frequency for the low frequency semicircle, $\pi = 3.14$, 'R' is the interfacial resistance and 'C' is the double layer capacitance at the interface, which is only slightly changed due to thermal cycling (figure 7-9). Therefore, crack propagation in the TBCs also induced a decrease in the relaxation frequency corresponding to the TGO/YSZ interface.

The resistance of the TGO/YSZ interface was obtained from the impedance measurements of three samples for each thermal cycling condition. The 100 hours thermally cycled samples show a significant difference in the interfacial resistance, which suggests that the microstructure of the interface is very different in each sample even when the thermal cycling condition is the same. Figure 7-17 shows the microstructures of the TBC samples with interfacial resistances of 3.8×10^4 Ω (sample 3) and 1.2×10^4 Ω (sample 1), which were exposed to the same thermal cycling condition. The sample with the higher resistance has a crack almost through the sample partly due to the damage caused during the cutting of the sample exhibits but mainly due to thermal cycling, whereas the sample with a lower resistance exhibits much less severe cracking. This further confirms that crack propagation causes the increase in the resistance of the TGO/YSZ interface.

7.5. Summary

Impedance measurements have been used to examine the degradation of TBC systems after thermal cycling at 1150°C and 1200°C. Three semicircles were found in the impedance spectra of the TBC samples, which correspond to the YSZ top coat, the TGO layer from oxidation, and the TGO/YSZ interface. The interfacial resistance and capacitance were induced due to the formation of a double layer and charge transfer at the TGO/YSZ interface. The microstructural examination of the TBC samples shows that cracks initiated and propagated during the thermal cycling, while the impedance measurements shows that the interfacial resistance increased with an increase in the thermal cycling time. Even for the samples thermally cycled for the same period, the interfacial resistance was also related to the length of cracks at the TGO/YSZ interface. The relaxation frequency corresponding to the TGO/YSZ interface also shows a gradual decrease due to thermal cycling. It is believed that crack propagation caused the decrease in the area of the TGO/YSZ interface and therefore increased the interfacial resistance. From this study, it was concluded that IS could be used as a non-destructive testing tool to determine crack propagation in TBCs.

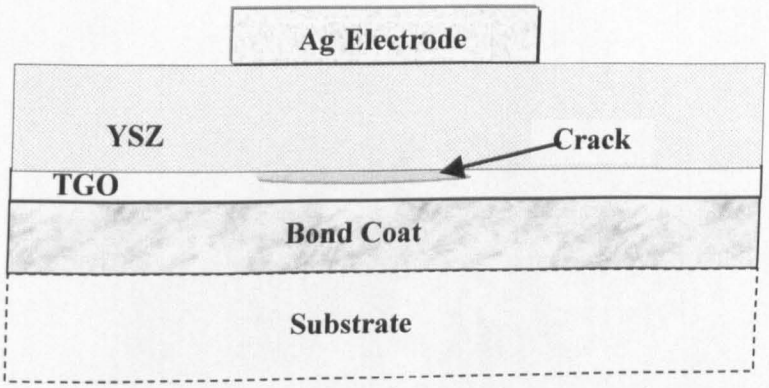

Figure 7-1: Schematic draw of TBC after thermal cycling.

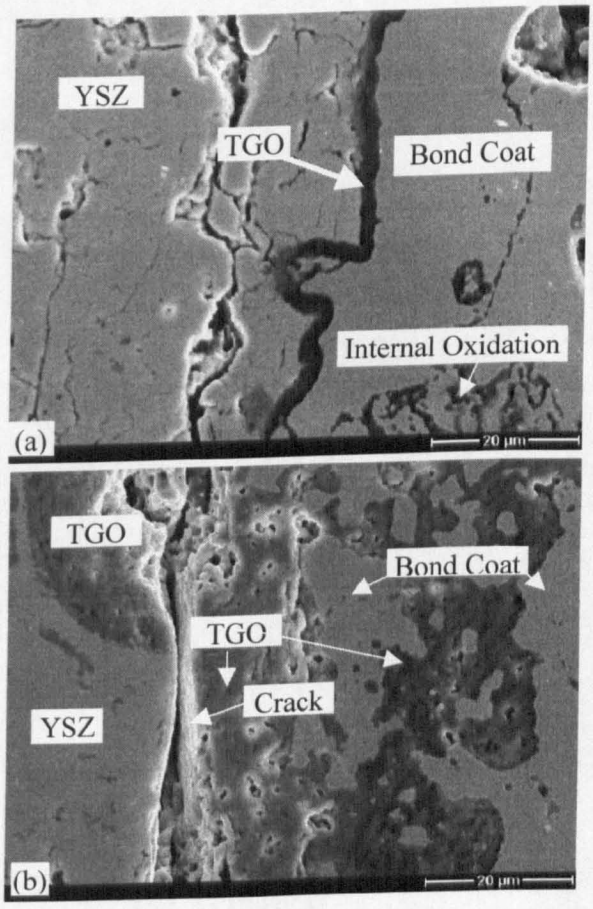

Figure 7-2: Scanning electron micrographs showing the cross sections of the samples aged at 1150°C in air for (a) 10 hours and (b) 1000 hours.

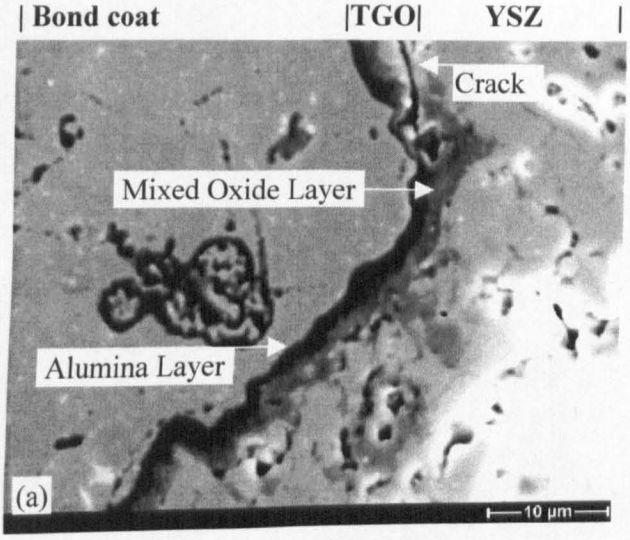
| Bond coat
|TGO|
YSZ
|
Crack
Mixed Oxide Layer
Alumina Layer
(a)
10 µm

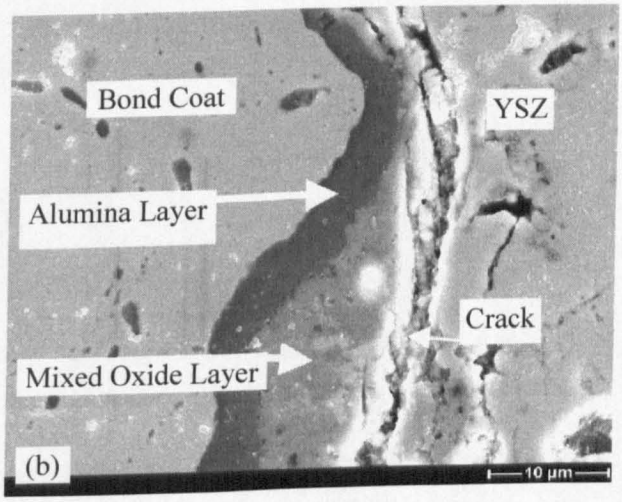
Bond Coat
YSZ
Alumina Layer
Crack
Mixed Oxide Layer
(b)
10 µm

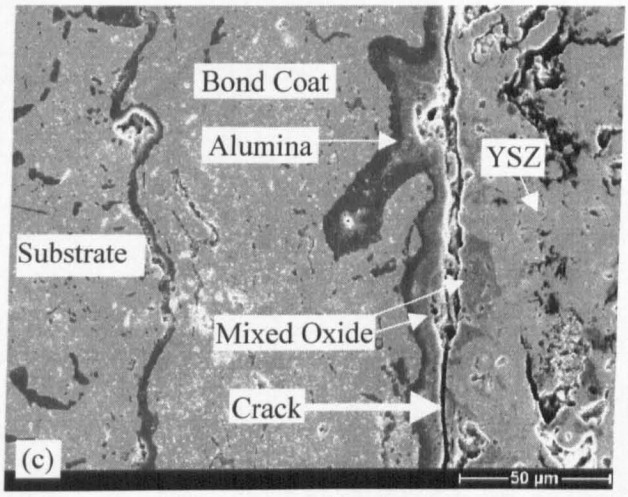

Figure 7-3: SEM images of TBC samples aged at 1200°C in air for different periods; (a) 5 hours, (b) 200 hours and (c) 400 hours.

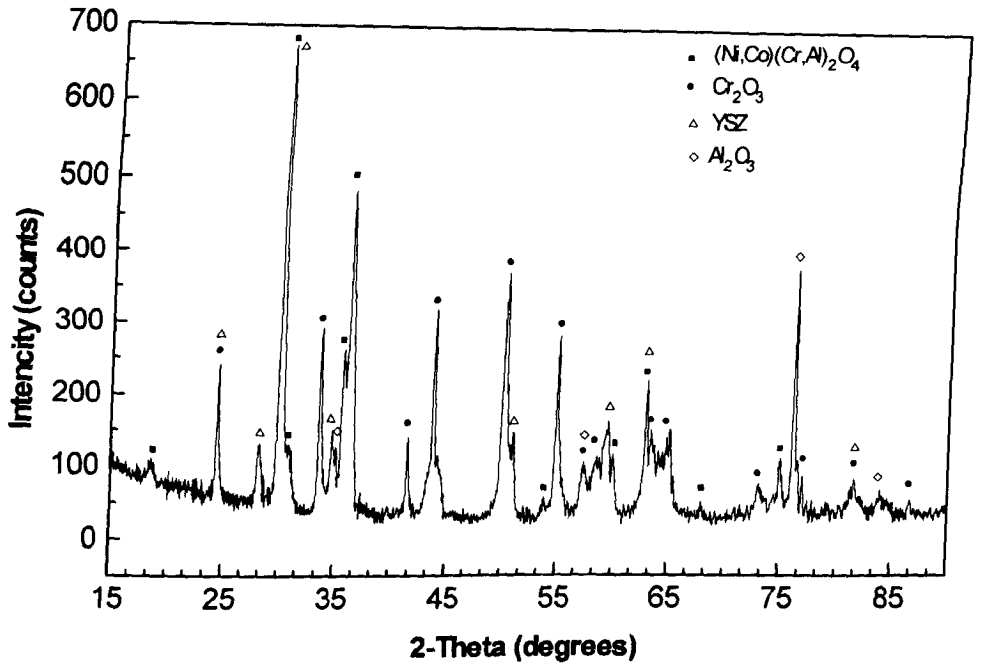

Figure 7-4: X-ray diffraction pattern of the oxide scales from the oxidation of the bond coat at 1150°C in air for 2000 hours.

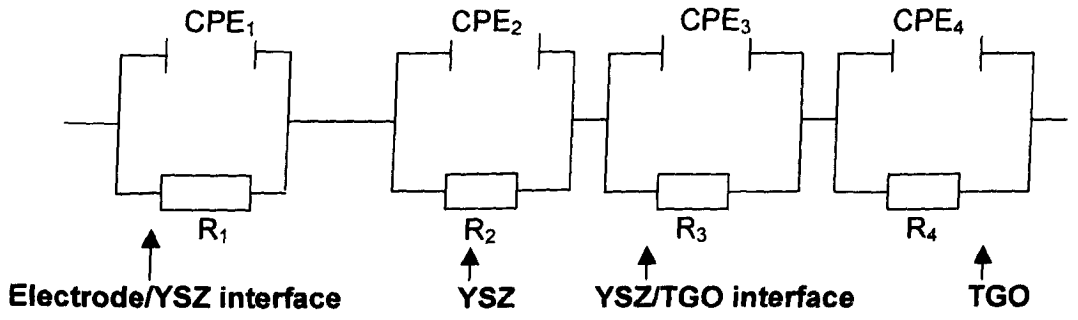

Figure 7-5: Equivalent circuit model for aged TBC sample.

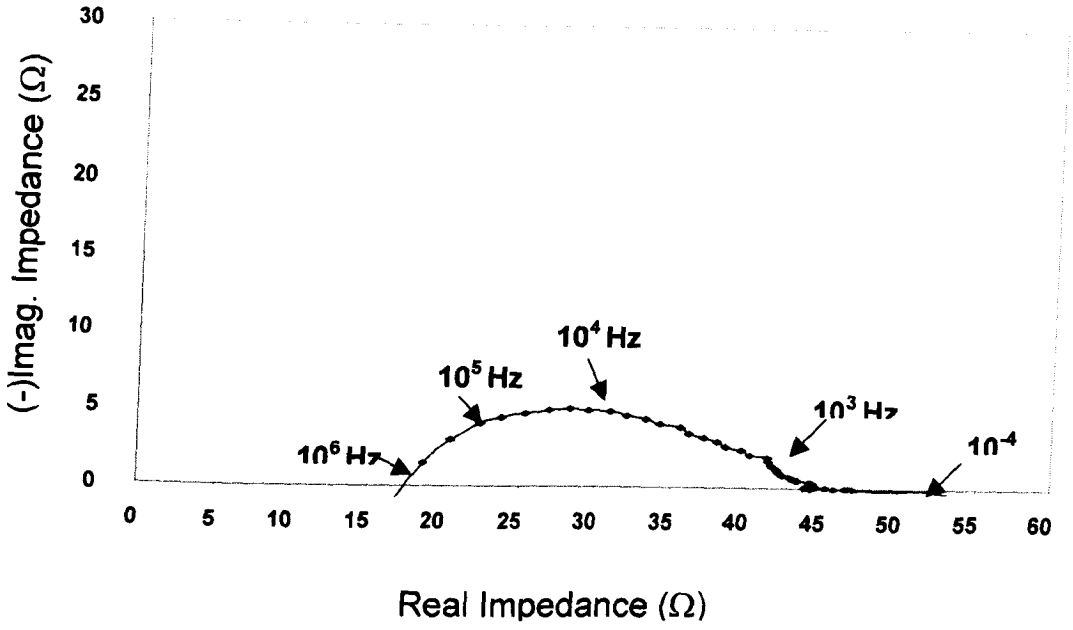

Figure 7-6: Complex plot of the bond coat aged at 1030°C in air for 100 hours.

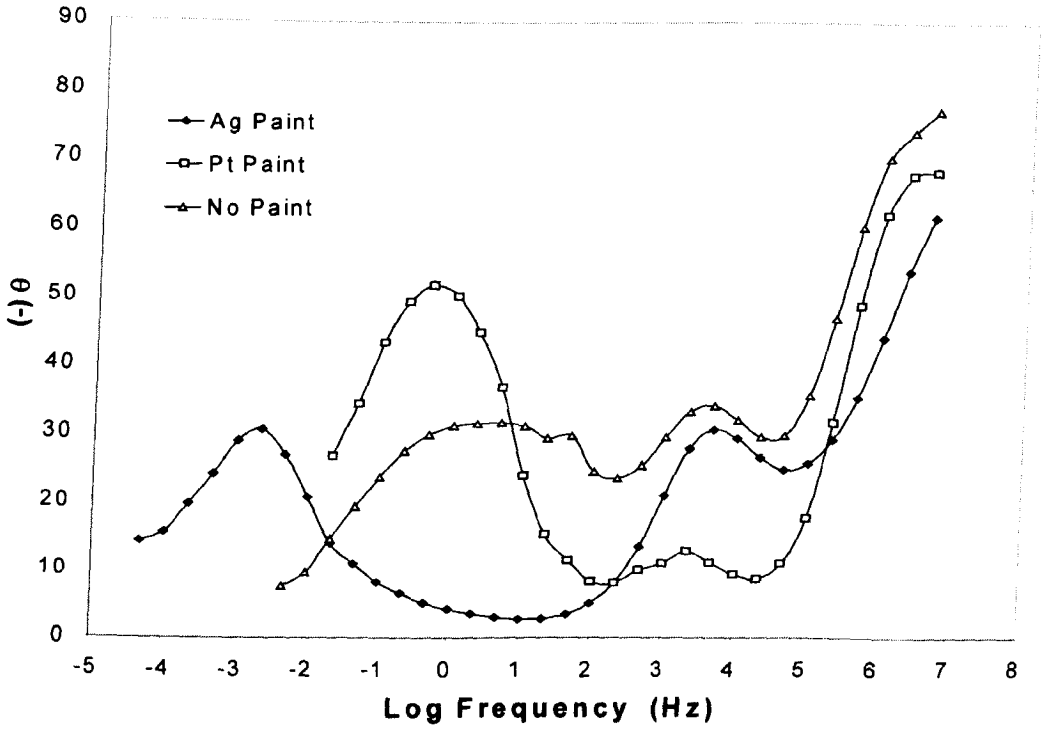

Figure 7-7: Phase angle vs. frequency from impedance measurements of TBC thermal cycled up to 1150°C in air for 200 hours.

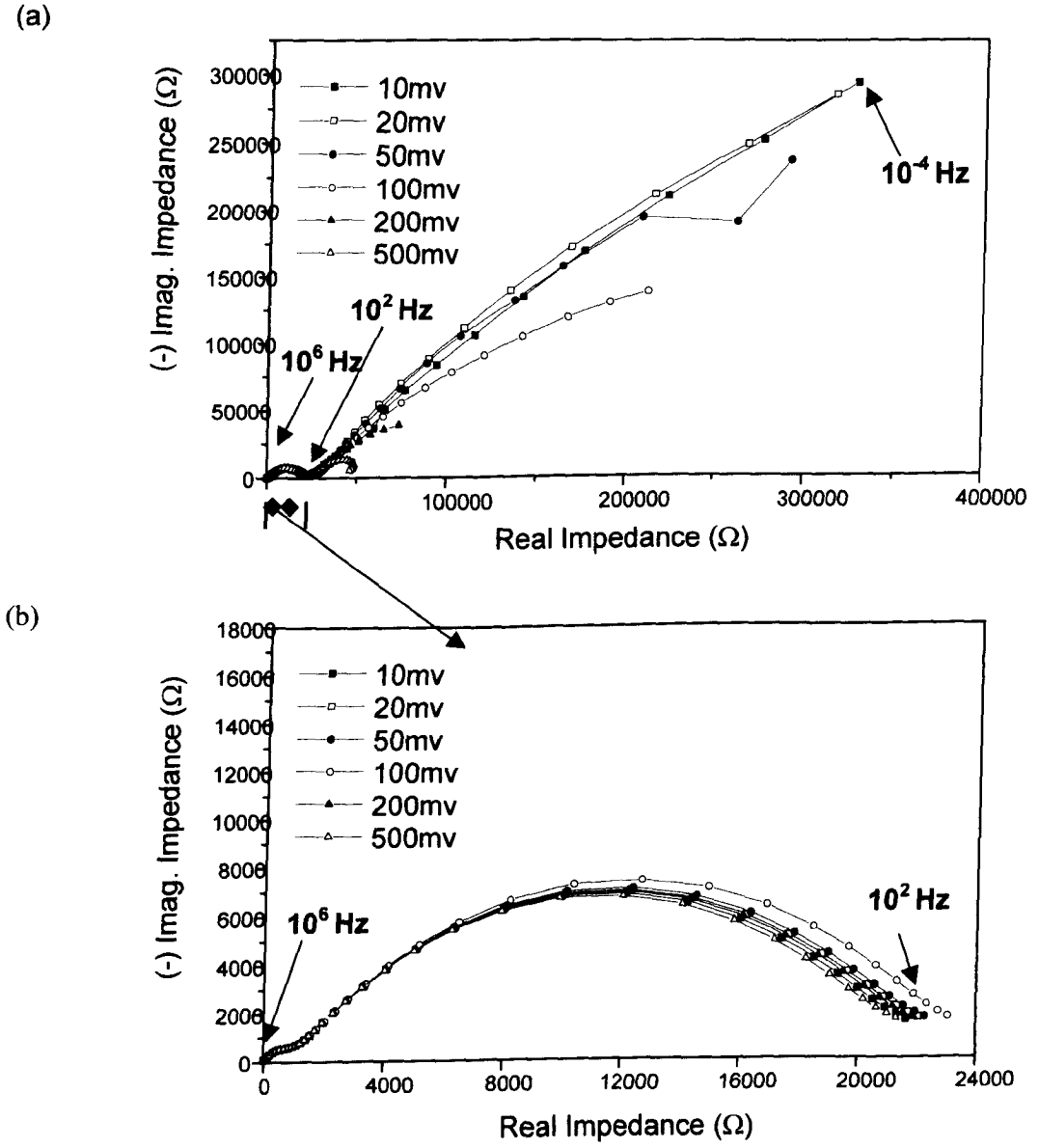

Figure 7-8: (a) Effect of applied voltage on the low frequency (3rd from left) semicircle in the Complex plots from impedance measurements of TBC samples thermally cycled up to 1200°C in air for 400 hours; (b) Effect of applied voltage on high (1st from left) and intermediate frequency (2nd from left) semicircle in the Complex plots from impedance measurements of TBCs thermally cycled up to 1200°C in air for 400 hours.

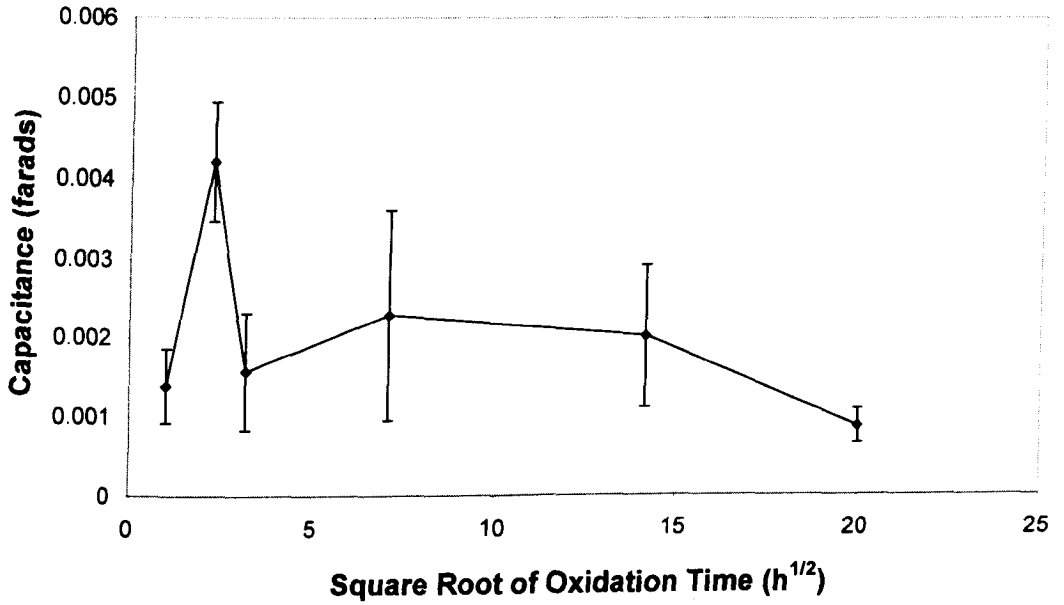

Figure 7-9: Interface capacitance vs. thermal cycling time from impedance measurements of TBC samples thermally cycled up to 1200°C in air.

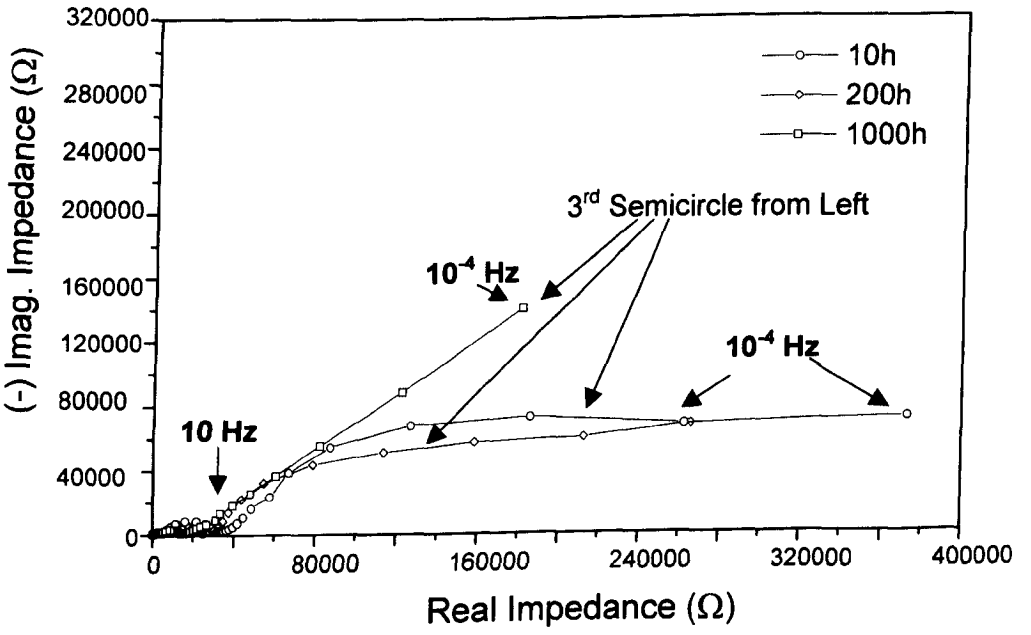

Figure 7-10: Complex plot from impedance measurements of TBC samples thermally cycled up to 1150°C in air.

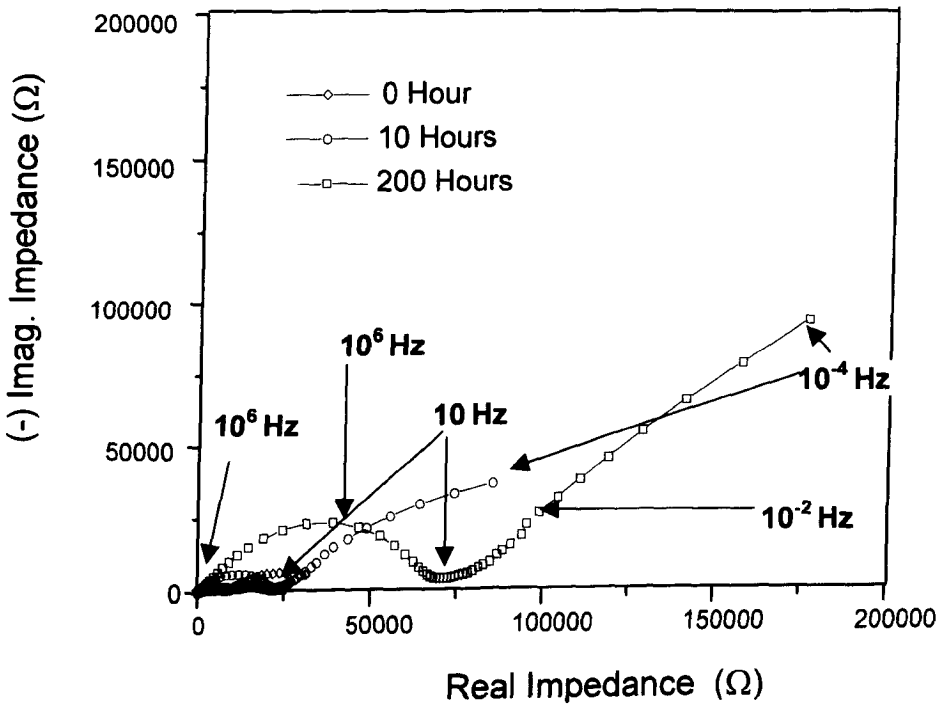

Figure 7-11: Complex plot from impedance measurements of TBC samples thermally cycled up to 1200°C in air.

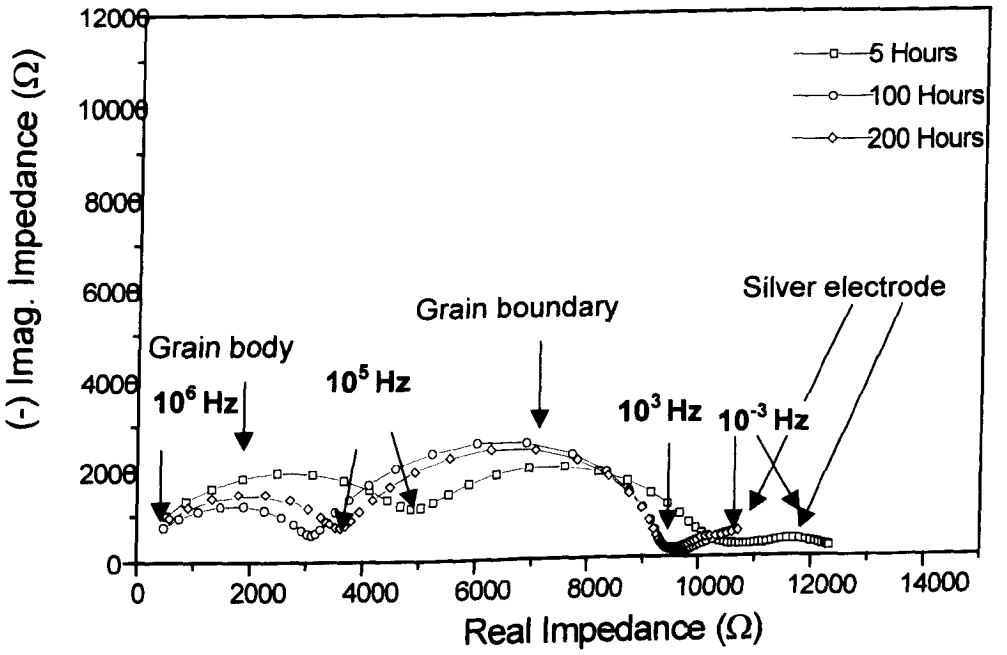

Figure 7-12: Complex plot from the measurements of YSZ thermally cycled up to 1200°C.

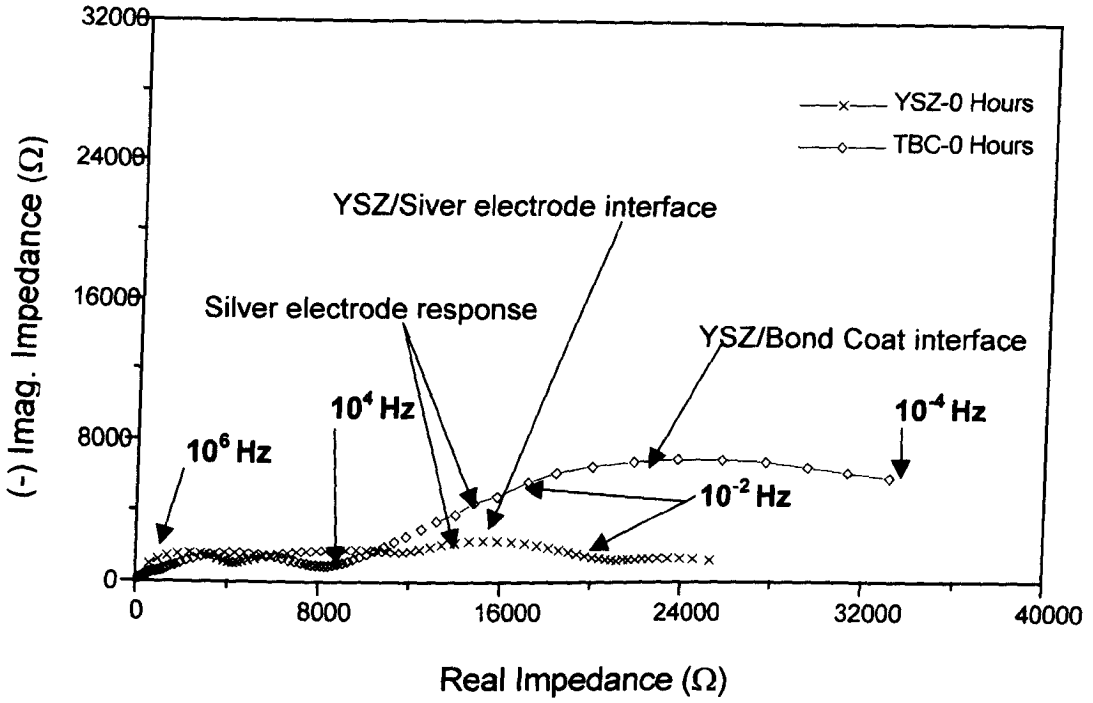

Figure 7-13: Complex plots from the measurements of the as-received YSZ and TBC samples.

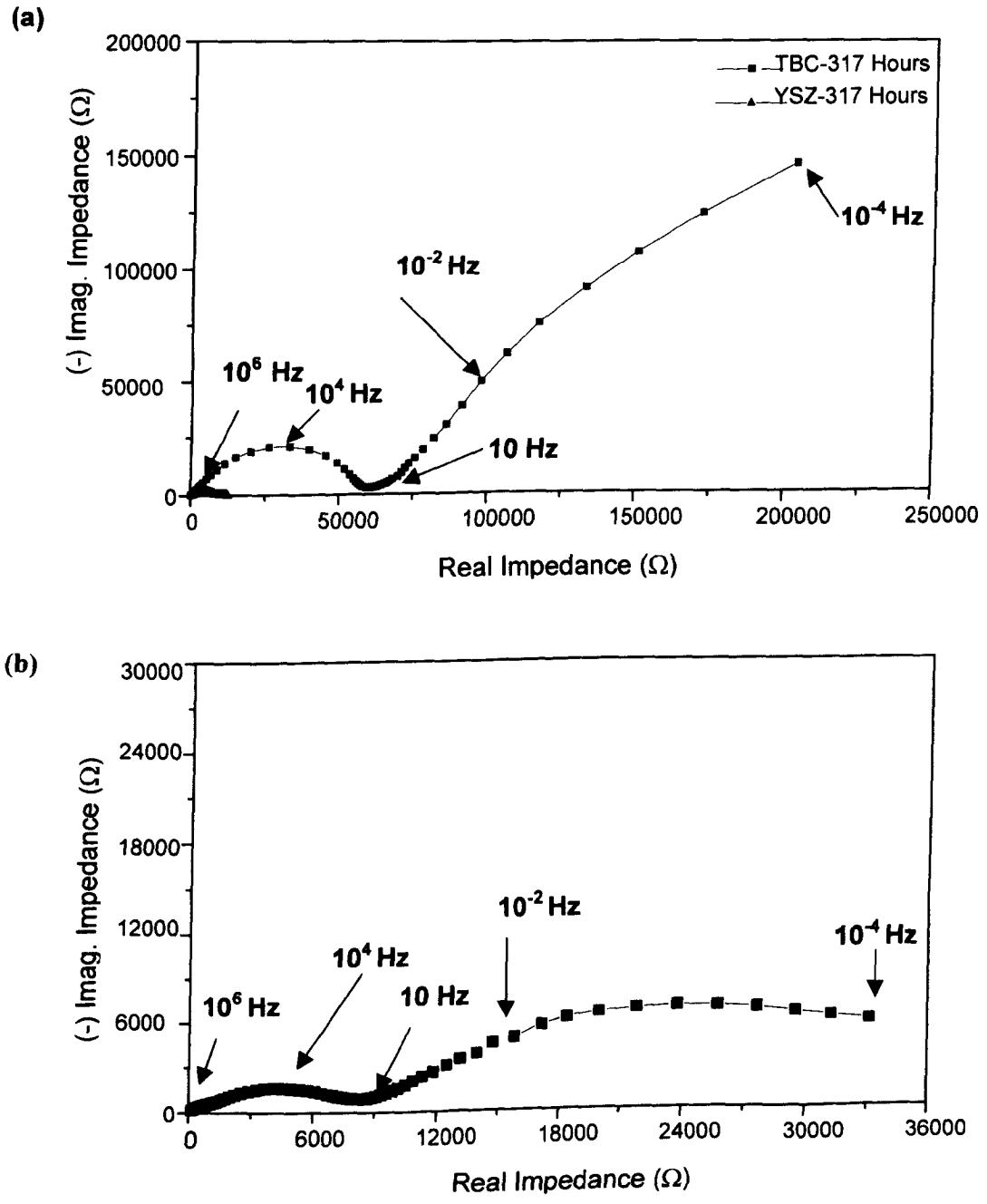

Figure 7-14: Complex plots (a) a TBC sample thermally cycled to 1200°C for 317 hours and a spalled YSZ top coat of a TBC sample thermally cycled to 1200°C for 317 hours; (b) a YSZ top coat of a TBC sample thermally cycled to 1200°C for 317 hours.

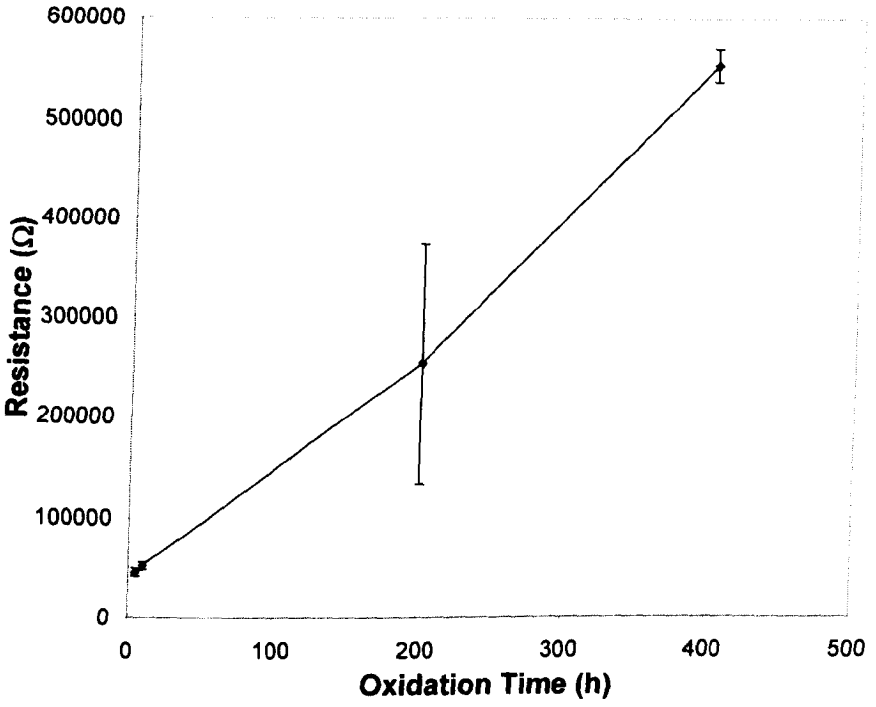

Figure 7-15: Interface resistance vs. oxidation time for the TBC thermally cycled up to 1200°C.

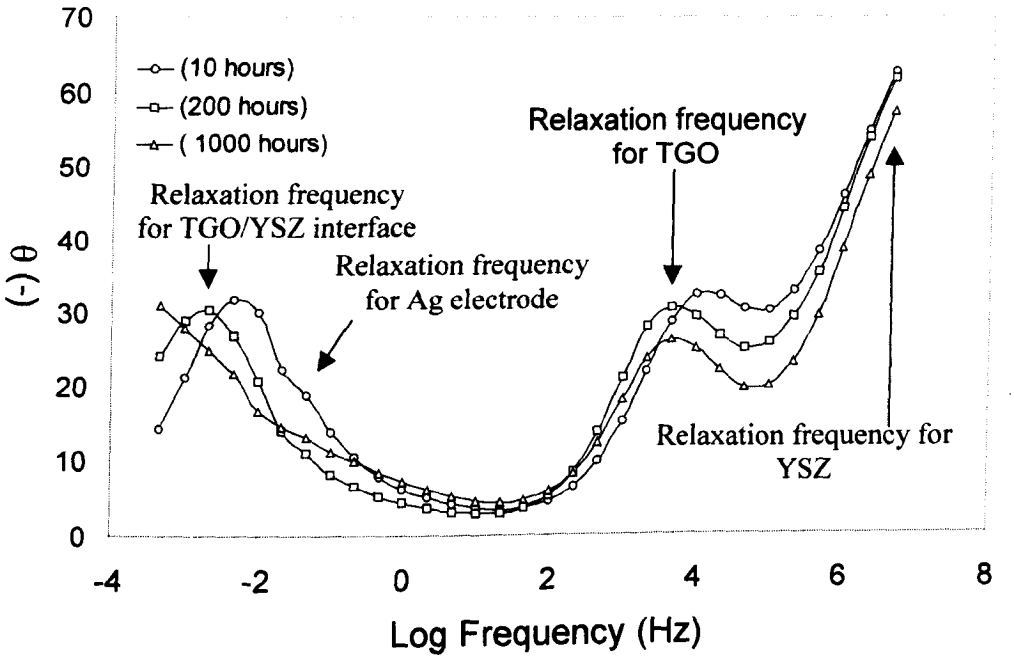

Figure 7-16: Phase angle vs. frequency from measurements of TBC samples thermally cycled up to 1150°C in air for 10 hour to 1000 hours.

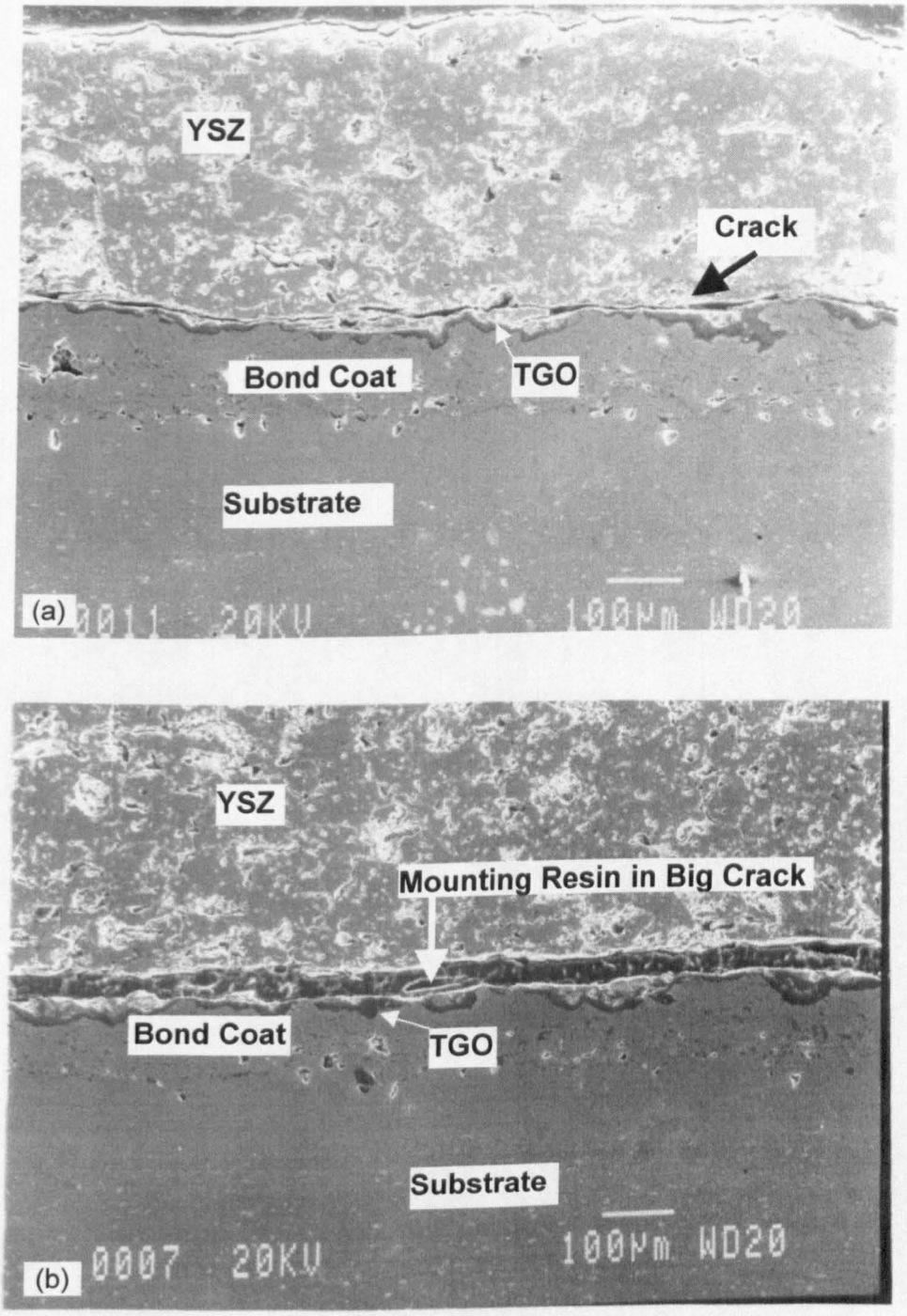

Figure 7-17: SEM photos of TBC samples thermally cycled up to 1200°C in air for 200 hours; (a) sample 1, (b) sample 3.

8. Summary and Suggestions for Future Work

8.1. Summary

Impedance spectroscopy (IS) has been successfully used to characterise thermally-grown oxides (TGOs) formed on nickel-based superalloy substrates and a NiCrCoAlY bond coat, and in the bond coat/yttrium stabilised zirconia (YSZ) interface of thermal barrier coating (TBC) systems. Impedance analysis gives the values of the resistance, capacitance, depression angle, and also relaxation frequencies. The microstructure of samples was examined using scanning electron microscopy coupled with energy despersive X-ray spectroscopy and an X-ray diffraction technique. All these physical methods are destructive methods, but they provided a clear picture of the samples after thermal ageing. The results obtained from impedance measurements were compared to the observations and the analyses obtained using these destructive techniques, which gave a very clear understanding about the impedance response of sample microstructures.

Electrical parameters were obtained from fitting the results of measured impedance diagrams using an equivalent circuit model based on the physical condition of samples. A relationship exists between the electrical parameters and the complex composition of oxides, formed at high temperature in air on alumina-forming nickel-based superalloy and bond coat samples without a YSZ top coat. Electrical resistance can give information about the protectiveness of the oxide layer. Capacitance can give information about the oxide layer thickness. Sudden resistance changes indicate defects in the oxide layer. Defects can be of any type, such as pores, cracks, compositional changes and microstructural changes. Sudden resistance changes give information about the defects caused by compositional or microstructural changes. If the resistance changes suddenly but capacitance does not, then the defects are physical in nature. Resistance was found to increase with the increase of oxide layer thickness. A sudden drop of resistance could happen if cracks were initiated in oxide scales. Silver paste could penetrate through these cracks and reduced the electrical resistance of the oxide scales.

The relaxation frequency was used to characterise the composition of the oxide layer formed on a nickel-based superalloy. The activation energy was used to characterise the oxide layer formed on the metallic bond coat. The activation energy for alumina, formed at various temperatures, is lower than the activation energy of pure alumina because of the impurities in the alumina layer formed in samples at high temperatures.

The YSZ coating failure in the TBC system is different from the failure of the oxide scale without a ceramic top coat. During high temperature oxidation, the TGO generates stresses and causes buckling or spallation of the TBC layer. In the TBC system, cracks occurred either at the TGO/YSZ interface or in TGO layer itself. Three semicircles were found in the impedance spectra of the TBC samples, which correspond to the YSZ top coat, the TGO layer from oxidation, and the TGO/YSZ interface. The TGO could have a two-layer structure. Firstly, a dark alumina-rich oxide layer formed and then a grey mixed oxide layer could form on top of that. IS was used to evaluate the effect of microstructural changes on the dark alumina layer, formed at 1030°C and 1200°C in air, for the TBC. The impedance response for oxide layers changed with the changing microstructure of the oxide layers. Electrical resistance increased with increasing alumina layer thickness. A similar activation energy and composition for the alumina-rich oxide layers, formed at 1030°C and 1200°C, indicated that a similarity for the alumina formed at both high temperature and low temperature. It was also observed that changes of activation energy were related to the changes happening in the microstructure of the TBC system. The activation energy of conduction through the oxide layer decreased with the formation of the grey mixed oxide layer on top of the dark alumina-rich oxide layer. For ageing at 1030°C, the activation energy for the oxide layer decreased with decreasing alumina content in the dark oxide layer with the formation of mixed oxide on top of the alumina layer. Ageing of TBC samples at 1200°C produced a TGO containing a mixed oxide with a reduced activation energy.

Impedance analysis for the characterisation of the TGO formed at high temperature, can represent the characteristic of oxides formed at low temperature. So damage

caused in the TBC system of a turbine engine at low temperature over several years can be studied in a laboratory environment at high temperature in several weeks. This facilitates research on the non-destructive evaluation of TBC degradation using IS in a laboratory environment.

The growth of the mixed oxide layer at 1150°C in air at the metal/YSZ interface was identified as a typical example of the degradation of a TBC system. Changes in the electrical properties of TGOs are related to those in their microstructure and microchemistry. The resistivity decreases with increasing oxidation time in the whole time range and the decreasing rate is much higher between 10 and 1000 hours than between 1000 and 2000 hours. During thermal cycling of TBCs, TGOs change from α-Al_2O_3 to a mixture of α-Cr_2O_3 and (Ni or Co)(Cr or Al)$_2O_4$ spinel and their microstructural and microchemical evolution are responsible for the changes in their electrical properties.

The microstructural examination of the TBC system showed that cracks initiated and propagated in the TGO layer and sometimes through the YSZ layer, parallel to the YSZ top coat. Impedance measurements have been used to examine the initiation and propagation of cracks in TBC samples after thermal cycling at 1200°C. Interfacial resistance and capacitance were induced due to the formation of a double layer and charge transfer at the TGO/YSZ interface. Microstructural examination of the TBC samples showed that cracks initiated and propagated during the thermal cycling, while the impedance measurements showed that the interfacial resistance increased with an increase in the thermal cycling time. Even for the samples thermally cycled for the same period, the interfacial resistance was also related to the length of cracks at the TGO/YSZ interface. The relaxation frequency corresponding to the TGO/YSZ interface also shows a gradual decrease due to thermal cycling. It is believed that crack propagation caused the decrease in the area of the TGO/YSZ interface and therefore, reduced the interfacial resistance.

From this research, it was concluded that IS can be used to monitor the degradation of high temperature alloys, with or without a TBC coating, during high temperature

ageing. IS is a powerful tool to examine oxidation phenomena. IS can monitor engine components by giving early warning of their degradation. It is a non-destructive method and it can be applied to industrial applications easily.

8.2. Suggestions for Future Work

Research work performed in this thesis has shown that IS is a suitable method for the non-destructive evaluation of the degradation of TBC systems. This may bring benefit to the routine, *in situ*, inspection of turbine engines. Much work is still needed in order to apply the benefits of this research in a commercial environment. With regard to the issues considered in this thesis, the following aspects are suggested for future work.

The YSZ in the TBC sample is a porous material and the TGOs formed at the YSZ/bond coat interface may penetrate into these pores in the YSZ grain boundaries. The change in the YSZ grain boundaries is an important factor leading to the degradation of the YSZ layer, which then may contribute to the failure of the TBC systems. It has been recognised in chapter 5 that the impedance of YSZ layer did not change with thermal ageing of the TBC samples. The high frequency semicircle in the impedance spectrum of TBC sample, used to deduce the impedance for the YSZ layer was mainly from the YSZ grains. Therefore, it did not change with thermal ageing of the TBC samples. The slight change observed in the intermediate frequency semicircle, which is associated mainly with the mixed oxide, may contain an impedance response from the YSZ grain boundaries. However, more detailed work on the thermal ageing effects on the YSZ grain boundaries in TBC samples is required to substantiate this proposition.

In chapter 6, it has been suggested that the impedance altered with changing composition and porosity of the TGOs in the TBC samples. It has been found that increased porosity in the TGO layer degraded the TBC systems. To go further one needs to separate the effect of porosity from the changes in the composition. A detailed study is necessary in order to establish a relationship between porosity and

the impedance response for the TGOs. In TGOs, the oxides of Cr, Ni and Co etc. were present as trace amounts in the alumina layer. Further study is required to demonstrate the effect of each of these oxides separately on the impedance response of the alumina layer.

In the research presented in chapter 7, the low frequency semicircle was identified for the TGO/YSZ interface. This low frequency semicircle changed with thermal ageing. The composition of the TGO changed before the formation of cracks. The YSZ is an ionic conductor and the TGO is an electronic conductor. A change in the TGO composition changed the TGO/YSZ interface and this may affect the impedance response of this interface. Further study is required to understand the relationship between the impedance and the composition of the TGO/YSZ interface.

The surface of the YSZ is rough. In this thesis, the silver or platinum paint, used for electrode preparation, was fired in a specific manner in order to get repeatable results. Any variation in firing condition could affect the impedance results, because of the variation of contact area or the level of penetration in to the TBC. A variation in the particle size of the paint could also effect the contact area. Thus it is not sensible to use paint as an electrode material to monitor continuously the growth of defects under the TBC layer. Therefore, it is necessary to develop an electrode system which will remain on the surface of the TBC without any kind of degradation of the electrode materials or changes of the contact area between the electrode and the TBC.

Platinum can withstand high temperatures without any oxidation. If the contact area between the platinum plate and the TBC surface can be improved, then it can be used as an electrode material for the continuous monitoring of engine components in operating conditions. Further study is required to improve the contact area between the platinum plate and the YSZ surface. After solving the electrode problem, the results of this thesis could be tested for long-term studies using commercial gas turbine engines under operating conditions.

References

M.S. Ali, S. Song and P. Xiao, (2002) "Evaluation of Degradation of Thermal Barrier Coatings using Impedance Spectroscopy", Journal of the European Ceramic Society, Volume 22, Issue 1, Pages 101-107.

J.H. Ambrus, C.T. Moynihan and P.B. Macedo, (1972), "Conductivity relaxation in a concentrated aqueous electrolyte solution", J. Phys. Chem., Volume 76, Pages 3287-3295.

S.T. Amaral and I.L. Muller, (1999), "Effect of silicate on passive films anodically formed on iron in alkaline solution as studied by electrochemical impedance spectroscopy", Corrosion, Volume 55(1), Pages 17-23.

M. Aoki and Y.–M. Chiang, (1996), "Solute segregation and grain boundary impedance in high-purity stabilised zirconia", Journal of American Ceramic Society, Volume 79, Pages 1169-1180.

R.D. Armstrong, T. Dickinson and P.M. Willis, (1974), "The a.c. impedance of powdered and sintered solid ionic conductors", Journal of Electroanalytical Chemistry, Volume 53, Pages 389-405.

R.D. Armstrong and M. Todd, (1995), "Interfacial electrochemistry", Solid State Electrochemistry, P.G. Bruce, (Edition), Cambridge University Press, Pages 265-291.

P. Barberis and A. Frichet, (1999), "Characterisation of Zircaloy-4 oxide layers by impedance spectroscopy", Journal of Nuclear Materials, Volume 273, Pages 182-191.

A.J. Bard and L.R. Faulkner, (1980), "Techniques Based on Concepts of Impedance", Chapter 9, Electrochemical Methods (Fundamentals and Application), John Wiley & Sons, Pages 316-369.

A.H. Bartlett and R.D. Maschio, (1995), "Failure Mechanisms of a Zirconia-8 wt% Yttria Thermal Barrier Coating", Journal of American Ceramic Society, Volume 78, Number 4, Pages 1018-1024.

J.E. Bauerle, (1969), "Study of solid electrolyte polarisation by a complex admittance method", Journal of Physics and Chemistry of Solids, Volume 30, Pages 2657-2670.

V.V. Belousov and B.S. Bokshtein, (1998), "Model of the Rapid Stage of Catastrophic Oxidation of Metals", Oxidation of Metals, Volume 50, Number 5-6, Pages 477-493.

A. Bieberle and L.J. Gauckler, (2000) "Reaction mechanism of Ni pattern anodes for solid oxide fuel cells", Solid State Ionics, Volume 135, Pages 337-335.

N. Birks and G.H. Meier, (1983), Introduction to High Temperature Oxidation of Metals, Edward Arnold, London.

N. Birks, G.H. Meier and F.S. Pettit, (December, 1994), "Forming Continuous Alumina Scales to Protect Superalloys", JOM, Pages 42-46.

N. Bonanos, B.C.H. Steele and E.P. Butler, (1987), "Characterisation of materials", Impedance Spectroscopy, Edited by J. R. Macdonald, John Willey & Sons, Pages 191-237.

S. Bose and J. DeMasi-Marcin, (1997), "Thermal Barrier Coating Experience in Gas Turbine Engines at Pratt & Whitney", Journal of Thermal Spray Technology, Volume 6(1), Pages 99-104.

M.C. Brant and L. Dessemond, (2000) "Electrical degradation of LSM-YSZ interfaces", Solid State Ionics, Volume 138, Pages 1-17.

P.G. Bruce and A.R. West, (1983), "The A. C. Conductivity of Polycrystalline LISICON $Li_{2+2x}Zn_{1-x}GeO_4$ and a Model for Intergranular Constriction Resistances", Journal of Electrochemical Society, Volume 130, Pages 662-669.

Z.A. Chaudhury, G.M. Newaz and T Ahmed, (1998), "Interface cracking due to isothermal heating in thermal barrier coatings (TBCs)", Journal of Material Science Letters, Volume 17, Pages 85-87.

Z.A. Chaudhury, G.M. Newaz, S.Q. Nusier and T. Ahmed, (1997), "Interfacial damage in EB-PVD thermal barrier coatings due to thermal cycling", Materials Science and Engineering, Volume A231, Pages 34-41.

Y.-M. Chiang, D.P. Birnie, and W.D. Kingery, (1997), Physical Ceramics, John Wiley and Sons, New York.

Y.-M. Chiang, E.B. Lavik and D.A. Blom, (1997), "Defect thermodynamics and electrical properties of nanocrystalline oxides: pure and doped CeO2, Nanostructured Materials, Volume 9, Pages 633-642.

J. Cho, H.M. Chan, M.P. Harmer and J.M. Rickman, (1998), "Influence of Yttrium Doping on Grain Misorientation in Aluminum Oxide", Journal of American Ceramic Society, Volume 81, Noumber 11, Pages 3001-3004.

B.J. Christensen, R.T. Coverdale, R.A. Olson, S.J. Ford, E.J. Garboczi, H.M. Jennings, and T.O. Mason, (1994), "Impedance Spectroscopy of Hydrating Cement-Based Materials: Measurement, Interpretation, and Application", Journal of the American Ceramic Society, Volume 77, Number 11, Pages 2789-2804.

S-Y. Chun, and N. Mizutani, (2001), "The transport mechanism of YSZ thin films prepared by MOCVD", Applied Surface Science, Volume 171, Pages 82-88.

N.D. Cogger and N.J. Evans, (1998), "An Introduction to Electrochemical Impedance Measurement", Technical Report Number 006, Solartron, Farnborough, UK.

K.S. Cole, and R.H. Cole, (1941), "Dispersion and adsoption in dielectrics I. alternating current characteristics", J. Chem. Phys., Volume 9, Pages 341-351.

P.T. Curtis, J. Gates and G.G. Margerison, (1993), "The selection of cyclic load frequency for the fatigue testing of fibre reinforced polymeric composites", Rae Technical Report 93017 (Farnborough, Guildford, UK).

C.L. Curtis, D.T. Gawne and M. Priestnall, (1994), "The processing and electrical properties of plasma-sprayed yttria-zirconia", Journal of Material Science, Volume 29, Pages 3102-3106.

F. Deflorian, L. Fedrizzi and S Rossi, (August 1998), "Electrochemical Impedance Spectroscopy and Fourier Transform Infrared Spectroscopy of Natural and Accelerated Weathering of Organic Coatings", Corrosion, Volume 54, Number 8, Pages 598-605.

C. Deslouis, M.C. Lafont, N. Pebere and D. You, (1993), "Corrosion inhibition of pure iron in natural solutions by electrochemical techniques", Corrosion Science, Volume 34, Pages 1567-1579.

L. Dessemond, R. Muccillo, M. Henault and M Kleitz, (1993), "Electric Conduction-Blocking Effects of Voids and Second Phases in Stabilised Zirconia", Applied Physics A (Solids and Surfaces), Volume A57, Pages 57-60.

P. Diaz, M.J. Edirisinghe and B. Ralph, (1996), "Microstructure changes and phase transformations in a plasma-sprayed zirconia-yttria-titania thermal barrier coating", Surface and Coating Technology, Volume 82, Pages 284-290.

T.J. Dunyak, W.W. Stiuchcomb and K.L. Reifsnider, (1992), "Examination of selected NDE techniques for ceramics composites damage detection", Page 3, Damage Detection in Composite Materials, ASTM, STP 1128, J. E. Masters (edition), American Society for Testing and Materials, Phyladelphia.

M.L. Escudero, J.L. Gonzalez-Carrasco, C. Garcia-Alonso and E. Ramirez, (1995), "Electrochemical impedance spectroscopy of preoxidized MA 956 superalloy during in vitro experiment", Biomaterials, Volume 16, Number 9, Pages 735-740.

A.G. Evans, M.Y. He and J.W. Hutchinson, (2001), "Mechanics-based scaling laws for the durability of thermal barrier coatings", Progress in Materials Science, Volume 46, Pages 249-271.

A.G. Evans, D.R. Mumm, J.W. Hutchinson, G.H. Meier and F.S. Pettit, (2001), "Mechanisms controlling the durability of thermal barrier coatings", Progress in Materials Science, Volume 46, Pages 505-553.

A.J. Feighery and J.T.S. Irvine, (1999), "Effect of alumina addition upon electrical properties of 8 mol.% yttria-stabilised zirconia", Solid State Ionics, Volume 121, Pages 209-216.

M.K. Ferber, A.A. Wereszczak, M. Lance, J.A. Haynes and M.A. Antelo, (2000), "Application of infrared imaging to the study of controlled failure of thermal barrier coatings", Journal of Materials Science, Volume 35, Pages 2643-2651.

J. Fleig, (2000), "The influence of non-ideal microstructures on the analysis of grain boundary impedance", Solid State Ionics, Volume 131, Pages 117-127.

J. Fleig and J Maier, (June, 1998), "A Finite Element Study on Grain Boundary Impedance of Different Microstructures", J. Electrochem. Soc., Volume 145, Noumber 6, Pages 2081-2089.

J. Fleig and J. Maier, (1999), "The impedance of ceramics with highly resistive grain boundaries: validity and limits of the brick layer model", Journal of the European Ceramic Society, Volume19, Pages 693-696.

J.G. Fletcher, A.R. West and J.T.S. Irvine, (August, 1995), "The AC Impedance Response of the Physical Interface Between Yttria-Stabilised Zirconia and $Yba_2Cu_3O_{7-X}$", Journal of Electrochemical Society, Volume 142, Number 8, Pages 2650-2654.

A.M. Freborg, B.L. Ferguson, W.J. Brindley and G.J. Petrus, (1998), "Modeling oxidation induced stresses in thermal barrier coatings", Materials Science and Engineering, Volume A245, Pages 182-190.

G. Garcia, A. Figueras, J. Llibre, M. Mokchah, G. Petot-Ervas, J. Calderer, (1998), "Yttria-stabilised zirconia obtained by MOCVD: application", Thin Solid Films, Pages 241-244.

M.F. Gillies, A.E.T. Kuiper and R. Coehoorn, (July, 2000), "Compositional, structural, and electrical characterisation of plasma oxidized thin aluminum layers for spin-tunnel junctions", Journal of Applied Physics, Volume 88, Number 1, Pages 429-434.

J.A. Grandle and S.R. Taylor, (May, 1997), "Electrochemical Impedance Spectroscopy as a Method to Evaluate Coated Aluminum Beverage Containers-Part 2: Statistical Analysis of Performance", Corrosion, Volume 53, Number 5, Pages 347-355.

S. Harada, Y. Ikeda, Y. Mizuta, Y. Sugita and A. Ito, (1995), "The inspection of delaminated defects in ZrO_2 coated material by infrared thermography techniques", Proceedings of the International Symposium on Thermographic NDT and E Techniques Symposium, Pages 47-52.

J.A. Haynes, E.D. Rigney, M.K. Ferber and W.D. Porter, (1996), "Oxidation and degredation of a plasma-sprayed thermal barrier coating system", Surface and Coatings Technology, Volume 86-87, Pages 102-108.

M.Y. He, A.G. Evans and J.W. Hutchinson, (May, 1998), "Effects of morphology on the decohesion of compressed thin films", Material Science and Engineering, Volume A245, Pages 168-181.

M.Y. He, A.G. Evans and J.W. Hutchinson, (2000), "The ratcheting of compressed thermally grown thin films on ductile substrates", Acta. mater., Volume 48, Pages 2593-2601.

L.M. Hodge, M.D. Ingram and A.R. West, (1976), "Impedance and modulus spectroscopy of polycrystalline solid electrolytes", Journal of Electroanalytical Chemistry, Volume 74, Pages 125-143.

Y. Ji, J. Liu, Z. Lu, X. Zhaw, T. He and W. Su, (1999), "Study on the properties of Al_2O_3-doped $(ZrO_2)_{0.92}(Y_2O_3)_{0.08}$ electrolyte", Solid State Ionics, Volume 126, Pages 277-283.

D. Jiles, (1994), "Electronic properties of semiconductors", Introduction to the Electronic Properties of Materials, D. Jiles (Edition), Chapman & Hall, Page130.

A.K. Jonscher, (1978), "Analysis of the alternating current properties of ionic conductors", Journal of Material Science, Volume 13, Pages 553-562.

A.K. Jonscher and J.-M. Reau, (1978), "Analysis of the complex impedance data for *-PdF_2", Journal of Material Science, Volume 13, Pages 563-570.

W.D. Kingery, H.K. Bowen and D.R. Uhlamann, (1976), "Electrical conductivity", Introduction to Ceramics, John Wiley & Sons, Page 851.

M. Kleitz, L. Dessemond and M.C. Steil, (1995), "Model for ion-blocking at internal interfaces in zirconias", Solid State Ionics, Volume 75, Pages 107-115.

O. Kubaschewski and B.E. Hopkins, (1967), Oxidation of metals and alloys, 2nd Edition, Butterworths, London.

G. Lang, and K.E. Heusler, (1998), "Remark on the energetics of interfaces exhibiting constant phase element behaviour", Journal of Electroanalytical Chemistry, Volume 457, Pages 257-260.

J. Lee, T.J. Chung and D.Y Kim, (2000), "Electrical and microstructural characterisation on nitrogen-stabilised zirconia", Solid State Ionics, Volume 136-137, Pages 39-44.

D.R. Lide, (1998), CRC Handbook of Chemistry and Physics, 79th Edition (1998-1999) CRC Press LLC.

S.H. Liu, (1985), "Fractal Model for the ac Response of a Rough interface", Phys. Rev. Lett., Volume 55, Pages 529-532.

H. Liu, C. Mojica-Calderon, S.B. Lyon and M.M. Stack, (1999), "In situ solid state electrochemical impedance spectroscopy of NiO scales", Solid State Ionics, Volume 126, Pages 363-372.

X.Q. Ma, S. Cho and M. Takemoto, (2001), "Acoustic emission source analysis of plasma sprayed thermal barrier coatings during four-point bend tests", Surface and Coating Technology, Volume 139, Pages 55-62.

J.R. MacDonald, (1987), Impedance Spectroscopy, John Wiley & Sons, Chichester.

J.R. Macdonald and D.R. Franceschetti, (1987), "Physical and electrochemical models", Impedance Spectroscopy, Edited by J. R. Macdonald, John Willey & Sons, Pages 84-132.

J.R. Macdonald and W.B. Johnson, (1987), "Fundamentals of Impedance Spectroscopy", Impedance Spectroscopy, Edited by J. R. Macdonald, John Willey & Sons, Pages 1-26.

P.B. Macedo, C.T. Moynihan, and R. Bose, (1972), "Role of ionic diffusion in polarisation in vitreous ionic conductors", Phys. Chem. Glass, Volume 13, Pages 171-176.

H.S. Maiti, and RN. Basu, (1986), "Complex-plane impedance analysis for semi-conducting barium titanate", Materials Research Bulletin, Volume 21, Pages 1107-1114.

F. Mansfeld, (May, 1981), "Recording and Analysis of AC Impedance Data for Corrosion Studies", Corrosion, Volume 36, Number 5, Pages 301-307.

R.A.. Miller, (March, 1997), "Thermal Barrier Coatings for Aircraft Engines: History and Directions", Journal of Thermal Spray Technology, Volume 6(1), Pages 35-42.

S.C. Miller, (1995), "Aero, Industrial and Marine Gas Turbines", Materials Engineering in Turbines and Compressors, Conference proceedings, The Institute of Materials, Volume 1, Pages 17-23.

A. Miszczyk, K. Darowicki and Z. Klenowicz, (July, 1997), "Use of Impedance Spectroscopy to Characterise Lining Performance in Simulated Flue Gas Desulfurization Systems", Corrosion, Volume 53, Number 7, Pages 572-580.

F.D. Morrison, D.C. Sinclair and A.R. West, (March, 2001), "Characterisation of Lanthanum-Doped Barium Titanate Ceramics Using Impedance Spectroscopy", Journal of the American Ceramic Society, Volume 84, Number 3, Pages 531-538.

A.J. Moses, (1978), The Practicing Scientist's Handbook, Van Nortrand Reinhold Company (New York, London etc.).

E.N.S. Muccillo and M. Kleitz, (1996), "Impedance Spectroscopy of Mg-Partially Stabilised Zirconia and Cubic Phase Decomposition", Journal of the European Ceramic Society, Volume 16, Pages 453-465.

J.J. Nevadunsky, and J.J. Lucas, (1975), "Early fatigue damage detection in composite materials", Journal of Composite Materials, Volume 9, Pages 394-408.

K. Ogawa, D, Minkov, T. Shoji, M. Sato, and H. Hashimoto, (1999), "NDE of degradation of thermal barrier coating by means of impedance spectroscopy", NDT&E International, Volume 32, Pages 177-185.

J. Pan, C. Leygraf, R.F.A. Jargelius-Pettersson and J. Linden, (1998), "Characterisation of High-Temperature Oxide Films on Stainless Steels by Electrochemical-Impedance Spectroscopy", Oxidation of Metals, Volume 50, Numbers 5/6, Pages 431-455.

Y.M. Park and G.M. Choi, (1999), "Microstructure and electrical properties of YSZ-NiO composites", Solid State Ionics, Volume 120, Pages 265-274.

X. Peng and D.R. Clarke, (2000), "Piezospectroscopic Analysis of Interface Debonding in Thermal Barrier Coatings", Journal of the American Ceramics Society, Volume 83, Number 5, Pages 1165-1170.

B.A. Pint and K.B. Alexander, (June, 1998), "Grain Boundary Segregation of Cation Dopants in α-Al2O3 Scales", J. Electrochem. Soc., Volume 145, Number 6, Pages 1819-1829.

W.J. Quadakkers and M.J. Bennett, (February 1994), "Oxidation induced lifetime limits of thin walled, iron based, alumina forming, oxide dispersion strengthened alloy components", Material Science and Technology, Volume 10, Pages 126-131.

I.D. Raistrick, (1987), "Electrical analogs of physical and chemical processes", Impedance Spectroscopy, Edited by J. R. Macdonald, John Willey & Sons. Pages 27-83.

U. Rammelt and G. Reinhard, (March, 1995), "Impedance analysis of conversion layers on iron", Electrochimica Acta, Volume 40, Issue 4, Pages 505-511.

G.H. Rhoderick, (1978), "Introduction and synopsis", Metal-Semiconductor Contacts, Clarence Press, Oxford, Pages 1-17.

D.W. Richerson, (1992), "Electrical Behaviour", Modern Ceramic Engineering (Properties, Processing and Use in Design), Second Edition (Revised and Expanded), Marcel Dekker Inc., Pages 204-249.

M. Saitoh, Y. Itoh and J. Ishii, (1995), " Evaluation of thermal barrier coating using infrared thermography", Proceedings of the International Symposium on Thermographic NDT and E Techniques Symposium, Pages 53-58.

G.V. Samsonov, (1973), The Oxide Handbook, IFI/Plenum, London.

A.P. Santos, R.Z. Domingues and M Kleitz, (1998), "Grain Boundary Blocking Effect in Tetragonal Yttria Stabilised Zirconia", Journal of the European Ceramic Society, Volume 18, Pages 1571-1578.

W. Scheider, (1975), "Theory of the frequency dispersion of electrode polarisation. Topology of networks with fractional power frequency dependence", J. Phys. Chem., Volume 79, Pages 127-136.

M. Schutze, (1997), Protective Oxide Scales and Their Breakdown, John Wiley & Sons.

V. Sergo and D.R. Clarke, (1998), "Observation of Subcritical Spall Propagation of a Thermal Barrier Coating" J. Am. Ceram. Soc., Volume 81, Number 12, Pages 3237-3242.

B.B. Seth, R.D. Conroy and M.J. Goulette, (1995), "Market Forces and Turbine Materials Innovations", Materials Engineering in Turbines and Compressors, Conference proceedings, The Institute of Materials, Volume 1, Pages 67-101.

E.A.G. Shillington and D.R. Clarke, (1999), "Spalling failure of thermal barrier coating associated with alumina depletion in the bond coat" Acta Mater., Volume 47, Page 1297-1305.

D.C. Sinclair, F.D. Morrison and A.R. West, (2000), "Application of combined impedance and electric modulus spectroscopy to characterise electroceramics", International Ceramics, Issue 2, Pages 33-37.

G.-L. Song, (2000), "Equivalent circuit model for AC electrochemical impedance spectroscopy of concrete", Cement and Concrete Research, Volume 30, Pages 1723-1730.

S.-H. Song and P. Xiao, (2001), "Microstructure evolution of the oxide film formed during high temperature oxidation of nickel evaluated by means of impedance spectroscopy", Scripta Mater, Volume 44, Pages 601-606.

B.C. Steele, (1989), High conductivity Solid Ionic Conductors, T. Takahashi, (Edition) World Scientific, Singapore.

M.C. Steil, F. Thevenot and M. Kleitz, (January, 1997), "Densification of Yttria-Stabilised Zirconia", Journal of Electrochemical Socciety, Volume 144, Number 1, Page 390-398.

H.M. Tawancy, N. Sridhar and N.M. Abbas, (1998), "Failure mechanism of a thermal barrier caoting system on a nickel-base superalloy", Journal of Material Science, Volume 33, Pages 681-687.

K. Teske, M. Al Daroukh, H. Langbein and H. Ullamann, (2000), "Temperature dependence of electrical conductivity of oxides with a range of stoichiometry under isostoichiometric conditions", Solid State Ionics, Volume 133, Pages 121-128.

I. Thompson and D. Campbell, (1994), "Interpreting Niquist Responses from Defective Coatings on Steel Substrates", Corrosion Science, Volume 36, Number 1, Pages 187-198.

O.K. Varghese and L.K. Malhotra, (May, 2000), "Studies of ambient dependant electrical behaviour of nanocrystalline SnO_2 thin films using impedance spectroscopy", Journal of Applied Physics, Volume 87, Number 10, Pages 7457-7465.

J.J. Vermoyal, A. Frichet, L. Dessemond and A. Hammaou, (1999), "AC impedance study of corrosion films formed on zirconium based alloys", Electrochimica Acta, Volume 45, Pages 1039-1048.

X. Wang, J. Mei, and P. Xiao, (2001), "Determining Oxide growth in the thermal barrier coatings non-destructively using impedance spectroscopy," J. Mater. Sci. Lett., Volume 20, Pages 47-49.

R. Waser and R. Hagenbeck, (2000), "Grain Boundary in dielectric and mixed conducting ceramics", Acta Materialia, Volume 48, Pages 797-825.

H. Wise and J. Oudar, (1990), "Oxide Layer Formation on Metal Surfaces", Chapter 11, Material Concepts in Surface Reactivity and Catalysis, San Diego: Academic Press.

P.K. Wright, (1998), "Influence of cyclic strain on life of a PVD TBC", Materials Science and Engineering, Volume A245, Pages 191-200.

D.G. Wirth, (1991) "Ceramic Substrate", Engineering Materials Handbook (Ceramics and Glasses), Volume 4, S.J. Schneider Jr. (Volume Chairman), ASM International, Pages 1107-1111.

Y. Zhu and C. Ding, (2000), "Characterisation of plasma sprayed nano-titania coatings by impedance spectroscopy", Journal of the European Ceramic Society, Volume 20, Pages 127-132.

D. Zhu and R.A. Miller, (1998), "Investigation of thermal high cycle and low cycle fatigue mechanisms of thick thermal barrier coatings", Materials Science and Engineering, Volume A245, Pages 212-223.